A CFD STUDY OF FLUID-STRUCTURE INTERACTION PROBLEMS FOR FLOATING OFFSHORE WIND TURBINES

Yuanchuan Liu

A thesis submitted in fulfilment of the requirements for the degree of Doctor of Philosophy

Department of Naval Architecture, Ocean and Marine Engineering
University of Strathclyde
Glasgow

June 2018

Declaration

This thesis is the result of the author's original research. It has been composed by the author and has not been previously submitted for examination which has led to the award of a degree.

Yuanchuan Liu

Signature: Yuanchuan Liu Date: 8/6/2018

Acknowledgements

First of all, I would like to express my sincere gratitude to my first supervisor Dr Qing Xiao, who has continuously supported me throughout my PhD with her patience and expertise in CFD. Dr Xiao has devoted a great deal of time and effort to guiding me in my research, which is very much appreciated.

I would like to thank my second supervisor Prof Atilla Incecik for offering his help and invaluable advice on my PhD. His enthusiasm for life and work has always inspired me.

I am thankful to Mr Christophe Peyrard and Mr Raffaello Antonutti from Électricité de France (EDF) for generously providing insightful suggestions and comments to my PhD research.

I would like to thank Mrs Thelma Will, Mrs Susan Pawson and all other staff in the department of NAOME for their kind help with all the administrative issues.

I would like to show my appreciation to my colleagues in the department of NAOME for assisting me in my research and all my friends in Glasgow for making my life more enjoyable.

I would like to acknowledge the full scholarship provided by University of Strathclyde and EDF via the University Research Studentship to support my PhD, and the access kindly granted by EDF to its Athos HPC facility for numerical simulations.

Finally, I am deeply indebted to my family for their everlasting love and encouragement, and to my beloved girlfriend Miss Ruoxin Li and her parents for their full understanding and support. I am truly grateful to Ruoxin for always keeping me company and making every day special.

Abstract

As one of the fastest growing renewable energy sources, wind energy is playing an increasingly important part in addressing the climate change and energy crisis issues the world is currently facing. The abundance of wind resource in offshore areas makes them a popular choice for turbine installation. In the past few years, several floating wind projects have emerged where wind turbines are installed far offshore in deep-water sites on moored platforms. Compared to land-based or offshore fixed-bottom wind turbines, an FOWT is a fully coupled system where the wind turbine with flexible blades and the floating platform with its mooring system interact with each other in wind and waves, which makes old design tools inadequate. This work aims to develop a fully coupled high-fidelity aero-hydro-mooring-elastic analysis tool, and to better understand the sophisticated fluid-structure interactions for FOWTs.

The numerical tool developed in this work takes advantage of the open source CFD toolbox OpenFOAM to accurately solve wind turbine aerodynamics and floating platform hydrodynamics, and utilises the open source MBD code MBDyn for structural dynamics within a multibody framework while modelling flexible bodies based on a nonlinear beam theory. Coupling of these two solvers is achieved by establishing an interface library to exchange data with the help of the TCP/IP protocol. Additionally, to tackle the complex mesh movement in FOWT simulations, a mesh motion solver is developed in OpenFOAM by combining the sliding mesh technique and the dynamic mesh morphing method. A mooring system analysis module comprising a quasi-static method and a lumped-mass based dynamic approach is also implemented to simulate mooring lines in an FOWT system.

A series of test cases is firstly studied to validate the various features of the tool, including basic fluid flow solving, modelling of wind turbine aerodynamics, hydrodynamic analysis of a floating structure with its mooring system, dynamic analysis of a riser or mooring line and coupled analysis of flow induced vibration of a flexible beam. The developed tool is then applied to analyse FSI problems of FOWTs under three different scenarios.

Firstly, a coupled aero-hydro-mooring analysis is carried out for the OC4 semi-submersible FOWT under regular waves and uniform wind speed. Blade flexibility is ignored, and mooring lines are solved using the quasi-static method. Interactions between the moored platform and the wind turbine are investigated, focusing on the effects of platform motion on the aerodynamic performance of the wind turbine and the impacts of wind turbine aerodynamics on the responses of the floating platform and its mooring system.

Subsequently, an aeroelastic analysis is conducted for the NREL 5-MW offshore wind turbine with flexible blades under uniform wind speed. Effects of blade flexibility on wind turbine aerodynamics and structural responses are studied using the developed CFD-MBD tool. The floating platform supporting the turbine is not directly modelled for simplicity and the influence of platform motion responses on the turbine are analysed via imposing a prescribed surge motion to the turbine base.

Fully coupled aero-hydro-mooring-elastic analysis is lastly carried out for the OC4 semi-submersible FOWT under a combined wind/wave condition to demonstrate the capabilities of the developed CFD-MBD tool. Responses of the floating system are investigated in terms of platform hydrodynamics, mooring system dynamics, wind turbine aerodynamics and blade structural dynamics. Interactions between the FOWT and fluid flow are analysed by visualising results obtained via the CFD approach.

Table of Contents

List of Figures

List of Tables

Nomenclature

Roman Symbols

A	Cross-sectional area of mooring line
$\boldsymbol{B}$	Transformation matrix from global to local mooring line segment reference frame
$\boldsymbol{C}$	Structural linear viscosity matrix
C_{AN}	Added mass coefficient of mooring line in normal direction
C_{AT}	Added mass coefficient of mooring line in tangential direction
C_{DN}	Drag coefficient of mooring line in normal direction
C_{DT}	Drag coefficient of mooring line in tangential direction
C_p	Pressure coefficient
D	Wind turbine diameter
E	Young's modulus
f_A	Inertia force of mooring line segment
f_D	Drag force of mooring line segment
$\boldsymbol{g}$	Gravitational acceleration vector
$\boldsymbol{K}$	Structural linear stiffness matrix
p	Fluid pressure
Q	Second invariant of the rate of strain tensor
r	Radial position along turbine blade
r/R	Relative radial position with respect to wind turbine radius
R	Radius of wind turbine
T	Tension force of mooring line
u_{rw}	Resultant wind speed

u_{surge}	Platform surge motion velocity
u_{wind}	Incoming wind speed
$\mathbf{U}$	Fluid velocity
$U_{FlapDef}$	Wind turbine blade flapwise deflection velocity
$\mathbf{U}_g$	Velocity of grid nodes
Ux	Axial component of fluid flow velocity
w	Weight per unit length of mooring line in water
$\mathbf{x}_g$	Displacement of mesh cell centres

Greek Symbols

α	Volume fraction variable
γ	Diffusion coefficient for mesh motion equation
$\boldsymbol{\varepsilon}$	Generalised strain vector
η	Free surface elevation
θ_{pitch}	Platform pitch motion angle
μ	Dynamic viscosity of fluid
μ_s	Artificial viscosity of fluid
μ_t	Turbulent dynamic viscosity of fluid
ν	Kinematic viscosity of fluid
ν_t	Eddy kinematic viscosity of fluid
ρ	Density of fluid
ρ_s	Density of solid
ω	Prescribed motion frequency
ω_{pitch}	Platform pitch motion angular velocity

Abbreviations

1D	One-dimensional
2D	Two-dimensional
3D	Three-dimensional
AMI	Arbitrary Mesh Interface
AOA	Angle of Attack
BEM	Blade Element Momentum
CFD	Computational Fluid Dynamics
CM	Centre of Mass
DoF	Degree of Freedom
DTU	Technical University of Denmark
EU	European Union
FAST	Fatigue, Aerodynamics, Structures, and Turbulence
FEA	Finite Element Analysis
FEM	Finite Element Method
FOWT	Floating Offshore Wind Turbine
FSI	Fluid-Structure Interaction
GDW	Generalized Dynamic Wake
GEBT	Geometrically Exact Beam Theory
IEA	International Energy Agency
KC	Keulegan-Carpenter
MARIN	Maritime Research Institute Netherlands
MBD	MultiBody Dynamics
MRF	Multiple Reference Frame

NREL	National Renewable Energy Laboratory
OC4	Offshore Code Comparison Collaboration, Continuation
OC5	Offshore Code Comparison Collaboration, Continuation, with Correlation
RANS	Reynolds Averaged Navier-Stokes
RAO	Response Amplitude Operator
RPM	Revolutions per Minute
SST	Shear Stress Transport
SWL	Still Water Level
TLP	Tension Leg Platform
UBEM	Unsteady Blade Element Momentum
VOF	Volume of Fluid

Chapter 1 Introduction

1.1 Background

1.1.1 Development of Offshore Wind Energy

Having used fossil fuels, such as coal, oil and gas, as major energy sources for centuries since the Industrial Revolution, the world is becoming increasingly concerned about their significant impacts on climate, including global warming, rising sea level and more frequent extreme weather. Climate change is a global threat affecting everyone in every country and people around the world are actively responding to the challenges it brings about. Turning to new forms of energy, which are clean and do not produce greenhouse gas emission, seems like a promising solution. On the other hand, the demand for energy has been continuously increasing. As fossil fuels are finite and non-renewable, new sources of energy must be adopted before they eventually become exhausted or are too costly to harvest. In order to address issues from both climate change and energy crisis, it has become increasingly essential to shift the reliance of human society on fossil fuels to other clean and renewable energy sources such as wind or solar power.

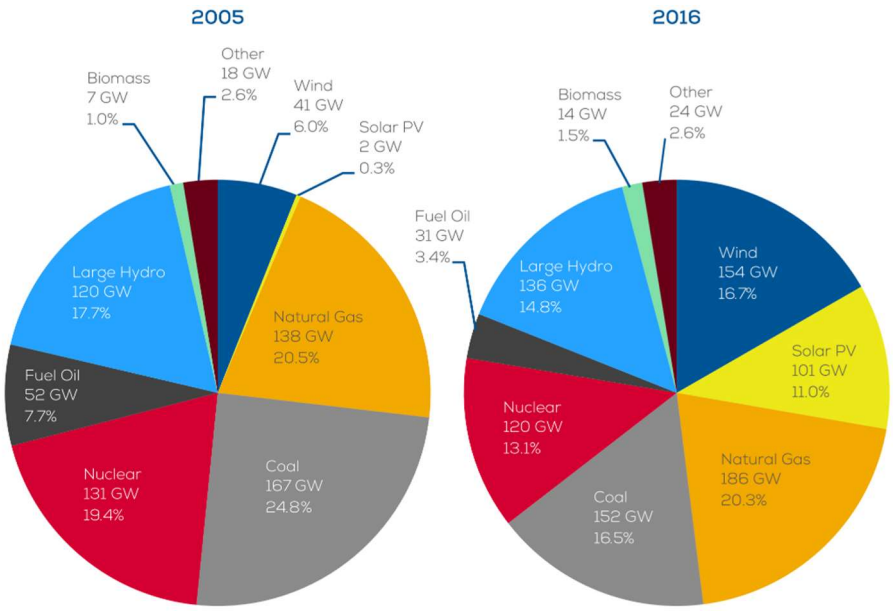

Figure 1.1 Share in total installed power capacity in the EU 2005-2016 (WindEurope, 2017d)

The world is embracing renewable energy rapidly and firmly. Take Europe for example. Figure 1.1 shows that the share of traditional fossil fuel coal in total installed power capacity has decreased significantly from 24.8% in 2005 to 16.5% in 2016, whereas renewable wind power has greatly increased its share from 6.0% to 16.7% during the same period in the European Union (WindEurope, 2017d). Similar trend can also be observed for other traditional or renewable energy sources. In 2016, a total of 24.5 GW of new gross power generation capacity were installed in the EU, 86% of which came from the renewable energy sector, marking a ninth year in a row when renewables contributed more than 55% of all additional power capacity. The overall share of renewables has thus almost doubled from 24% of the total power capacity in 2005 to 46% in 2016.

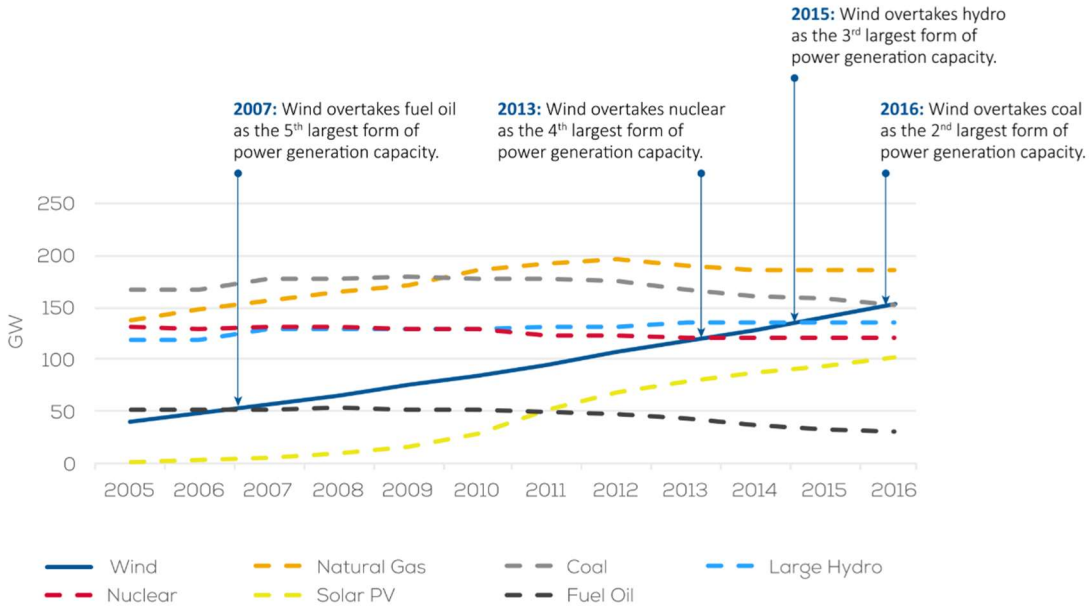

Figure 1.2 Cumulative power capacity installed in the EU 2005-2016 (WindEurope, 2017d)

Among all the renewable energy sources, wind energy now holds the largest share in the cumulative power capacity. Figure 1.2 demonstrates the continuous increase of the cumulative power capacity generated from wind over the past decade. Starting from 2007, strong investment in wind energy has helped it successively overtake fuel oil, nuclear and hydro in the cumulative power capacity and finally surpass coal in 2016 with a total installed capacity of 153.7 GW, making wind the 2nd largest form of power

generation capacity within the European Union (WindEurope, 2017d). In 2016, wind energy accounts for 59.2% of new renewable power installations, and it is estimated that an additional capacity of 50 GW will be installed from 2017 to 2020 (WindEurope, 2017c), exhibiting the great confidence the energy market currently has in the renewable wind sector.

To extract energy from wind, wind turbines are traditionally installed onshore in rural open fields with good wind resource. However, in the past few years, an increasing number of wind turbines are installed in offshore areas. Figure 1.3 shows the cumulative and annual power capacity from offshore wind installed in the EU from 2000 to 2016. In 2016, 1.5 GW of additional power capacity from 338 grid-connected offshore wind turbines was installed, bringing its total installed capacity up to 12.6 GW (WindEurope, 2017a). By 2020, the cumulative installed capacity of offshore wind is projected to nearly double, amounting to 24.6 GW.

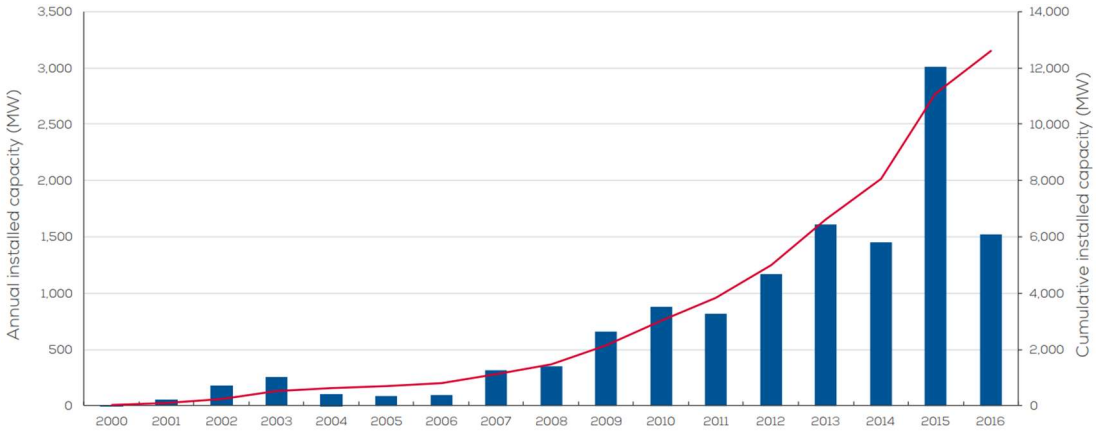

Figure 1.3 Cumulative and annual offshore wind installations in the EU 2000-2016 (WindEurope, 2017a)

The growing interest in offshore wind is primarily attributed to the great potential in wind resource. WindEurope (2017b) estimates that the offshore wind resource potential in theory is between 2,600 TWh and 6,000 TWh per year, which is enough to meet 80%-180% of the total electricity demand in the EU. Additionally, compared to inland, installing wind turbines offshore has other advantages (Jonkman, 2007). The wind in offshore areas tends to be stronger and more consistent than on land, and there

are less turbulence intensity and smaller wind shear. Besides, public concerns about visual disturbance and noise caused by onshore turbines can also be minimized.

To exploit even more abundant wind resource, the offshore wind industry is installing wind turbines further away from shore in even deeper water sites, as shown in Figure 1.4. These turbines are normally installed on fixed structures. Based on the water depth of the installation sites, different types of structures are currently adopted, such as monopiles (0-30 m) and jackets (25-50 m) shown in Figure 1.5. However, as the water depth further increases to over 50 meters, it becomes economically infeasible to build fixed supporting structures and floating foundations should be employed to bring down the cost in manufacturing and installation (Jonkman, 2007).

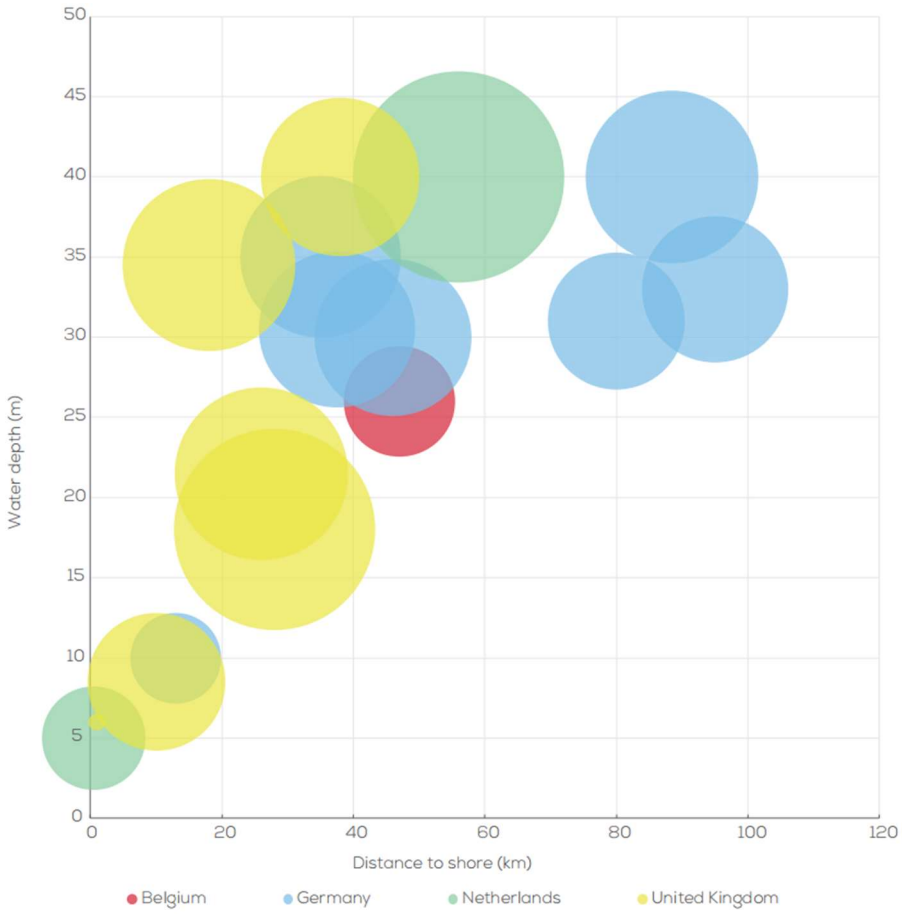

Figure 1.4 Average water depth and distance to shore of offshore wind farms under construction in the EU during 2016 (WindEurope, 2017a)

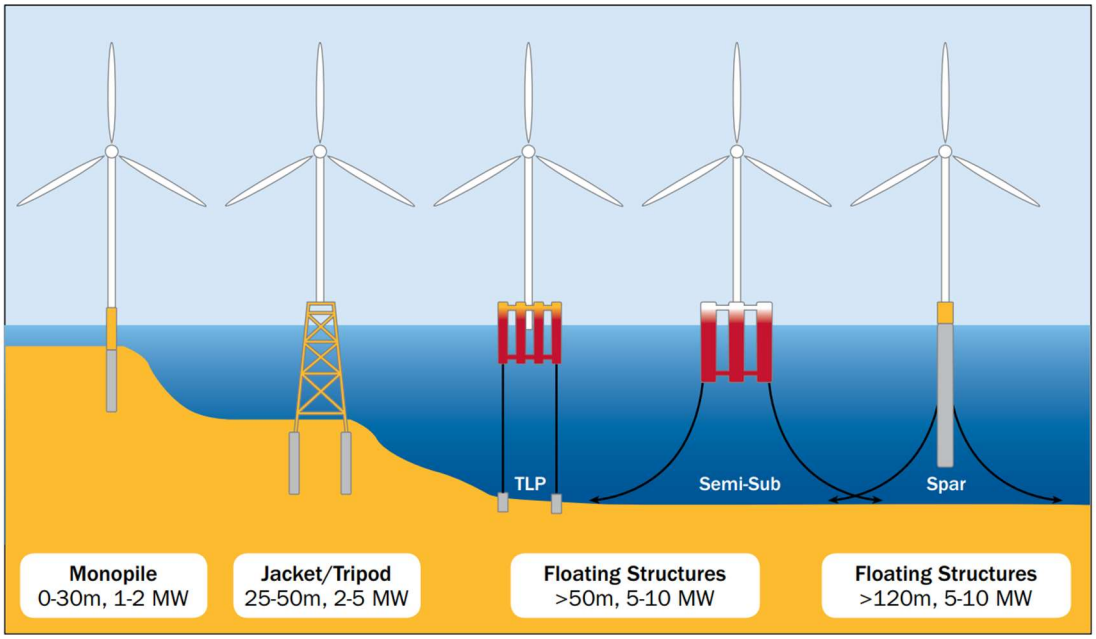

Figure 1.5 Types of offshore wind turbine foundations (EWEA, 2013)

Over the past few years, various types of Floating Offshore Wind Turbines (FOWT) have been designed and tested, as shown in Figure 1.6. One of the major differences between these designs is the type of the floating foundation used by an FOWT to support its upper wind turbine. Figure 1.5 illustrates the three main types of floating supporting structures: Tension Leg Platform (TLP), semi-submersible and Spar, all of which are adapted from the oil and gas industry. In 2008, Blue H Technologies from the Netherlands made the first attempt in FOWT by installing a TLP-based test turbine with a rated capacity of 80 kW off the coast of Italy (EWEA, 2013). In the following year, the world's first full-scale 2.3 MW FOWT demonstration project Hywind Demo was installed near the coast of Norway (Statoil, 2009). Hywind Demo was based on a Spar design and it proved that the floating concept was feasible by operating flawlessly for eight years and producing electricity of more than 40 GWh until the project completed in 2017. The success of the Hywind Demo project led to the operation of the world's first full-scale commercial floating wind farm Hywind Scotland, which consists of five 6 MW floating turbines operating in waters exceeding 100 m of depth in the North Sea off the coast of Peterhead, Scotland (BBC, 2017). Other well-known tested designs include the 2 MW WindFloat system supported by a tri-column semi-submersible, which was developed by Principle Power and installed off the Portuguese

coast in 2011 (Principle Power, 2011), and the 1:8 scaled floating concrete semi-submersible VolturnUS from University of Maine in 2013, which was later developed into an on-going 12 MW floating offshore wind pilot project called New England Aqua Ventus I (University of Maine, 2017).

(a) Blue H Technologies

(b) Hywind Demo

(c) WindFloat

(d) VolturnUS

Figure 1.6 Various designs of floating offshore wind turbines (source: Wikipedia)

1.1.2 Challenges in Designing Floating Offshore Wind Turbines

The abundance of wind resource far offshore and the vast deep-water sites suitable for installation make FOWTs very promising. However, from the perspectives of

engineering design and operation, compared to the wind turbines installed on land or offshore fixed-bottom structures, there are several key challenges present for FOWTs, which need to be overcome before they could be widely applied.

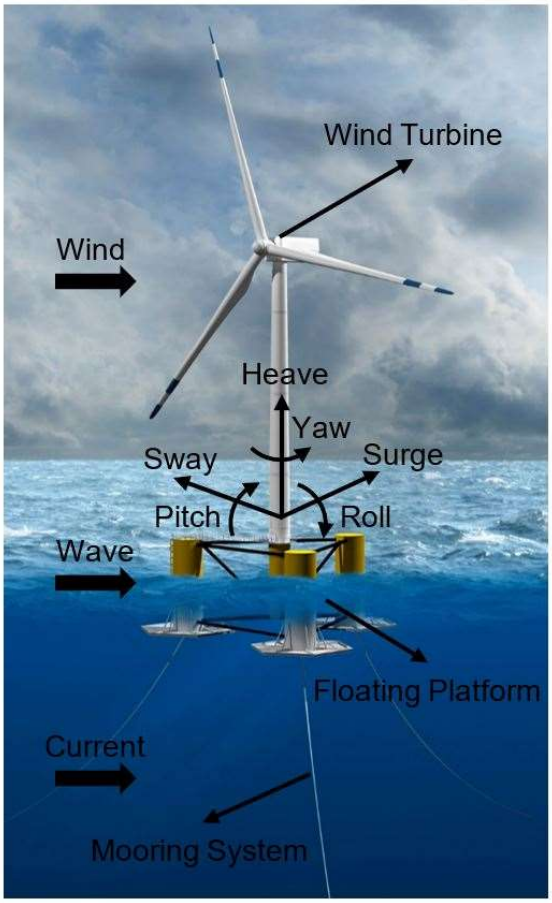

Figure 1.7 Components of a floating offshore wind turbine (source: energy.gov)

An FOWT is a multi-component system, mainly consisting of a wind turbine generating electricity (including rotor, nacelle and tower), a floating platform supporting the wind turbine and a mooring system to maintain the position of the floating platform, as illustrated in Figure 1.7. Unlike its fixed counterpart, a wind turbine installed on a floating structure is constantly moving due to the complex environmental condition in which an FOWT operates. Apart from the loadings from wave and current directly acting on the floating platform, the wind loading exerted upon the wind turbine also contributes to the overall system loading, and thus influences the dynamic motion response of the floating system. Meanwhile, the six Degrees-of-Freedom (DoF) motion of the system, i.e. three translational modes—

surge, sway and heave, and three angular modes—roll, pitch and yaw, changes the position and orientation of the wind turbine, which in turn influences the relative wind velocity experienced by the turbine and thus its aerodynamic performance, i.e. power generation. The inclusion of the mooring system further complicates the overall FOWT system response. The platform is restrained by the mooring system while the mooring force it provides is also dependant on the response of the platform. Figure 1.8 demonstrates how the various components of an FOWT interact with each other. It is thus important to take these coupling effects into account when an FOWT is designed.

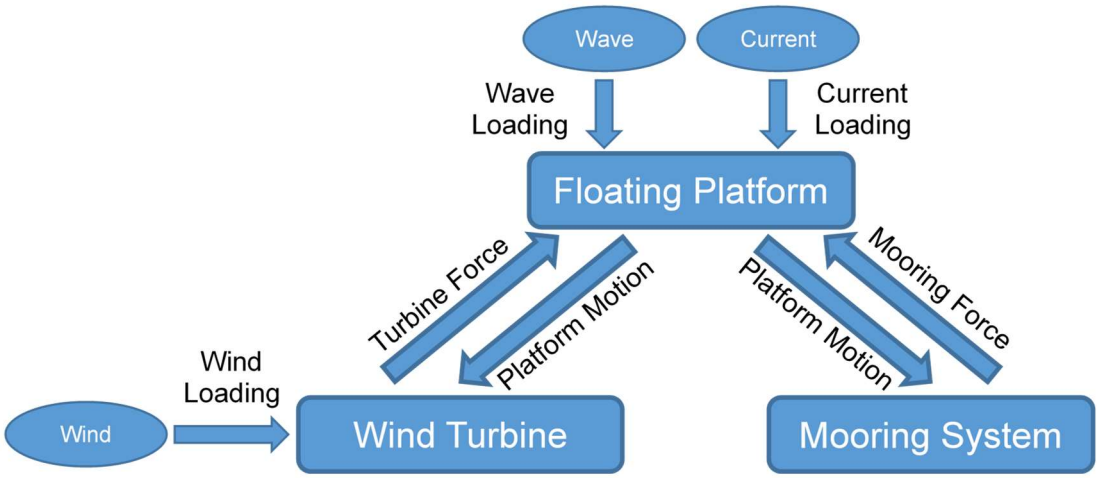

Figure 1.8 Coupling between components of a floating offshore wind turbine

In addition, modern offshore wind turbines are larger in size compared to land-based ones so as to achieve better power capacity and thus reduce economic costs. For a typical offshore wind turbine with a rated power capacity of 5 MW, the diameter of its rotor is more than 120 meters (Jonkman et al., 2009). When exposed to unsteady wind, these turbine blades are subject to substantial aerodynamic loading, leading to significant blade deformation as illustrated in Figure 1.9, which in turn influences the power generated by the turbine. On the other hand, repeated blade deformation due to unsteady cyclic wind loading gives rise to other long-term structural problems such as fatigue. The recent trend of installing floating wind turbines far offshore in deep-water sites only makes the challenges brought by blade deformation more pronounced. These turbines are even larger than those installed on fixed structures, making these floating wind turbine blades more susceptible to structural deformation. For example, the blade

length of the first commercial FOWT Hywind Scotland reaches 75 m, almost the wing span of an Airbus airplane (BBC, 2017). Besides, as a floating wind turbine is installed on a supporting platform as discussed earlier, the six DoF motion of the platform directly exerts impacts on turbine aerodynamic loading and consequently blade deformation in a periodic manner, which further exacerbates the structural fatigue problem. As a result, it is necessary to consider both turbine aerodynamics and structural dynamics during the design stage.

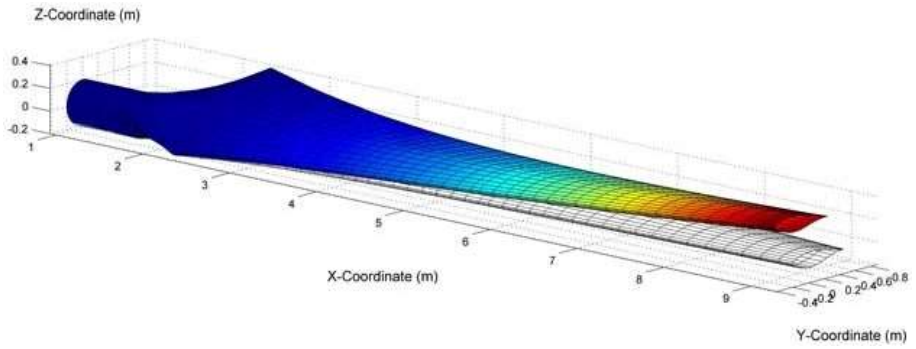

Figure 1.9 Illustration of blade deformation (source: Eolos Wind Energy Research, University of Minnesota)

The challenges brought about by installing wind turbines on floating structures make old design tools developed for fixed-bottom wind turbines inadequate to new generations of FOWTs. It is thus essential to develop new generations of fully coupled aero-hydro-mooring-elastic tools, which can perform Fluid-Structure Interaction (FSI) analysis for FOWTs under variable wind, wave and current conditions. These tools should be able to model the interaction between a flexible wind turbine and a floating platform including its mooring system simultaneously (EWEA, 2013).

1.2 Critical Review

Over the past few years, along with the growing interest in offshore wind energy, lots of research concerning FOWTs has been carried out numerically in various fields. Based on the different aspects of an FOWT they focus on, these studies can be roughly categorised into the following five groups: wind turbine aerodynamics, structural flexibility, floating platform hydrodynamics, mooring system analysis and fully coupled FOWT analysis. In this section, various numerical methods most commonly

used within each group is reviewed briefly due to the many subjects involved in this problem.

1.2.1 Wind Turbine Aerodynamics

Several numerical models have been developed for aerodynamic analysis of offshore wind turbines, including Blade Element Momentum (BEM) theory, vortex method, generalised actuator disc models and direct CFD modelling. All of these methods have been extended to deal with wind turbine aerodynamics in FOWT simulations.

1.2.1.1 BEM Theory

The BEM theory is one of the oldest used for wind turbine aerodynamics. Nowadays, it is still widely adopted in engineering tools as it is computationally efficient. Examples are the well-known FAST (Fatigue, Aerodynamics, Structures, and Turbulence) developed at National Renewable Energy Laboratory (NREL), FLEX5 developed at Technical University of Denmark (DTU) and the commercial software package GH-Bladed developed by GH (Garrad Hassan) Ltd. BEM combines the two-dimensional (2D) blade element theory and one-dimensional (1D) global momentum theory, and solves the axial and tangential induction factors at each blade element in an iterative manner (Moriarty and Hansen, 2005).

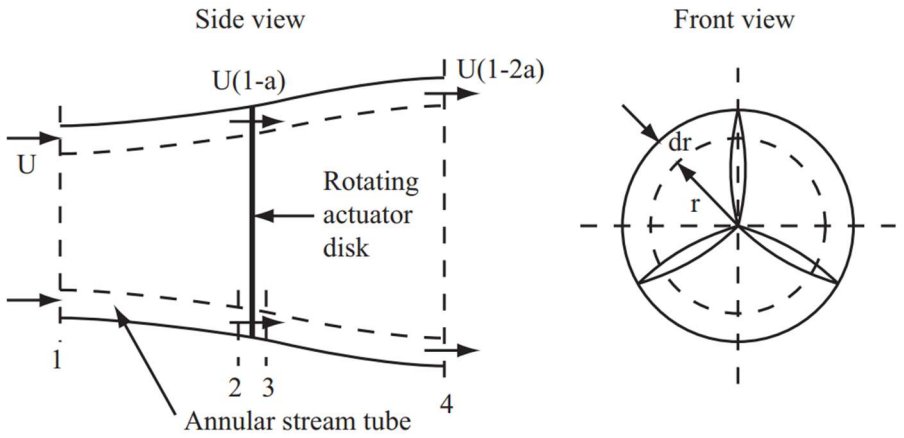

Figure 1.10 Schematic of momentum theory for wind turbine analysis (Manwell et al., 2010)

Figure 1.10 illustrates the basic concepts of the momentum theory adopted in BEM. This method can provide satisfactory results when reasonable sectional airfoil aerodynamic data is provided, i.e. airfoil lift and drag coefficients as functions of Angle of Attack (AOA) and/or Reynolds number (Hansen et al., 2006), which in turn stresses the importance of accurate input of sectional airfoil data. A large amount of studies have been carried out for wind turbine aerodynamic analysis with BEM-based tools (Roddier et al., 2010; Jonkman and Matha, 2011; Kumari Ramachandran, 2013; Ma and Hu, 2013; Proskovics et al., 2013; Karimirad and Michailides, 2015; Gould and Burris, 2016).

Due to its simplicity, the original BEM model has its limitations. Several empirical correction models have been implemented to overcome these limitations. For example, BEM applies a tip-loss correction model to account for the influence of vortices shed from the blade tip into the wake on the induced velocity (Glauert, 1935). A similar correction is applied for vortices shed near the rotor hub. Other correction models include the Glauert correction for large induction factor cases when a turbine operates at high tip speed ratios, the skewed wake correction for tilt and yaw conditions and the dynamic inflow model for the sudden change in turbine operating conditions (Moriarty and Hansen, 2005; Hansen et al., 2006; Wang et al., 2016).

The accuracy of the wind turbine aerodynamic loads predicted by BEM methods, however, largely depends on the correction models they adopt and the airfoil aerodynamic coefficients. In addition, BEM assumes that the forces acting on blade elements are two-dimensional and fluid flow in the spanwise direction is ignored. However, the spanwise flow along turbine blades is present especially for heavily loaded rotors (Moriarty and Hansen, 2005).

1.2.1.2 Vortex Method

Apart from the BEM methods, vortex methods are also used to model wind turbine aerodynamics. A vortex model represents rotor blades, trailing and shed vorticity in the wake with the use of lifting lines or surfaces, as illustrated in Figure 1.11. Vortex distributions are determined either as a prescribed wake or a free wake (Wang et al.,

2016). In comparison to BEM models, vortex models can be used to describe the three-dimensional (3D) flow around a wind turbine and thus provide better insights into the development of wind turbine wake (Sebastian and Lackner, 2012; Jeon et al., 2014).

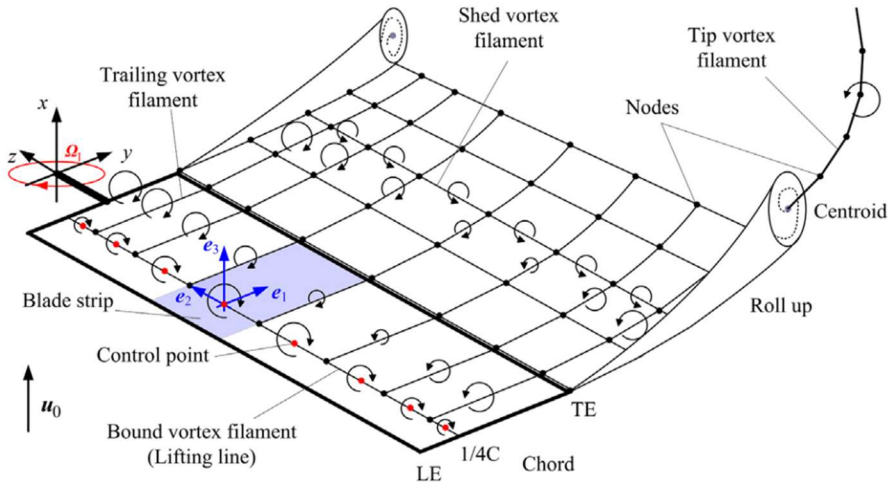

Figure 1.11 Schematic of vortex wake model (Qiu et al., 2014)

Sebastian and Lackner (2012) developed a free vortex wake code Wake Induced Dynamics Simulator (WInDS). A series of validation tests were carried out for fixed-bottom wind turbines. Good agreement was achieved between numerical results and test data. Farrugia et al. (2014) investigated the aerodynamic performance of a model FOWT and compared the predicted results from an open source free-wake vortex code with experimental measurements. Jeon et al. (2014) analysed the unsteady aerodynamics of an FOWT undergoing prescribed platform pitch motion. It was shown that when the platform moved in the upward direction, the turbine rotor experienced a turbulent wake state. Qiu et al. (2014) studied the aerodynamic loading of a wind turbine under blade pitching and yawing conditions at various wind speeds using a time-accurate free-vortex method. Predicted results including rotor torque and locations of tip vortex cores in the wake agreed well with measured data.

However, as the vortex methods are based on the assumption of inviscid flow condition, the viscous effects are neglected in these codes, which may cause significant problem when strong flow separation occurs around turbine blades. In addition, these methods

tend to suffer from the stability problems when vortex elements approach each other as indicated by Hansen et al. (2006).

1.2.1.3 Generalised Actuator Disc Models

Generalised actuator disc models are a group of numerical models closely associated with the BEM theory as they also adopt tabulated airfoil data and the momentum conservation law (Sørensen and Shen, 2002). Unlike BEM methods, these models are normally combined with 3D Navier-Stokes equations and thus can be used to study the dynamics of wind turbine wake. The geometry of the wind turbine is not fully resolved while its effects on the flow field are taken in consideration by including an additional force term in the momentum equation (Wang et al., 2016). Based on the representation of the force term, there are currently three actuator models available: actuator disc, actuator line and actuator surface, as illustrated in Figure 1.12 (Sanderse et al., 2011).

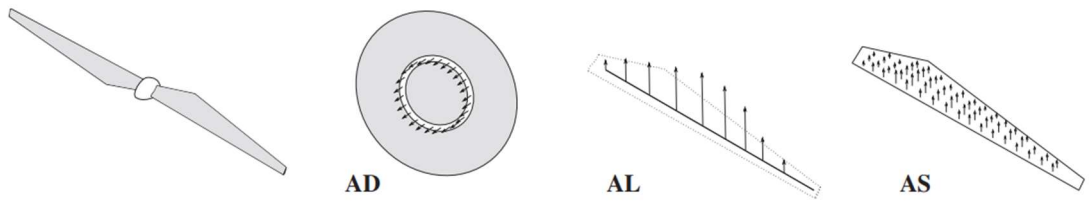

Figure 1.12 Illustration of actuator disc, line and surface concepts (Sanderse et al., 2011)

In the actuator disc model, a wind turbine is modelled as the swept disc surface in the rotor plane (Gundling et al., 2015). The force acting on the turbine is assumed to be evenly distributed in the azimuthal direction. To overcome the limitations of the axisymmetric actuator disc model, an actuator line model was further developed by representing a turbine blade as a line and the blade force as distributed loads in the radial direction (Sørensen and Shen, 2002). Similar to the BEM theory, a turbine blade is divided into a number of elements and local forces acting on an element are calculated using predefined airfoil lift and drag coefficients. The actuator line model was further extended to an actuator surface model (Shen et al., 2009), where a planar surface is used to represent a turbine blade to improve the accuracy in predicting wind

turbine aerodynamics. However, additional pressure and skin-friction distribution on the airfoil surface is needed (Sanderse et al., 2011).

The generalised actuator disc models have been applied to a number of wind turbine simulations. de Vaal et al. (2014) applied the actuator disc method to study the effects of a prescribed platform surge motion on the aerodynamic performance of a wind turbine rotor and the induced velocity. Li et al. (2015b) investigated the wake flow of an FOWT experiencing periodical platform surge and pitch motions with an unsteady actuator line model coupled with 3D Reynolds Averaged Navier-Stokes (RANS) equations. Kim et al. (2015) proposed an improved actuator surface model to eliminate the unexpected induced velocity due to circulation and the need for tip-loss correction, and validated the proposed approach with the NREL 5-MW wind turbine.

Compared to the BEM methods, codes based on the generalised actuator disc models can be used to model the interference between multiple wind turbines in a wind farm configuration as they are able to simulate the development of turbine wake. Sasan et al. (2014) investigated the wake interaction between two model-scale wind turbines in tandem using an actuator line approach. The numerical simulation well captured the development of the interacting wake. van der Laan et al. (2015) estimated the power production of a two-turbine model with an actuator disc method. However, as an extension to the BEM theory, these models still require an input of tabulated airfoil data from experimental measurement as well as the various empirical correction models.

1.2.1.4 Direct CFD Modelling

Similar to the generalised actuator disc models, direct CFD modelling solves 3D Navier-Stokes equations. However, instead of simplifying a wind turbine as a disc, line or surface, the turbine rotor is fully resolved with surface mesh in the direct CFD modelling approach, as shown in Figure 1.13. The need of empirical corrections models and predetermined airfoil aerodynamic data is thus eliminated. Besides, the spanwise flow along turbine blades for heavily loaded rotors, which is neglected in the aforementioned methods, can be directly predicted by CFD (Moriarty and Hansen,

2005; Li et al., 2012). Furthermore, detailed flow field characteristics obtained from CFD results, such as flow separation and vortex evolution, can be visualised and examined at any location to provide insights into the underlying causes of sophisticated physical phenomena (Snel, 2003).

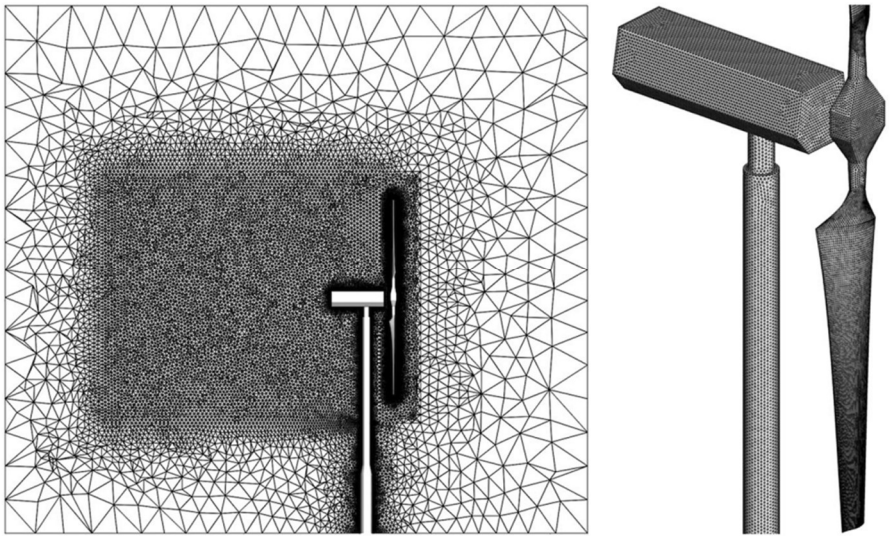

Figure 1.13 Illustration of computational mesh used in direct CFD modelling of wind turbine aerodynamics (Hsu et al., 2014)

Thanks to the advantages mentioned above, many researchers have applied direct CFD modelling to analyse the aerodynamic performance of a wind turbine rotor (Nilay and Lyle, 2006; Lanzafame et al., 2013; Make and Vaz, 2015; Zhang et al., 2017) or the interference between rotor and tower (Zahle et al., 2009; Hsu and Bazilevs, 2012; Li et al., 2012; Santoni et al., 2017). Besides, Li et al. (2015a) investigated the flow field in the wake region for two in-line wind turbines and analysed the wake interference effects. Miao et al. (2016) further analysed the effects of yawed wake from the upstream turbine on the downstream turbine.

In addition to simulations for fixed-bottom wind turbines, effects of platform motion on wind turbine aerodynamics in an FOWT scenario have also been studied by imposing a prescribed platform motion to the wind turbine. For example, Tran et al. (2014) investigated the unsteady aerodynamic performance of a wind turbine in response to various prescribed sinusoidal platform pitching motion amplitudes and frequencies using software package STAR-CCM+. By comparing CFD results

obtained from STAR-CCM+ with those from other tools, such as unsteady Blade Element Momentum (UBEM), FAST with BEM and Generalized Dynamic Wake (GDW), it was found that although good agreement was achieved for all cases at small oscillation amplitudes, large discrepancies occurred when the oscillation amplitude increased to 4 degrees. This was explained in their work via pointing out the limitations of the simplified methods used in modelling the dynamic interaction between wind turbine and wake, which is induced by the platform motion. As an extension of their work, Tran and Kim (2016a) analysed an FOWT system under a prescribed sinusoidal surge motion. It is interesting to note that, with the inclusion of the surge motion, the unsteady aerodynamic thrust and power varied considerably among different tools (i.e. FAST, CFD and UBEM), which are also related to the imposed oscillation frequency and amplitude of the surge motion. Other similar studies include Zhao et al. (2014); Sivalingam et al. (2015); Wu et al. (2015); Wu and Nguyen (2017).

1.2.2 Structural Flexibility

Modern wind turbine blades are susceptible to large deformation as they are subject to substantial aerodynamic loading from wind. In order to deal with the structural flexibility of turbine blades, three numerical methods are currently adopted, including the modal approach, beam theory and 3D finite element analysis.

1.2.2.1 Modal Approach

The modal approach is a very effective way to solve turbine blade deformation. It describes the deformation of a turbine blade as a linear combination of several mode shapes, which are usually computed using a finite element code in advance (Wang et al., 2016). Figure 1.14 shows the first and second mode shapes of an example wind turbine. In doing so, the number of DoFs is considerably reduced and simulations can run very fast. As a result, this method has been coupled with BEM-based aerodynamic codes and is widely used in many engineering design tools, such as FAST, FLEX5 and GH-Bladed.

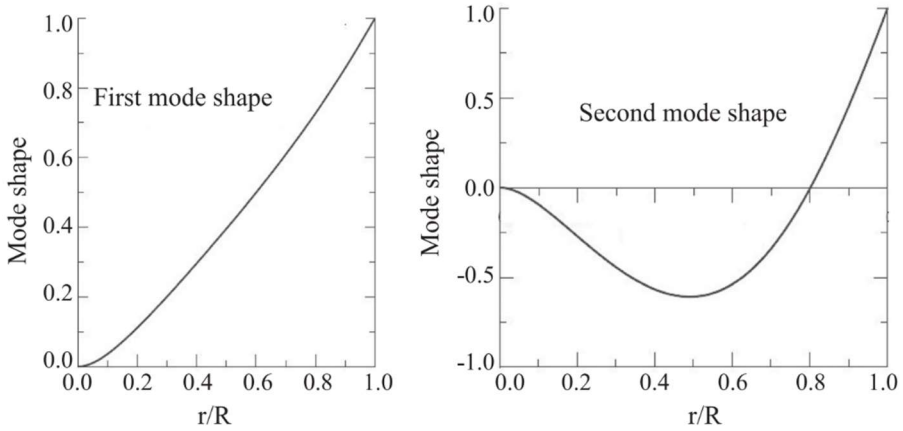

Figure 1.14 Illustration of first and second mode shapes of an example wind turbine (Wang et al., 2016)

The modal approach has also been implemented into CFD solvers to analyse aeroelastic problems of wind turbines. Carrión et al. (2014) carried out both static and dynamic aeroelastic analysis on wind turbines using the compressible flow CFD solver Helicopter Multi-Block (HMB2), where structural deformation of blades was solved with a modal approach. Horcas et al. (2017) coupled a finite volume code for fluid flow with a reduced order modal model for structural deflection, and performed FSI simulations for the DTU 10 MW turbine.

Although it is computationally efficient, the accuracy of the modal approach is limited by the number of the DoFs considered. For example, engineering tools like FAST only use the initial three or four mode shapes, such as 1st and/or 2nd order flapwise and edgewise deflections. It is thus insufficient for some complex situations involving more deformations like torsional twist, which is important for flutter analysis (Hansen, 2007; Sackniess, 2010; Zhang and Huang, 2011). In addition, the linear assumption of the modal approach means that it is not suitable for cases with large blade deflection (Wang et al., 2016).

1.2.2.2 Beam Theory

To overcome the limitations of the modal approach, some other engineering tools like HAWC2 developed by DTU deal with blade elasticity using a more sophisticated beam theory. The FAST code was also recently updated to include a new structural module

BeamDyn based on the beam theory (Wang et al., 2017). The beam theory models a 3D turbine blade as a 1D beam with varying cross-sectional structural properties. Compared to the modal approach, the beam theory is capable of handling more DoFs and takes geometric nonlinearities into consideration, thus leading to a better representation of blade deformation. As a result, some recent studies (Meng et al., 2009; Jeong et al., 2014; Wang et al., 2014; Manolas et al., 2015; Guntur et al., 2016; Rafiee et al., 2016; Ferede et al., 2017) have focused on the coupling of BEM codes with structural solvers based on the beam theory.

As a wind turbine is comprised of a series of rigid or flexible components, such as blades and nacelle, the beam theory is normally implemented in a MultiBody Dynamics (MBD) framework. In the MBD model shown in Figure 1.15, the whole turbine structure is discretised into a number of bodies, which are interconnected via kinematic constraints. These bodies can be either rigid components like hub and nacelle, or flexible parts such as blades and tower which are modelled as beams.

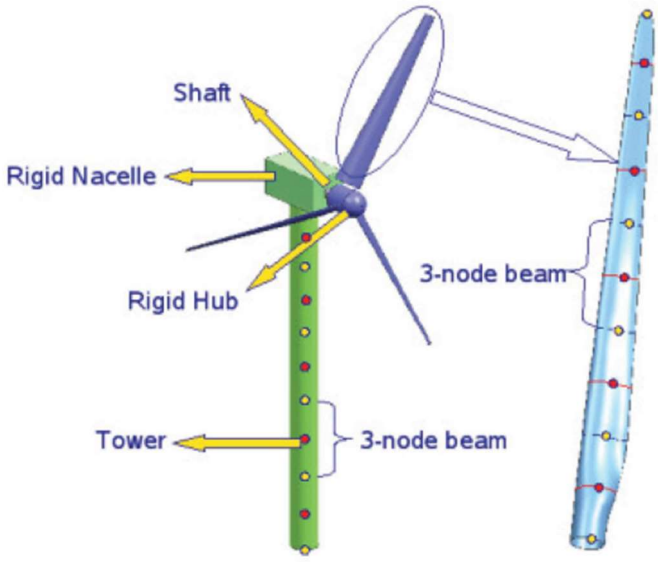

Figure 1.15 A Multi-Body representation of a wind turbine (Meng, 2011)

Some researchers have attempted to couple CFD solvers and MBD codes with beam modelling features, and applied their tools to wind turbine FSI. Pierangelo and Jayanarayanan (2011) coupled a CFD solver with an open source general-purpose multibody code MBDyn, and studied the NREL phase VI rotor under both unyawed

and yawed conditions. Yu and Kwon (2014) applied a loosely coupled CFD-CSD tool to the NREL 5-MW reference wind turbine and found that blade torsional deformation significantly reduced its aerodynamic loads and the tower interference, resulting in the oscillation of blade flapwise deformation. Li et al. (2015c) combined an overset dynamics CFD solver with a MBD structural solver, and analysed the NREL 5-MW wind turbine under wind shear and turbulent wind conditions. Heinz et al. (2016a) developed a coupled model with the structural model of HAWC2 and the CFD solver EllipSys3D and conducted a series of comparative tests against BEM-based version of HAWC2. Good agreement between the two approaches was achieved for various cases, indicating that low-fidelity engineering tools can provide good results under normal conditions. Heinz et al. (2016b) further applied the tool to the DTU 10-MW wind turbine in a standstill condition and analysed the edgewise vortex-induced vibration of the turbine blade under various wind conditions. (Liu et al., 2017a) coupled a CFD solver to the MBD solver MBDyn and investigated the aeroelastic performance of the NREL 5-MW wind turbine considering the tower shadow effects. At current stage, the above coupled FSI numerical modelling studies are limited to a fixed-bottom wind turbine without considering the platform motion associated with a floating offshore wind turbine.

1.2.2.3 3D Finite Element Analysis

Advanced 3D Finite Element Analysis (FEA) has been widely applied to structural dynamics in various fields including ship and offshore structure design. By setting up a 3D model as illustrated in Figure 1.16, wind turbine geometry and structural properties can be better described compared to simplified models such as the modal approach and 1D beam representation. In addition, detailed stress distribution along turbine blades can be obtained and analysed for structural strength assessment. As a result, some recent studies have coupled wind turbine aerodynamics solvers with 3D FEA codes to carry out aeroelastic analysis for wind turbines.

Bazilevs et al. (2011); Bazilevs et al. (2012) proposed a Kirchhoff–Love shell model for wind turbine structural dynamics and coupled it with a CFD solver based on Finite Element Method (FEM) for aerodynamics. The coupled FSI tool was then applied to

study the NREL 5 MW offshore wind turbine rotor. Hsu and Bazilevs (2012) further extended their tool to simulate a full wind turbine including nacelle and tower. Haselbach et al. (2016) performed a comprehensive aeroelastic investigation of trailing edge damage in a wind turbine blade on a high-fidelity 3D FEA model established in ANSYS and analysed the effects of geometrical non-linear cross-section deformation and trailing-edge wave formation on energy release rates. Lee et al. (2017) extracted the surface pressure information from CFD modelling and then applied the aerodynamic loading to a 3D structural model of the NREL Phase VI wind turbine using a 1-way FSI analysis.

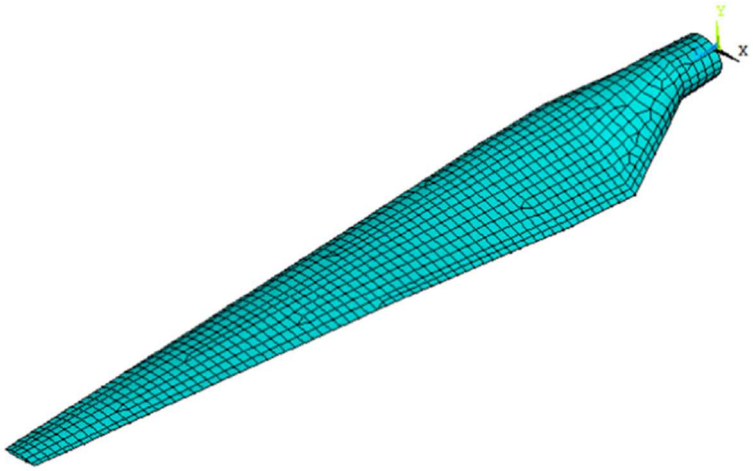

Figure 1.16 Illustration of a 3D finite element model of a wind turbine blade (Wang et al., 2016)

However, as modern turbine blades are normally constructed with composite materials consisting of various layers, it is often a difficult and tedious work to create FEM models (Wang et al., 2016). Besides, these methods are relatively more demanding in computational resources compared to approaches based on the beam theory. On the other hand, for slender structures like turbine blades, the beam theory can usually produce accurate results in structural deformation and internal structural loading (Li et al., 2015c). Therefore, the beam theory is still widely adopted for structural dynamics analysis of flexible turbine blades and is thus used in this thesis.

1.2.3 Floating Platform Hydrodynamics

Unlike wind turbines installed on fixed-bottom structures, an FOWT is installed on a floating platform. Excited by the hydrodynamic loads from wave and current, the floating platform has 6DoF motion. Two numerical methods are commonly used for modelling these loads for FOWTs: potential flow theory and CFD.

1.2.3.1 Potential Flow Theory

The potential flow theory has been widely adopted in ship hydrodynamics and ocean engineering due to its fast speed and good accuracy for a large number of applications, such as sea-keeping analysis of ships and motion response of offshore structures in waves. As floating platforms used for FOWTs are adapted from typical offshore structures in the oil and gas industry, this theory has been employed by most engineering tools, such as FAST and Flex5, for hydrodynamic analysis of FOWTs.

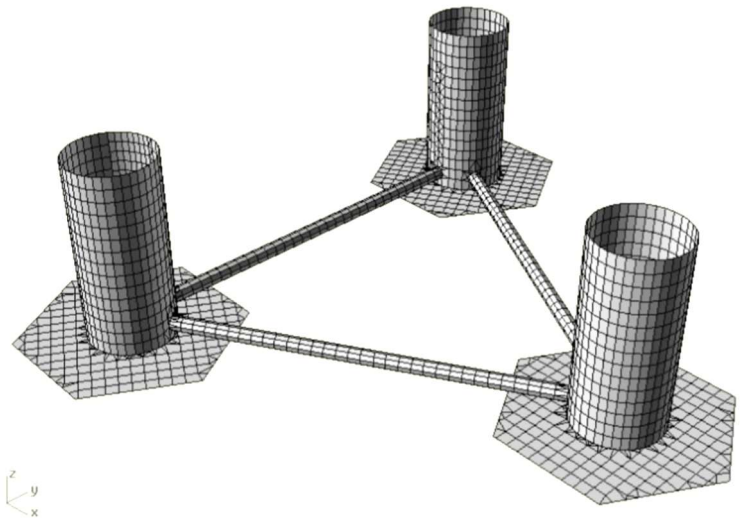

Figure 1.17 WAMIT model for a three-column semi-submersible (Cermelli et al., 2009)

The potential flow theory assumes the fluid flow around a structure to be irrotational, inviscid and incompressible and it decomposes the wave-structure interaction into separate radiation and diffraction components via linearization. 3D panel methods, such as WAMIT, are normally used to solve the boundary value problem of the Laplace's equation regarding velocity potential. Figure 1.17 illustrates the WAMIT

model for a three-column semi-submersible. These methods can produce hydrostatic restoring, added mass and linear radiation damping coefficients as well as wave exciting forces in frequency domain (WAMIT, 2017), which are then transformed to time domain using a convolution technique and motion equations for the structure are established in time domain. Due to the inviscid flow assumption, a potential-flow model is unable to consider the nonlinear viscous drag on the structure resulting from flow separation. A quadratic drag force approximated using Morison's equation (Morison et al., 1950) is usually applied to take viscous effects into account. Loadings from other parts of the system, i.e. wind turbine and mooring system, should also be included in the motion equations. Subsequently, motion responses of the structure are solved in time domain.

The potential flow theory has been adopted by many in hydrodynamic analysis for FOWTs. For example, Cermelli et al. (2009) investigated motion responses of an FOWT supported by a three-column semi-submersible named WindFloat using a time domain potential-flow based program TimeFloat. Roald et al. (2013) compared the hydrodynamic performance of two FOWT concepts supported by a TLP and a Spar, respectively. Effects of second-order hydrodynamic loading on a semi-submersible FOWT were analysed by Bayati et al. (2014). It was found that difference-frequency second-order hydrodynamics excited the platform motion response at its natural frequencies. Shen et al. (2016) studied the viscous effects on a TLP-type FOWT and concluded that the viscous forces on the column and pontoons contributed to higher harmonic excitation in structure pitch motion. Han et al. (2017) carried out fully coupled time domain simulations for a submerged TLP with small water plane area. Effects of second-order wave loads on the dynamics of the FOWT were found to be slightly larger in an extreme sea state than in a moderate sea state.

1.2.3.2 CFD

Although potential-flow based codes are fast and accurate in many situations, the linear assumption makes them inadequate for highly nonlinear problems, such as cases with large structure motion responses (Nematbakhsh et al., 2013). Meanwhile, the approximated viscous drag requires an additional quadratic damping coefficient,

which relies on experimental test data (Coulling et al., 2013; Tran and Kim, 2015). On the other hand, CFD solvers simulate the interaction between waves and a floating structure via directly solving 3D nonlinear Navier-Stokes equations and are thus capable of handling nonlinear cases. In addition, viscous effects are inherently taken into consideration by these solvers thanks to the inclusion of fluid viscosity in their equations. As a result, although more time-consuming compared to potential-flow based codes, CFD has been more and more used in FOWT hydrodynamic studies. Figure 1.18 shows the CFD model for the DeepCwind semi-submersible.

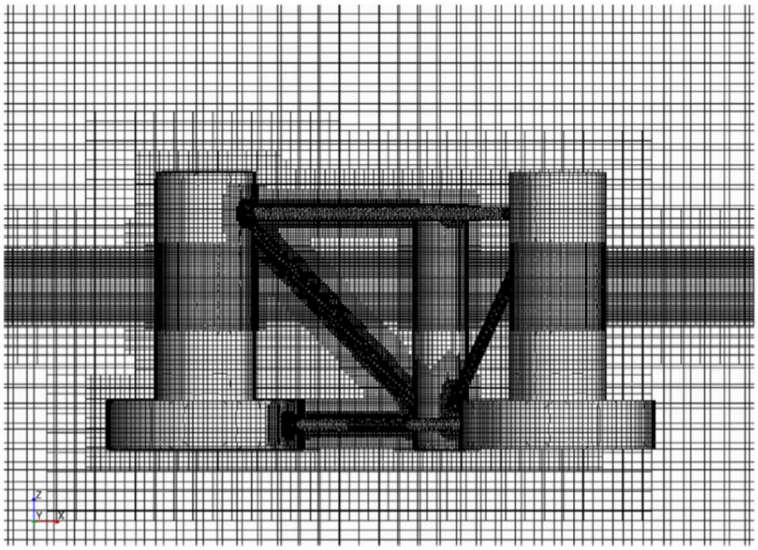

Figure 1.18 CFD model for the DeepCwind semi-submersible (Tran and Kim, 2015)

Nematbakhsh et al. (2014) developed a CFD model based on an immersed boundary method and studied the motion of a 5 MW Spar-type FOWT in moderate and extreme sea states under irregular wave conditions. With their method, they successfully captured strong nonlinear effects, such as the complete submergence of the platform tank and tether slacking, which is rather difficult to accurately predict with commonly used simplified potential-flow based models. In a subsequent work, Nematbakhsh et al. (2015) extended their study to wave-induced responses of a Tension Leg Platform (TLP) wind turbine in deep water. A comparison between the results from the CFD model and a finite element model based on the potential flow theory indicated that large discrepancies exist between the results at large wave amplitudes obtained from these two different methods. Tran and Kim (2015) investigated the hydrodynamic

responses of the DeepCwind semi-submersible platform using the commercial CFD software package STAR-CCM+. Their modelling results showed generally good agreement with experimental test data. Subbulakshmi and Sundaravadivelu (2016) studied the effects of heave plate on heave damping of a Spar-type FOWT. Detailed parametric studies were conducted for single and two heave plates. It was found that heave damping effects were more significant when the diameter ratio between the Spar and the heave plate were increased.

1.2.4 Mooring System Analysis

Mooring systems are an essential part in designing floating structures including FOWTs. The mooring system of a floating system can provide restoring forces and moments to balance environmental loadings and help maintain its position at sea, especially for those three DoF motion responses (surge, sway and yaw) where hydrostatic restoring forces/moments are not present. A mooring system is usually comprised of several mooring lines. Based on whether the inertial force induced by the motion of mooring lines is modelled, there are currently two groups of methods available for mooring system analysis: quasi-static methods and dynamic methods.

1.2.4.1 Quasi-static Methods

Quasi-static methods assume that the shape and tension of a mooring line at any given instant are static while ignoring the dynamic loadings due to the acceleration and velocity of the mooring line.

The simplest form of a mooring line is modelled as a massless spring with constant stiffness. A linear force-displacement relationship directly derived from Hooke's law is established to estimate the mooring force from the displacement of the structure studied. This method is widely adopted by potential-based codes for computing structural responses in frequency domain (Zhang et al., 2013). However, the linear assumption becomes invalid when large structure displacement is present and/or weight from mooring lines are comparable to that of the floating structure.

Catenary equation is another commonly used quasi-static method which is able to model the geometrical nonlinearity of catenary mooring lines with portions lying on seabed as shown in Figure 1.19. It offers an analytical solution to the shape and tension distribution of a mooring line by taking into account the weight and buoyancy of the line and establishing a nonlinear relationship between mooring restoring force and the position of the line fairlead connected to the floating structure. Due to its simplicity and good accuracy in predicting nonlinear restoring force from mooring lines, this method has been used to deal with mooring system analysis of FOWTs by many engineering tools, such as FAST (Jonkman, 2007), as well as CFD-based codes (Tran and Kim, 2015). If hydrodynamic loadings from wave and current and seabed friction effects are to be considered for a mooring line, a discretised version of the catenary equation has to be formulated by dividing the line into a series of segments and solved numerically in an iterative way (Wang et al., 2010).

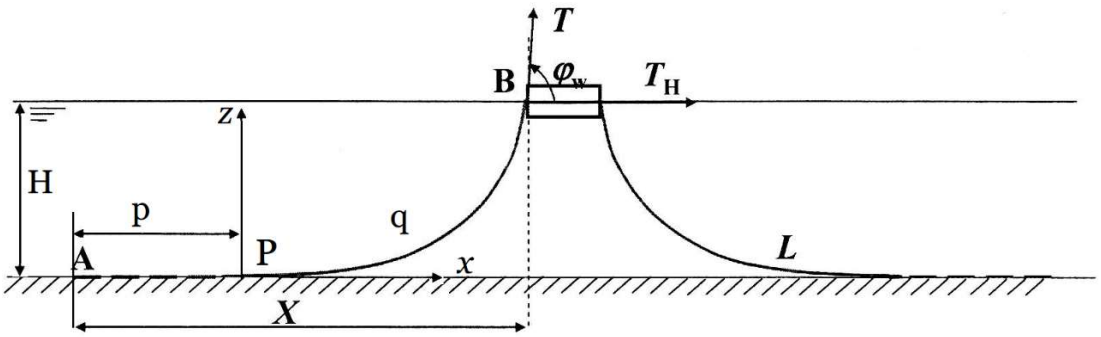

Figure 1.19 Illustration of catenary mooring lines

1.2.4.2 Dynamic Methods

Although quasi-static methods have been previously used to model mooring systems in FOWTs, as dynamic effects are neglected in their formulation, these methods are unable to predict the dynamic tension force of mooring lines, which is much larger than the static line tension force and is of great importance in structural strength design of mooring lines (Masciola et al., 2013). Dynamic methods, on the other hand, take into consideration the inertial force and internal damping associated with mooring line motion via establishing dynamic equations of motion based on Newton's second law. As a result, compared to quasi-static models, dynamic models are able to accurately

predict mooring line tension as well as motion responses of floating structures (Sethuraman and Venugopal, 2013). Antonutti et al. (2018) compared the line tension force from both a dynamic analysis code and a quasi-static model to experimental data. Results from dynamic simulations agreed remarkably well with data obtained from experiment, while the quasi-static method considerably underestimated line tension force. Waris and Ishihara (2010) studied the influence of mooring line models on the dynamic responses of a tri-floater FOWT. It was observed that applying a linear quasi-static model overestimated surge response near resonance peak compared to a nonlinear dynamic model. Hall et al. (2014) further found out that the inaccuracies of quasi-static mooring models exerted impacts on the response of rotor blades.

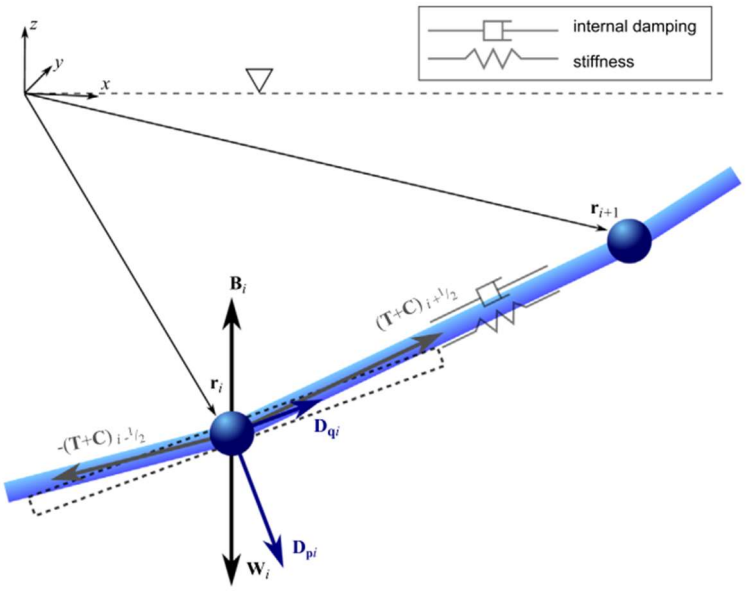

Figure 1.20 Illustration of a lumped mass model for mooring lines (Hall and Goupee, 2015)

The lumped mass model first emerged for nonlinear transient motion of cables in the late 1950s (Walton and Polachek, 1959, 1960) and has since been extended for mooring line dynamic analysis (Nakajima et al., 1982). This method discretised a mooring line into a series of concentrated masses connected by massless springs, as shown in Figure 1.20. Equations of motion regarding nodal displacements are established for each mass. The lumped mass model is able to consider the axial elasticity of mooring lines as well as internal material damping. It has been proven effective for dynamic analysis of mooring lines and been used in various FOWT

simulations. Sethuraman and Venugopal (2013) studied the hydrodynamic response of a stepped-spar FOWT using the commercial modelling tool OrcaFlex, which models mooring lines based on the lumped mass method. Hall and Goupee (2015) validated a lumped mass mooring line model against the DeepCwind semi-submersible FOWT experiment and very good agreement in fairlead tension was achieved.

FEA is also a popular choice in modelling mooring line dynamics. An important difference between the lumped mass model and FEA is the form of polynomial interpolation functions adopted to discretise external and internal forces as well as mass and stiffness matrices (Van den Boom, 1985). In fact, the lumped mass model can be considered as a special case of FEA, where a linear interpolation function is selected (Masciola et al., 2014). Using high-order interpolations functions and advanced numerical integration strategies to augment stability, FEA is capable of producing accurate results with less discretisation resolution compared to a lumped mass model (Masciola et al., 2014). Waris and Ishihara (2012) applied a finite element mooring model to analyse the dynamic responses of an FOWT with heave plates. Both catenary and tension leg mooring systems were studied. The tension leg system was found to be highly restrained in heave, pitch and roll responses.

1.2.5 Fully Coupled FOWT Analysis

Table 1.1 summarises all numerical methods reviewed in previous sections for different aspects of fully coupled FOWT analysis. Each method is compared to other approaches listed within the same group and marked as Good, Better or Best according to its modelling accuracy.

Table 1.1 Summary of numerical methods available for FOWT analysis

Aspects	Numerical Methods	Modelling Accuracy
Wind Turbine Aerodynamics	BEM Theory	Good
	Vortex Method	Better
	Generalised Actuator Disc Models	Better
	Direct CFD Modelling	Best

Structural Flexibility	Modal Approach	Good
	Beam Theory/MBD	Better
	3D FEA	Best
Floating Platform Hydrodynamics	Potential Flow Theory	Good
	CFD	Better
Mooring System Analysis	Quasi-static Methods	Good
	Dynamic Methods	Better

In recent years, numerous design tools able to carry out fully coupled analysis for FOWTs have shown up. Table 1.2 presents an overview of all the engineering tools which participated in the Offshore Code Comparison Collaboration, Continuation (OC4) project set up by International Energy Agency (IEA) Wind. Some of these tools like SIMO/RIFLEX were originally developed for designing floating structures in the oil and gas industry and later extended to include additional modules for wind turbine aerodynamics, while others such as HAWC2 and FAST were previously aeroelastic codes for wind turbines with newly implemented hydrodynamic features. Almost all the tools listed in Table 1.2 deal with wind turbine aerodynamics based on the BEM theory and adopt the linear potential flow theory and/or Morison's equation for platform hydrodynamics. Structural flexibility of turbines blades is mostly handled via either the modal approach or the beam theory while both quasi-static and dynamic mooring system analysis models are still widely used. These tools are fast in terms of computational time and are suitable for the initial design stage when a large number of cases need be simulated. A great amount of fully coupled FOWT studies have been performed using these tools (Jonkman, 2009; Roddier et al., 2010; Jonkman and Matha, 2011; Robertson and Jonkman, 2011; Ma and Hu, 2013; Bachynski et al., 2014; Karimirad and Michailides, 2015; Oguz et al., 2018). However, due to the complexity of the FOWT problem and previously discussed shortcomings of the theories used by these engineering tools, specifically on aerodynamics and hydrodynamics, it is necessary to ensure they are validated before applying them to design FOWTs. The Offshore Code Comparison Collaboration, Continued, with Correlation (OC5) still in

progress under the IEA Wind Research Task 30 was initiated to address these issues (Robertson et al., 2015; Robertson et al., 2016; Robertson et al., 2017).

Table 1.2 Overview of various FOWT design tools participating in the OC4 project (Robertson et al., 2014b)

Code	Code Developer	OC4 Participant	Structural Dynamics	Aerodynamics	Hydrodynamics	Mooring Model
FAST	NREL	NREL, CENTEC, IST, Goldwind, CSIC	T: Mod/MB P: Rigid	(BEM or GDW)+DS	PF + QD + (QTF)	QS
FAST v8	NREL	NREL	T: Mod/MB P: Rigid	(BEM or GDW)+DS	PF + ME	QS
CHARM3D+ FAST	TAMU+ NREL	ABS	T: Mod/MB P: Rigid	(BEM or GDW)+DS	PF + ME + (MD + NA) + (IP + IWL)	FE/Dyn
OPASS+ FAST	CENER+ NREL	CENER	T: Mod/MB P: Rigid	(BEM or GDW)+DS	PF + ME	LM/Dyn
UOU+FAST	UOU+NREL	University of Ulsan	T: Mod/MB P: Rigid	(BEM or GDW)+DS	PF + QD	QS
Bladed	GH	GH, CGC, POSTECH	T: Mod/MB P: MB	(BEM or GDW)+DS	ME + (IWL+ IP)	QS
Bladed Advanced Hydro Beta	GH	GH	T: Mod/MB P: MB	(BEM or GDW)+DS	PF + ME + (IWL)	QS
OrcaFlex	Orcina	4Subsea	T: FE P: Rigid	BEM, GDW, or FDT	PF + ME	LM/Dyn
HAWC2	DTU	DTU	T: MB/FE P: MB/FE	(BEM or GDW)+DS	ME	FE/Dyn
hydro-GAST	NTUA	NTUA	T: MB/FE P: MB/FE	BEM or FWV	PF + ME + (IP)	FE/Dyn
Simo+Riflex+ AeroDyn	MARINTEK+ NREL	CeSOS	T: FE P: FE	(BEM or GDW)+DS	PF+ME	FE/Dyn
Riflex-Coupled	MARINTEK	MARINTEK	T: FE P: Rigid	BEM+FDT	PF + ME + (IWL)	FE/Dyn
3Dfloat	IFE-UMB	IFE	T: FE (co-rotated) P: FE	BEM+FDT	ME + (IWL)	FE/Dyn
SWT	SAMTECH	SAMTECH & IREC	T: FE+Mod/MB P:FE+Mod/MB	BEM or GDW	ME + (IWL)	FE/Dyn
DeepLinesWT	PRINCIPIA-IFPEN	PRINCIPIA	T: FE P: FE	BEM+DS	PF + ME + (MD + QTF/NA) + (IP + IWL)	FE/Dyn
SIMPACK+ HydroDyn	SIMPACK	SWE	T: Mod/MB P: Rigid	BEM or GDW	PF + QD	QS
CAsT	University of Tokyo	University of Tokyo	T: FE W: FE	BEM	ME	QS
Wavec2Wire	WavEC	WavEC	T: N/A P: Rigid	N/A	PF + QD	QS
WAMSIM	DHI	DHI	T: N/A P: Rigid	N/A	PF + QD	QS

T = turbine
P = platform
Mod = modal
MB = multi-body
FE = finite element
N/A = not applicable

BEM = blade-element/momentum
GDW = generalized dynamic wake
DS = dynamic stall
FDT = filtered dynamic thrust
FWV = free-wake vortex

PF = potential flow theory
ME = Morison eq.
MD = mean drift
QTF = quadratic transfer function
NA = Newman's approximation
IP = instantaneous position
IWL = instantaneous water level
QD = quadratic drag

QS = quasi-static
Dyn = dynamic
LM = lumped mass

On the other hand, in terms of wind turbine aerodynamics and platform hydrodynamics, although direct CFD modelling is more time-consuming, it has the best accuracy compared to other approaches used in engineering tools as shown in Table 1.1. Other advantages of adopting direct CFD modelling includes the inherent consideration of viscous effects and 3D effects without additional input from experiment, and the ability to visualise and examine detailed flow field at any position to provide insights into sophisticated physical phenomena, as discussed in Sections 1.2.1.4 and 1.2.3.2.

Previously, CFD has been mainly used in analysing either wind turbine aerodynamic or platform hydrodynamics without taking into consideration the coupling effects between them. In recent years, thanks to the rapid advances in computer technology, some researchers have studied the coupled response of an FOWT system under both wind and wave environmental conditions using CFD tools to well reflect the real situation. Ren et al. (2014) carried out CFD analysis of a 5 MW floating wind turbine system supported by a TLP under coupled wave-wind conditions using the commercial software FLUENT with their User Defined Function (UDF). The numerical results were validated against experimental data. It was pointed out that though hydrodynamic forces played a dominant role in the dynamic surge response of a floating system, the aerodynamic forces contributed to the average/mean surge response of the system. Quallen et al. (2014) performed a full-system, two-phase CFD simulation with an OC3 spar-type FOWT model considering both the wind and wave excitation forces. By comparing CFD results with those from FAST simulations, the predicted surge motion variation with CFD modelling was 25% less than the results from FAST, likely due to a constant drag coefficient adopted in FAST. Quallen and Xing (2016) further extended their CFD code by adding a variable-speed generator-torque controller and its functions in controlling generator speed and torque were studied in a coupled analysis of the OC3 spar-type FOWT. Tran and Kim (2016b) modelled a fully coupled aero-hydrodynamic OC4 semi-submersible FOWT using a dynamic fluid body interaction method coupled with an overset moving grid technique embedded in the commercial CFD software STAR-CCM+. A comparison between the CFD results with FAST data showed overall good agreement. However, in terms of maximum wind turbine power, as large as four-fold discrepancy is revealed between the power predicted from the CFD calculations and that from FAST, along with a 32.2% difference in the predicted average mooring tension, indicating the importance of accurate full-system FOWT simulations. Leble and Barakos (2016) coupled a 3D multi-block structured CFD solver HMB2 for wind turbine aerodynamics and a Smoothed Particle Hydrodynamics (SPH) code for floating platform hydrodynamics. Coupled aero-hydrodynamic analysis was performed for a 10 MW FOWT, and external loadings from wind and wave were analysed as well as 6 DoF motion responses of the floating system. Liu et al. (2017b) developed a CFD solver using the

sliding mesh technique and investigated the coupling effects between different components of the OC4 semi-submersible FOWT model.

These researchers have made significant progress in coupled FOWT simulations using CFD methods. However, the aforementioned studies mainly focused on modelling the aerodynamics and hydrodynamics of FOWT systems. As to structural flexibility and mooring system analysis, simplifications were usually made. In their models, turbine blades were assumed to be rigid and structural flexibility were simply neglected. Furthermore, quasi-static mooring analysis methods were employed without considering dynamic effects.

As a result, further work is still required to develop a fully coupled high-fidelity analysis tool for FOWT applications, including flexible turbine blade modelling and dynamic mooring system analysis. With the help of such a tool, complex FOWT FSI problems can be better understood. Meanwhile, as a supplementary means to expensive experimental tests, it can also help validate and calibrate existing engineering tools.

1.3 Objectives of Thesis

The main objectives of this research are to develop a fully coupled high-fidelity aero-hydro-mooring-elastic analysis tool for FOWTs in combined wind/wave conditions, and to gain a better understanding of the underlying physics and sophisticated interaction between wind/wave and an FOWT as well as the influence of different components on each other within the system. In this tool, wind turbine aerodynamics and floating platform hydrodynamics are studied using a CFD approach based on an open source CFD toolbox OpenFOAM (https://www.openfoam.org/) so as to achieve best accuracy. The structural dynamics of turbine blades is solved using an open source MultiBody Dynamics code MBDyn (https://www.mbdyn.org), which is able to model flexible bodies using the Geometrically Exact Beam Theory (GEBT). Mooring systems can be analysed via either quasi-static or dynamic methods. This tool is not designed to replace existing computationally efficient engineering codes but rather serves as a supplementary way to experiment for validating and calibrating these codes.

In order to accomplish this goal, several successive steps are taken due to the complexity of this study:

1. Develop a high-fidelity CFD tool for coupled aero-hydro-mooring analysis of FOWTs under combined wind/wave conditions and study the interactions between the wind turbine and floating platform of an FOWT. In this step, turbine blades are treated as rigid and a quasi-static approach is employed to model mooring systems for simplification.

2. Implement an aeroelastic analysis tool for offshore wind turbines with flexible blades by coupling a CFD flow solver with an MBD structural solver, which is capable of modelling flexible bodies based on the beam theory, and analyse the effects of blade elasticity on wind turbine aerodynamics. At this stage, effects of the floating platform in an FOWT system are simplified by imposing a prescribed motion to the turbine base.

3. Integrate the above tools into a high-fidelity aero-hydro-mooring-elastic analysis tool using a coupled CFD-MBD approach, and investigate wind turbine aerodynamics, blade structural dynamics, platform hydrodynamic and mooring system dynamics of an FOWT under combined wind/wave conditions.

1.4 Outline of Thesis

The structure of this thesis is outlined as follows.

Chapter 1 introduces the background of this study by providing an overview of the development of offshore wind energy and pointing out the challenges in designing FOWTs. The commonly used numerical methods in analysing various aspects of FOWTs in previous investigations are then briefly reviewed.

In Chapter 2, the fully coupled CFD-MBD tool developed in this project for numerical analysis of FOWTs in combined wind/wave conditions is introduced. Detailed description of the various numerical methods and techniques adopted in the present

tool is presented, including CFD modelling of fluid flow, calculation of structural response with MBDyn, CFD mesh motion handling and analysis of mooring system.

Due to the complexity of the problems investigated, Chapter 3 presents a series of case studies to validate the various components of the developed fully coupled tool by comparing results from the present code with published experimental and numerical data. These studies include basic flow modelling, wind turbine aerodynamics analysis, floating platform hydrodynamics analysis, dynamic analysis of a flexible riser and fully coupled analysis of an oscillating flexible cantilever.

The following three chapters focus on the application of the numerical tool to FOWT problems at different development stages, which correspond to the three steps to achieve the final goal as described in Section 1.3. A coupled aero-hydro-mooring analysis of the OC4 semi-submersible FOWT under combined wind/wave conditions is firstly conducted in Chapter 4 without considering blade flexibility and mooring line dynamics. Effects of the dynamic motions of the floating platform on the wind turbine aerodynamic performance and the impacts of the wind turbine aerodynamics on the behaviour of the floating platform and on the mooring system responses are examined.

Chapter 5 then presents an aeroelastic analysis of the NREL 5-MW offshore wind turbine with flexible blades under both fixed-bottom and prescribed platform surge motion conditions. Effects of blade flexibility and platform surge motion on wind turbine aerodynamics and structural responses are investigated.

A fully coupled aero-hydro-mooring-elastic analysis is lastly carried out in Chapter 6 for the OC4 semi-submersible FOWT under a combined wind/wave condition to demonstrate the capabilities of the developed CFD-MBD tool. Wind turbine aerodynamics, blade structural dynamics, floating platform hydrodynamic and mooring line dynamics of the FOWT are analysed.

In Chapter 7, conclusions and summaries are finally drawn and recommendations for future research are provided.

Chapter 2 Numerical Methods

As the interaction between wind/wave and an FOWT is complicated, several numerical techniques are utilised in the fully coupled FSI analysis tool developed in this project, including fluid flow modelling, structural response calculation, CFD mesh motion handling and mooring system analysis. Figure 2.1 depicts the structure of the present FSI tool, where built-in features in OpenFOAM and MBDyn are indicated in black; the wave modelling module marked in red is incorporated from a previously developed solver (Cha and Wan, 2011; Cao and Wan, 2014); new functions implemented in this project are highlighted in blue. In this chapter, these techniques are described in detail, and the overall modelling procedure of the present tool is presented.

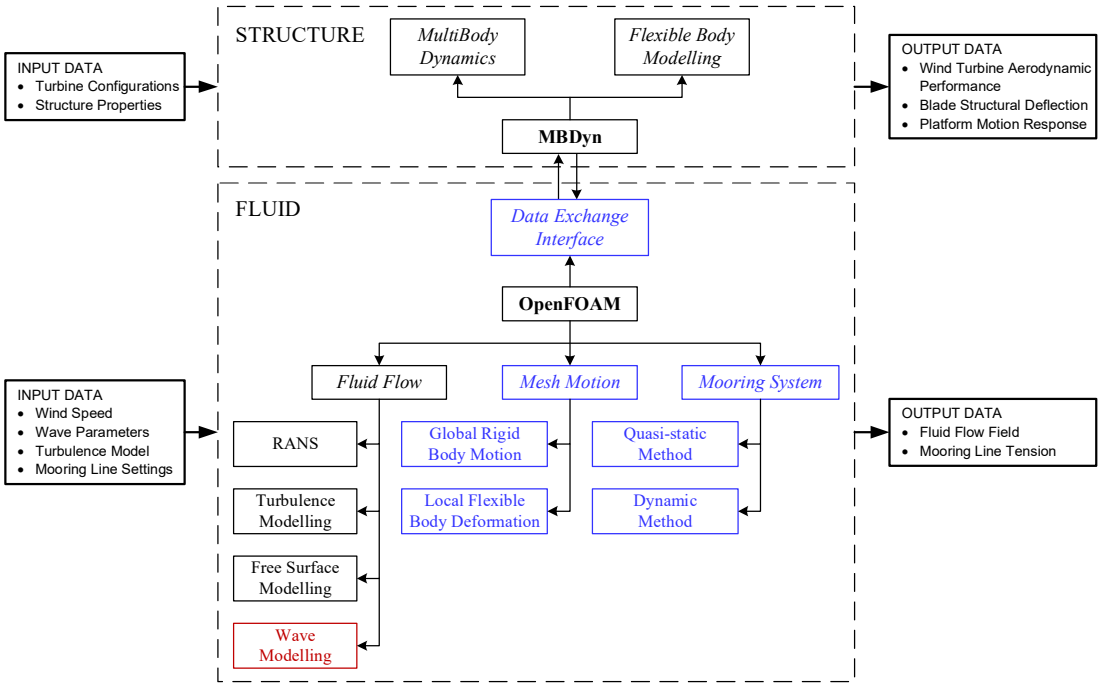

Figure 2.1 Structure of the fully coupled FSI analysis tool for FOWTs: Black–Built-in, Red–Incorporated, Blue–Developed

2.1 Fluid Flow Modelling

Numerical simulation of fluid flow in the FOWT FSI problem is performed based on the open source CFD toolbox OpenFOAM. As an open source project, OpenFOAM offers free access to its source code so that anyone can use it freely and modify the code to meet their own requirement. In addition, continuous development of

OpenFOAM over the past decade has resulted in the implementation of numerous commonly used numerical modules and libraries, making it easy to build new libraries and solvers. As a result, OpenFOAM has recently become increasingly popular in academia and industry, and it is adopted throughout this project.

In this section, mathematical models used in OpenFOAM for FOWT applications are presented, including governing equations of fluid flow, turbulence modelling for flow with high Reynolds number and free surface capturing for two-phase fluid flow. A wave modelling library developed in OpenFOAM for wave generation and damping is also described.

2.1.1 Governing Equations of Fluid Flow

The fluid flow around an FOWT is assumed to be transient, incompressible and viscous. In this study, the flow field is obtained by solving the following continuity and Reynolds-Averaged Navier-Stokes (RANS) equations in an Arbitrary Lagrangian-Eulerian (ALE) form:

$$\nabla \cdot \mathbf{U} = 0 \tag{2.1}$$

$$\frac{\partial \rho \mathbf{U}}{\partial t} + \nabla \cdot (\rho(\mathbf{U} - \mathbf{U}_g)\mathbf{U}) = -\nabla p_d - \mathbf{g} \cdot \mathbf{x} \nabla \rho + \nabla \cdot (\mu_{eff} \nabla \mathbf{U}) + \nabla \mathbf{U} \cdot \nabla \mu_{eff} + \mathbf{f}_\sigma \tag{2.2}$$

where $\mathbf{U}$ and $\mathbf{U}_g$ represent velocity of flow field and grid nodes, respectively; $p_d = p - \rho \mathbf{g} \cdot \mathbf{x}$ is pressure of flow field obtained by subtracting the hydrostatic part $\rho \mathbf{g} \cdot \mathbf{x}$ from total pressure p; $\mathbf{g}$ is the gravity acceleration vector; ρ is the fluid density; $\mu_{eff} = \rho(\nu + \nu_t)$ denotes the effective dynamic viscosity of fluid, in which ν and ν_t are the kinematic and eddy viscosity, respectively; $\mathbf{f}_\sigma$ is the surface tension term included for completeness although its effects are negligible in this study.

2.1.2 Turbulence Modelling

In typical FOWT simulations, Reynolds number can be as high as 10^7 and fluid flow is fully turbulent. It is thus necessary to utilise turbulence modelling in this study. OpenFOAM provides various turbulence models and the high-Reynolds-number two-

equation k - ω shear stress transport (SST) turbulence model (Menter, 2009) is adopted as the closure for the RANS equations throughout this project. The k - ω SST turbulence model combines the standard k - ω and k - ε models by adopting the standard k - ω model near the boundary layer and switching to the standard k - ε model in the far-field.

The governing equations for the turbulent kinetic energy k and the specific dissipation rate ω are defined as follows:

$$\frac{\partial \rho k}{\partial t} + \nabla \cdot \left(\rho \mathbf{U} k \right) = \nabla \cdot \left(\Gamma_k \nabla k \right) + \tilde{P}_k - D_k \tag{2.3}$$

$$\frac{\partial \rho \omega}{\partial t} + \nabla \cdot \left(\rho \mathbf{U} \omega \right) = \nabla \cdot \left(\Gamma_\omega \nabla \omega \right) + P_\omega - D_\omega + Y_\omega \tag{2.4}$$

where Γ_k and Γ_ω represent the effective diffusivity of the turbulent kinetic energy k and the specific dissipation rate ω, respectively; $\tilde{P}_k$ and P_ω are the turbulence production terms while D_k and D_ω denote the turbulence dissipation terms; Y_ω is the cross-diffusion term introduced by blending the standard k - ω and k - ε models. The specific dissipation rate ω is the rate at which turbulence kinetic energy is converted into thermal internal energy per unit volume and time, and it is related to the turbulence dissipation rate ε as $\omega = \frac{\varepsilon}{k\beta^*}$, where β^* is a model constant set to 0.09 (Menter, 2009).

The effective diffusivities Γ_k and Γ_ω are calculated by:

$$\Gamma_k = \mu + \alpha_k \mu_t \tag{2.5}$$

$$\Gamma_\omega = \mu + \alpha_\omega \mu_t \tag{2.6}$$

where μ and μ_t are the dynamic and turbulent viscosity, respectively; α_k and α_ω are blended coefficients using the relations shown below:

$$\phi = F_1 \phi_1 + \left(1 - F_1 \right) \phi_2 \tag{2.7}$$

in which ϕ_1 represents constants in the standard k - ω model (α_{k1} , $\alpha_{\omega 1}$, …), ϕ_2 denotes constants in the standard k - ε model (α_{k2} , $\alpha_{\omega 2}$, …) and ϕ is the corresponding constant of the k - ω SST model (α_k , α_ω , …). The blending function F_1 is calculated using the following formulae:

$$\begin{aligned} F_1 &= \tanh\left(\arg_1^4\right) \\ \arg_1 &= \min\left[\max\left(\frac{\sqrt{k}}{\beta^* \omega y}, \frac{500\nu}{y^2\omega}\right), \frac{4\rho\alpha_{\omega 2}k}{CD_{k\omega}^+ y^2}\right] \\ CD_{k\omega}^+ &= \max\left(CD_{k\omega}, 10^{-10}\right) \\ CD_{k\omega} &= 2\rho\alpha_{\omega 2}\nabla k \cdot \frac{\nabla\omega}{\omega} \end{aligned} \tag{2.8}$$

The turbulent viscosity μ_t is defined as:

$$\mu_t = \frac{\rho a_1 k}{\max\left(a_1\omega, b_1 S F_2\right)} \tag{2.9}$$

where S is the strain rate magnitude $S = \sqrt{2S_{ij}S_{ji}}$ and F_2 is a second blending function $F_2 = \tanh\left\{\left[\max\left(\frac{2\sqrt{k}}{\beta^*\omega y}, \frac{500\nu}{y^2\omega}\right)\right]^2\right\}$.

The production term $\tilde{P}_k$ for k equation is calculated by:

$$\tilde{P}_k = \min\left(\mu_t S^2, c_1\beta^*\rho k\omega\right) = \rho\min\left(\nu_t S^2, c_1\beta^* k\omega\right) \tag{2.10}$$

The production term P_ω for ω equation is defined as:

$$P_\omega = \gamma\frac{1}{\nu_t}\tilde{P}_k \tag{2.11}$$

where γ is a blended constant via Eq. (2.7).

The dissipation terms D_k and D_ω are determined as follows:

$$D_k = \beta^* \rho k \omega \tag{2.12}$$

$$D_\omega = \beta \rho \omega^2 \tag{2.13}$$

in which β is also a blended constant using Eq. (2.7).

The cross-diffusion term Y_ω for ω equation is defined as:

$$Y_\omega = 2\left(1-F_1\right)\rho\alpha_{\omega 2}\nabla k \cdot \frac{\nabla \omega}{\omega} = \left(1-F_1\right)CD_{k\omega} \tag{2.14}$$

Table 2.1 lists all the coefficients used in the k-ω SST turbulence model.

Table 2.1 Coefficients for the k-ω SST turbulence model

α_{k1}	α_{k2}	$\alpha_{\omega 1}$	$\alpha_{\omega 2}$	β_1	β_2	γ_1	γ_2	β^*	a_1	b_1	c_1
0.85	1.0	0.5	0.856	0.075	0.0828	0.556	0.44	0.09	0.31	1.0	10.0

Wall functions are adopted throughout the project for near-wall treatment.

2.1.3 Free Surface Modelling

For two-phase problems like FOWT simulations, two types of fluid with different density and viscosity are present. The Volume of Fluid (VOF) method (Hirt and Nichols, 1981) is adopted in OpenFOAM to capture the interface or free surface between the two fluids. In this method, a volume fraction variable denoted as α is defined for each cell, representing the ratio of volume occupied by a certain type of fluid (air or water) in one cell. For a two-phase air-water flow, this variable α complies with the distribution as follows:

$$\begin{cases} \alpha = 0, & air \\ \alpha = 1, & water \\ 0 < \alpha < 1, & free\ surface \end{cases} \tag{2.15}$$

The volume fraction variable α is governed by the following transport equation:

$$\frac{\partial \alpha}{\partial t} + \nabla \cdot [(\mathbf{U} - \mathbf{U}_g)\alpha] + \nabla \cdot [\mathbf{U}_r(1-\alpha)\alpha] = 0 \tag{2.16}$$

To better capture the free surface, a bounded compression technique (Rusche, 2002) is adopted which introduces an additional third compression term on the left-hand side of the transport equation, where $\mathbf{U}_r$ is an artificial velocity field used to compress the interface. The compression term only functions near free surface due to the inclusion of $(1-\alpha)\alpha$ and does not affect the solution of α outside the transition region. The compression velocity $\mathbf{U}_r$ is formulated based on the maximum velocity magnitude within the transition region and is oriented perpendicular to the interface using the normal vector of the interface. For detailed information, please refer to Rusche (2002). Coupled with Navier-Stokes equations, the transport equation for the volume fraction is solved to obtain α of each cell and free surface is then determined.

For two-phase flow problems, fluid physical properties, such as density and viscosity, are calculated as weighted averages based on the volume fraction of water and air in one cell as follows:

$$\rho = \alpha\rho_l + (1-\alpha)\rho_g \tag{2.17}$$

$$\mu = \alpha\mu_l + (1-\alpha)\mu_g \tag{2.18}$$

where subscripts l and g denote liquid and gas, respectively.

The surface tension term $\mathbf{f}_\sigma$ in Eq. (2.2) is related to the volume fraction variable α via the following equation:

$$\mathbf{f}_\sigma = \sigma\kappa\nabla\alpha \tag{2.19}$$

where σ is a constant coefficient of surface tension and is set to $\sigma = 0.07 kg/s^2$ in this study; κ represents the curvature of free surface defined as follows:

$$\kappa = -\nabla \cdot \left(\nabla\alpha / |\nabla\alpha|\right) \tag{2.20}$$

The surface tension term only takes effect at the free surface and equals zero elsewhere.

2.1.4 Wave Modelling

FOWTs operating at sea are subject to significant hydrodynamic loading from ocean waves. It is thus necessary to include wave modelling features to the coupled tool.

2.1.4.1 Wave Generation

A wave generation module previously developed by Professor Decheng Wan's research group in Shanghai Jiao Tong University is incorporated in the present code, which is able to model various types of waves including linear wave, Stokes 2nd order wave, freak wave, solitary wave, irregular wave etc. (Shen et al., 2013; Cao and Wan, 2014; Shen and Wan, 2016). One of the common ways to generate waves numerically is to simulate physical piston-type or flap-type wave-makers used in experimental wave tanks by specifying the movement of mesh boundaries. However, these approaches require the whole computational mesh to be updated every time step, which increases computational cost. In this tool, numerical waves are generated by specifying free surface elevation and velocity distribution at the inlet boundary with various wave theories (Baudic et al., 2001). This method has been proven to be very effective and mesh movement is also avoided. Two commonly used regular wave theories are presented below.

- *Linear Wave Theory*

For linear waves, the following equation is used to describe the free surface elevation:

$$\eta = A\cos\theta \tag{2.21}$$

The horizontal and vertical components of fluid velocity distribution are represented in the equations below:

$$u = \frac{\pi H}{T}\frac{\cosh k(z+d)}{\sinh kd}\cos\theta \tag{2.22}$$

$$w = \frac{\pi H}{T}\frac{\sinh k(z+d)}{\sinh kd}\sin\theta \tag{2.23}$$

where A and $H = 2A$ denote wave amplitude and wave height; T represents wave period; k is wave number; d stands for water depth and $\theta = kx - \omega t$ is the phase.

- *Stokes 2nd Order Wave Theory*

In Stokes 2nd order wave theory, free surface elevation is defined as:

$$\eta = \frac{H}{2}\cos\theta + \frac{H}{8}\left(\frac{\pi H}{L}\right)\frac{\cosh kd}{\sinh^3 kd}\left(\cosh 2kd + 2\right)\cos 2\theta \tag{2.24}$$

The horizontal and vertical components of fluid velocity distribution are calculated using the following equations:

$$u = \frac{\pi H}{T}\frac{\cosh k(z+d)}{\sinh kd}\cos\theta + \frac{3}{4}\frac{\pi H}{T}\left(\frac{\pi H}{L}\right)\frac{\cosh 2k(z+d)}{\sinh^4 kd}\cos 2\theta \tag{2.25}$$

$$w = \frac{\pi H}{T}\frac{\sinh k(z+d)}{\sinh kd}\sin\theta + \frac{3}{4}\frac{\pi H}{T}\left(\frac{\pi H}{L}\right)\frac{\sinh 2k(z+d)}{\sinh^4 kd}\sin 2\theta \tag{2.26}$$

where L represents wave length while other parameters remain the same as defined in linear wave theory.

2.1.4.2 Wave Damping

To alleviate wave reflection from the boundary, a wave damping module is also integrated into the present FSI analysis tool (Cha and Wan, 2011; Shen et al., 2014), which sets up a wave damping zone, i.e. sponge layer (Larsen and Dancy, 1983), near the outlet boundary as illustrated in Figure 2.2. The sponge layer takes effect by adding an additional artificial viscous term as a source term to Eq. (2.2). The new term is defined as:

$$\mathbf{f}_s = -\rho\mu_s\mathbf{U} \tag{2.27}$$

where μ_s is the artificial viscosity calculated by the following equation:

$$\mu_s(x) = \begin{cases} \alpha_s \left(\dfrac{x - x_0}{L_s} \right)^2, & x > x_0 \\ 0, & x \le x_0 \end{cases} \tag{2.28}$$

in which α_s defines the damping strength for the sponge layer; x denotes the coordinates of the grid cells in the x direction; x_0 and L_s represent the start position and length of the sponge layer. A recommended value for L_s is twice the length of the simulated wave. The artificial viscous term is only effective for those cells belonging in the sponge layer and is equal to zero elsewhere. An outflow boundary condition is also defined for the outlet boundary to balance the flux introduced from the inlet boundary.

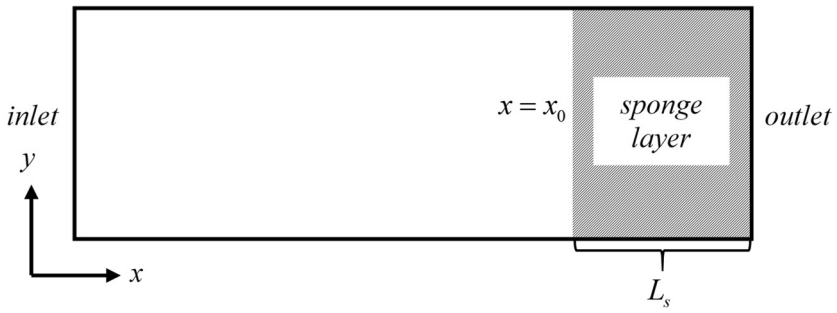

Figure 2.2 Sketch of sponge layer for wave damping

2.2 Structural Response Calculation

Structural responses of an FOWT include 6 DoF rigid body motion of the whole floating system and deformation of its flexible turbine blades. Calculation of FOWT structural responses in this project is carried out using a general purpose MultiBody Dynamics analysis software MBDyn. Released under the GNU's General Public License (GPL) 2.1, it can be used and distributed freely with its source code available to the public just like OpenFOAM. Based on the MultiBody Dynamics theory, MBDyn is able to model a multibody system consisting of both rigid and flexible bodies. Originally developed for rotorcraft applications, for example, helicopters and tiltrotors (Ghiringhelli et al., 1999), MBDyn was later applied to micro aerial vehicles (Benedict et al., 2011) and wind turbines (Meng et al., 2009; Pierangelo and Jayanarayanan,

2011). This section presents an overview of the MultiBody Dynamics theory adopted by MBDyn as well as how flexible structures are modelled based on the beam theory.

2.2.1 MultiBody Dynamics

A complex structure like an FOWT can be considered as a multibody system, which is composed of rigid bodies, i.e. floating platform, nacelle and hub, and flexible parts such as blades and tower. These bodies/parts are connected by kinematic constraints. For example, the turbine tower is fixeded to the floating platform, which imposes a clamp constraint where no relative translation and rotation between the two parts are allowed. Dynamics of such a multibody system can be solved by codes like MBDyn which adopt the MultiBody Dynamics theory.

MBDyn adopts a Lagrange multiplier or redundant coordinate set formulation for a multibody system (Ghiringhelli et al., 2000). Compared to the reduced coordinate set method where only a minimum number of DoFs is used to describe the motion of the system, a redundant formulation allows 6 DoF motion for each body and constraints are enforced by Lagrange multipliers (Pierangelo and Jayanarayanan, 2011). Although more DoFs are introduced, the current approach allows a simple and flexible formulation to easily model large systems with complex structures (Masarati, 2000).

For each body of the system, Newton-Euler equations of motion are established in the differential-algebraic form as a set of first-order equations together with the constraint equation, resulting in a system of Differential-Algebraic Equations (DAE) as follows:

$$\mathbf{M}\dot{\mathbf{x}} = \mathbf{p} \tag{2.29}$$

$$\dot{\mathbf{p}} + \boldsymbol{\phi}_{\mathbf{x}}^{\mathrm{T}}\boldsymbol{\lambda} = \mathbf{f}\left(\mathbf{x}, \dot{\mathbf{x}}, t\right) \tag{2.30}$$

$$\boldsymbol{\phi}\left(\mathbf{x}, t\right) = 0 \tag{2.31}$$

where $\mathbf{M}$ is the inertia matrix of a body, i.e. mass and moment of inertia; $\mathbf{x}$ represents the vector of the generalised coordinates including both translational and rotational parameters in the global reference frame; the dot operator above a variable denotes its derivative with respect to time; $\mathbf{p}$ stands for the momentum vector of the body

containing both linear and angular components; ϕ is a set of kinematic constraints applied on the body and $\phi_{\mathbf{x}}^{\mathrm{T}}$ represents the Jacobian of ϕ with respect to the generalized coordinates vector $\mathbf{x}$; $\boldsymbol{\lambda}$ denotes the vector of the Lagrange multipliers for the constraints; $\mathbf{f}$ is the external force and moment vector exerted upon the body, including centrifugal and Coriolis forces due to rotation, and might be related to its displacement and velocity as well as time. An implicit multistep integration scheme is applied to solve the system of equations (Masarati et al., 2014).

2.2.2 Flexible Structure Modelling

In order to model flexible bodies in MBDyn, a finite volume approach for the multibody formulation of three-node beam elements based on the Geometrically Exact Beam Theory (GEBT) is implemented (Ghiringhelli et al., 2000). In this method, a flexible body can be modelled as one or more beam elements, each of which can be divided into three beam element portions by two evaluation points (squares) as indicated in Figure 2.3. The three beam element portions are associated with three reference points (circles), which represents the elastic axis of the beam. Those reference points do not necessarily need to be on a straight line and can be offset from the geometrical nodes (triangles), where equilibrium equations are established considering both external and internal forces as well as moments.

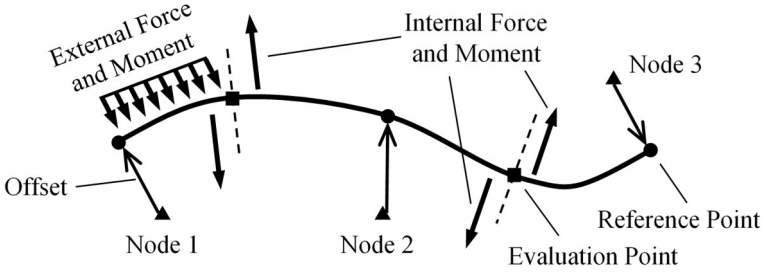

Figure 2.3 Illustration of a finite volume three-node beam in MBDyn

External force and moment are integrated over every beam element portion related to a reference point and later translated to the corresponding node. Meanwhile, internal forces and moments are evaluated at the cross sections of the evaluation points and they are related to the geometrical strains and curvatures via the constitutive law specified by the user in the following manner:

$$\begin{pmatrix} F_x \\ F_y \\ F_z \\ M_x \\ M_y \\ M_z \end{pmatrix} = f\left[\begin{pmatrix} \varepsilon_x \\ \gamma_y \\ \gamma_z \\ \kappa_x \\ \kappa_y \\ \kappa_z \end{pmatrix}, \begin{pmatrix} \dot{\varepsilon}_x \\ \dot{\gamma}_y \\ \dot{\gamma}_z \\ \dot{\kappa}_x \\ \dot{\kappa}_y \\ \dot{\kappa}_z \end{pmatrix}\right] \tag{2.32}$$

where F_x is the axial force component; F_y and F_z are the shear force components; M_x is the torsional moment component; M_y and M_z are the bending moment components; ε_x is the axial strain component; γ_y and γ_z are the shear strain components; κ_x is the torsional curvature component; κ_y and κ_z are the bending curvature components; the dot operator above a variable denotes its derivative to time; f is an arbitrary function defining the constitutive law.

A variety of constitutive laws are available to users in MBDyn to meet various requirements. A general linear viscoelastic constitutive law is adopted in this study and can be described with the following equation:

$$\mathbf{F} = \mathbf{K}\boldsymbol{\varepsilon} + \mathbf{C}\dot{\boldsymbol{\varepsilon}} \tag{2.33}$$

where $\mathbf{F}$ is a generalised internal force vector; $\boldsymbol{\varepsilon}$ is a generalised strain vector and $\dot{\boldsymbol{\varepsilon}}$ is a generalised strain rate vector; $\mathbf{K}$ is a linear stiffness matrix, which need be provided by users for every cross section; $\mathbf{C}$ is a linear viscosity matrix associated with internal structural damping, which is assumed to be proportional to $\mathbf{K}$.

A system of equilibrium equations, i.e. Eq. (2.29)-(2.31), is then established and solved for the position and orientation as well as velocities of all geometrical nodes representing either a rigid body or a component of a beam element.

2.3 CFD Mesh Motion Handling

One of the challenges for a fully coupled numerical simulation of a floating offshore wind turbine with flexible blades is how to handle the motion of the CFD mesh to

represent the complex structural responses of the system. As is shown in Figure 2.4, in addition to the rotational motion (revolution) of the wind turbine around its hub and platform-induced 6-DoF motion, flexible turbine blades are also subject to the deflections in both out-of-plane (flapwise) and in-plane (edgewise) directions relative to the rotor plane as well as the twist deformation along the blade pitch axis due to the exerted unsteady wind loading.

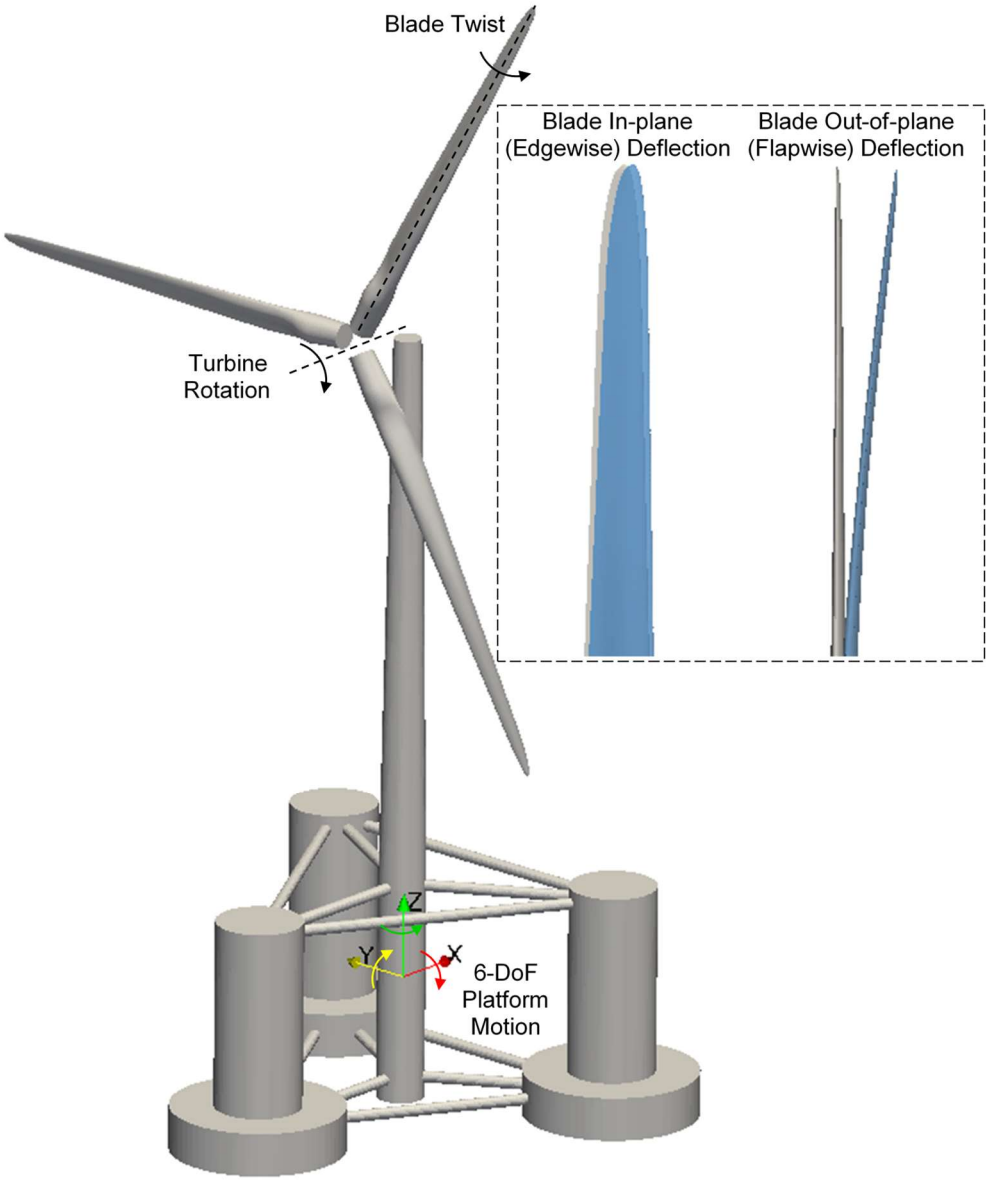

Figure 2.4 Illustration of complex structural responses involved in simulations of a semi-submersible FOWT (Robertson et al., 2014a) with flexible blades (light grey region shows un-deflected blade while light blue region shows deflected blade)

Based on their motion characteristics, these responses can be categorised into the following two groups:

1. Global rigid body motion, i.e. platform 6 DoF motion and turbine rotation, where parts or the whole of the system have the same global translational or rotational movement;

2. Local flexible body deformation, such as flapwise and edgewise deflections and torsional twist of a turbine blade, where a body has nonuniform responses locally in different regions and the shape of the body changes.

However, the current mesh motion library in OpenFOAM is unable to cope with both global rotational motion and local structural responses at the same time. It is thus necessary to develop a new mesh motion library for fully coupled FOWT simulations.

In this section, the mesh motion library implemented in the present tool is described. Section 2.3.1 details the method used to deal with global rigid body motion while the approach adopted to address local flexible body deformation is presented in section 2.3.2.

2.3.1 Global Rigid Body Motion

As the wind turbine of an FOWT is attached to its floating platform, the 6 DoF platform motion is also superimposed to the turbine. However, the rotation centre of the platform is different from the revolution centre of the turbine, which makes it difficult for traditional mesh motion techniques, such as mesh morphing, to update the CFD mesh. Currently, one of the common practices to deal with the global rigid body motion of an FOWT is to employ an overset or Chimera grid technique (Quallen et al., 2014; Tran and Kim, 2016b), where a system of multiple layers of disconnected component grids overlapping each other is used to discretise the flow domain, as demonstrated in Figure 2.5. As the overset grid technique is able to update component grids independently, it is undoubtedly rather powerful and suits the FOWT applications quite well. However, it is not easily accessible due to various reasons. For example, to access commercial CFD software packages with the overset grid capability

such as STAR-CCM+ used by Tran and Kim (2016b; 2018), a license has to be obtained. On the other hand, for some in-house codes like the CFDShip-Iowa (Quallen et al., 2014), the FoamedOver library (Boger et al., 2010) and the naoe-FOAM-SJTU solver implemented in OpenFOAM (Shen et al., 2015), either the commercialized overset grid assembly software SUGGAR or an improved version Suggar++, is utilised to generate the domain connectivity information (DCI), which also requires costly licence keys.

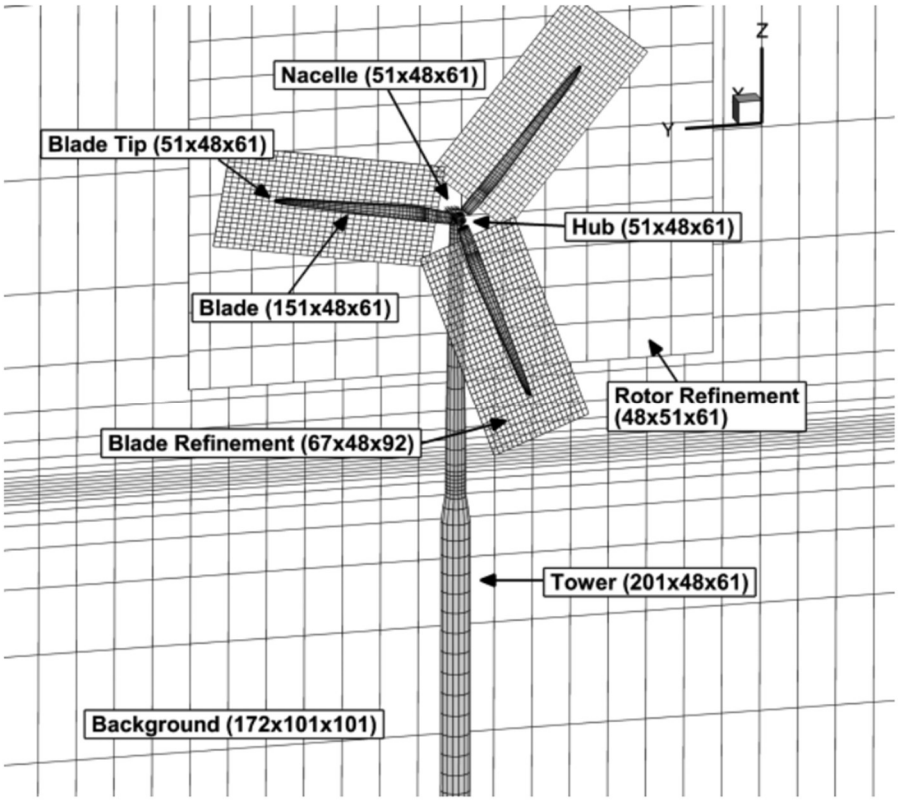

Figure 2.5 Illustration of overset grid design for an FOWT (Quallen et al., 2014)

In this project, a built-in sliding mesh technique in OpenFOAM termed AMI (Arbitrary Mesh Interface) is adopted and further adapted to cope with the global rigid body motion in FOWT applications instead of developing a complex overset grid approach. The AMI technique is designed for rotating machinery problems like turbine revolution, and it allows simulations across disconnected but adjacent mesh domains which are either stationary or moving relative to one another (OpenFOAM, 2011). For example, in order to model the rotation of a wind turbine, a pair of sliding mesh

surfaces (AMI surfaces) are created, which must be axisymmetric about the rotation axis of the turbine to avoid invalid mesh overlapping when rotation is applied. The surfaces divide the whole computational domain into two separate cell zones, i.e. the rotor zone encompassing the turbine blades and the stator zone as shown in Figure 2.6. Flow field data, such as velocity and pressure, is exchanged at the AMI surfaces via numerical interpolation. Wind turbine rotation can then be simulated by specifying a rotational motion for all the cells within the rotor zone.

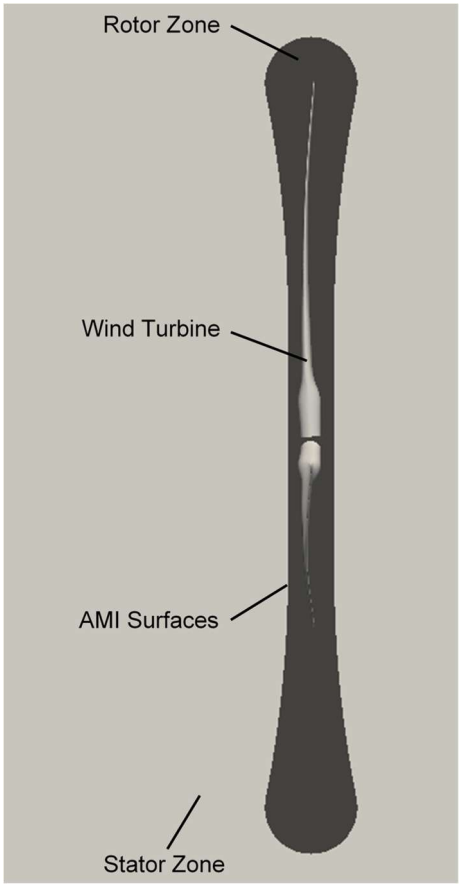

Figure 2.6 Illustration of AMI and cell zones in OpenFOAM

The concept of modelling rotational motion with the AMI technique is expanded in this project to the simulation of 6 DoF platform motion, specifically, the three rotational motion responses of an FOWT system. Take platform pitching motion for example. Geometrically, two pairs of cylindrical AMI sliding mesh surfaces are generated as shown in Figure 2.7, i.e. an inner smaller pair for the rotating wind turbine and an outer larger pair of surfaces surrounding the whole FOWT system. Since the

upper wind turbine also undergoes the pitching motion, the outer sliding mesh surface is extended to completely cover the turbine. The axis of the inner cylindrical surface coincides with the rotation axis of the wind turbine, while the axis of the outer surface points through the centre of mass of the platform and is perpendicular to the wave propagation direction. It is worth noting that, when all three rotational motion responses are modelled, a more versatile spherical topology is available and has to be applied instead of a cylindrical one.

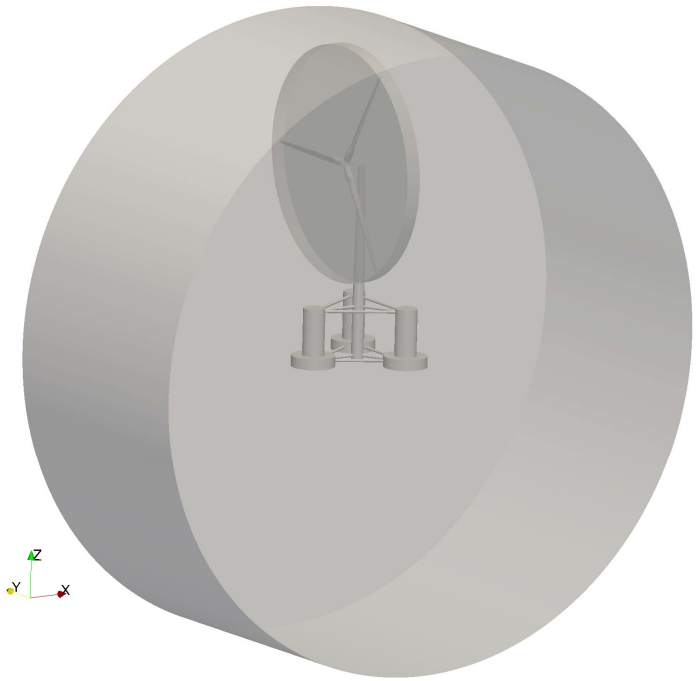

Figure 2.7 AMI surfaces of an FOWT

The whole computational grid is thus split into three separate cell zones by the two pairs of AMI surfaces as sketched in Figure 2.8, i.e. the inner cell zone in black, the middle cell zone in grey and the outer cell zone in white. Different rigid body motions are then applied to corresponding cell zones. One of the limitations in the current implementation of the mesh motion library is that the motion of a cell zone can only be prescribed as a predefined sinusoidal or linear function, such as the constant rotational speed of turbine revolution. However, in a fully coupled simulation, the motion responses of an FOWT are constantly calculated and updated. To address this issue, the mesh motion library is extended to accept predicted system responses as input of cell zone motion.

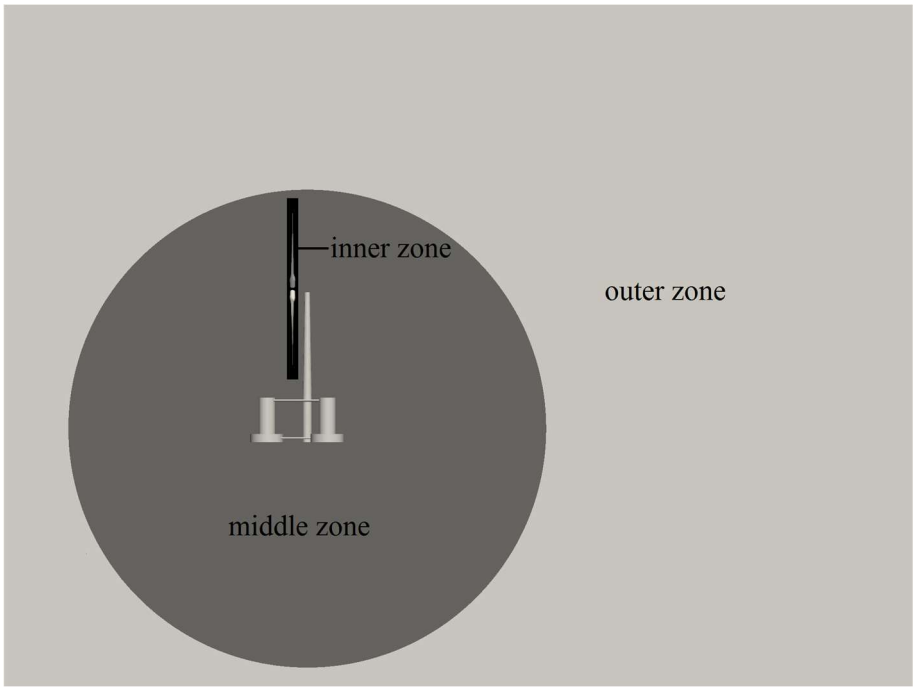

Figure 2.8 Cell zones of an FOWT

When an FOWT system is in motion, the outer zone only moves in the translational directions thus the inlet and outlet boundaries remain vertical, which is important for wave generation. The middle zone experiences the rotational motion responses (pitch for this case but all 3DoF for cases with a spherical AMI interface) as well as the translational components, while the inner zone undergoes all the platform motion responses together with the prescribed wind turbine rotation. As an ALE formulation is employed for the governing equations as shown in Eq. (2.2), mesh motion is automatically taken into consideration and water waves are able to propagate without distortion. By adopting the AMI technique to deal with rotational motion and separating the whole domain into several cell zones with their specific mesh motions, it is now possible to handle the global rigid body motion of an FOWT in an easy and more accessible way compared to the overset grid technique.

2.3.2 Local Flexible Body Deformation

The local deformation of flexible bodies like turbine blades is calculated in the structural solver MBDyn and transferred to the CFD solver at the fluid-structure interface, i.e. the representation of the turbine in both models. As mentioned earlier, a

flexible wind turbine blade is simplified as a beam-like structure in MBDyn and modelled as a series of 3-node beam elements consisting of geometrical nodes. On the other hand, the same geometry is discretised into a complex surface grid comprising a large number of points in the CFD mesh, as shown in Figure 2.9. The gap between the level of complexity in describing the same geometry within the two different models leads to a pair of un-matched/non-conformal interfaces. It is therefore necessary to firstly establish a mapping scheme to exchange data between CFD and MBD models.

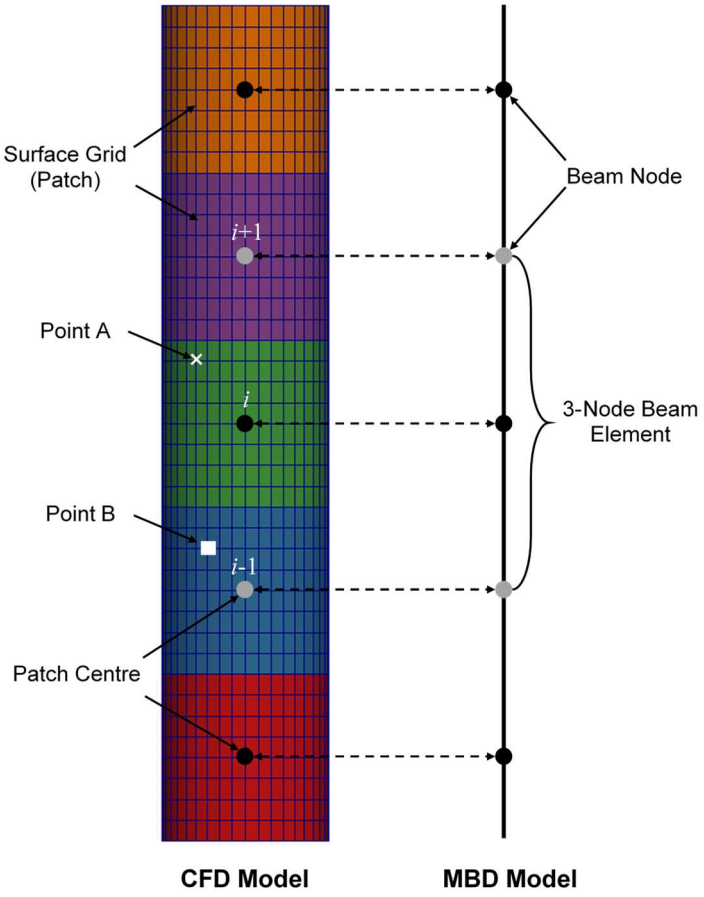

Figure 2.9 Diagram for mapping information between CFD and MBD models

Figure 2.9 illustrates the mapping between the two models. In the CFD model, the surface grid of the structure is decomposed into several small patches, each of which corresponds to a beam node in the MBD model. In addition, a centre is defined for every patch in the CFD grid and has the same kinematic information, i.e. position and orientation in the global reference frame, as the corresponding beam node in the MBD model via a motion data exchange.

The position of each point on every patch of the CFD surface grid is then determined using the kinematics of the patch centres. In order to minimise the deterioration of grid quality and maintain smooth transition of the surface grid between adjacent patches in the CFD model, a linear interpolation scheme (Pierangelo and Jayanarayanan, 2011; Li et al., 2015c) is implemented in the present tool by calculating the position of every point with the information from the centre of the patch it belongs to and the centre of its adjacent patch. For example, point A (marked as cross) in Figure 2.9 uses the kinematics of patch centres *i* and *i*+1 while point B (marked as square) needs the information from patches *i* and *i*-1. The following formula describes the interpolation scheme for the position of point A:

$$\mathbf{X} = \xi\left(\mathbf{X}_i + \mathbf{R}_i\mathbf{d}_i\right) + \left(1-\xi\right)\left(\mathbf{X}_{i+1} + \mathbf{R}_{i+1}\mathbf{d}_{i+1}\right) \tag{2.34}$$

where **X** represents the position of a point or a patch centre; **R** denotes the transformation matrix of a patch centre due to rotation; **d** is the distance vector pointing from a patch centre to the point; $\xi \in [0,1]$ stands for the normalised location of the point along the line connected by the two patch centres.

When the mapped surface mesh in the CFD model is obtained, the interior mesh must also be updated to make sure that the CFD mesh is still valid. In order to perform mesh update, the built-in dynamic mesh motion solver provided in OpenFOAM is utilised, which calculates the displacement of the internal mesh cell centres by solving the following Laplace mesh motion equation (Jasak and Tukovic, 2006):

$$\nabla \cdot \left(\gamma \nabla \mathbf{x}_g\right) = 0 \tag{2.35}$$

where $\mathbf{x}_g$ is the displacement of internal mesh cell centres; γ represents the diffusion coefficient of the equation. OpenFOAM provides a variety of functions for γ and an inverse quadratic form of $\gamma = 1/r^2$ is selected throughout this project, where r is the distance from mesh cell centres to structure boundaries. When this function is adopted, the influence of boundary motion is largely exerted upon cells close to the structure

and decreases rapidly when r increases. As a result, mesh quality near the structure can be best preserved.

To solve the Laplace mesh motion equation, the displacement of all the points on the turbine surface mesh is required as the boundary condition. However, the motion data transferred from MBDyn is expressed in the global reference frame, meaning that the global rigid body motion is also included in the displacement results. If the displacement data is directly utilised as the boundary condition of Eq. (2.35), provided that a converged solution can be obtained, large displacement of grid cells will also lead to the deterioration of the overall quality of the computational mesh. In order to address this issue, the global rigid body motion is firstly subtracted from the point displacement of the turbine surface mesh to obtain a temporary value. The mesh motion solver then takes the temporary point displacement of the structure boundaries as the boundary condition of Eq. (2.35). Meanwhile, as the AMI surfaces divide the whole computational domain into separate cell zones, as shown in Figure 2.8. When the mesh motion equation is assembled, only the cells inside the cell zone encompassing the turbine are taken into account while those in other cell zones are kept static by directly setting their displacement to zero, so that the size of the matrix can be reduced, and the computational time is thus decreased.

Once the displacement of internal cell centres is obtained, interpolation is performed to obtain the displacement of internal mesh points, which is then added to the initial position of all points to determine their updated position resulting from local blade deformation. Lastly, points in the rotor cell zone are rotated as a whole in a manner of rigid body motion to take global turbine rotation into consideration. If platform-induced 6-DoF motion is considered, they also need be applied. In such a way, the mesh motion library developed in the present tool is able to handle both global rigid body motion and local flexible body deformation experienced by an FOWT.

2.4 Mooring System Analysis

As mooring systems are essential in station-keeping for floating structures, a mooring system analysis module is developed in this project under the OpenFOAM framework

to calculate the mooring restoring force provided for an FOWT system. This module includes both quasi-static and dynamic methods discussed in Section 1.2.4. Although the dynamic method is able to predict more accurate results compared to the quasi-static method by taking into consideration dynamic effects such as inertial forces, it requires an initial condition for its shape and tension distribution, which can be achieved by performing a quasi-static calculation at the start of a simulation. As a result, both methods are implemented for the present tool.

2.4.1 Quasi-static Method

In the present quasi-static method, it is assumed that a mooring line is always in the 2D $O'x'z'$ plane defined by the anchor and fairlead of the mooring line, as illustrated in Figure 2.10. The local mooring line reference frame $O'x'y'z'$ rotates about the vertical axis of the global reference frame $Oxyz$ for an angle of θ, which is usually referred to as the arrangement angle of the mooring line in a mooring system.

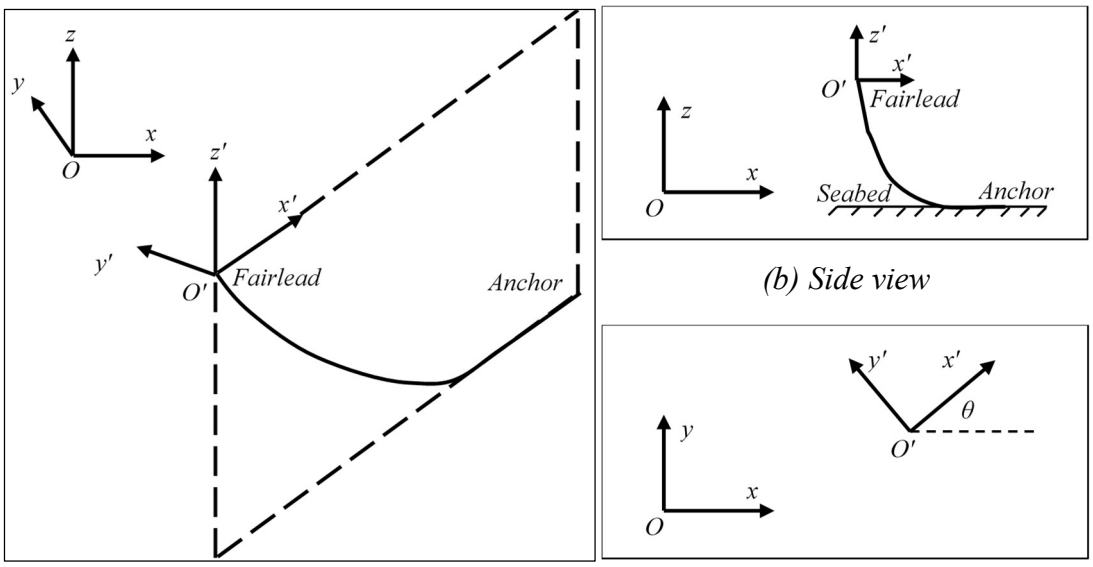

(a) 3D view *(b) Side view* *(c) Top view*

Figure 2.10 Definition of the mooring line reference frame

Although an analytical formulation, i.e. catenary equation, is present for mooring lines of the catenary shape, it cannot be applied to taut lines, i.e. without line portions lying on seabed. In order to simulate mooring lines of both catenary and taut shapes, a

discretised approach is utilised by dividing a mooring line into a given number of segments with identical length (Fan et al., 2012). For each segment, only tension force and weight in water are considered while hydrodynamic loadings from current and wave are neglected for simplicity, as shown in Figure 2.11.

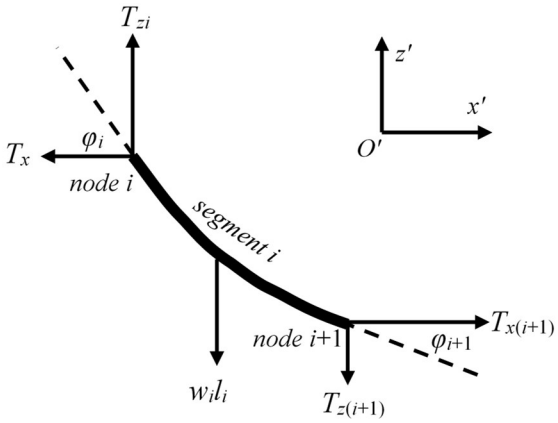

Figure 2.11 Sketch of force equilibrium for segment i in quasi-static mooring line analysis model

Equations of static equilibrium can be established for segment *i* in both horizontal and vertical directions as follows:

$$\begin{cases} T_{x(i+1)} = T_{xi} \\ T_{z(i+1)} = T_{zi} - w_i l_i \end{cases} \tag{2.36}$$

where T_x and T_z represent horizontal and vertical components of tension force at the two nodes (*i* and *i*+1) connected by segment *i*; w_i stands for segment weight per unit length in water, i.e. excluding buoyancy from weight in air; l_i denotes the unstretched or original length of the segment.

The tension force on the segment is also linked to its elongation in the following way:

$$s_i = l_i \left(1 + \frac{T_i}{E_i A_i} \right) \tag{2.37}$$

where s_i is stretched segment length after elongation; $T_i = \sqrt{T_{xi}^2 + T_{zi}^2}$ represents the total tension force at node *i* (T_{i+1} at node *i*+1 can also be used for calculation); E_i and A_i denote the Young's modulus and cross-sectional area for the segment, separately.

In addition, geometric constraints are present between node coordinates and stretched segment length (Wang et al., 2010):

$$\begin{cases} s_i \cos\varphi_i = x'_{i+1} - x'_i = \Delta x' \\ s_i \sin\varphi_i = z'_i - z'_{i+1} = \Delta z' \end{cases} \tag{2.38}$$

where φ_i is the included angle between T_i and T_{xi}; x' and z' are the horizontal and vertical coordinates of a node in the local mooring line reference frame, respectively; $\Delta x'$ and $\Delta z'$ are the absolute difference between coordinates of nodes *i* and *i*+1 in Ox' and Oz' directions, separately.

In order to obtain the tension force and coordinates of each node of a mooring line, the above equations are solved in a piecewise manner. Figure 2.12 shows the flowchart for the quasi-static mooring line analysis method adopted in the present tool. For a mooring line divided into *n* segments, there are a total number of *n*+1 nodes, which are numbered from 0 (fairlead) to *n* (anchor). At the start of the simulation, the horizontal and vertical tension forces at the fairlead, i.e. T_{x0} and T_{z0}, are set to some assumed values. For example, a reasonable estimation would be the total weight of the mooring line in water. The tension forces at the node adjacent to the fairlead, i.e. T_{x1} and T_{z1}, can be obtained from Eq. (2.36). As the coordinates at the fairlead of the mooring line are already known, x'_1 and z'_1 of node 1 can also be estimated using Eq. (2.37) and (2.38). Following the same procedure, the tension forces and coordinates of all nodes along the mooring line can be predicted, including the anchor (node *n*).

However, as with the fairlead, the coordinates of the anchor are also provided in advance. By comparing the predicted and actual coordinates of the anchor, error functions can be defined and computed as follows:

$$\begin{cases} errX = x'_n - x'_{anchor} \\ errZ = z'_n - z'_{anchor} \\ errTotal = \sqrt{errX^2 + errZ^2} \end{cases} \tag{2.39}$$

where *errX* and *errZ* represent the differences between predicted coordinates, i.e. x'_n and z'_n, and actual values, i.e. x'_{anchor} and z'_{anchor}, respectively; *errTotal* denotes the total difference.

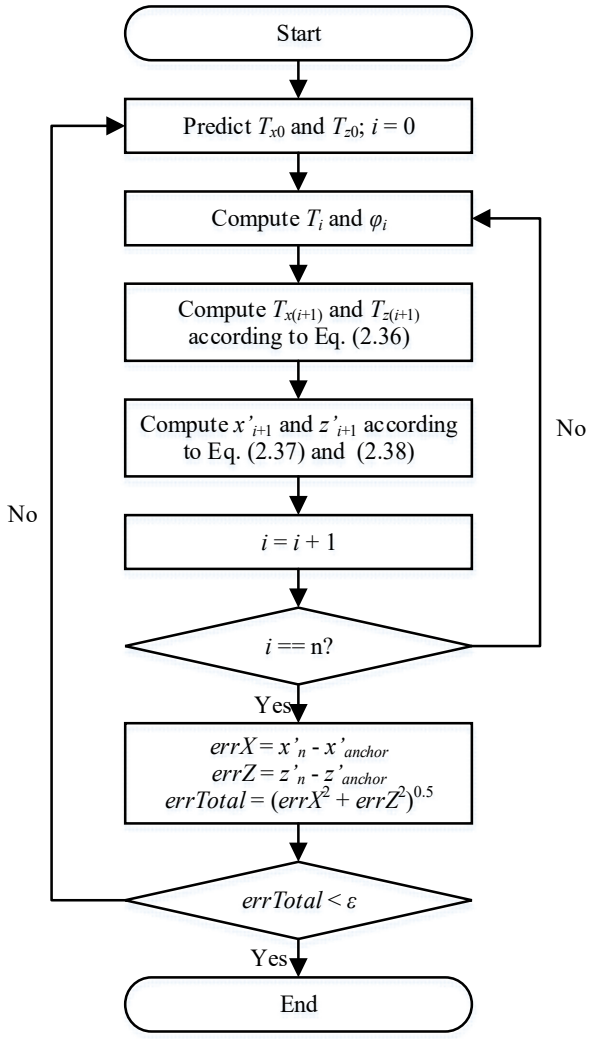

Figure 2.12 Flowchart for quasi-static mooring line analysis method

The total difference variable *errTotal* is used to determine whether the current solution complies with the constraints imposed by the anchor. The assumed tension forces at the fairlead, i.e. T_{x0} and T_{z0}, are corrected, and the whole procedure is repeated

typically for about 20 iterations until the convergence criterion $errTotal < \varepsilon$ is satisfied, where ε is the tolerance specified.

If the piecewise substitution process is skipped, this problem can be generalised as how to find the solution to the following system of equations:

$$\begin{cases} x'_{anchor} = f\left(T_{x0}, T_{z0}\right) \\ z'_{anchor} = g\left(T_{x0}, T_{z0}\right) \end{cases} \tag{2.40}$$

where f and g are nonlinear functions of variables $\left(T_{x0}, T_{z0}\right)$. In the present tool, a generalised Newton-Raphson method is adopted to solve Eq. (2.40).

For a mooring line of the catenary shape, a portion of the line lies on the seabed and special treatment is required to handle the interaction between the mooring line and the seabed. In the present model, a simplified kinematic constraint is applied. During the simulation, if one node is predicted to be below the seabed, its vertical coordinate z'_i is set equal to z'_{anchor} while the vertical tension force T_{zi} at the node is directly set to zero, which is also applied to all other nodes following the current node.

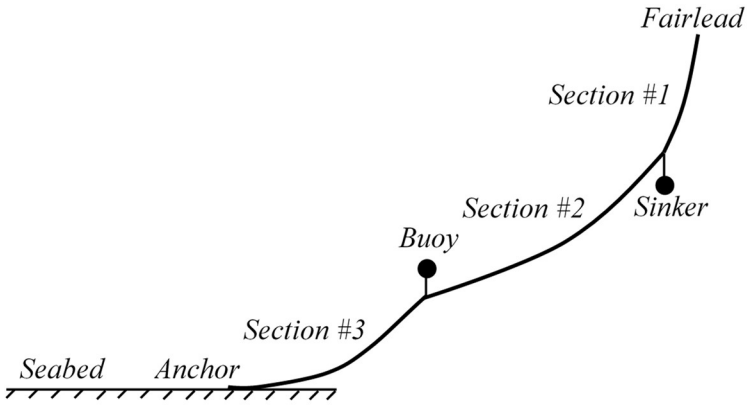

Figure 2.13 Sketch of a multi-component mooring line

In deep-water applications, a mooring line is usually made of several components with different structural properties (Nakajima et al., 1982), such as chains and wires, to improve its restoring force characteristics while maintaining relatively low weight. Figure 2.13 illustrates a multi-component mooring line. The current implementation of the quasi-static method is able to model mooring lines with multiple components.

Firstly, a line is divided into a number of segments as previously discussed, and then certain segments are combined into different sections. In some situations, a buoy (additional buoyancy) or a sinker (additional weight) is attached to a mooring line (Smith and Colin, 2001), which can also be simulated in the present tool by adding new sections at the position of the attachment and subsequently modifying the weight of the node connecting the two adjacent sections.

2.4.2 Dynamic Method

2.4.2.1 Lumped Mass Model

A 3D lumped mass method is implemented in the present project to perform dynamic analysis for mooring lines. As previously discussed in Section 1.2.4.2, a lumped mass model discretises a mooring line into n+1 concentrated masses (nodes) connected by n massless springs (segments), as illustrated in Figure 2.14. As a result, it is sometimes referred to as the Spring-Mass model.

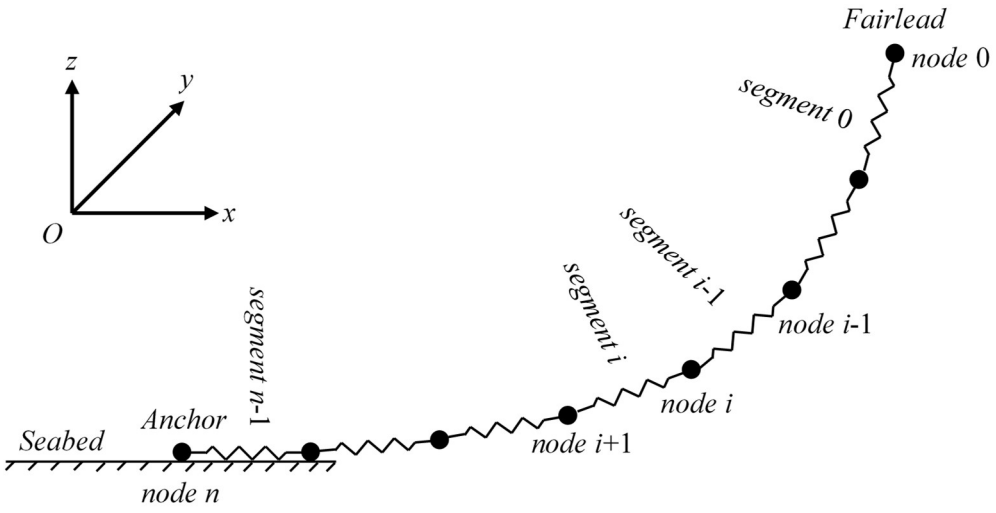

Figure 2.14 Sketch of a 3D lumped mass model

Although similar to the discretised quasi-static model introduced in Section 2.4.1, the lumped mass model concentrates line weight to individual nodes while weight is distributed on segments in the quasi-static model. Besides, in the lumped mass model, segments are always straight, which is not the case for the quasi-static model as shown in Figure 2.11.

2.4.2.2 Transformation Matrices

Unlike the quasi-static model, the lumped mass model is described in 3D space. As a result, a local reference frame is defined for every segment, as shown in Figure 2.15. For segment *i* connecting nodes *i* and *i*+1, the origin of its reference frame is located at node *i*+1. The tangential direction is denoted by ξ, pointing from node *i*+1 to node *i*, while the other two normal directions are represented by η and ζ, respectively.

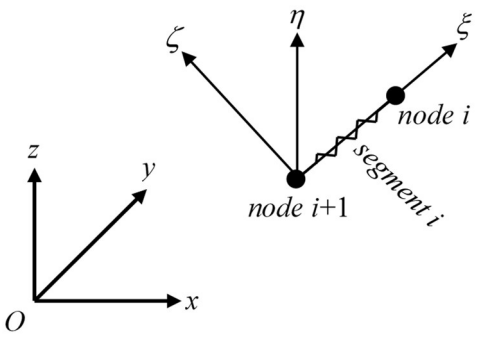

Figure 2.15 Sketch of local reference frame for segment i in lumped mass method

In order to obtain the transformation matrices between the global and local reference frames, let us first assume that there is a vector $\vec{F} = F_x\vec{i} + F_y\vec{j} + F_z\vec{k}$ in the global $Oxyz$ reference frame. In the local segment reference frame, the same vector can be expressed as $\vec{F} = F_\xi\vec{\xi} + F_\eta\vec{\eta} + F_\zeta\vec{\zeta}$. On the other hand, the three unit vectors of the local reference frame, i.e. $\vec{\xi}$, $\vec{\eta}$ and $\vec{\zeta}$, can also be expressed using the unit vectors of the global reference frame, i.e. $\vec{i}$, $\vec{j}$ and $\vec{k}$, as follows:

$$\begin{cases} \vec{\xi} = \xi_x\vec{i} + \xi_y\vec{j} + \xi_z\vec{k} \\ \vec{\eta} = \eta_x\vec{i} + \eta_y\vec{j} + \eta_z\vec{k} \\ \vec{\zeta} = \zeta_x\vec{i} + \zeta_y\vec{j} + \zeta_z\vec{k} \end{cases} \tag{2.41}$$

Substituting Eq. (2.41) into the expression of $\vec{F}$ in the local segment reference frame $\vec{F} = F_\xi\vec{\xi} + F_\eta\vec{\eta} + F_\zeta\vec{\zeta}$, we have:

$$\begin{aligned} & F_\xi \vec{\xi} + F_\eta \vec{\eta} + F_\zeta \vec{\zeta} \\ &= F_\xi \left(\xi_x \vec{i} + \xi_y \vec{j} + \xi_z \vec{k} \right) + F_\eta \left(\eta_x \vec{i} + \eta_y \vec{j} + \eta_z \vec{k} \right) + F_\zeta \left(\zeta_x \vec{i} + \zeta_y \vec{j} + \zeta_z \vec{k} \right) \\ &= \left(F_\xi \xi_x + F_\eta \eta_x + F_\zeta \zeta_x \right) \vec{i} + \left(F_\xi \xi_y + F_\eta \eta_y + F_\zeta \zeta_y \right) \vec{j} + \left(F_\xi \xi_z + F_\eta \eta_z + F_\zeta \zeta_z \right) \vec{k} \\ &= F_x \vec{i} + F_y \vec{j} + F_z \vec{k} \end{aligned} \tag{2.42}$$

By reorganising Eq. (2.42), the following relation between the two sets of coordinates in local and global reference frames can be obtained:

$$\begin{pmatrix} \xi_x & \eta_x & \zeta_x \\ \xi_y & \eta_y & \zeta_y \\ \xi_z & \eta_z & \zeta_z \end{pmatrix} \begin{pmatrix} F_\xi \\ F_\eta \\ F_\zeta \end{pmatrix} = \begin{pmatrix} F_x \\ F_y \\ F_z \end{pmatrix} \tag{2.43}$$

Let $\mathbf{B}$ denotes the transformation matrix from the global to the local reference frame. Then the 3×3 matrix on the left side of Eq. (2.43) represents $\mathbf{B}^{-1}$, which transforms a vector from the local reference frame to the global one. As the columns of $\mathbf{B}^{-1}$ are orthogonal unit vectors, i.e. $\vec{\xi}$, $\vec{\eta}$ and $\vec{\zeta}$, $\mathbf{B}^{-1}$ is an orthonormal matrix according to linear algebra. As a result, the inverse of $\mathbf{B}^{-1}$ is equal to its transpose and $\mathbf{B}$ can be expressed as the following:

$$\mathbf{B} = \left(\mathbf{B}^{-1} \right)^{-1} = \left(\mathbf{B}^{-1} \right)^T = \begin{pmatrix} \xi_x & \xi_y & \xi_z \\ \eta_x & \eta_y & \eta_z \\ \zeta_x & \zeta_y & \zeta_z \end{pmatrix} \tag{2.44}$$

For segment *i* shown in Figure 2.15, the tangential unit vector $\vec{\xi}$ can be computed as follows:

$$\vec{\xi} = \left(\vec{X}_i - \vec{X}_{i+1} \right) \Big/ \left| \vec{X}_i - \vec{X}_{i+1} \right| \tag{2.45}$$

where $\vec{X}$ stands for the coordinates of nodes in the global reference frame. The other two normal unit vectors $\vec{\eta}$ and $\vec{\zeta}$ can be any vectors satisfying the orthogonal constraint. Subsequently, the transformation matrices $\mathbf{B}$ and $\mathbf{B}^{-1}$ between the global and local reference frames are obtained and applied in later calculations.

2.4.2.3 Hydrodynamic Forces on Segment

In order to calculate the hydrodynamic loads exerted on mooring lines, Morison's equation (Morison et al., 1950) is commonly adopted, which categorises these forces into two components: drag force and inertia force. In the lumped mass model, hydrodynamic forces are firstly computed for line segments and then transformed to nodes.

According to Morison's equation, the drag force acting on a segment is related to both flow velocity and segment velocity, as shown in Figure 2.16. For segment *i*, its velocity $\vec{V}_i'$ is estimated as $\vec{V}_i' = \left(\vec{V}_i + \vec{V}_{i+1}\right)/2$, where $\vec{V}_i$ and $\vec{V}_{i+1}$ are velocities of nodes *i* and *i*+1 expressed in the global reference frame, respectively. Let $\vec{U}_i$ denote flow velocity at segment *i*. Then the relative flow velocity with respect to the segment can be expressed as $\vec{U}_i - \vec{V}_i$ in the global reference frame. As Morison's equation is defined in the local reference frame, the relative flow velocity is transformed to the local frame as $\vec{u}_i = \mathbf{B}_i\left(\vec{U}_i - \vec{V}_i'\right)$.

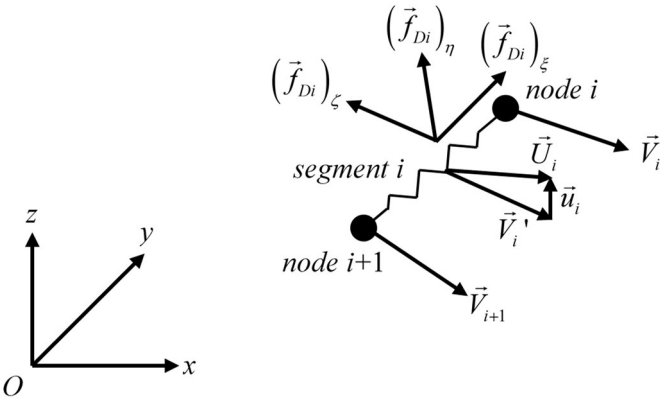

Figure 2.16 Sketch of velocity and drag force for segment i in lumped mass method

Drag force $\vec{f}_{Di}$ is composed of two parts: $\left(\vec{f}_{Di}\right)_T$ in the tangential direction and $\left(\vec{f}_{Di}\right)_N$ in the normal direction, which are computed using the following equations:

$$\begin{cases} \left(\vec{f}_{Di}\right)_T = \frac{1}{2}\rho_w C_{DT}\pi d_i l_i \left|\left(\vec{u}_i\right)_T\right|\left(\vec{u}_i\right)_T \\ \left(\vec{f}_{Di}\right)_N = \frac{1}{2}\rho_w C_{DN} d_i l_i \left|\left(\vec{u}_i\right)_N\right|\left(\vec{u}_i\right)_N \end{cases} \tag{2.46}$$

where ρ_w represents fluid density; C_{DT} and C_{DN} stand for drag coefficients in tangential and normal directions, separately; d_i denotes segment diameter; l_i is segment length; $\left(\vec{u}_i\right)_T$ and $\left(\vec{u}_i\right)_N$ are tangential and normal components of $\vec{u}_i$, respectively.

As ξ denotes the tangential direction, the component of $\vec{u}_i$ in ξ direction, i.e. $\left(\vec{u}_i\right)_\xi$, is equal to $\left(\vec{u}_i\right)_T$ and thus $\left(\vec{f}_{Di}\right)_\xi = \left(\vec{f}_{Di}\right)_T$.To express $\vec{f}_{Di}$ as a 3×1 vector in the local reference frame, $\left(\vec{f}_{Di}\right)_N$ need be further decomposed in η and ζ directions. By applying $\left(\vec{u}_i\right)_N = \sqrt{\left(\vec{u}_i\right)_\eta^{\,2} + \left(\vec{u}_i\right)_\zeta^{\,2}}$, the three components of $\vec{f}_{Di}$ in the local frame can be obtained as follows:

$$\begin{cases} \left(\vec{f}_{Di}\right)_\xi = \frac{1}{2}\rho_w C_{DT}\pi d_i l_i \left|\left(\vec{u}_i\right)_\xi\right|\left(\vec{u}_i\right)_\xi \\ \left(\vec{f}_{Di}\right)_\eta = \frac{1}{2}\rho_w C_{DN} d_i l_i \sqrt{\left(\vec{u}_i\right)_\eta^{\,2} + \left(\vec{u}_i\right)_\zeta^{\,2}}\left(\vec{u}_i\right)_\eta \\ \left(\vec{f}_{Di}\right)_\zeta = \frac{1}{2}\rho_w C_{DN} d_i l_i \sqrt{\left(\vec{u}_i\right)_\eta^{\,2} + \left(\vec{u}_i\right)_\zeta^{\,2}}\left(\vec{u}_i\right)_\zeta \end{cases} \tag{2.47}$$

Similarly, the three components of inertia force $\vec{f}_{Ai}$ in ξ, η and ζ directions can be computed using Eq. (2.48).

$$\begin{cases} \left(\vec{f}_{Ai}\right)_\xi = \rho_w C_{AT} A_i l_i \left(\vec{a}_i\right)_\xi \\ \left(\vec{f}_{Ai}\right)_\eta = \rho_w C_{AN} A_i l_i \left(\vec{a}_i\right)_\eta \\ \left(\vec{f}_{Ai}\right)_\zeta = \rho_w C_{AN} A_i l_i \left(\vec{a}_i\right)_\zeta \end{cases} \tag{2.48}$$

where C_{AT} and C_{AN} represent added mass coefficients in tangential and normal directions, respectively; A_i denotes cross-sectional area of segment; $\vec{a}_i$ is the relative flow acceleration with respect to the segment in the local reference frame.

2.4.2.4 Equation of Motion for Node

In the lumped mass method, the equation of motion is established for every node in the global reference frame. For node *i*, the various forces acting on it are illustrated in Figure 2.17 and its motion is governed by the following equation according to Newton' second law:

$$M_i \ddot{\vec{X}}_i = \vec{F}_{T(i-1)} - \vec{F}_{Ti} + \vec{F}_{Di} + \vec{F}_{Ai} - \vec{W}_i \tag{2.49}$$

where M_i denotes mass of node *i*; $\ddot{\vec{X}}_i$ represents acceleration vector of node *i*; $\vec{F}_{T(i-1)}$ and $\vec{F}_{Ti}$ are tension force vectors of segments *i*-1 and *i*, respectively; $\vec{F}_{Di}$ and $\vec{F}_{Ai}$ are drag and inertia force vectors applied to node *i*; $\vec{W}_i$ is weight of node *i* in water.

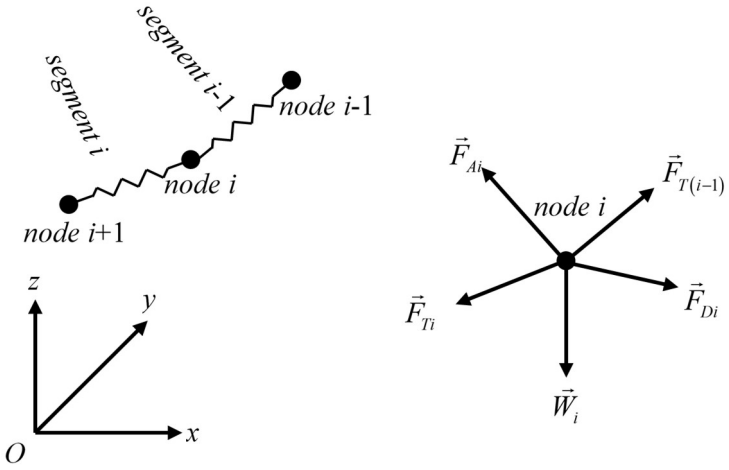

Figure 2.17 Sketch of forces exerted on node i in lumped mass method

As mentioned in Section 2.4.2.1, the lumped mass model concentrates/lumps line mass to individual nodes. This is achieved by combining half of the mass of two adjacent segments and then assigning it to the node joining the segments, as expressed in the following equation:

$$M_i = \frac{1}{2}\left(m_{i-1} + m_i\right) \tag{2.50}$$

where m_{i-1} and m_i stand for mass of segments *i*-1 and *i*, separately, as shown in Figure 2.17. It is worth pointing out that fairlead and anchor only have half the mass of other nodes as they are only connected by one segment, respectively. Node weight in water $\vec{W}_i$ is computed in the same way as M_i.

The tension force vector $\vec{F}_{Ti}$ of segment *i* is always in the tangential direction of the segment, i.e. $\vec{\xi}$ obtained from Eq. (2.45), and thus can be expressed as $\vec{F}_{Ti} = T_i\vec{\xi}$, in which T_i is the magnitude of tension force and is calculated as:

$$T_i = E_i A_i \left(\left|\vec{X}_{i+1} - \vec{X}_i\right| / l_i - 1\right) \tag{2.51}$$

The variables in Eq. (2.51) have the same definitions as in Eq. (2.37).

In order to obtain the drag and inertia force vectors $\vec{F}_{Di}$ and $\vec{F}_{Ai}$ of node *i*, the hydrodynamic forces on segments, i.e. $\vec{f}_{Di}$ and $\vec{f}_{Ai}$ defined in Section 2.4.2.3, are firstly transformed from the local reference frame to the global one using the transformation matrix $\mathbf{B}^{-1}$ computed in Section 2.4.2.2. Subsequently, the forces on segments are distributed to adjacent nodes, as demonstrated in Eq. (2.52):

$$\begin{aligned} \vec{F}_{Di} &= \frac{1}{2}\left(\mathbf{B}_{i-1}^{-1}\vec{f}_{D(i-1)} + \mathbf{B}_i^{-1}\vec{f}_{Di}\right) \\ \vec{F}_{Ai} &= \frac{1}{2}\left(\mathbf{B}_{i-1}^{-1}\vec{f}_{A(i-1)} + \mathbf{B}_i^{-1}\vec{f}_{Ai}\right) \end{aligned} \tag{2.52}$$

2.4.2.5 Solution Procedure

Now that all terms in Eq. (2.49) are defined, if information of all nodes at time *t* is known, including position $\vec{X}_t$, velocity $\dot{\vec{X}}_t$ and acceleration $\ddot{\vec{X}}_t$, the Newmark Beta method (Newmark, 1959) is adopted in the present project to solve their motion data

at time $t+\Delta t$, where Δt is the time step used in the simulation. Following Low and Langley (2006), the kinematics of nodes at time $t+\Delta t$ can be expressed as:

$$\begin{aligned}
\vec{X}_{t+\Delta t} &= \vec{X}_t + \Delta\vec{X} \\
\dot{\vec{X}}_{t+\Delta t} &= \frac{\gamma}{\beta\Delta t}\Delta\vec{X} - \left(\frac{\gamma}{\beta} - 1\right)\dot{\vec{X}}_t - \Delta t\left(\frac{\gamma}{2\beta} - 1\right)\ddot{\vec{X}}_t \\
\ddot{\vec{X}}_{t+\Delta t} &= \frac{1}{\beta(\Delta t)^2}\Delta\vec{X} - \frac{1}{\beta\Delta t}\dot{\vec{X}}_t - \left(\frac{1}{2\beta} - 1\right)\ddot{\vec{X}}_t
\end{aligned} \tag{2.53}$$

where $\Delta\vec{X}$ is the increment of node position $\vec{X}$ from time t to $t+\Delta t$; γ and β are coefficients of the Newmark Beta method ($0 \le \gamma \le 1$ and $0 \le \beta \le 0.5$) and are normally set to 0.5 and 0.25, respectively.

As all forces applied to nodes are directly related to their kinematics, Eq. (2.49) can be rewritten as:

$$M\ddot{\vec{X}}_{t+\Delta t} = \vec{F}\left(\vec{X}_{t+\Delta t}, \dot{\vec{X}}_{t+\Delta t}, \ddot{\vec{X}}_{t+\Delta t}\right) \tag{2.54}$$

where $\vec{F}\left(\vec{X}_{t+\Delta t}, \dot{\vec{X}}_{t+\Delta t}, \ddot{\vec{X}}_{t+\Delta t}\right)$ represents all terms on the right side of Eq. (2.49).

Substituting Eq. (2.53) into Eq. (2.54), we have:

$$\vec{H}\left(\Delta\vec{X}\right) = \frac{M}{\beta(\Delta t)^2}\Delta\vec{X} - \frac{M}{\beta\Delta t}\dot{\vec{X}}_t - M\left(\frac{1}{2\beta} - 1\right)\ddot{\vec{X}}_t - \vec{F}\left(\Delta\vec{X}\right) = 0 \tag{2.55}$$

Eq. (2.55) is implicit regarding $\Delta\vec{X}$ and is solved iteratively using the Newton-Raphson method:

$$\Delta\vec{X}^{k+1} = \Delta\vec{X}^k - \frac{\vec{H}\left(\Delta\vec{X}^k\right)}{\vec{H}'\left(\Delta\vec{X}^k\right)} \tag{2.56}$$

where the subscripts k and $k+1$ denote the kth and $(k+1)$th iterations in solving $\Delta\vec{X}$; $\vec{H}'\left(\Delta\vec{X}^k\right)$ represents the derivative of $\vec{H}\left(\Delta\vec{X}\right)$ with respect to $\Delta\vec{X}$ and is

approximated as $\vec{H}'\left(\Delta\vec{X}^k\right) \approx \frac{M}{\beta\left(\Delta t\right)^2}$. This approximation does not affect the accuracy of the solution as $\vec{H}'\left(\Delta\vec{X}\right)$ is only used to provide convergence (Low and Langley, 2006).

After every iteration, node kinematics are updated according to Eq. (2.53) and subsequently all forces in Eq. (2.54) are calculated using the new $\Delta\vec{X}$. The solution is considered to be converged when the convergence criterion $\left|\Delta\vec{X}^{k+1} - \Delta\vec{X}^k\right| < \varepsilon$ is satisfied, where ε is the tolerance specified.

2.5 Coupling Procedure

When a fully coupled simulation is performed, both the CFD solver, i.e. OpenFOAM, and the MBD code, i.e. MBDyn, run simultaneously as individual computer processes. Data exchange between the two codes is achieved with the help of the TCP/IP communication protocol, using a client/server model. An interface library is implemented in OpenFOAM by adopting the motion and force exchange functions provided in MBDyn, serving as the bridge connecting the flow and structural solvers.

Figure 2.18 shows the modelling procedure used in the present fully coupled FSI analysis tool. At the start of a simulation, MBDyn creates a TCP/IP socket and acts as the server, while the client OpenFOAM connects to the socket, establishing a two-way communication. In general, the fluid force and moment integrated in the CFD solver for every patch as well as the restoring forces from the mooring system are transferred to MBDyn. Using the force data, MBDyn calculates the structural response of the system, i.e. the kinematics of the geometric nodes, and then transfers the structural motion data back to the CFD solver. The CFD mesh is then updated via the mesh motion library for both global motion and local deformation, followed by an update of the flow field. Communication between OpenFOAM and MBDyn is performed at each iteration so that a strong coupling is achieved with robust and quick convergence. Within each time step, data is exchanged between OpenFOAM and MBDyn typically for about 5 iterations until the flow field eventually converges. MBDyn then continues

its iteration with the external loading received from the last data transfer until converged structural responses are obtained.

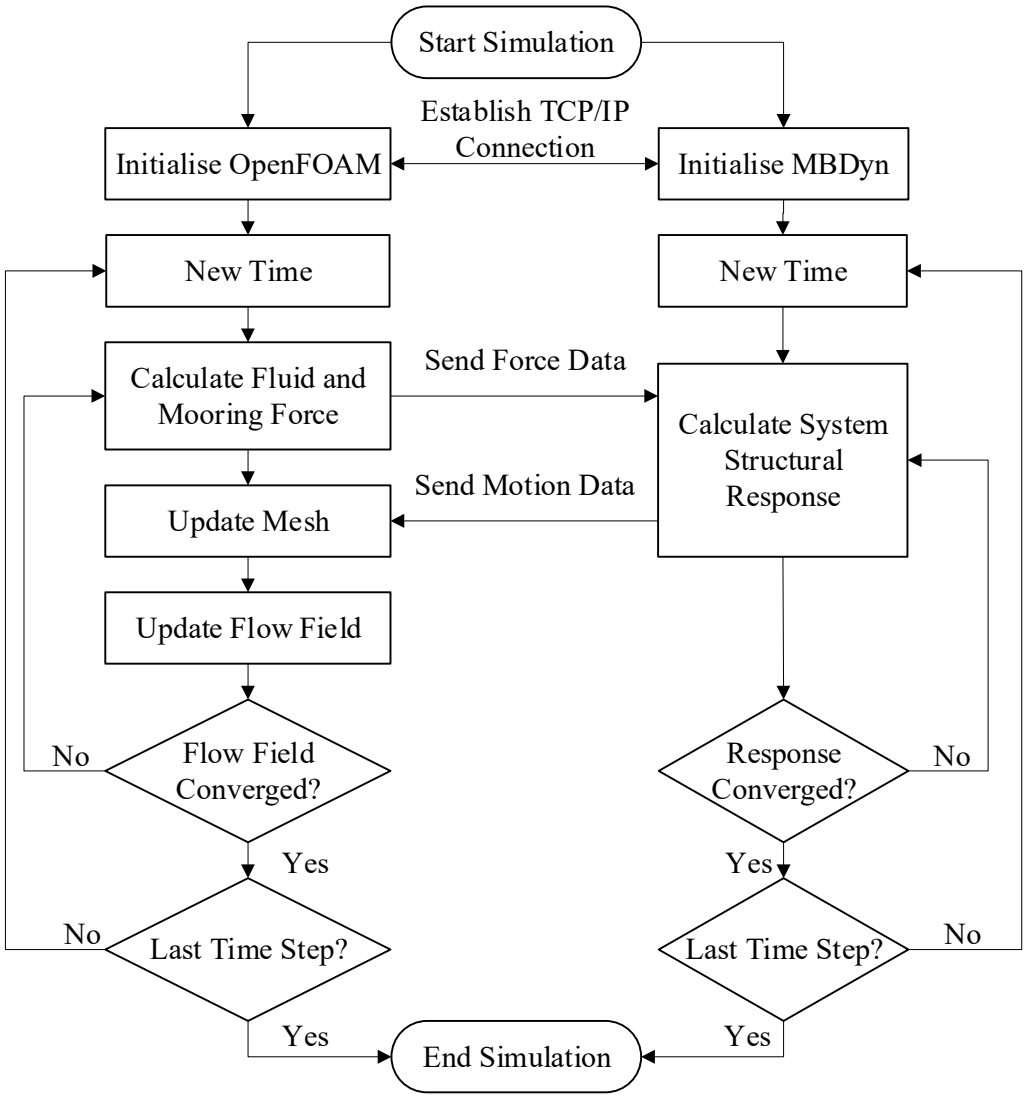

Figure 2.18 Flowchart for coupling OpenFOAM with MBDyn

2.6 Concluding Remarks

In this chapter, the fully coupled numerical tool developed under the CFD-MBD framework is presented. The various numerical methods and techniques adopted in the present tool are discussed in detail. The open source CFD toolbox OpenFOAM is utilised to model fluid flow, including turbulence modelling with the k - ω SST turbulence model and free surface capturing via the VOF method. A wave modelling

module is incorporated for wave generation and damping in a numerical wave tank. The open source MBD code MBDyn is employed for calculating the structural response of rigid and flexible components in a multibody system. A mesh motion solver is developed in OpenFOAM to handle complex mesh movement in FOWT simulations due to both global rigid body motion, such as platform 6DoF motion and wind turbine rotation, and local flexible body deformation, i.e. turbine blade deflection. A mooring system analysis module is also implemented in OpenFOAM and is able to model mooring lines using either quasi-static or dynamic methods. The two separate solvers OpenFOAM and MBDyn are coupled via an interface library implemented to exchange loading and response data.

With the implemented features, the present fully coupled CFD-MBD tool is capable of numerically simulating and analysing various problems in the field of naval architecture and ocean engineering, including:

- Aerodynamics of wind turbines
- Hydrodynamics of floating structures with mooring systems in waves
- Quasi-static and dynamic analysis of mooring lines/risers
- Interaction of fluid and rigid/flexible structures

Chapter 3 Validation Studies

The fully coupled FSI analysis tool developed in this project consists of various modules. In this chapter, a series of test cases is simulated and analysed to validate these components individually.

Analysis of a cylindrical structure under forced heave oscillation is firstly carried out in Section 3.1 to validate the basic flow solver in OpenFOAM. In Section 3.2, numerical simulations of the NREL Phase VI wind turbine under various wind conditions are then performed to validate the capability of the developed tool in modelling wind turbine aerodynamics. Subsequently, the DeepCwind semi-submersible platform with its mooring system is investigated in Section 3.3 to validate the hydrodynamic modelling feature of the present tool. In Section 3.4, a flexible hanging riser subject to prescribed motion at its top end is then analysed to validate the dynamic mooring analysis module. Lastly, the coupling between OpenFOAM and MBDyn is validated by studying the flow induced oscillation of a flexible cantilever beam in the wake of a fixed square in Section 3.5.

3.1 Forced Oscillation of a Cylindrical Structure

In this section, the forced oscillation of a cylindrical structure is investigated to validate the basic fluid flow solver in OpenFOAM. This case was studied by Tao et al. (2000) to analyse the viscous damping, including both skin friction and form drag, of a TLP column experiencing the “springing” vibration of high frequency and small amplitude.

3.1.1 Model Description

Following Tao et al. (2000), the TLP column is simplified as a cylindrical structure while its vibration is modelled by prescribing a sinusoidal motion function in the heave direction, as illustrated in Figure 3.1. The cylinder investigated in the present study has a diameter of 0.457 m and a draft of 1.219 m. Due to the high-frequency and small-amplitude characteristics of the heave oscillation, disturbance of free surface is very small and thus its effects are not considered in the numerical simulations (Tao et al.,

2000). No turbulence model is applied as the influence of turbulence on damping is considered to be negligible for this case (Tao et al., 2000).

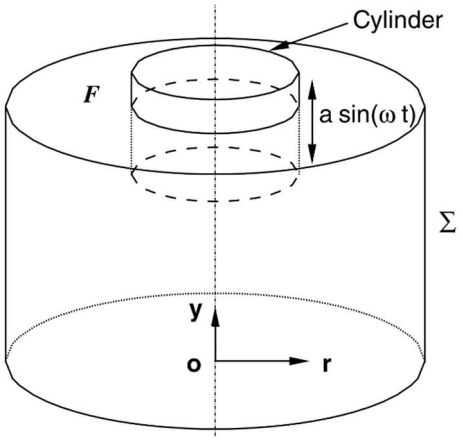

Figure 3.1 Illustration of forced heave oscillation of a cylindrical structure (Tao et al., 2000)

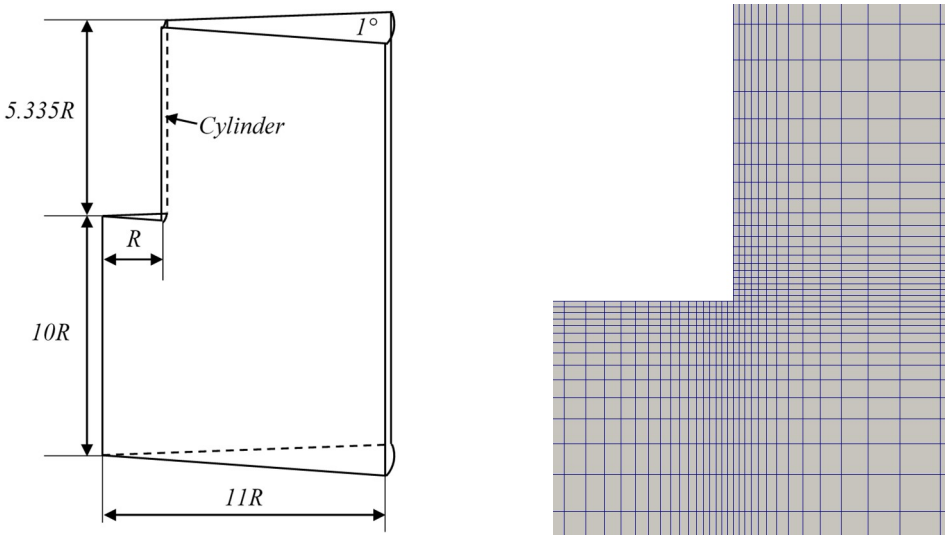

(a) Computational domain *(b) Detailed mesh near bottom edge*

Figure 3.2 Sketch of computational model for forced oscillation of a cylinder (R denotes radius of cylinder)

Figure 3.2(a) demonstrates the computational domain for the forced heave oscillation case, where all dimensions are expressed using the radius of the cylinder *R*. As the cylinder is axisymmetric about its vertical axis, only a slice of 1° wedge is modelled with one layer of grid cells to reduce computational cost, and the built-in wedge boundary condition provided in OpenFOAM is applied to the front and back wedge surfaces. Grid cells are distributed towards the bottom edge of the model as illustrated

in Figure 3.2(b) to better capture the vortices shed from this region due to the forced heave oscillation. The overall grid count for this wedge case is 5856. Forces calculated from the present wedge model are subsequently multiplied by 360 to obtain the corresponding data for the whole cylinder model.

3.1.2 Damping Coefficient Calculation

As free surface is not modelled in this study, wave damping is neglected. Nonetheless, due to viscous effects, damping force is still present for the oscillating cylinder and can be decomposed into skin friction due to viscous shear stress and form drag associated with vortex shedding and flow separation.

In order to analyse viscous damping, the hydrodynamic force acting upon the cylinder in the heave direction is firstly calculated, which comprises two components: a normal component F_n obtained by integrating pressure over the surface of the structure and a tangential component F_t computed through shear stress integration. For either component, it can be represented in the realm of the potential flow theory as:

$$F = -\mu\ddot{z} - \lambda\dot{z} \tag{3.1}$$

where F represents either of the two hydrodynamic force components, i.e. F_n and F_t; μ stands for added mass; λ denotes linear damping coefficient; z is the forced heave motion. By assuming the cylinder is forced to oscillate at a given amplitude a and a prescribed oscillatory frequency ω, i.e. $z = a\sin\omega t$, Eq. (3.1) can be written as:

$$F = \mu\omega^2 a\sin\omega t - \lambda\omega a\cos\omega t = F_s\sin\omega t + F_c\cos\omega t \tag{3.2}$$

where F_s represents the part of F in phase with the forced heave motion z and F_c denotes the other part in phase with velocity of the structure. These two parts can be decomposed by processing the time history curve of F with Fourier analysis.

Comparing left and right terms of Eq. (3.2), the damping coefficient λ can be obtained using the following equation:

$$\lambda = -\frac{F_c}{a\omega} \tag{3.3}$$

Eq. (3.3) can be applied to both normal and tangential components of the total hydrodynamic force to calculate the linear damping coefficients associated with skin friction and form drag.

3.1.3 Effects of Oscillation Amplitude

The frequency of forced heave oscillation is set to 0.41 Hz, which is the natural frequency of the cylinder, while the oscillation amplitude is varied and its effects on viscous heave damping are investigated. Tao et al. (2000) normalised the oscillation amplitude a with the radius of the cylinder R and defined the Keulegan-Carpenter (KC) number as follows:

$$KC = \frac{2\pi a}{2R} \tag{3.4}$$

Three cases with different KC numbers are studied, as listed in Table 3.1. A time step size of 0.0025 s, i.e. 1/1000 of the oscillation period, is adopted. Damping coefficient results obtained from the present numerical simulations and Tao et al. (2000) are shown in Figure 3.3, together with the experimental data of Thiagarajan and Troesch (1994).

Table 3.1 Simulation cases for forced oscillation of a cylindrical structure

Case	1	2	3
KC	0.1	0.4	0.8
Oscillation Amplitude a (cm)	0.727	2.909	5.819

The damping coefficient from skin friction with respect to KC number is plotted in Figure 3.3. It is found that this component is independent of KC and remains constant within the range of KC studied, which is in very good agreement with the results predicted by Tao et al. (2000). On the other hand, a linear relationship exists between the total damping coefficient, including both skin friction and form drag, and KC. A

similar trend can also be observed for the results from Tao et al. (2000) as well as experimental data (Thiagarajan and Troesch, 1994), which validates the basic fluid flow solver in OpenFOAM.

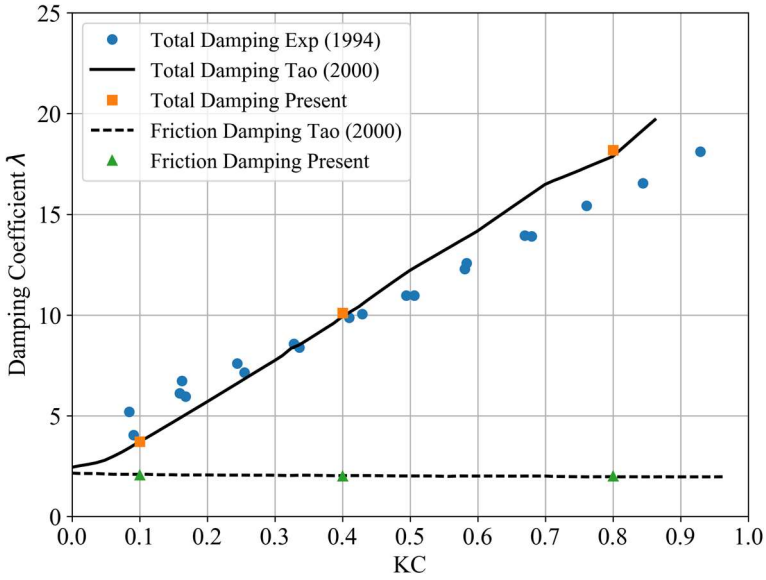

Figure 3.3 Total and friction damping coefficient λ versus KC for forced oscillation of a cylindrical structure

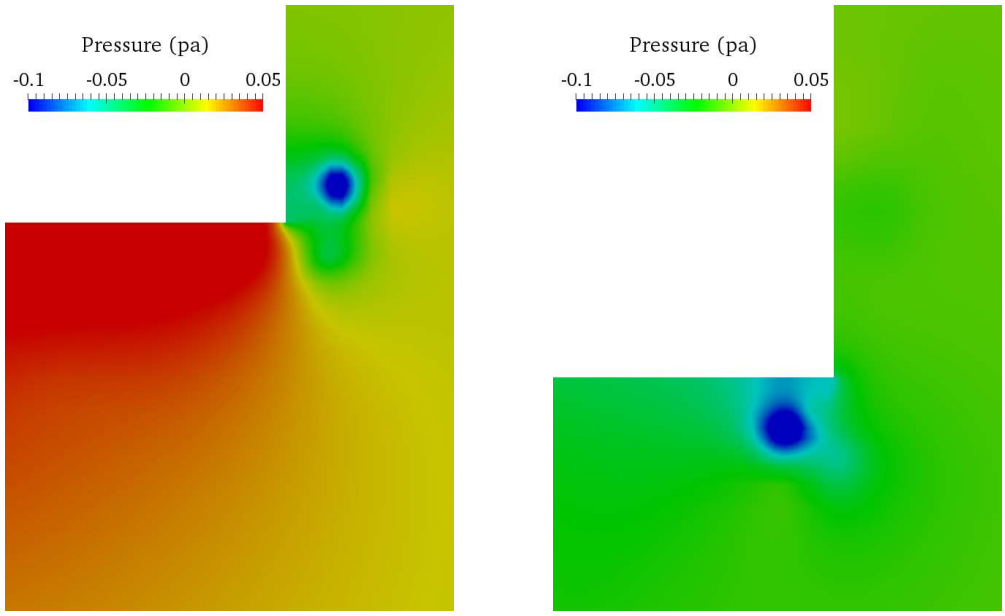

Figure 3.4 Pressure field variation near bottom edge for forced oscillation of a cylindrical structure

Figure 3.4 illustrates the pressure field near the bottom edge of the cylinder at two separate time instants within one oscillation cycle. The region coloured in blue

represents a decrease in pressure, which is related to viscous effects such as vortex shedding. In addition, the forced heave oscillation of the cylinder also results in the variation of the pressure field.

3.2 Aerodynamics of the NREL Phase VI Wind Turbine

The NREL Phase VI wind turbine is studied in this section to validate the tool in numerical modelling of wind turbine aerodynamic performance. This turbine was initially designed for the applications under onshore scenarios, and the availability of experimental data (Hand et al., 2001) from NREL makes it a popular benchmark case in the research area of wind turbines.

3.2.1 Model Description

The NREL Phase VI wind turbine is a two-bladed upwind model and each blade adopts the NREL S809 airfoil profile as shown in Figure 3.5 (a) at most of its span-wise cross sections. The length of the blade is 5.029 m from tip to the rotation axis. Of all the configurations tested by NREL, a tip pitch angle of 3 degrees is used and zero yaw angle is applied in the present study. Figure 3.5 (b) displays a CAD model for the wind turbine. As can be seen from the figure, the hub, nacelle and tower parts are excluded from our numerical model for simplification. Detailed geometric parameters can be found in the NREL report (Hand et al., 2001).

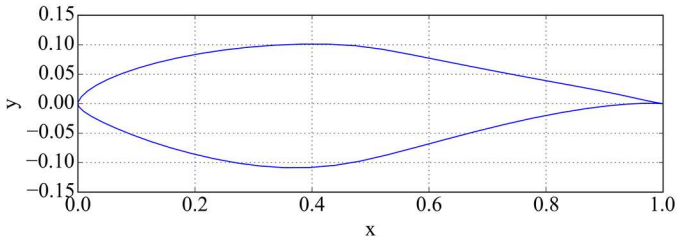

(a) Profile of the NREL S809 airfoil

(b) CAD model of the wind turbine

Figure 3.5 Geometry of the NREL Phase VI wind turbine

Figure 3.6 shows the overall computational domain, i.e. a cylindrical domain with a diameter of 5D, where D is the diameter of the rotor. The inlet and outlet boundaries are 1.5D and 4D away from the rotor, respectively. The rotational motion of the wind turbine is handled by the aforementioned AMI sliding mesh technique. The rotor is surrounded by a small cylindrical domain and the surfaces connecting the two domains are defined as the AMI sliding interfaces. To model a bottom-fixed wind turbine, the inner small cylinder region (or rotor cell zone) rotates around a predefined axis while the outer domain (or stator cell zone) maintains static.

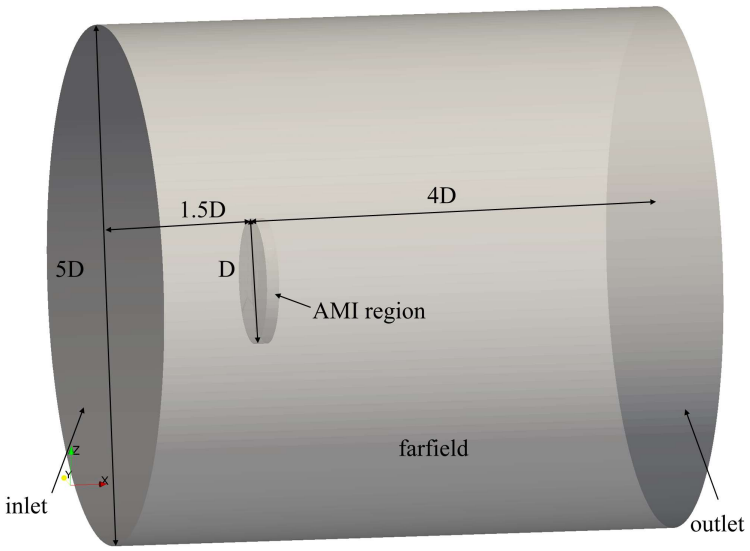

Figure 3.6 Computational domain for the NREL Phase VI wind turbine

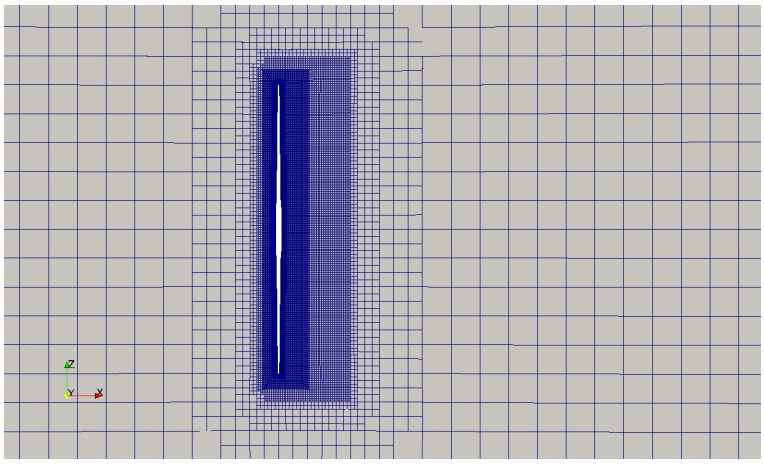

(a) Overall view

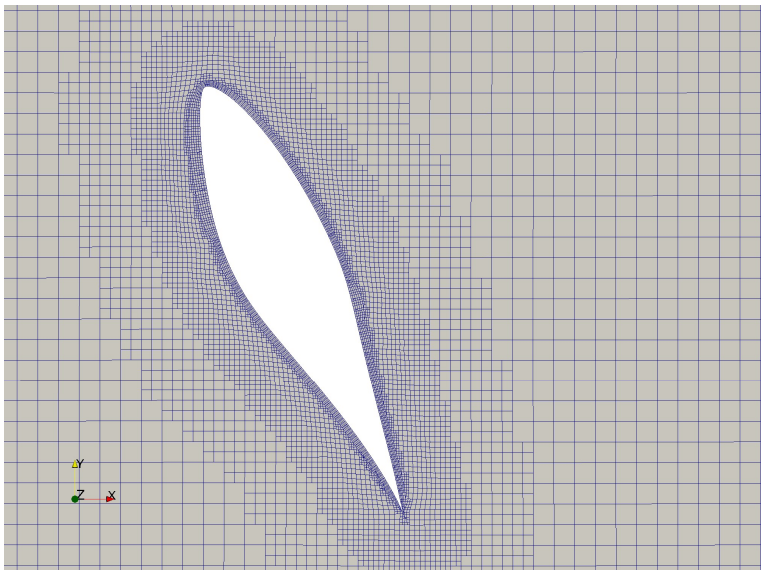

(b) Detailed view

Figure 3.7 Computational mesh for the NREL Phase VI wind turbine

The built-in snappyHexMesh utility in OpenFOAM is adopted for mesh generation. This utility is very powerful yet easy to use and is capable of generating hexahedra dominant mesh (OpenFOAM, 2013). An illustration of the overall computational mesh can be seen in Figure 3.7 as well as the detailed sectional view of the refined mesh near the turbine blade. Four different incoming wind velocities, i.e. 5, 10, 15 and 25 m/s, are investigated and the rotational speed of the turbine rotor is fixed at 72 RPM (revolutions per minute) for all four cases. The Reynolds number based on sectional chord length is within the range of $[5\times10^5, 5\times10^6]$ and the k-ω SST turbulence model presented in Section 2.1.2 is utilised to model turbulent fluid flow. A time step size of 2×10^{-6} s is used for all cases.

3.2.2 Thrust and Torque

Thrust and torque are two important aerodynamic performance parameters for a wind turbine as they represent the integral loading on the turbine. Thrust is defined as the integrated force component normal to the rotor plane while torque is the integrated moment component parallel to the rotating axis of the wind turbine as defined in the following equations:

$$T = \oint_S p\mathbf{n} \cdot \mathbf{dS}$$
$$Q = \oint_S (\mathbf{r} \times p\mathbf{n}) \cdot \mathbf{dS} \tag{3.5}$$

where **dS** is the area vector of an infinitesimal surface, **n** is the direction vector normal to the rotor plane (pointing in the downwind direction) and **r** is the distance vector from the rotation centre to the surface.

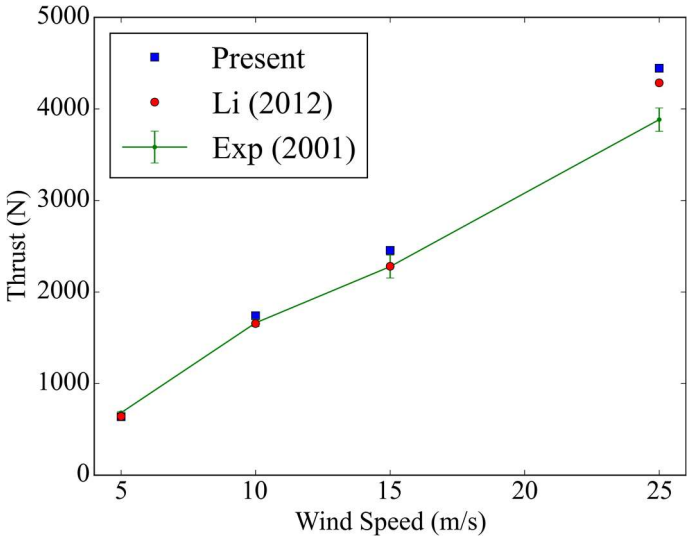

(a) Thrust

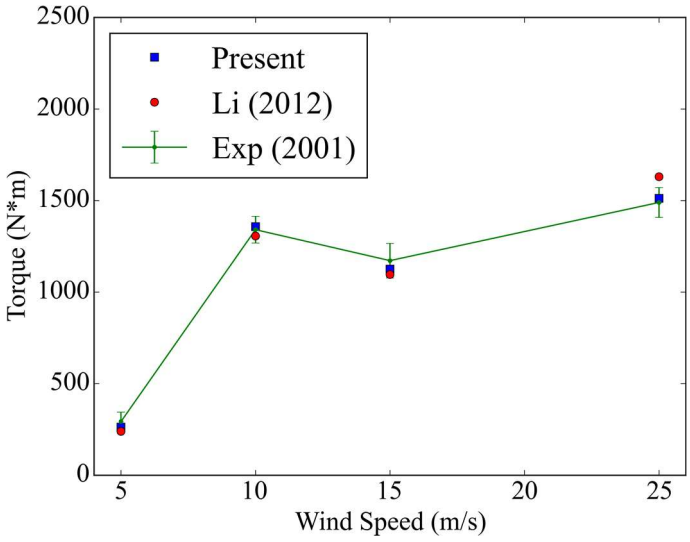

(b) Torque

Figure 3.8 Comparison of thrust and torque with available experimental and numerical results for the NREL Phase VI wind turbine

Due to the unsteadiness caused by the rotational motion of blades, both thrust and torque vary with time. The results presented here are obtained by averaging the time history curves over the last turbine rotation cycle. A comparison between the averaged turbine thrust and torque results predicted by the present code and the experimental data obtained from the NREL report (Hand et al., 2001) is demonstrated in Figure 3.8. The error bars in the figures represent the standard deviation from experimental tests. As is seen from the figures, an overall good agreement is achieved for the present results and experimental data, except for an over-prediction of 11% in thrust for the case with a wind speed of 25 m/s, where stalled flow and separation are significant, and it is thus difficult to predict accurately (Li et al., 2012). In addition, CFD results by Li et al. (2012) are also plotted for comparison. both our calculated thrust and torque agree well with those from Li's paper, demonstrating the capability of the present CFD solver for modelling wind turbine aerodynamics.

3.2.3 Pressure Coefficients

Pressure coefficient can reflect local fluid flow information in a more detailed manner than thrust and torque. It is defined as:

$$C_p = \frac{P_0 - P_\infty}{0.5\rho\left[U^2 + (\omega r)^2\right]} \tag{3.6}$$

where P_0 is the measured pressure at a given location; P_∞ is the reference pressure in the far field and is zero in this case; U stands for the wind velocity; ω is the rotational speed of the wind turbine and r denotes the distance between the section of the specified location and the rotation centre.

Figure 3.9 shows the comparison between the pressure coefficients predicted from our CFD simulations and data measured experimentally by NREL for four different wind velocities. Three cross sections are investigated, i.e. r/R = 0.3 (close to blade root), 0.63 (in the middle of blade), 0.95 (close to blade tip), where R is the radius of the turbine rotor. As can be seen from the figures, the predicted pressure coefficients on both pressure and suction surfaces along the turbine blade agree quite well with the

experimental data for four wind conditions, which further validates the present tool for wind turbine simulations. Specifically, our CFD results capture the peaks near the leading edge on the suction side of the blade at the wind speed of 10 m/s, which were also measured in the experimental tests.

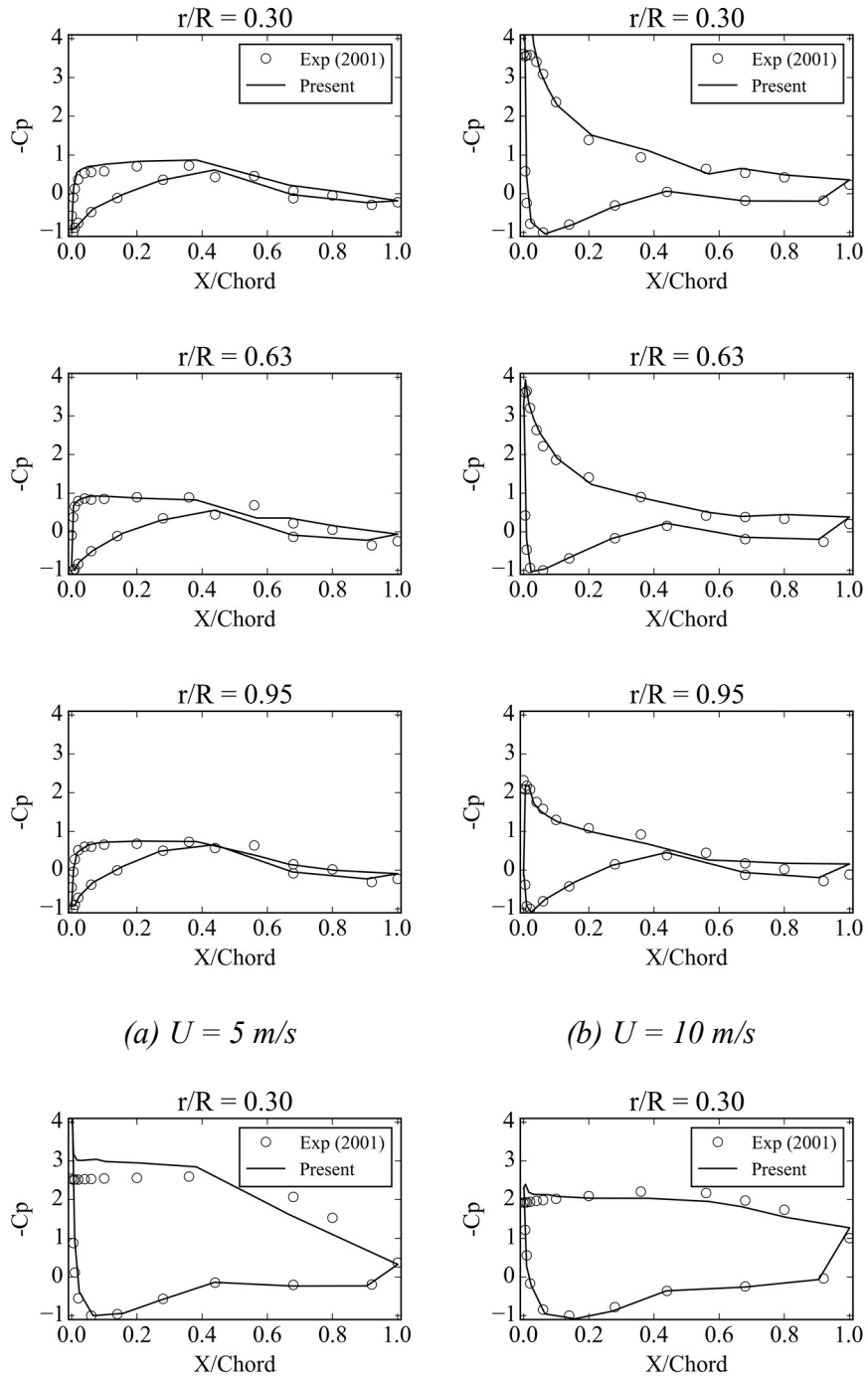

(a) U = 5 m/s *(b) U = 10 m/s*

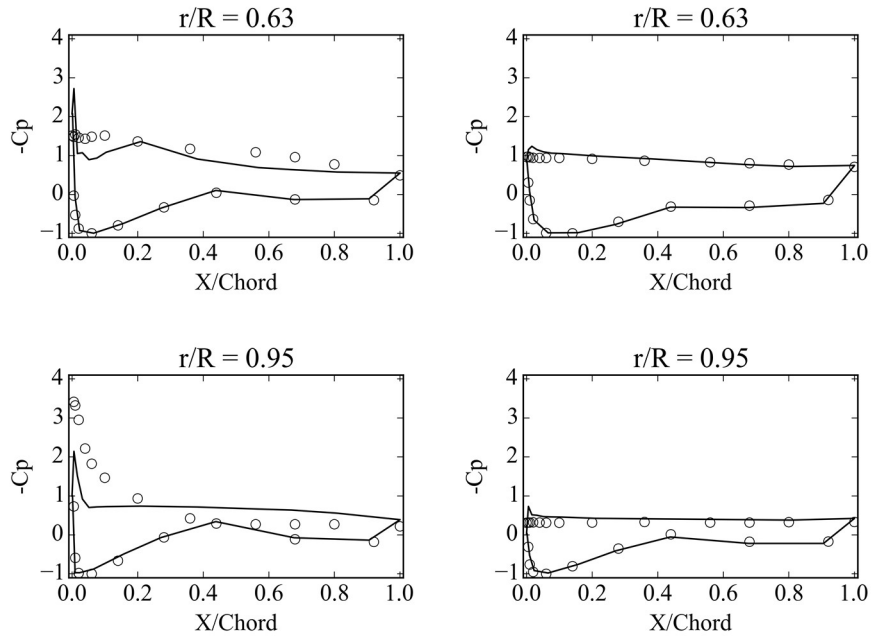

(c) U = 15 m/s *(d) U = 25 m/s*

Figure 3.9 Pressure distribution along blade at different wind velocities for the NREL Phase VI wind turbine ('-' represents the negative sign)

3.3 Hydrodynamics of the DeepCwind Semi-Submersible Platform

In order to validate the tool in modelling hydrodynamics of floating structures, the DeepCwind semi-submersible platform used in Phase II of the OC4 FOWT project (Robertson et al., 2014a) is investigated in this section. Experimental studies were previously carried out on a 1/50th-scale model (Coulling et al., 2013). Model test data can thus be compared with the numerical results obtained from the present tool.

3.3.1 Model Description

Figure 3.10 illustrates the DeepCwind semi-submersible platform studied in this case. The platform consists of one centre column (diameter: 6.5 m) supporting the wind turbine tower, three large offset columns (diameter: 12 m) with cylindrical bases (diameter: 24 m), and a series of small horizontal and diagonal cross braces (diameter: 1.6 m) used to connect the four columns. The distance between the centres of the three offset columns is 50 m. Table 3.2 lists the gross properties of the platform, including

mass and moment of inertia, location of Centre of Mass (CM) below still water level (SWL) as well as draft. All data is represented in full scale.

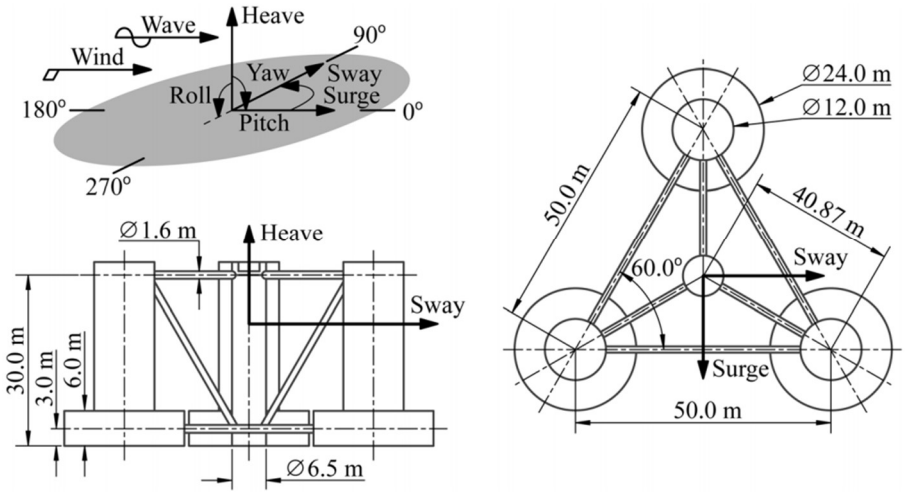

Figure 3.10 Definition of the DeepCwind semi-submersible platform (Coulling et al., 2013)

Table 3.2 Gross properties of the DeepCwind semi-submersible platform

Properties	Unit	Value
Platform mass, including ballast	kg	13,444,000
Displacement	m^3	13986.8
CM below SWL along platform centreline	m	14.4
Draft	m	20
Platform roll inertia about CM	$kg \cdot m^2$	8.011×10^9
Platform pitch inertia about CM	$kg \cdot m^2$	8.011×10^9
Platform yaw inertia about platform centreline	$kg \cdot m^2$	1.391×10^{10}

In order to maintain its position under wave and/or wind conditions, the platform is equipped with a mooring system composed of three mooring lines of catenary shape. These three lines are 120° apart and numbered successively, as sketched in Figure 3.11. The radius of the mooring system is 837.6 m. Properties for the mooring system are summarised in Table 3.3. The fairlead of each line is attached to the base of one of the three offset columns, 14 m below SWL.

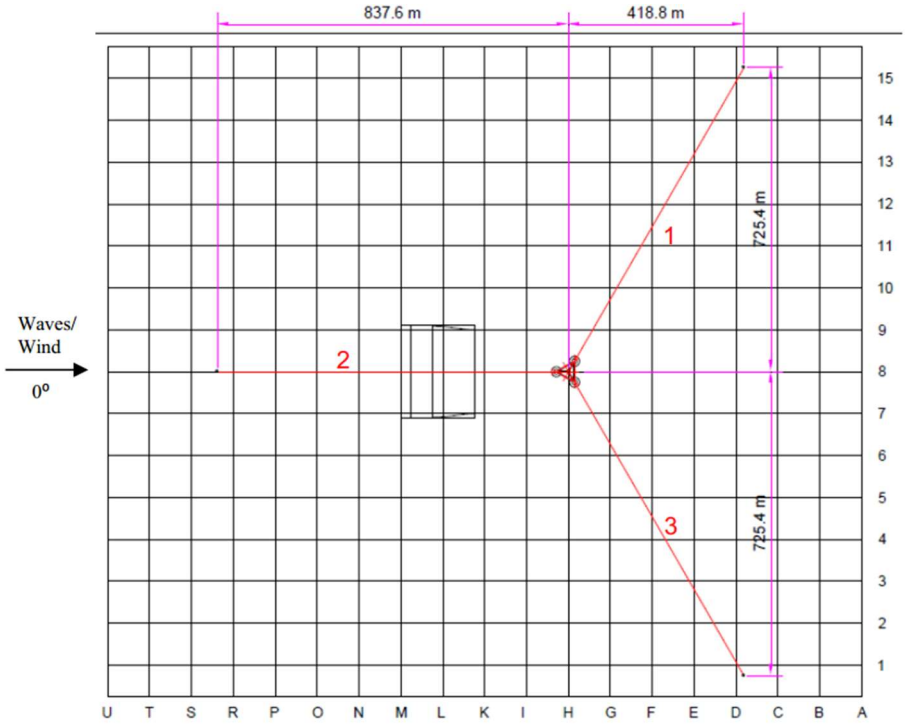

Figure 3.11 Layout of the mooring system (Robertson et al., 2014a)

Table 3.3 Gross properties of the mooring system

Properties	Unit	Value
Number of mooring lines	-	3
Angle between adjacent lines	°	120
Depth to anchors below SWL (water depth)	m	200
Depth to fairleads below SWL	m	14
Radius to anchors from platform centreline	m	837.6
Radius to fairleads from platform centreline	m	40.868
Unstretched mooring line length	m	835.5
Mooring line diameter	m	0.0766
Equivalent mooring line mass	kg/m	113.35
Equivalent mooring line mass in water (buoyancy excluded)	kg/m	108.63
Equivalent mooring line extensional stiffness	MN	753.6

Figure 3.12 demonstrates the computational domain adopted for the present CFD simulation. The distance between the left inlet boundary for wave generation and the

platform is one wave length denoted as L. The outlet boundary on the right side is 2L away from the platform to provide enough space for wave damping. The two side boundaries are 2L apart with the platform located along the centreline. Water depth D is 200 m and the top boundary is 100 m above the free surface.

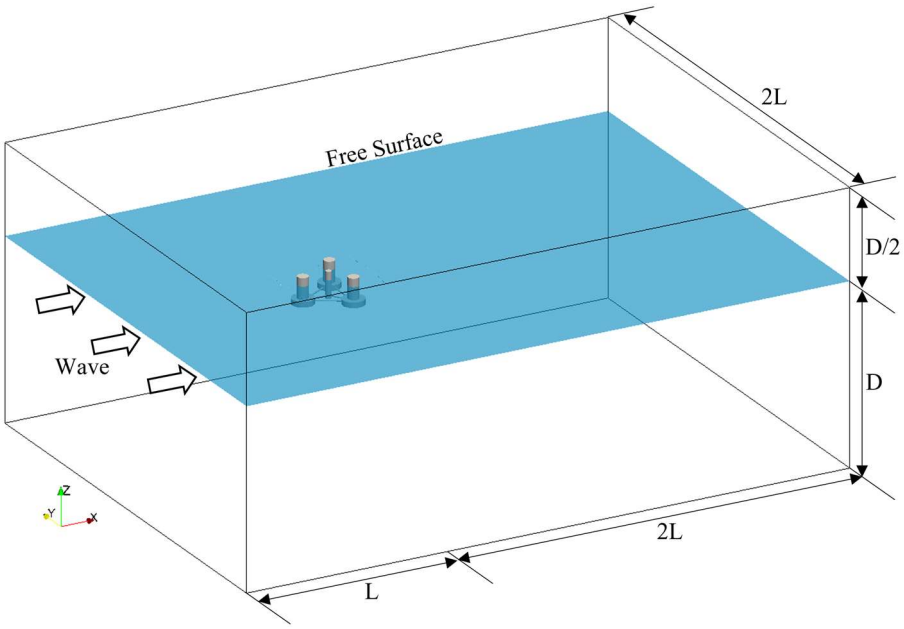

Figure 3.12 Computational domain for the DeepCwind semi-submersible platform

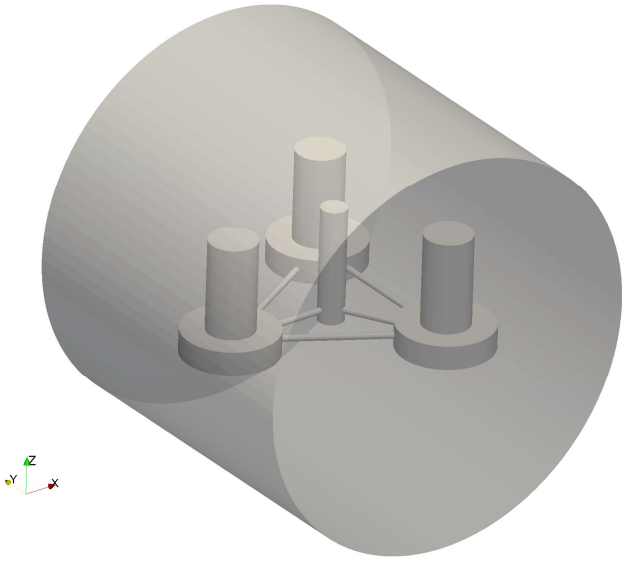

Figure 3.13 AMI domain surrounding the floating platform with pitch motion

To deal with the movement of the OC4 semi-submersible platform, the AMI sliding mesh technique described in Section 2.3.1 is adopted by creating a cylindrical region

surrounding the platform, as shown in Figure 3.13, so that the pitch motion is modelled by rotating the AMI region. The centre of the region is located at the centre of rotation of the platform. The surge and heave motions are represented by the rigid body motion of the overall computational domain including the AMI region so that the deterioration of mesh quality experienced with mesh deformation techniques is avoided.

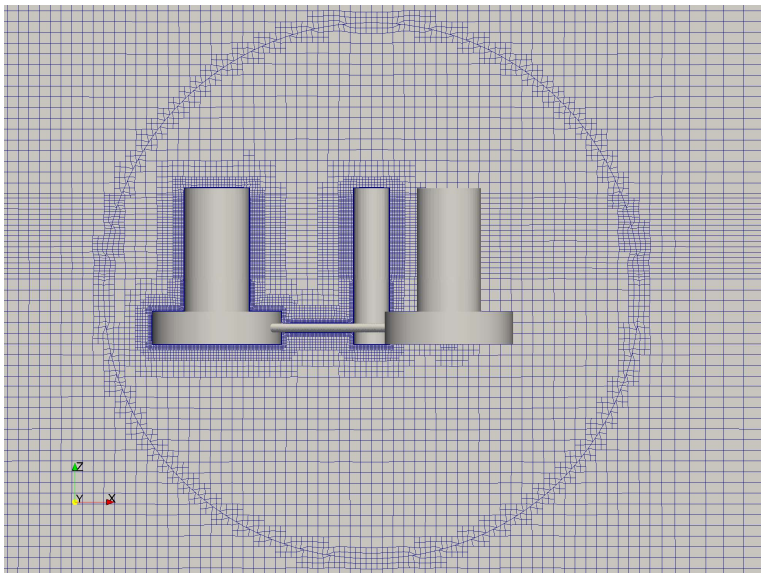

(a) Overall view

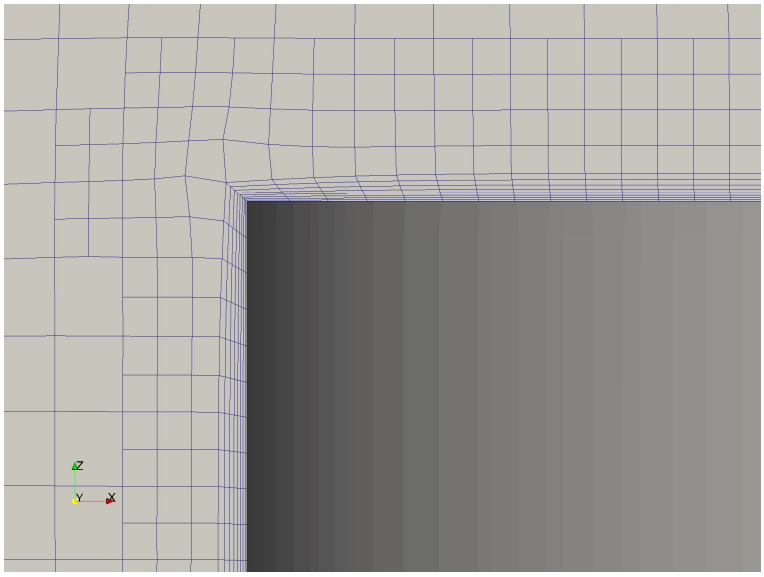

(b) Detailed view near the base column

Figure 3.14 Mesh for the OC4 semi-submersible platform

Three sets of computational mesh with different grid density are generated using the built-in utility snappyHexMesh to ensure that mesh-independent results are obtained.

Figure 3.14(a) shows the medium-sized mesh for the platform. The mesh is refined near the free surface and the platform to better capture the interaction between incoming waves and the structure. Figure 3.14(b) illustrates the refined mesh near the base column of the platform. Eight layers of boundary layer cells are extruded from the platform surface with a growth ratio of 1.2 and the first cell height away from the surface is 0.012 m to ensure that y+ is within the range of [30, 300] and wall functions are adopted for near wall treatment in the k - ω SST turbulence model. Table 3.4 summarises the estimated RAOs for three sets of mesh under the same incident wave condition. A maximum deviation of -3.42% indicates that the results are mesh-independent. Therefore, a medium grid is applied for later comparison and simulation.

Table 3.4 Mesh-sensitivity test for RAO of floating platform under regular waves: wave amplitude – 3.79 m, wave period – 12.1 s (percentage in parentheses shows the difference over data obtained with fine grid)

Grid	Cell Number (in million)	Surge (m/m)	Heave (m/m)	Pitch (°/m)
Coarse	2.35	0.5982 (-1.56%)	0.2878 (-1.44%)	0.2442 (-3.21%)
Medium	3.14	0.5965 (-1.84%)	0.2820 (-3.42%)	0.2470 (-2.10%)
Fine	4.55	0.6077 (-)	0.2920 (-)	0.2523 (-)

3.3.2 Mooring Restoring Force

The mooring system is an essential component of the floating platform. In order to ensure that the mooring system is correctly configured in this study, a series of numerical tests is carried out using the quasi-static mooring line analysis module developed in the present tool while the platform is not directly modelled. The fairleads of all the three mooring lines are forced to translate in surge and sway DoFs from -20 m to 20 m, and the predicted total restoring force from the mooring system is compared to both experimental data and results from FAST's quasi-static mooring module reported in the work of Coulling et al. (2013). Comparison shown in Figure 3.15 demonstrates that the results from the present simulations agree very well with experimental data, indicating that the current mooring line analysis module is capable of predicting the static characteristics of the mooring system.

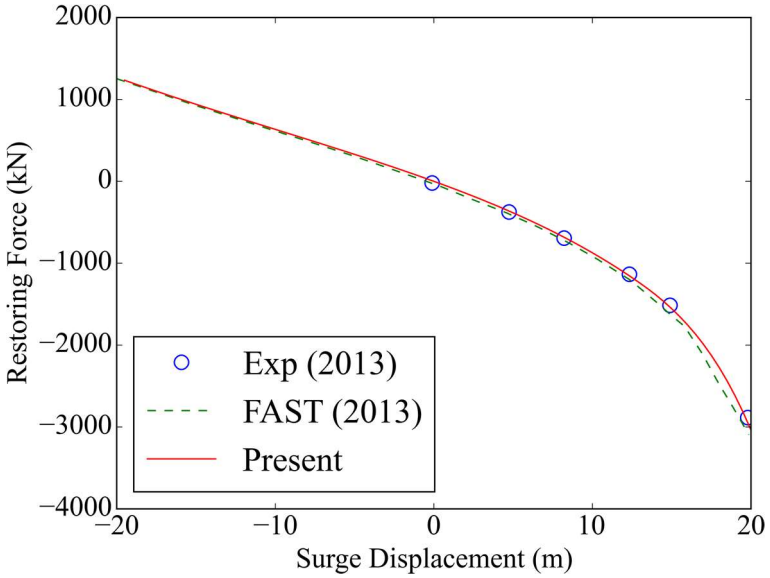

(a) Surge

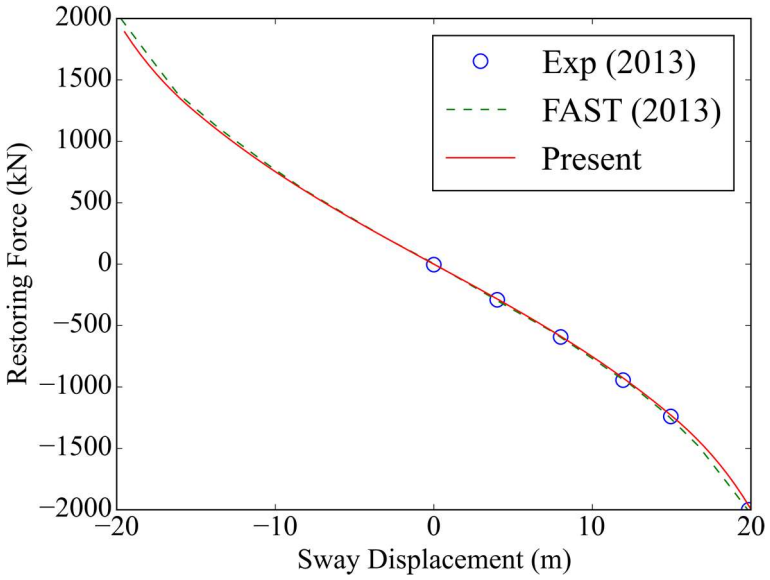

(b) Sway

Figure 3.15 Comparison of surge and sway mooring restoring force

3.3.3 Hydrodynamic Response in Regular Waves

The hydrodynamic response of the floating platform is then investigated under a regular wave condition with a wave amplitude of 3.79 m and a wave period of 12.1 s to match the experimental study (Coulling et al., 2013). The wave modelling module presented in Section 2.1.4 is firstly validated by simulating the wave in a 2D numerical wave tank without considering the influence of the platform. The time history of wave elevation at the location of x = 0 m, i.e. the centre of the platform if it is present, is

plotted in Figure 3.16. The distance between the inlet boundary and the probe is about one wave length. Results obtained using the Stokes 2nd order wave theory, i.e. Eq. (2.24), are also shown in Figure 3.16 for comparison. Very good agreement between the theoretical and simulated results is achieved with a difference of less than 1.5%, demonstrating the good accuracy of the present tool in modelling regular waves.

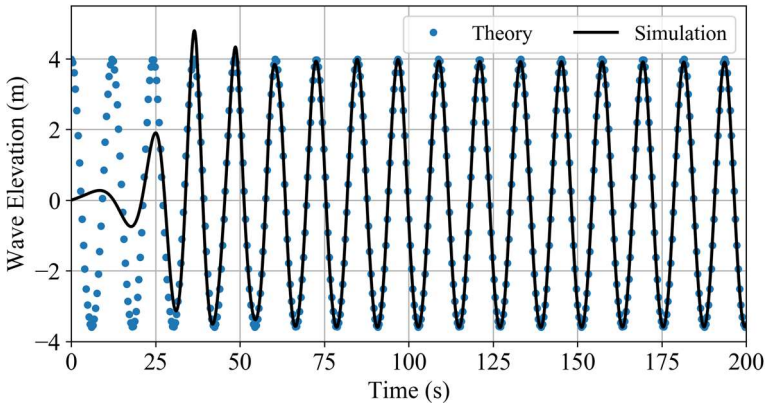

Figure 3.16 Comparison of time history plots of wave elevation at location x = 0 m between theory and numerical simulation

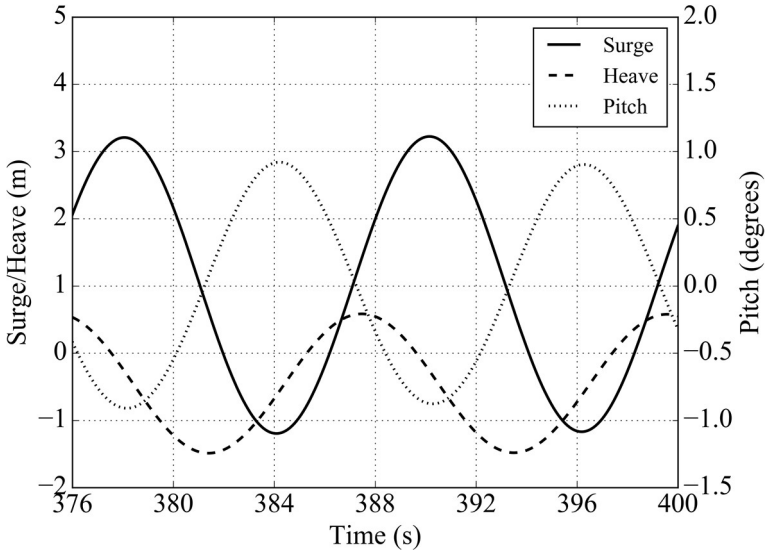

Figure 3.17 Time history for the responses of the platform under regular waves

Subsequently, the interaction between the regular wave and the platform in a 3D wave tank is studied, as illustrated in Figure 3.12. The three platform DoFs with the most significant responses in head wave conditions, i.e. surge, heave and pitch, are analysed. Figure 3.17 shows the time history curves for these three DoFs over two motion cycles. To exclude the effects of disturbance from the initial start-up stage, CFD simulation

runs for 400 s to achieve a nearly periodic quasi-steady state. It should be noted that the mean heave motion is below zero due to the imbalance between the imposed gravity force and the calculated vertical mooring loading of the floating system and the predicted buoyancy force. This might also be related to the decrease of pressure on the base of the platform as a result of fluid flow. The surge motion also has a mean value of 0.8686 m because of the drift force in waves.

Surge, heave and pitch motion amplitudes are estimated by averaging the amplitudes within the last two cycles. These values are then normalised by the amplitude of the regular wave to obtain the response amplitude operator (RAO). A comparison is made and illustrated in Figure 3.18 for the motion RAO results from the present simulation with the model test data and those from FAST (Coulling et al., 2013) as well as another CFD simulation (Tran and Kim, 2016b). The present tool predicts very similar RAOs in comparison to other data under the regular wave condition.

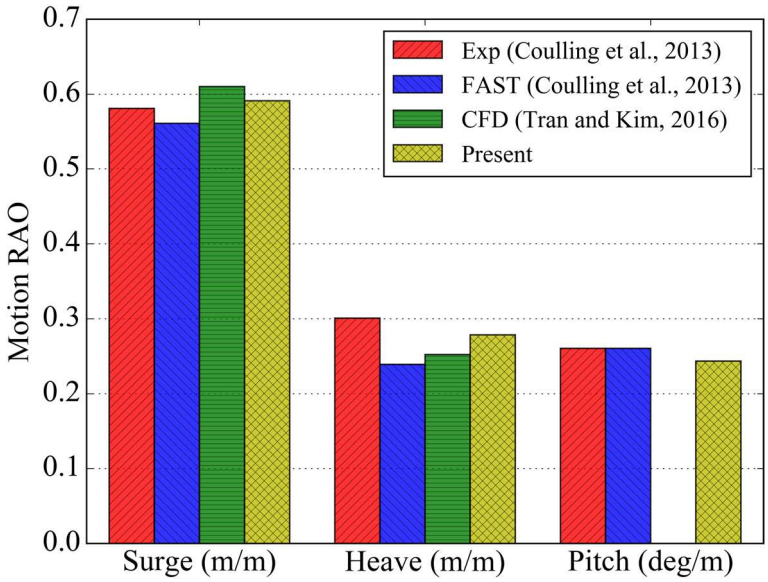

Figure 3.18 Comparison of RAO for platform surge, heave and pitch responses

The mooring line tensions for lines #1 and #2 defined in Figure 3.11 are plotted in Figure 3.19. It is clear that both the mean and peak tensions for line #2 in the head wave direction are larger than for line #1 in the back wave direction due to the drift force. Similar to the motion response RAO, a mooring line tension RAO is defined by normalising the tension amplitude with the incident wave amplitude.

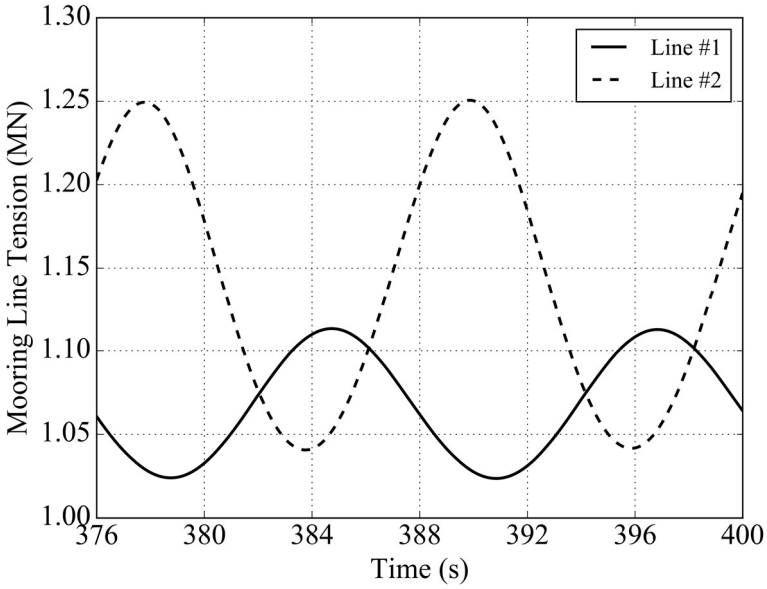

Figure 3.19 Time history of tension for mooring lines #1 and #2 under regular waves

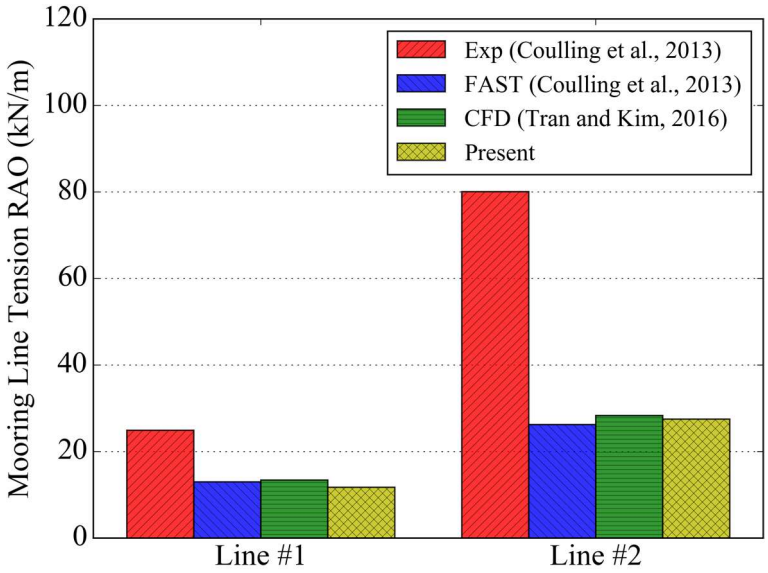

Figure 3.20 Comparison of tension RAO for mooring lines #1 and #2

Figure 3.20 shows the comparison of present results with other experimental and numerical data. Good agreement is observed between the results obtained from three numerical simulations based on different tools, although they all significantly under-predicted the line tensions for both lines compared to the experiment. The discrepancy might result from the application of a static mooring analysis model rather than a dynamic model. This phenomenon was also noted in the work of Coulling et al. (2013) and Tran and Kim (2016b). On the other hand, investigations of Masciola et al. (2013),

Hall and Goupee (2015) and Antonutti et al. (2018) with a dynamic mooring model predicted similar results to the experiment, which gives an indication that a more accurate dynamic mooring model should be adopted. Nevertheless, the platform motion RAOs do not seem to be largely affected by the quasi-static mooring model used in the present study, as demonstrated in Figure 3.18.

3.3.4 Free Decay Tests

Free decay tests are usually performed in a wave tank to determine the natural period of a floating system. The three DoF motion responses (surge, heave and pitch) of great significance in head wave conditions are tested in the present study. It is worth mentioning that the cable bundle used to transmit data from the floating system to computers in the model tests provided an additional surge stiffness of 7.39 kN/m, which was estimated by matching the surge natural period from the free decay test data (Coulling et al., 2013) and is also taken into consideration in present simulations.

The natural periods of the three DoF motion responses are summarised in Table 3.5. Comparison of present results to experimental data and results from FAST and other CFD simulations (Tran and Kim, 2015) reveals good agreement.

Table 3.5 Comparison of natural periods of the OC4 semi-submersible platform from free decay tests (Unit: s)

DoF	Exp (Coulling et al., 2013)	FAST (Coulling et al., 2013)	CFD (Tran and Kim, 2016b)	Present
Surge	107	107	108.1	107.2
Heave	17.5	17.3	17.8	17.5
Pitch	26.8	26.8	25.2	27.4

In addition to natural periods, damping ratios can also be obtained from free decay tests, which are of equal importance for an accurate prediction of the dynamic motion responses of a floating system. Figure 3.21(a) demonstrates the heave free decay response of the floating system with an initial heave displacement of 3 m. Damping ratios are calculated with two consecutive amplitudes, indicated as the square markers in Figure 3.21(a). Figure 3.21(b) shows the heave damping ratios over the initial cycle

amplitude in the free decay test. It is obvious that the results predicted by the present CFD tool are in good agreement with other published data.

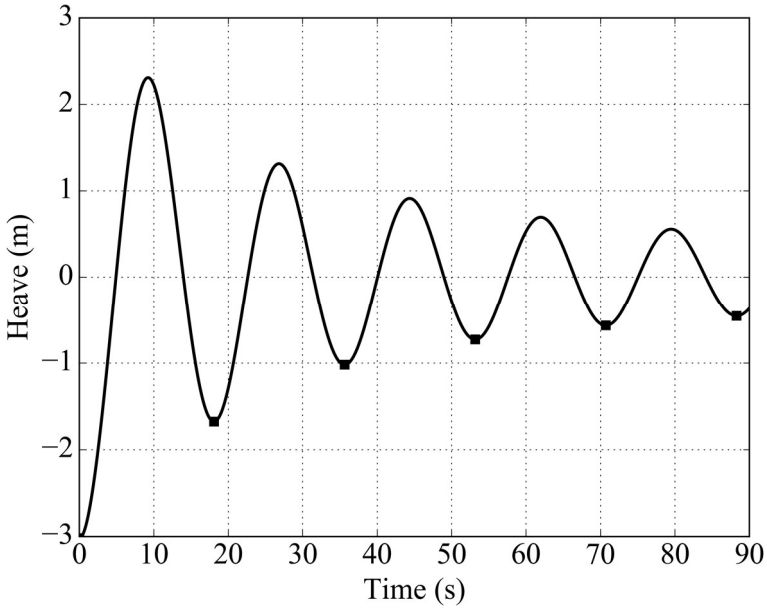

(a) Dynamic heave response with an initial heave displacement of 3 m

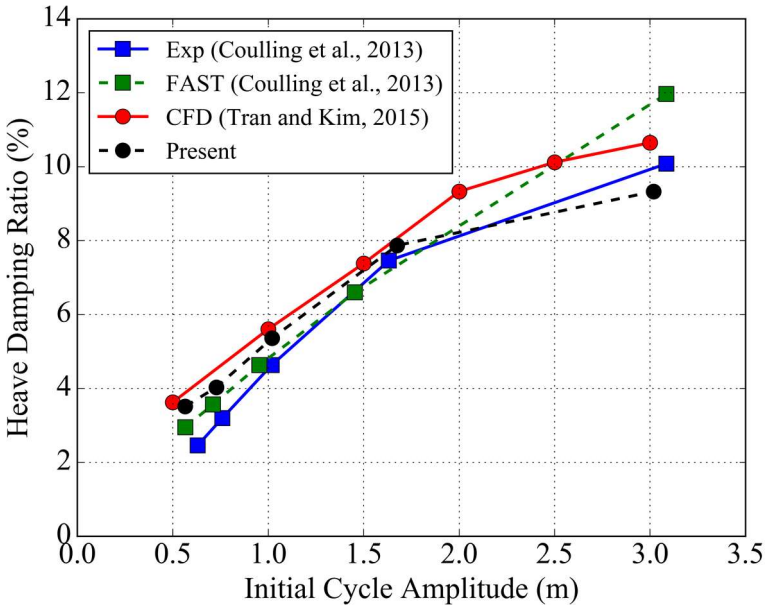

(b) Comparison of heave damping ratios

Figure 3.21 Heave free decay simulation results

3.4 Dynamic Analysis of a Flexible Hanging Riser

The dynamic mooring analysis method developed in the present tool is validated with a flexible hanging riser case previously studied by Low and Langley (2006). A riser is

similar to a mooring line as they are both slender and flexible structures subject to hydrodynamic loading as well as platform motion, and thus can be solved using the same numerical methods. The flexible hanging riser case is listed as one of the validation cases by the well-known commercial software OrcaFlex for dynamic line analysis (https://www.orcina.com/SoftwareProducts/OrcaFlex/Validation/index.php) and is therefore selected to validate our own dynamic analysis code. The lumped mass method is also adopted by Low and Langley (2006) as well as OrcaFlex.

3.4.1 Model Description

Table 3.6 lists the principal properties for the flexible hanging riser case studied by Low and Langley (2006). The riser is 170 m long when there is no tension force applied. The top end of the riser is 5 m below water surface and it is thus completely submerged in water with infinite depth to exclude effects of free surface and seabed. The tangential component is set to 0 for both drag and added mass coefficients.

Table 3.6 Properties of the flexible hanging riser

Properties	Unit	Value
Total Unstretched Length L	m	170
Horizontal Distance between Two Ends L_H	m	100
Vertical Distance between Two Ends L_V	m	50
Top End below Water Surface D_T	m	5
Diameter d	m	0.396
Mass per Unit Length m	kg/m	165
Weight per Unit Length in Water (Buoyancy Excluded) w	N/m	410
Extensional Stiffness EA	MN	500
Tangential Drag Coefficient C_{DT}	-	0
Normal Drag Coefficient C_{DN}	-	1
Tangential Added Mass Coefficient C_{AT}	-	0
Normal Added Mass Coefficient C_{AN}	-	1
Number of Segments n	-	68

Figure 3.22 plots the shape of the riser predicted by the present tool while it is static in still water without considering hydrodynamic loadings. Due to the gravitational force, the riser hangs between its two ends. Results from Low and Langley (2006) are also displayed in Figure 3.22 for comparison and excellent agreement is achieved with the present data, which further demonstrates the good accuracy of the quasi-static solver developed in the mooring system analysis module.

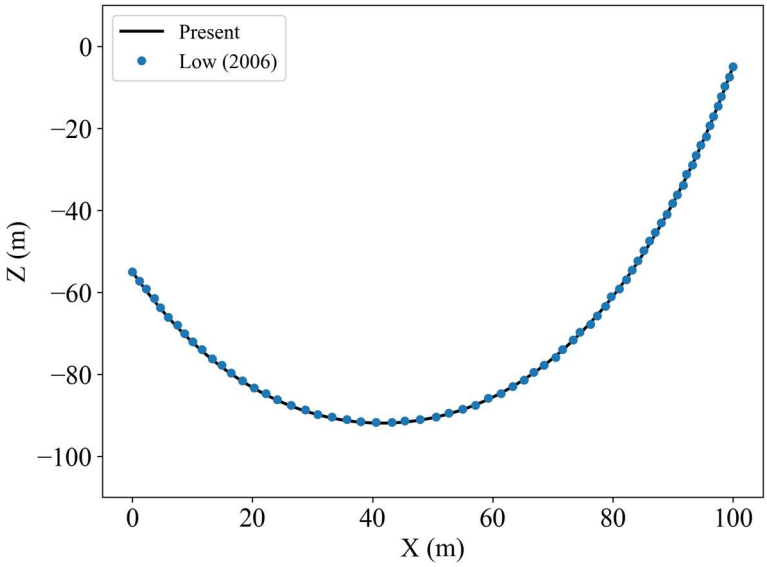

Figure 3.22 Static shape of the flexible hanging riser

3.4.2 Dynamic Analysis

In order to validate the dynamic analysis code, a series of test cases is set up by prescribing sinusoidal motion functions to the top end of the riser while the bottom end is fixed. Table 3.7 lists the three test cases studied, which have the same motion amplitude of 10 m and motion period of 27 s but differ from each other in the motion direction, including surge (X), sway (Y) and heave (Z). For the prescribed surge and heave motion cases, the riser always moves in the XoZ plane as shown in Figure 3.22, while it oscillates in the out-of-plane direction under the prescribed sway motion condition. These cases are simulated to analyse the responses of the riser, mainly the tension force at the top end, when it is connected to a floating platform experiencing wave-induced motions.

Table 3.7 Motion parameters of the top end for the flexible hanging riser

Case	Motion Direction	Motion Amplitude (m)	Motion Period (s)
1	Surge	10	27
2	Sway	10	27
3	Heave	10	27

Figure 3.23 shows the time history plots of the tension force measured at the top end of the riser under three different motion conditions. Strong nonlinearity can be observed for the surge motion case, where secondary peaks are clearly shown in addition to the primary peaks. This can be explained by the slack or hanging configuration of the riser. The nonlinear responses are also present for the heave motion case although they are less severe compared to the surge case. The sway motion case exhibits almost linear tension variation with respect to the prescribed motion. As the sway motion is symmetric about the XoZ plane, the frequency of the tension is twice that of the motion. Figure 3.23 also demonstrates the results obtained by Low and Langley (2006), which are in very good agreement with those predicted using the present dynamic analysis code. As a result, the mooring system analysis module developed in the FSI tool is successfully validated.

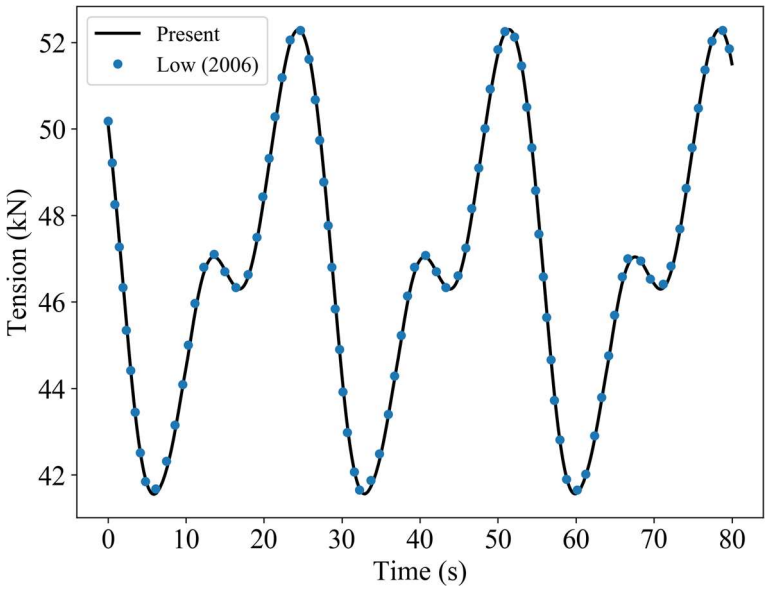

(a) Surge motion

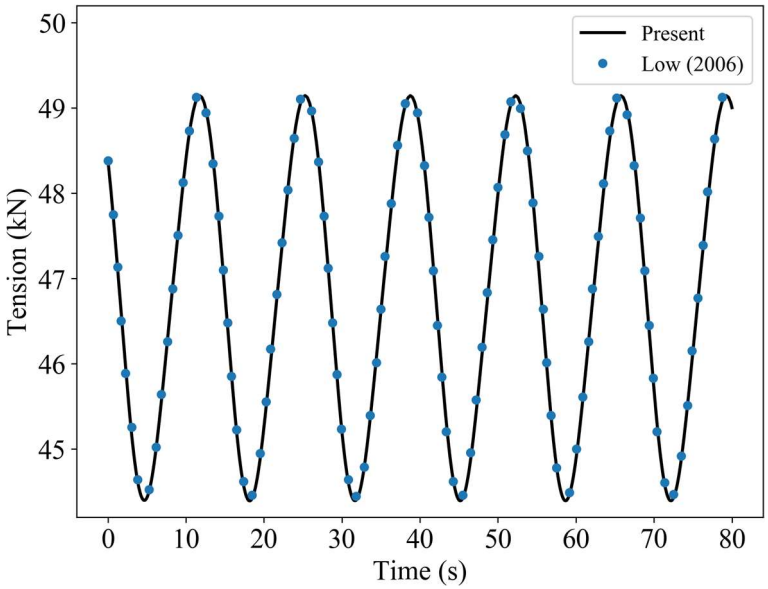

(b) Sway motion

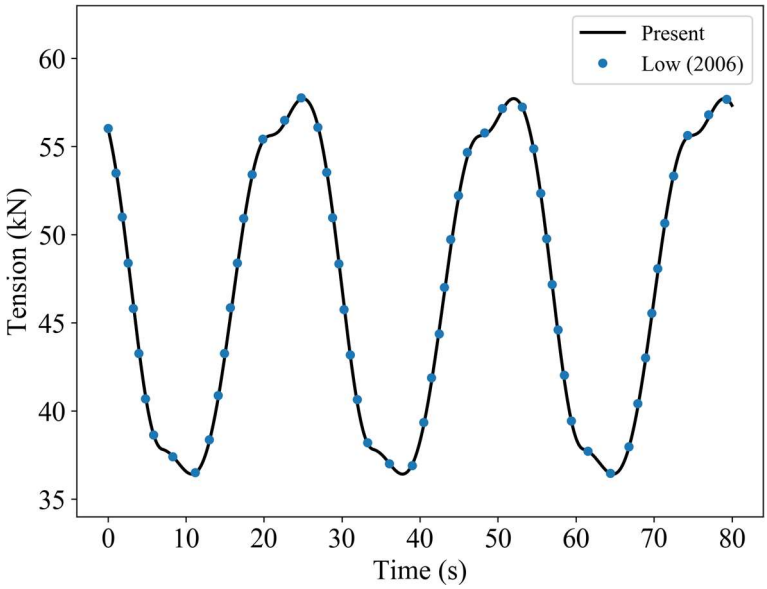

(c) Heave motion

Figure 3.23 Time history data of tension force at top end of the flexible hanging riser

3.5 Flow Induced Oscillation of a Flexible Cantilever Beam

To validate the developed tool for FSI applications, a benchmark case of flow induced oscillation of a flexible cantilever beam is investigated, which has previously been studied by many researchers focusing on coupling fluid and structural solvers (Wood et al., 2010; Habchi et al., 2013).

3.5.1 Model Description

In this case, a flexible cantilever beam is attached to a rigid square cylinder in free stream, as shown in Figure 3.24. At a sufficiently large Reynolds number, vortices appear in the wake of the cylinder, and the vortex-induced unsteady forces exerted on the cantilever beam lead to the oscillating motion of the flexible beam. The physical properties of both fluid and solid are listed in Table 3.8.

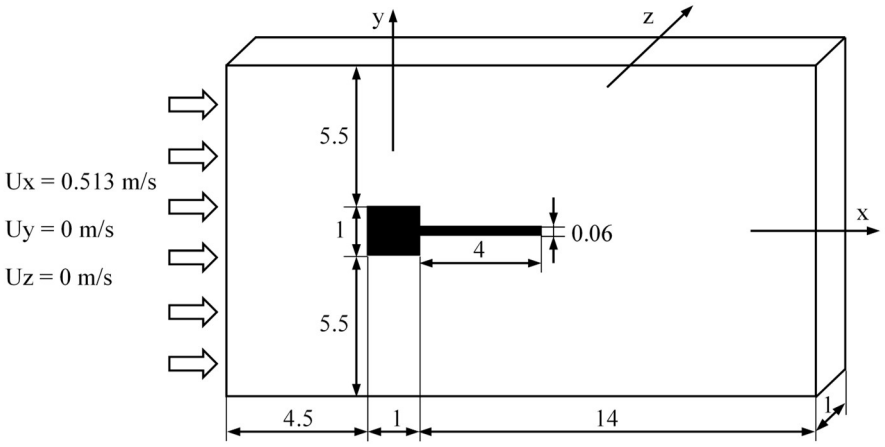

Figure 3.24 Illustration of a flexible cantilever beam attached to a fixed rigid square in free stream (Dimensions in cm)

Table 3.8 Physical properties of the flexible cantilever beam

Properties		Unit	Value
Solid	Density ρ_s	kg/m^3	100
	Young's Modulus E	Pa	2.5E5
	Poisson's Ratio	-	0.35
Fluid	Density ρ_f	kg/m^3	1.18
	Kinematic Viscosity ν_f	m^2/s	1.54E-5

Figure 3.25 illustrates the computational mesh with a total number of 18,904 structured cells for the CFD solver. The mesh is deliberately refined near the solid boundaries to better capture the rapid variance of the flow field. Only one layer of grid cells is deployed in z direction to constrain the fluid flow in two-dimensional xoy plane. The boundary conditions for the fluid flow are specified as follows. A constant velocity of

0.513 m/s is imposed at the left inlet boundary and zero pressure is applied at the right outlet boundary. The symmetry boundary condition is assumed at the top and bottom while an empty boundary condition, which in OpenFOAM indicates a 2D simulation, is employed for the front and back planes. The Reynolds number based on the side length of the square is 333, and thus no turbulence model is applied in this case.

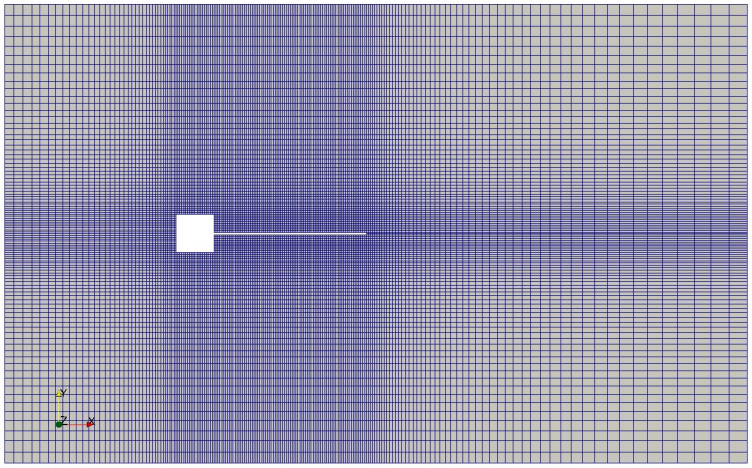

Figure 3.25 CFD mesh of the flexible cantilever beam used in OpenFOAM

In the MBD model, the flexible cantilever beam is represented by 4 beam elements as shown in Figure 3.26. Two adjacent beam elements share one geometrical node. As each beam element consists of 3 geometrical nodes, the total number of nodes is 9. All nodes are evenly distributed with an interval of 0.5 cm. The leftmost node is attached to the rigid square and is thus kept fixed while the square is not modelled in MBDyn.

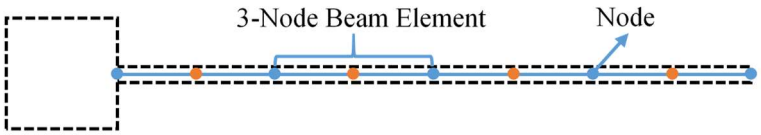

Figure 3.26 MBD model of the flexible cantilever beam

3.5.2 Structural Response

The displacement in y direction of the beam tip, i.e. the free end of the cantilever beam, with respect to time is plotted in Figure 3.27(a). The oscillation of the beam induced by vortex shedding from the front cylinder gradually develops into a harmonic mode as shown in Figure 3.27(a). Meanwhile, Figure 3.27(b) illustrates the shape of the

beam at different time instants represented by a series of dashed curves over one oscillation period. The trajectory of every geometrical node is represented by a solid curve in a distinctive colour.

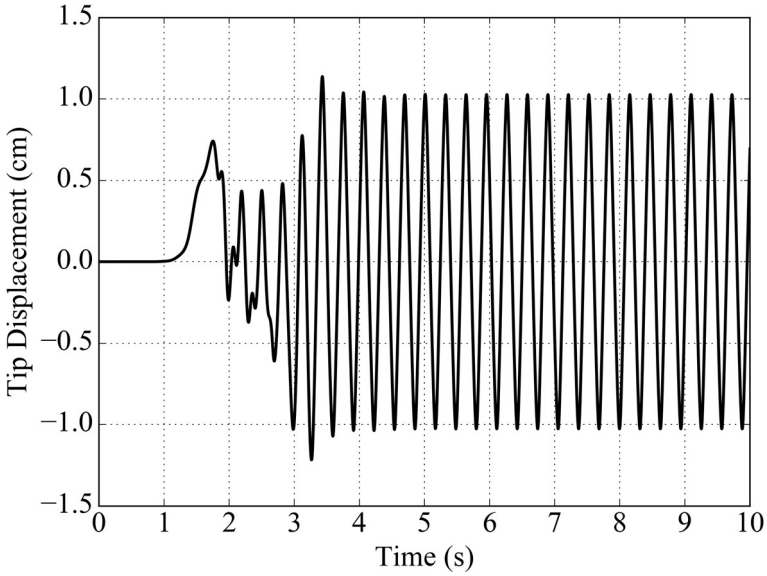

(a) Time history of the beam tip displacement in y direction

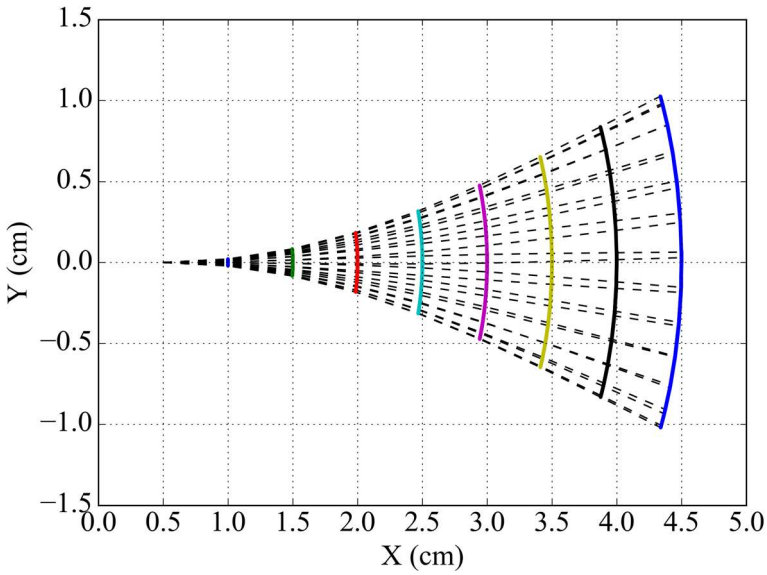

(b) Shape of the beam over one oscillation cycle

Figure 3.27 Oscillation of the flexible cantilever beam

The amplitude and frequency of the tip oscillation over the last five cycles are extracted from the time history curve in Figure 3.27(a) and they are 1.03 m and 3.18 Hz, respectively. The results are then compared with other available data as summarised in Table 3.9. As can be seen, a good agreement between the present results and those

obtained with other numerical methods is obtained, indicating that the fully coupled CFD-MBD tool developed in this study is capable of handling FSI simulations for flexible beam-like structures.

Table 3.9 Comparison of tip displacement amplitude and oscillation frequency for the flexible cantilever beam

	Tip Displacement Amplitude (cm)	Oscillation Frequency (Hz)
Present	1.03	3.18
Habchi et al. (2013)	1.02	3.25
Wood et al. (2010)	1.15	2.94
Mathieu et al. (2009)	0.95	3.17
Matthies and Steindorf (2003)	1.18	3.13

3.5.3 Flow Field

Snapshots of the flow field around beam are shown in Figure 3.28 at four subsequent time instants to demonstrate the interaction between the flow field and the flexible beam, where the flow field is coloured by z component of vorticity vector. It can be clearly seen that the deformation of the beam diverts the Von Karman vortex street induced by the front cylinder to the upper and lower right corners of the domain, rather than in the downstream direction for a rigid beam case. The tip oscillation of the beam also leads to the generation of tip vortices travelling away from the beam, which is in accordance with the results presented in the work of Habchi et al. (2013).

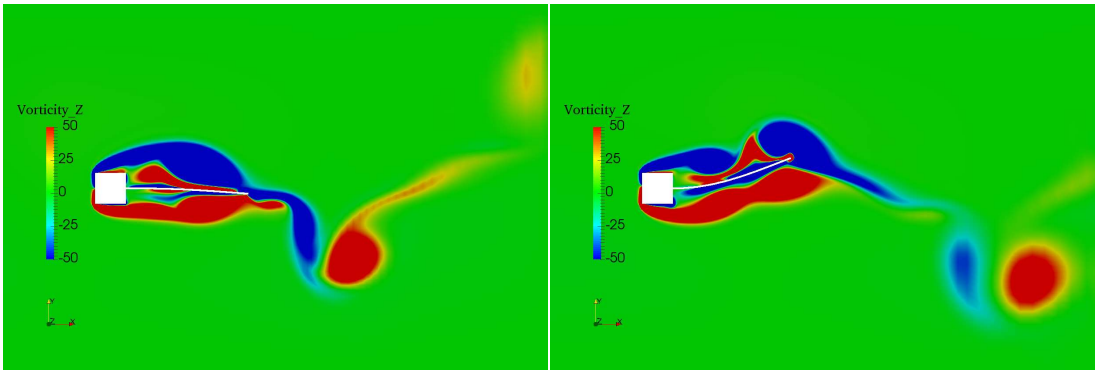

(a) Time = T0 *(b) Time = T0 + T/4*

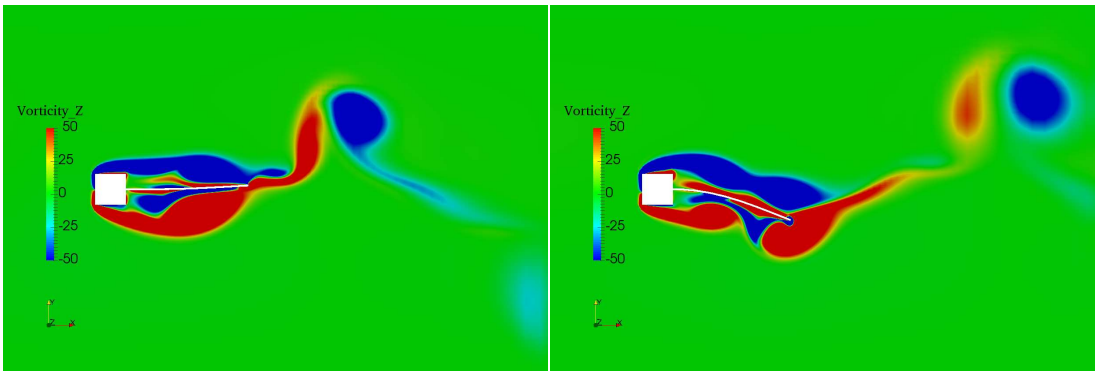

(c) Time = T0 + T/2 *(d) Time = T0 + 3T/4*

Figure 3.28 Snapshots of flow field coloured by the z component of vorticity vector for the flexible cantilever beam

3.6 Concluding Remarks

In this chapter, five test cases with different computational models and working conditions are set up to validate the various features of the fully coupled CFD-MBD tool developed in this project.

For the case of forced heave oscillation of a cylindrical structure presented in Section 3.1, the viscous damping coefficients resulting from both skin friction and form drag are calculated. Effects of oscillation amplitude on the viscous damping in the heave direction are investigated by keeping the oscillation frequency unchanged while varying the amplitude, corresponding to the variation of the KC number within the range of 0.1-0.8. The damping coefficient from skin friction is found to remain constant regardless of the KC number studied while the total viscous damping coefficient increases linearly with KC. Good agreement is achieved between present results and published data, which validates the basic flow solver.

In Section 3.2, the two-bladed NREL Phase VI wind turbine is studied to validate the aerodynamic modelling feature of the tool. The aerodynamic thrust and torque of the wind turbine under different wind speed conditions are calculated and compared with experimental and numerical data available. In addition, the pressure coefficients along the turbine blade at different radial sections, i.e. r/R = 0.3, 0.63 and 0.95, are also extracted and agree generally well with the experimental results.

The hydrodynamic modelling feature is validated in Section 3.3 by investigating the DeepCwind semi-submersible platform designed for the OC4 FOWT project. The restoring force provided by the mooring system under prescribed platform surge and sway motion is firstly predicted to validate the quasi-static mooring line analysis module. The motion responses of the floating platform under regular waves are then simulated using the present tool to obtain the motion and mooring tension RAOs. Free decay tests are also carried out to calculate the natural periods and damping ratios in various DoFs of the platform.

In Section 3.4, a flexible hanging riser is analysed to validate the dynamic mooring line analysis module. Prescribed sinusoidal motion functions are imposed to the top end of riser in surge, sway and heave directions to simulate the impacts of platform motion while the bottom end remains fixed. Strong nonlinearity is observed for the time history curve of the tension force measured at the top end, which agrees remarkably well with published data from other researchers.

Finally, the FSI problem of a flexible cantilever beam attached to a fixed square in the fluid flow of constant incoming current speed is investigated with the fully coupled CFD-MBD tool in Section 3.5. The unsteady flow field induced by vortex shedding from the square excites the oscillatory motion of flexible cantilever beam. The oscillation amplitude and frequency at the beam tip are within the range of previous predictions, which validates the capability of MBDyn in modelling beam-like structures as well as the coupling procedure between the two separate codes, i.e. OpenFOAM and MBDyn.

Chapter 4 Aero-Hydro-Mooring Analysis of a Semi-Submersible Floating Offshore Wind Turbine

In this chapter, the fully coupled FSI analysis tool is applied to the OC4 DeepCwind semi-submersible FOWT in combined conditions of wind and waves. As the first step towards our goal, some simplifications are made in the present study. Specifically, wind turbine blades are modelled as rigid and thus blade elasticity is not considered. Meanwhile, the mooring system of the FOWT is solved with the quasi-static analysis method stated in Section 2.4.1. Detailed description about the model is provided in Section 4.1, while numerical results obtained from the present tool regarding the mutual interactions between the wind turbine and its supporting platform are analysed and discussed in Section 4.2.

4.1 Model Description

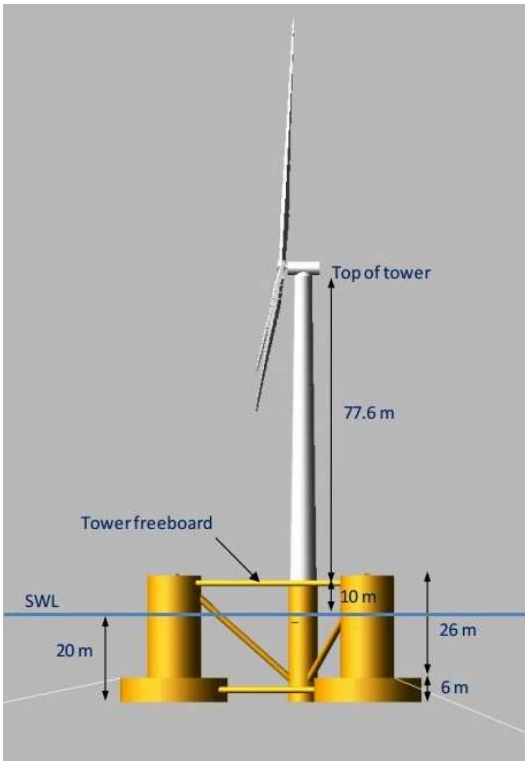

Figure 4.1 Definition of the OC4 semi-submersible FOWT (Robertson et al., 2014a)

Figure 4.1 shows the semi-submersible FOWT studied in Phase II of the OC4 project investigated in the present work. The whole system consists of the NREL 5-MW

baseline wind turbine designed for offshore applications (Jonkman et al., 2009), the OC4 tower, the DeepCwind semi-submersible platform (Robertson et al., 2014a) supporting the tower and a catenary mooring system. The platform and its mooring system have been studied previously in Section 3.3. In this section, descriptions of the floating offshore wind system are presented.

Table 4.1 Comparison between data published by NREL and properties used in MARIN's model tests

Gross Properties	NREL	MARIN
Overhang of wind turbine	5 m	10.58 m
Shaft tilt angle of wind turbine	5°	0°
Pre-cone angle of wind turbine	2.5°	0°
Blade mass	17,740 kg	16,450 kg
Blade second mass moment of inertia	11,776,047 kg·m^2	13,940,000 kg·m^2
Nacelle mass	240,000 kg	274,940 kg
Nacelle pitch inertia	Not specified	22 440 000 kg·m^2
Hub mass	56,780 kg	72,870 kg
Total tower-top mass	350,000 kg	397,160 kg
Tower mass	249,718 kg	302,240 kg
Center of mass (CM) above SWL (still water level) for tower	43.4 m	44.6 m
Platform mass, including ballast	13,473,000 kg	13,444,000 kg
CM location below SWL along platform centreline	13.46 m	14.4 m
Platform roll inertia about CM	6.827×10^9 kg·m^2	8.011×10^9 kg·m^2
Platform pitch inertia about CM	6.827×10^9 kg·m^2	8.011×10^9 kg·m^2
Platform yaw inertia about CM	1.226×10^{10} kg·m^2	1.391×10^{10} kg·m^2

In 2011, a series of model tests on a 1/50th-scale semi-submersible FOWT was carried out at Maritime Research Institute Netherlands' (MARIN's) offshore wind/wave basin, aiming to calibrate and validate the currently available FOWT modelling tools, such

as FAST (Coulling et al., 2013; Robertson et al., 2014b). Although the geometry defined in the report published by Robertson et al. (2014a) was adopted in the tests, some adjustments were made during the fabrication process. Details about the geometry definition can be found in the work published by Coulling et al. (2013) and the major discrepancies between the data from NREL's reports and those used in the tests in terms of gross properties are compared in Table 4.1. It should be noted that all published data represented are associated with a full-scale device.

An important change for the wind turbine model used in the experimental tests was that both the shaft tilt angle and pre-core angle were set to zero as the turbine blades were designed to be almost rigid. As a result, the potential deformation of the blades could be neglected. Other variations are mainly in relation to the mass and inertia properties of various parts of the system. For example, the mass of a blade was decreased from 17,740 kg to 16,450 kg in the tests, possibly due to the material and fabrication reasons. The parameters and gross properties used in the model tests are employed in the present work so that validation could be made against model test data. Since the motion responses of an FOWT need to be solved as an entire system when performing a dynamic analysis, the mass and inertia properties of the system are determined in advance by utilising the parallel axis theorem. Table 4.2 lists the gross properties of the FOWT system.

Table 4.2 Gross properties of the OC4 semi-submersible FOWT system

Properties	Unit	Value
Total mass of the system	kg	14,143,400
System CM location below SWL	m	10.21
Roll inertia about system CM	$kg \cdot m^2$	1.314×10^{10}
Pitch inertia about system CM	$kg \cdot m^2$	1.317×10^{10}
Yaw inertia about platform centreline	$kg \cdot m^2$	1.393×10^{10}

4.2 Results and Discussion

In this section, numerical results obtained using the developed tool are presented and discussed, focusing on the effects of the platform on wind turbine aerodynamic

performance and the impacts of the wind turbine on hydrodynamic and mooring responses of the floating platform under combined wind/wave conditions.

4.2.1 Aerodynamics of the NREL 5-MW Wind Turbine

The aerodynamics of the NREL 5-MW wind turbine is firstly studied in full scale without the floating platform and will be used for later comparison with the data of a floating wind turbine. The geometry of the three-bladed NREL 5-MW wind turbine adopted in the CFD simulations is created using the blade model file published by Hsu (2015) and is illustrated in Figure 4.2. The turbine rotor connecting the three blades and the nacelle are not modelled for simplicity.

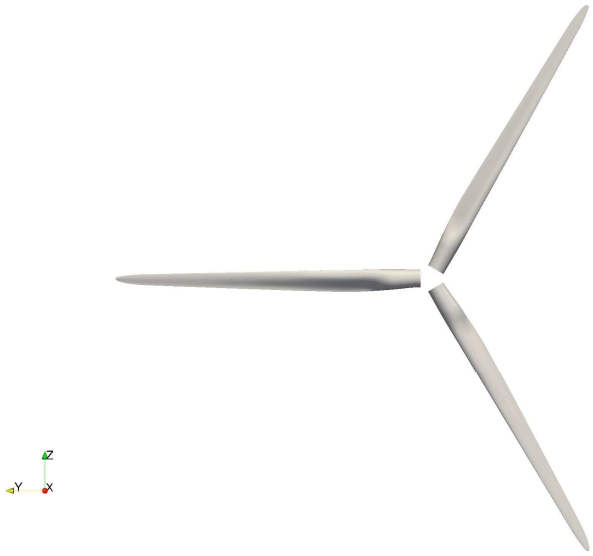

Figure 4.2 Illustration of the NREL 5-MW wind turbine

CFD simulations are known to be dependent on the computational grid used. In order to balance the accuracy of numerical results and the computational cost, a mesh-sensitivity test is carried out. Three sets of grids are generated with different grid density while all other parameters remain unchanged. The medium-sized mesh of the wind turbine is shown in Figure 4.3. The regions near the blade tips and blade roots are intentionally refined to better capture the tip and root vortices. Eight layers of boundary layer cells are extruded from the turbine surface with a growth ratio of 1.2 and the first cell height away from the turbine surface is 0.004 m to ensure that y+ is

within the range of [30, 300] and wall functions are adopted for near wall treatment in the k-ω SST turbulence model.

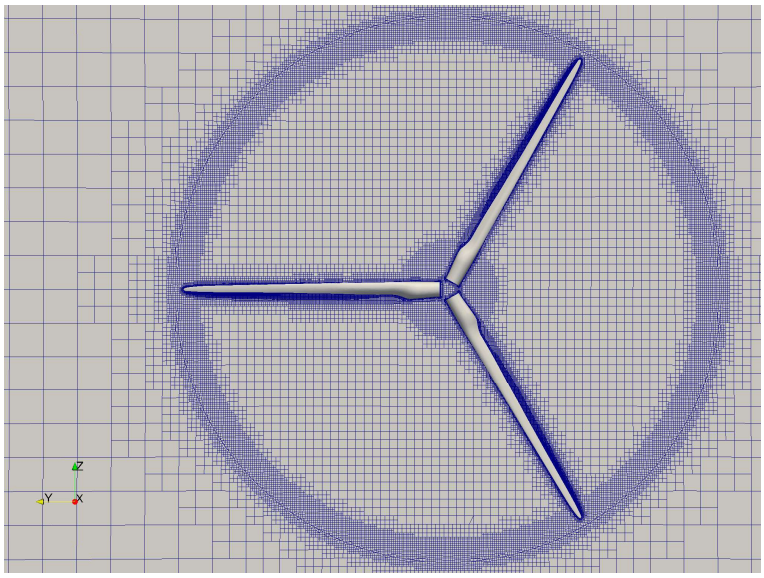

(a) Overall view

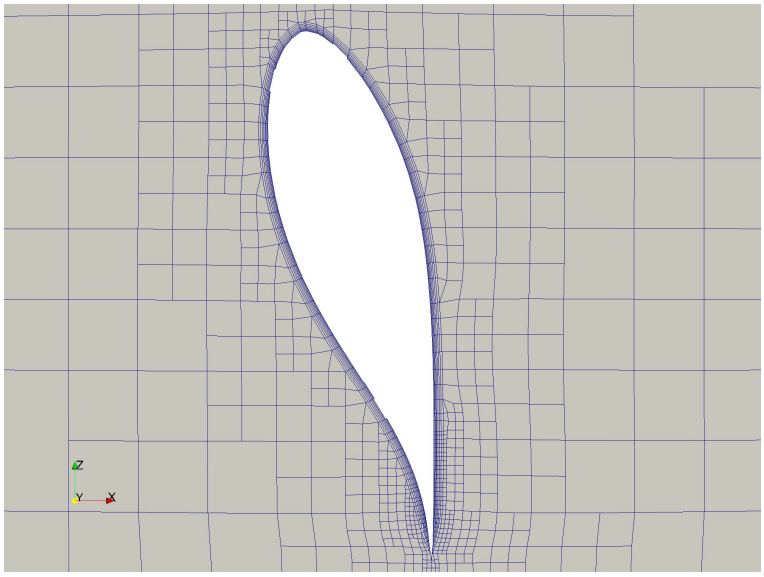

(b) Detailed view near turbine blade

Figure 4.3 Mesh for the NREL 5-MW wind turbine

One specific operating condition taken from Coulling et al. (2013) is selected for the mesh-sensitivity test. The incoming wind speed is 7.32 m/s, and the turbine rotor rotates at a speed of 4.95 RPM with a collective blade pitch angle of 6.4 degrees. The aerodynamics of the NREL 5-MW wind turbine is studied in full scale without the floating platform and will be used for later comparison with the data of a floating wind

turbine. Figure 4.4 shows the time history of wind turbine aerodynamic thrust and torque from the three sets of mesh.

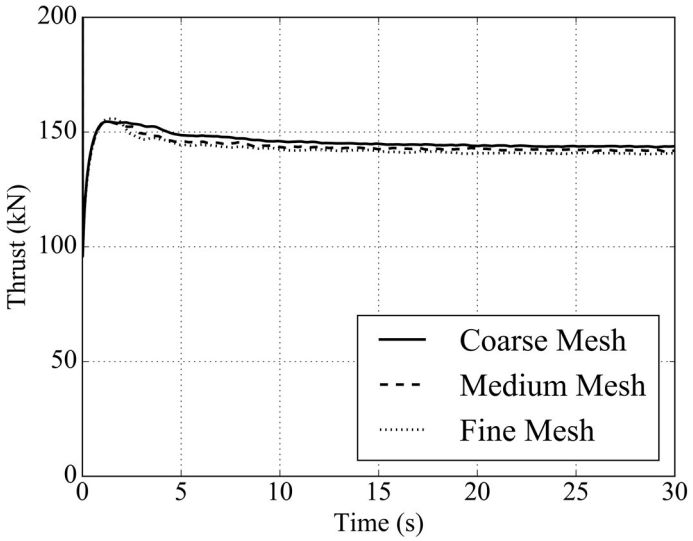

(a) Thrust

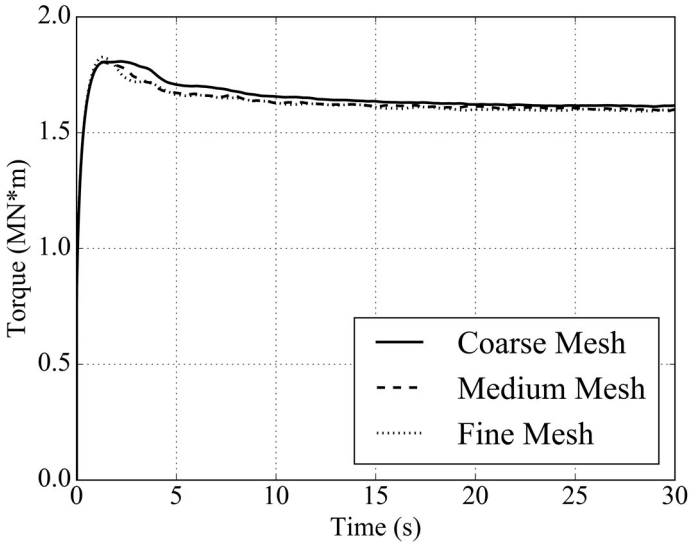

(b) Torque

Figure 4.4 Time history data of NREL 5-MW wind turbine aerodynamic performance

To eliminate the initial start-up effects, the thrust and torque are averaged from 20 s to 30 s to obtain time-averaged values, which are then listed in Table 4.3. Results are also presented in percentage difference over data obtained with fine grid. It can be clearly seen that the difference for both thrust and torque between medium and fine mesh is below 1%, indicating that the results are independent of the grid. Thus, the medium

mesh is selected for later simulations to balance computational accuracy and the computing time needed to complete the calculation.

Table 4.3 Mesh-sensitivity test results for NREL 5-MW wind turbine aerodynamic performance (percentage in parentheses shows difference over data from fine grid)

Grid	Cell Number (in million)	Thrust (kN)	Torque (MN*m)
Coarse	3.83	143.8 (+2.13%)	1.617 (+1.19%)
Medium	5.73	142.0 (+0.85%)	1.602 (+0.25%)
Fine	10.26	140.8 (-)	1.598 (-)

4.2.2 Effects of Floating Platform on Wind Turbine Aerodynamics

In order to study the influence of the floating platform imposed upon the aerodynamics of the wind turbine, a fully coupled CFD simulation is carried out for the OC4 FOWT in full scale. In this section, we will analyse the aerodynamic thrust and torque of the wind turbine and compare them with any available data.

Figure 4.5(a) demonstrates the computational domain for the FOWT simulation. Compared to the domain shown in Figure 3.12 used for the platform only simulation in Section 3.3, the top boundary is lifted up to 1.5D (water depth D: 200 m), i.e. 300 m, from the free surface to provide enough space for the wind turbine (rotor diameter: 126 m) while other dimensions remain the same. Meanwhile, in addition to waves, wind blows from the left boundary into the domain.

Figure 4.5(b) illustrates the cross-sectional view of the mesh at the xoz plane. Settings used to generate the medium-sized mesh for the aerodynamics of the NREL 5-MW wind turbine in Section 4.2.1 and for the hydrodynamics of the DeepCwind semi-submersible platform in Section 3.3.1 are applied for consistency. Mesh refinement is applied near the free surface as well as in the vicinity around turbine blade tip and root vortex regions. Nearly 10 million cells are generated using the built-in snappyHexMesh utility in OpenFOAM. The cylindrical AMI surfaces encompassing the whole floating system can also be clearly observed, which are adopted to handle the global rigid body motion, as previously discussed in Section 2.3.1.

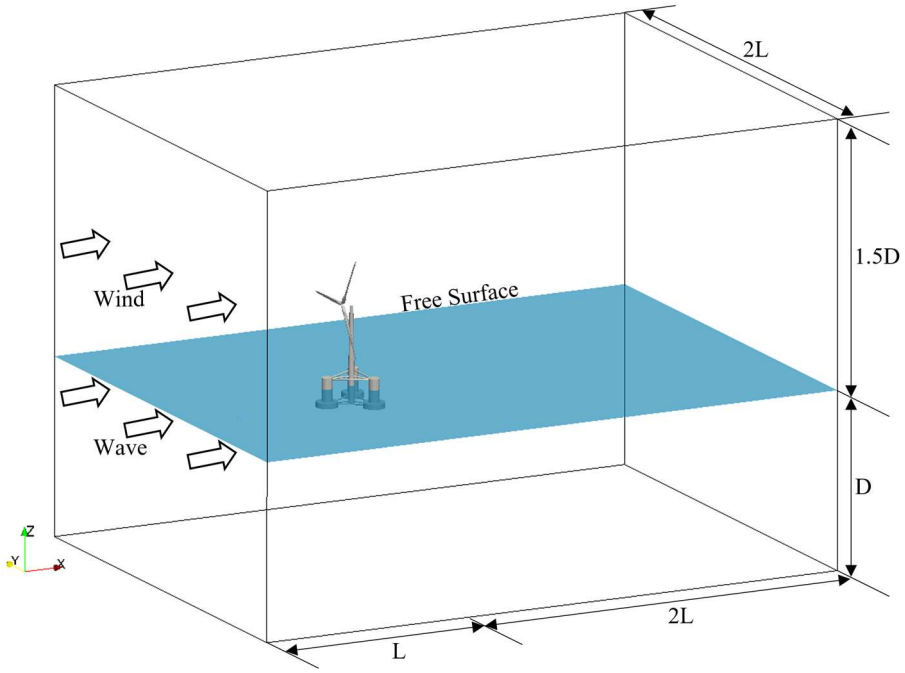

(a) Computational domain

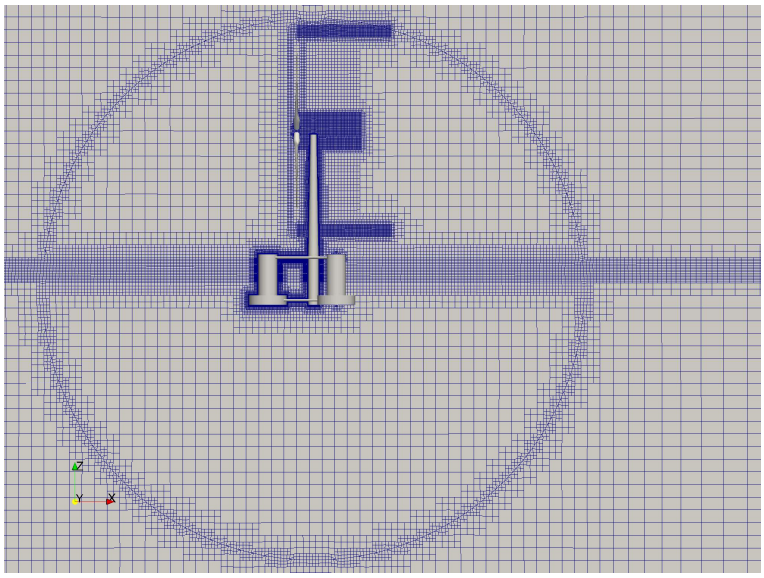

(b) Computational mesh

Figure 4.5 CFD model of the OC4 semi-submersible FOWT

The environmental conditions are the combinations of the regular wave previously studied in Section 3.3.3 and uniform wind speed from the experiment (Coulling et al., 2013), which are summarised in Table 4.4, so that influence of the wind turbine on the platform can be analysed. Two cases are set up where the wave parameters remain the same while two different wind speed and rotation speed configurations are adopted to

study the impacts imposed by wind speed. In Case #1, wind speed is 7.32 m/s and turbine rotation speed is 4.95 RPM, the same as in Section 4.2.1. In Case #2, the uniform wind speed is 11 m/s and rotation speed is 11.89 RPM, which is closer to the rated operating condition of the NREL 5-MW wind turbine and thus can better reflect the system responses under design working conditions. The wind condition in Case #2 is the same as that in the work of Tran and Kim (2016b), which makes it possible to compare relevant results from two different CFD codes. For both cases, the quasi-static mooring system analysis module is adopted to handle mooring line modelling, as in the platform only case of Section 3.3.

Table 4.4 Environmental conditions for the OC4 semi-submersible FOWT

Case #	1	2
Wave Amplitude (m)	3.79	
Wave Period (s)	12.1	
Wind Speed (m/s)	7.32	11
Rotor Speed (RPM)	4.95	11.89
Rotor Rotation Period (s)	12.1	5.046

To exclude the effects of disturbance from the initial start-up stage, simulations were carried out for 350 s to achieve a nearly periodic quasi-steady state. During the simulations, the aerodynamic thrust and torque of the FOWT are recorded and results over the last four wave cycles are used for further data analysis. Both thrust and torque are translated to the local wind turbine coordinate system so that they are consistent with the definition in Eq. (3.5) and can be compared with the data from the fixed turbine simulation in Section 4.2.1.

A comparison of the aerodynamic thrust and torque is made for the floating wind turbine simulation and the fixed turbine simulation in Case #1 and is illustrated in Figure 4.6, where the data from fixed turbine is extracted from the case with a medium mesh density. It is easily seen that the instantaneous thrust and torque are time dependent due to the motion of the floating platform, while the time-averaged thrust and torque are quite similar to those from the fixed turbine simulations.

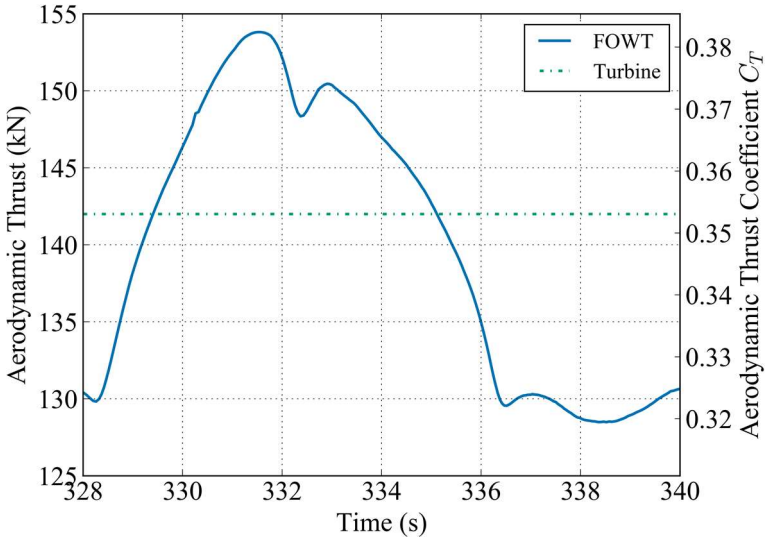

(a) Thrust

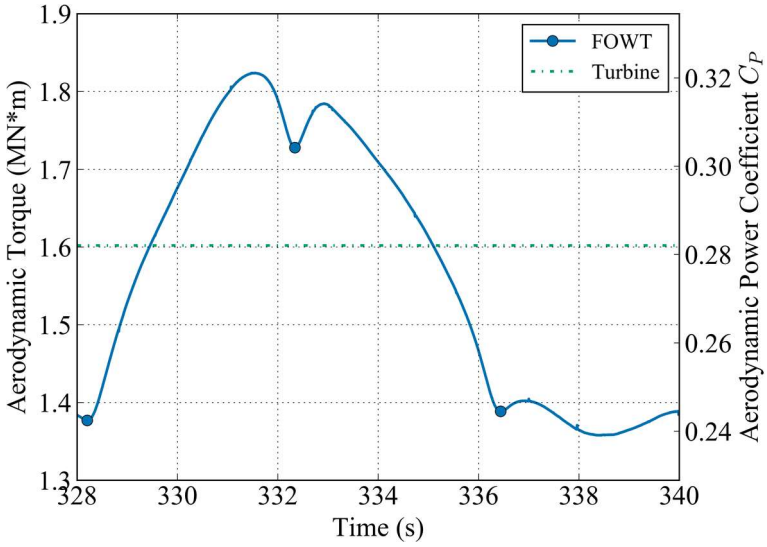

(b) Torque

Figure 4.6 Aerodynamic thrust and torque on wind turbine for Case #1

Table 4.5 summarises the minimum and maximum thrust and torque, where thrust and power coefficients are also listed. It is shown that the variance for the thrust is in the range of [-9.56%, +8.36%] while the torque experiences a large variation from -15.11% to +14.23%. It is expected that when the FOWT system works under rough environmental conditions, these time variations of thrust and torque will be certainly profound, leading to a subsequent variable power output by the wind turbine.

Table 4.5 Aerodynamic performance of FOWT under different working conditions (data in parentheses shows thrust coefficient C_T and power coefficient C_P)

	Thrust (kN)			Torque (MN*m)		
	Case #1	Case #2	Tran (2016)	Case #1	Case #2	Tran (2016)
Minimum	128.42 (0.32)	308.33 (0.34)	632 (0.7)	1.36 (0.24)	1.94 (0.24)	3.17 (0.4)
Maximum	153.87 (0.38)	398.54 (0.44)	721 (0.79)	1.83 (0.32)	2.88 (0.36)	4.25 (0.53)

It is also noted that there are a few local minima along the aerodynamic torque curve, which are highlighted as circular markers in Figure 4.6(b), i.e. at the time instants of around 328, 332 and 336 s. These sudden drops of torque, about 5% of the averaged torque, occur when three turbine blades pass in front of the tower in sequence, also known as tower shadow effects. This could be partially reinforced by the time interval of around 4s between two adjacent markers, i.e. one third of the turbine rotation period for a three-bladed turbine. It is therefore clear that Time = 328 s coincides with the instant time when Blade #1 passes in front of the tower, and Time = 332 s and 336 s are for Blades #2 and #3, respectively. The decrease in torque is equivalent to the loss in power as turbine power is defined as torque multiplied by rotational speed. These sudden decreases can also be identified from the aerodynamic thrust curve.

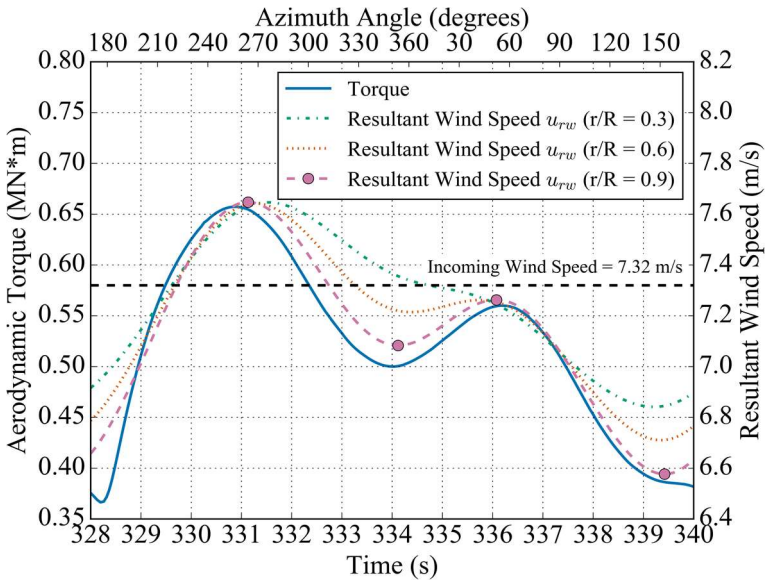

Figure 4.7 Aerodynamic thrust and torque on Blade #1 for Case #1

To better understand the tower shadow effects, we analyse the individual torque from a single blade, for example, Blade #1. Figure 4.7 shows the aerodynamic torque on Blade #1 with respect to both time and its azimuth angle (α), defined in Figure 4.8. Three turbine blades are numbered according to the order in which each blade passes in front of the tower starting from Time = 0 s. Since the turbine rotates clockwise, when viewing from the incoming wind direction, the initial azimuth angle (α) for Blade #1 is 150° while for Blade #2 and #3 it is 30° and 270° respectively. At about Time = 328 s, a dip of the turbine torque is seen from Figure 4.6(b), which is caused by the torque drop of Blade #1 when it is passing in front of the tower as is clearly indicated by its azimuth angle (α) of 180 degrees in Figure 4.7. Similarly, for the other two time-instants at Time = 332 s and 336 s, the local descent of the overall turbine torque displayed in Figure 4.6(b) are induced by the tower shadow effects when Blades #2 and #3 are passing across the tower.

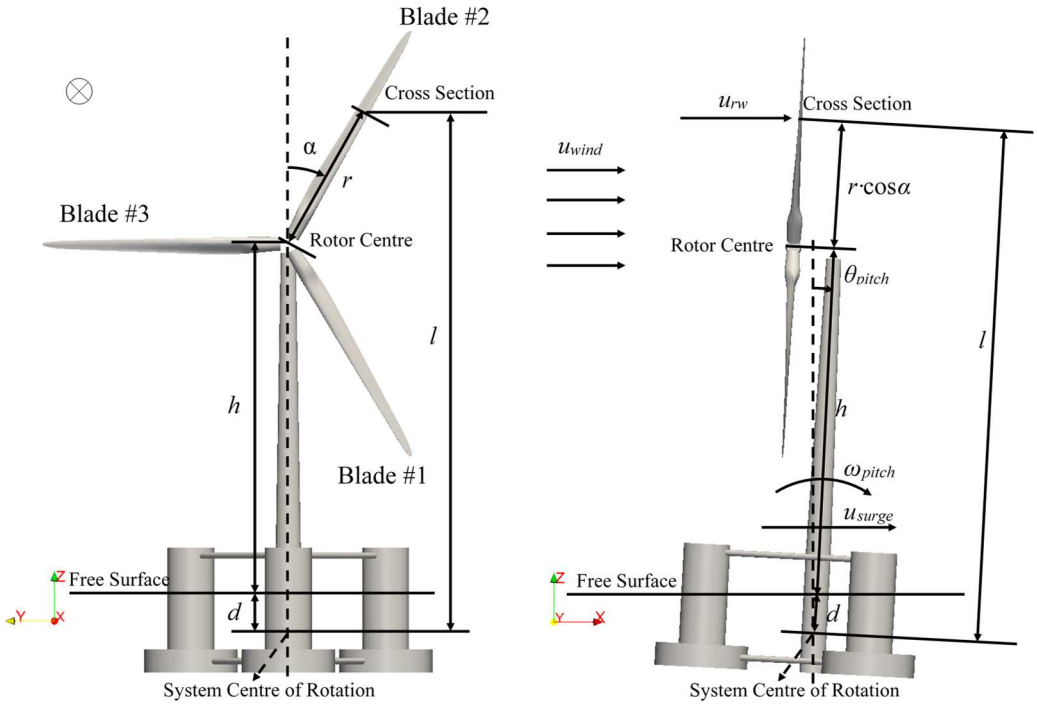

(a) YOZ plane *(b) XOZ plane*

Figure 4.8 Definition of azimuth angle and blade numbering (⊗ indicates wind direction)

Apart from the tower shadow effects, the variation of the aerodynamic torque is directly related to the movement of the floating platform. To better grasp the relationship between wind turbine torque and platform movement, the resultant wind speed component parallel to the wind direction, as defined in Eq. (4.1), is plotted at three cross sections of Blade #1 in Figure 4.7.

$$u_{rw} = u_{wind} - \left[u_{surge} + \omega_{pitch} \cdot \left(r \cdot \cos\alpha + h + d \right) \cdot \cos\theta_{pitch} \right] \tag{4.1}$$

where u_{wind} and u_{surge} are the incoming wind speed and the FOWT system surge velocity, separately; θ_{pitch} and ω_{pitch} are the system pitch angle and rotational velocity, respectively; α denotes the blade azimuth angle; r represents the distance from the blade cross section to the rotor centre while h and d are the height of the tower and the distance from the system centre of rotation to free surface as shown in Figure 4.8.

The cross sections are selected at 30%, 60% and 90% of the blade measuring from the hub centre, i.e. r/R = 0.3, 0.6 and 0.9 in Figure 4.7. A strong correlation between the torque on Blade #1 and the resultant wind speed (u_{rw}) at its cross sections can be observed. Taking the curve at r/R = 0.9 as an example, we can see that the torque curve follows the same trend as the resultant speed, i.e. it initially increases with u_{rw} and then decreases. As the resultant wind speed determines the wind speed experienced by the blade undergoing the platform 3DoF motions, it is expected that large thrust and torque occur when the incoming wind speed is high, which partially explains the positive correlation between the time-history of blade torque and the resultant wind speed shown in Figure 4.7.

As the aerodynamic toque is the integral representation of pressure on the blade, we plot the pressure coefficient distribution along the blade at three cross sections in Figure 4.9, at two typical time instants (i.e. Time = 331 s and 339.5 s), when the blade torque reaches its maximum and minimum respectively in Figure 4.7. As expected, at Time=331 s, the pressure difference between the pressure and suction surfaces is larger than that at Time = 339.5 s, resulting in the maximum torque. This is in accordance with the discussion we presented in the above section.

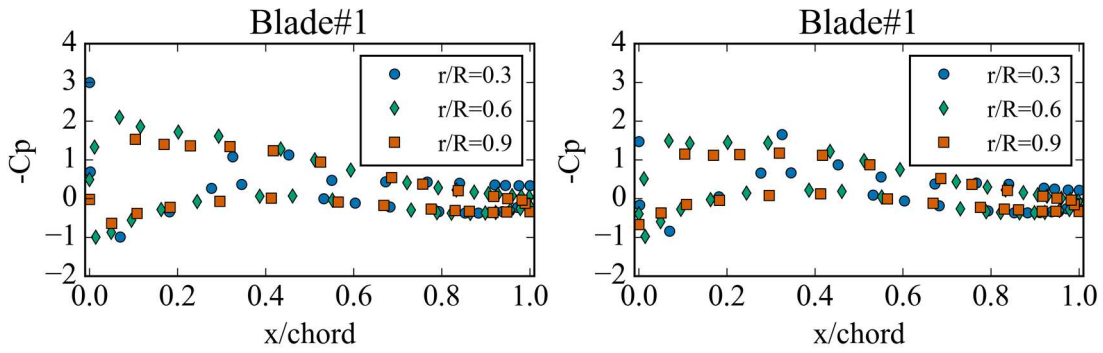

(a) Time = 331 s *(b) Time = 339.5 s*

Figure 4.9 Pressure coefficient distribution for three cross sections of Blade #1 at different time ('-' represents the negative sign)

To discuss the potential variation of turbine performance under different operating conditions such as incoming wind speed and turbine rotational velocity, we extend our above study to Case #2. Figure 4.10 presents the aerodynamic thrust and torque for Case #2 at a higher wind speed and turbine rotation speed than Case #1. As compared to Figure 4.6, where the relevant curves are shown for Case #1, the aerodynamic torque varies more in Case #2, indicated by the occurrences of local minima at a regular time interval, due to a higher frequency of the blades passing across the tower in one wave period for Case #2. A comparison is made for the minimum and maximum thrust and torque between Cases #1 and #2 in Table 4.5. The difference between the two extrema is larger for Case #2 than for Case #1.

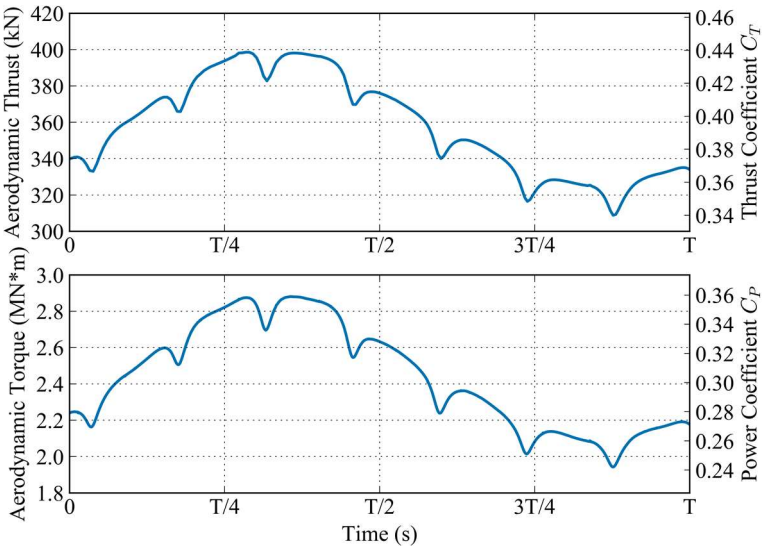

Figure 4.10 Aerodynamic thrust and torque on FOWT for Case #2: T – wave period

Table 4.6 Comparison between model test data and present results for a fixed wind turbine under various environmental conditions

		Mean wind speed (m/s)	Rotor speed (RPM)	Thrust (kN)
Model Test data (Coulling et al., 2013)		7.32	4.95	126.1
		11.23	7.78	202.7
		16.11	9.19	381.7
Present	Case #1	7.32	4.95	142.0
	Case #2	11	11.89	353

To compare the results of the only two CFD studies so far on this FOWT problem, data from Tran and Kim (2016b) is also listed in Table 4.5, where the same environmental condition denoted as Case #2 was applied. It can be seen that although the difference between the minima and maxima is very similar for two simulations, both our predicted thrust and torque are smaller than the data provided by Tran and Kim (2016b). This is likely due to the different turbine configurations used in these two studies. Although the same NREL 5-MW turbine geometry is adopted in both studies, turbine parameters are adjusted. The present study utilises the gross properties from MARIN's model test (Coulling et al., 2013), while Tran and Kim (2016b) adopted NREL's definition (Jonkman et al., 2009). In particular, the shaft tilt angle and pre-cone angle of the turbine are different as are listed in Table 4.1. In addition, a collective blade pitch angle of 6.4° is applied in this work as was used in MARIN's model test. However, this value is set to zero in the simulations carried out by Tran and Kim (2016b). Previous CFD study by Zhao et al. (2014) with an identical NREL 5-MW wind turbine geometry using an OpenFOAM solver revealed that increasing blade pitch angle at high wind speed conditions could significantly decrease turbine thrust by as much as 50%. Although the present wind speed was not modelled by Zhao et al. (2014), the effects of blade pitch angle on turbine aerodynamic thrust and torque were clearly demonstrated, thus providing sufficient evidences that large discrepancy for thrust and torque between ours and Tran and Kim (2016b) could be attributed to different setting of the above mentioned angles. It is also worth mentioning that the appearance of small thrust and torque can be partially manifested by the model test data in Table 4.6, where mean thrust from the model tests and the present simulations

is summarised with a fixed turbine at various environmental conditions. Although the condition for Case #2 was not experimentally tested, comparison among other similar conditions indicates that the present numerical modelling results are sensible.

Figure 4.11 demonstrates the vortex contour of the second invariant of the rate of strain tensor Q (Li et al., 2012) coloured by velocity component Ux for Case #1 within one wave cycle, where the free surface is coloured by surface elevation. As can be clearly seen from these figures, strong vortices appear in the vicinity of blade tips and roots. The presence of the tower also results in a complex flow wake behind the tower. Such detailed flow map and its relation to Fluid-Structure-Interaction (blade and tower) is useful to identify potential means for improving turbine power output at its design stage, which is currently not possible to achieve using engineering tools like FAST.

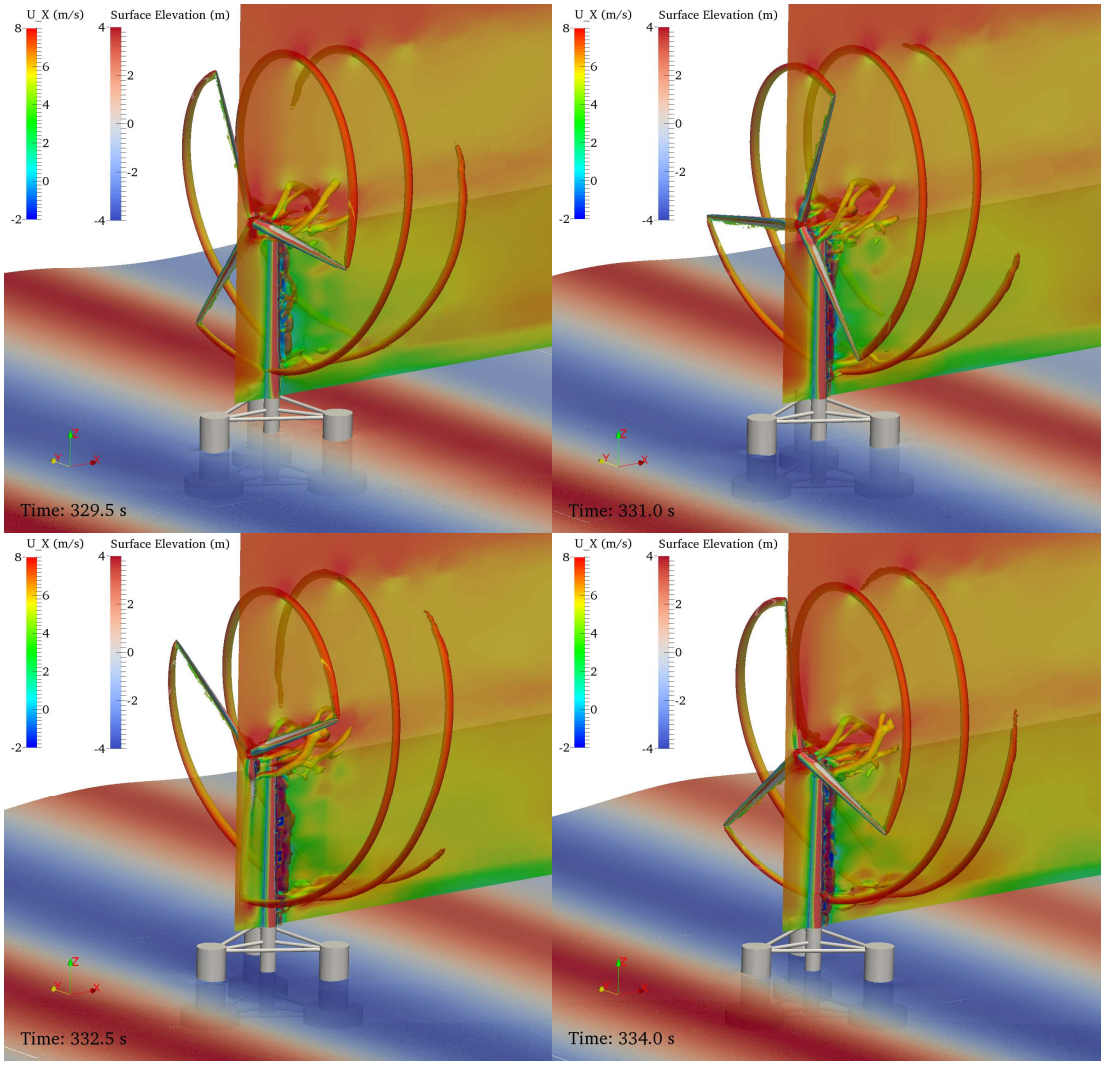

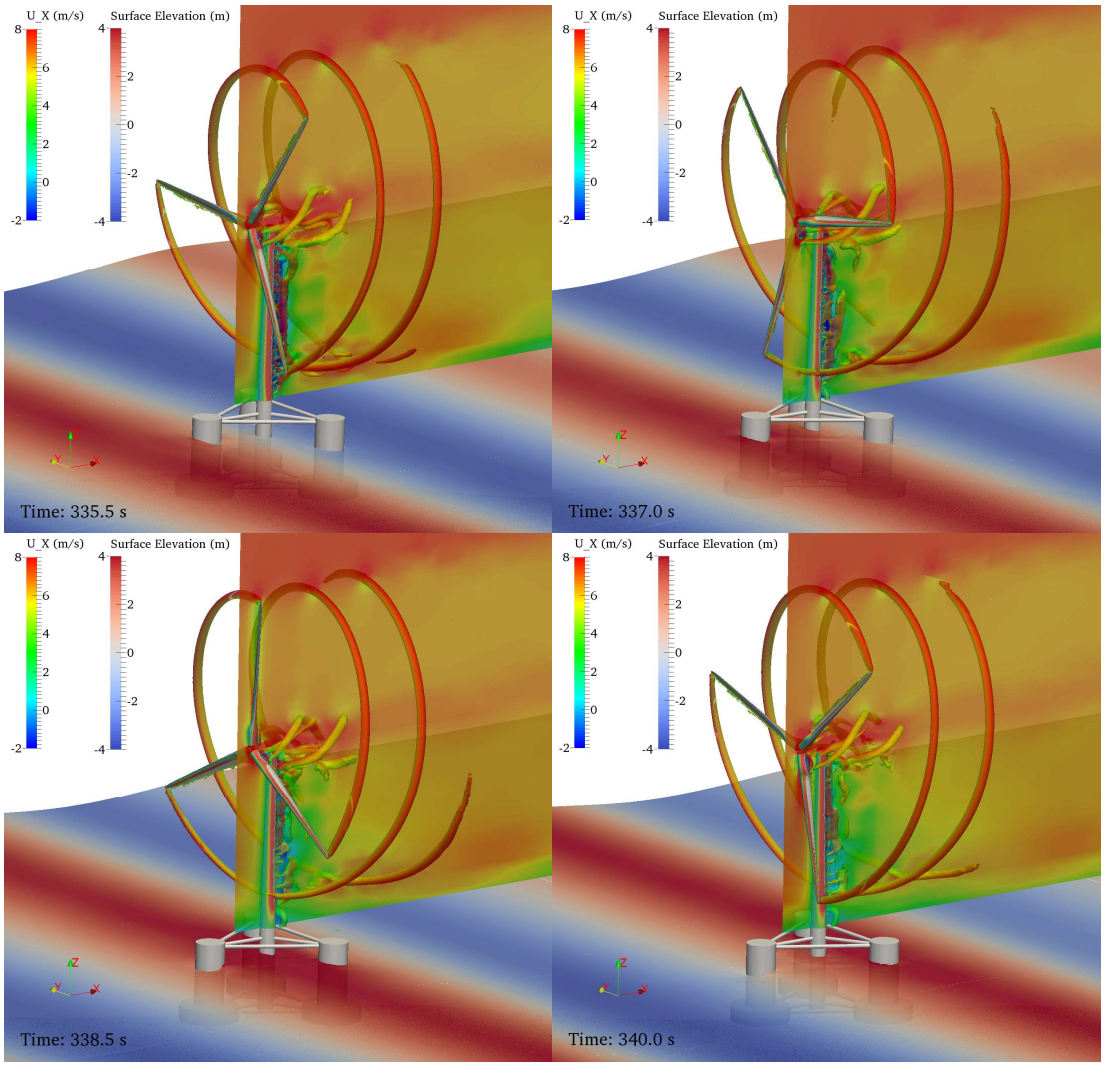

Figure 4.11 Vortex contour (Q = 0.25) coloured by velocity component Ux and free surface coloured by surface elevation for Case #1 over one wave period

4.2.3 Effects of Wind Turbine on Floating Platform Hydrodynamic Responses

In this section, the impacts of the wind turbine on the platform are studied by comparing its motion responses under different working conditions, i.e. with/without a wind turbine under operation and with different wind velocity and turbine rotation speed as listed in Table 4.4.

Time history curves for the surge, heave and pitch motion responses of the floating platform under the combined regular waves and steady wind are plotted in Figure 4.12 for both Case #1 and #2. Compared to Figure 3.17, where only the floating platform in regular waves is present as studied in Section 3.3.3, some discrepancies can be

observed. A comparison is made in terms of the motion RAOs as well as the time-averaged values over the last four wave periods for the three degrees of freedom and listed in Table 4.7, together with the data from Tran and Kim (2016b). It has to be mentioned that because of the unavailability of MARIN test data for the wind and wave conditions simulated herein, the comparison is only made with the work from Tran and Kim (2016b).

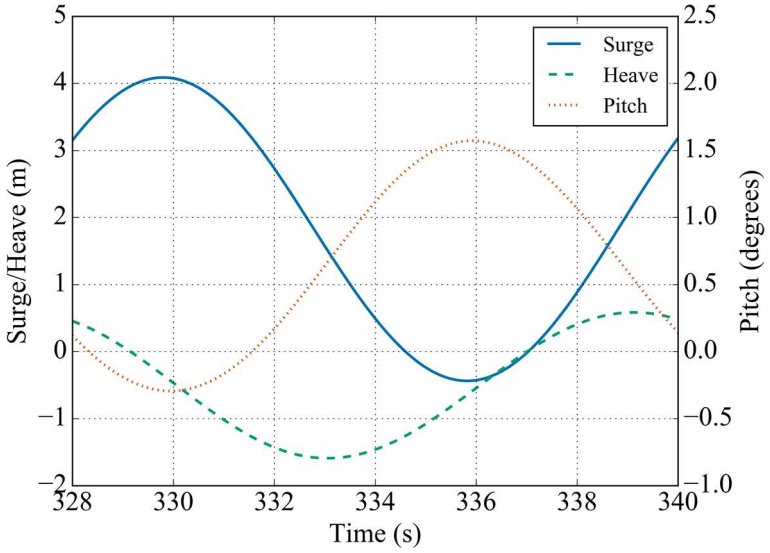

(a) Case #1

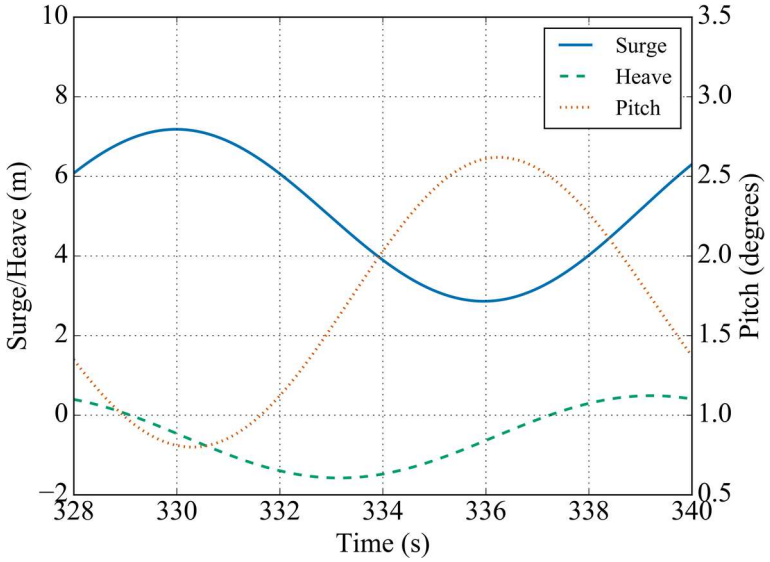

(b) Case #2

Figure 4.12 Time history curves for the motion responses of the floating platform under combined regular waves and steady wind

Table 4.7 Comparison for RAO and mean values of the floating system motion responses under different working conditions (percentage in parentheses shows the difference over data under wave only condition)

	RAO (m/m, m/m, °/m)				Mean value (m, m, °)			
	Wave only	Case #1	Case #2	Tran (2016)	Wave only	Case#1	Case #2	Tran (2016)
Surge	0.5965	0.6051 (+1.44%)	0.5947 (-0.30%)	0.5937	0.8686	1.8619	5.0866	9.62
Heave	0.2820	0.2876 (+1.99%)	0.2739 (-2.87%)	0.2850	-0.4538	-0.5030	-0.5391	-0.26
Pitch	0.2470	0.2496 (+1.05%)	0.2424 (-1.86%)	0.2995	0.0156	0.6416	1.7022	3.24

It is easily seen that the RAOs for all three motion responses do not change very much in the present study, with a variation of less than 3%, when the turbine operates at a constant rotation speed in a steady wind speed condition. The surge and heave RAOs from Tran and Kim (2016b) also agree well with our results, with the only exception of the pitch RAO, where the deviation from the no-wind condition is as large as 21%. As is pointed out in Section 4.2.2, this might be attributed to the different gross properties of the FOWT used in both studies, such as the turbine mass and platform pitch inertia indicated in Table 4.1. Nevertheless, the very close agreement for the predicted surge and heave RAOs between two different tools demonstrates again the good capability of our CFD tool developed for the study of the hydrodynamics of an FOWT.

Figure 4.13 illustrates both the hydrodynamic and aerodynamic loading in the wave propagation direction acting on the floating system for Case #1. Compared to the large variation of the hydrodynamic force at a magnitude order of 10 MN, the aerodynamic force merely changes by about 30 KN as already indicated in Figure 4.6 and acts almost like a constant loading, which partially explains why the surge RAO is not affected significantly by the operating wind turbine. The barely noticeable change for the RAO of other two motion responses can be justified in a similar manner. It is also worth mentioning that although a wind turbine can exert aerodynamic damping upon

its supporting platform (Coulling et al., 2013), the additional damping is generally small for the studied cases with relatively small wind speed and large wave height. As a result, the effects of aerodynamic damping on platform motion RAO are negligible.

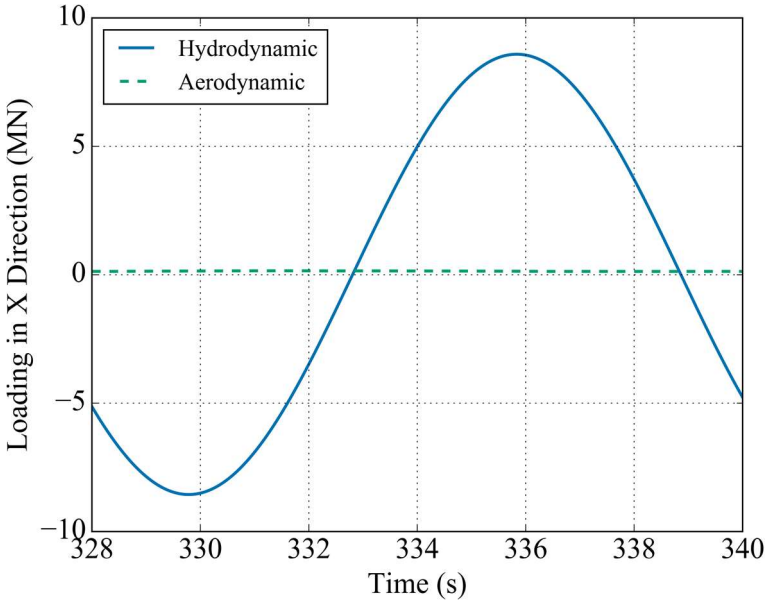

Figure 4.13 Comparison between hydrodynamic and aerodynamic loading on the floating system for Case #1

In contrast to the above motion RAOs, the mean motion responses are remarkably affected by the presence of an operating wind turbine. It is shown from Table 4.7 that the mean surge increases greatly from 0.8686 m under the wave only condition, to 1.8619 m for Case #1, and further to 5.0866 m for Case #2, where the wind speed and turbine rotation speed increase. The mean pitch of the platform shifts from near zero to 0.642 degrees for Case #1 and 1.7 degrees for Case #2. Obviously, the aerodynamic thrust induced by the operating turbine, pushes the platform further away in the downwind direction thus leads to an increase in the mean surge.

Meanwhile, the pitching moment resulting from the thrust, due to the large distance from the turbine rotation centre to the system mass centre, which is about 100 m, generates a non-zero mean pitch angle. Since the aerodynamic thrust for Case #2 is larger than Case #1, the time-averaged surge and pitch are also more significant. An even larger thrust obtained from the work of Tran and Kim (2016b) yields the maximum surge and pitch motions among all the cases shown in Table 4.7.

As to the heave motion, the mean value also changes, although to a relatively less degree than the other two motion responses. The downward movement is possibly attributed to the positive mean pitch angle, which alters the attitude of the floating platform. The mean heave response deviation obtained by Tran and Kim (2016b) is also not to be neglected as it varies from zero to -0.26 m possibly due to the larger mean pitch angle.

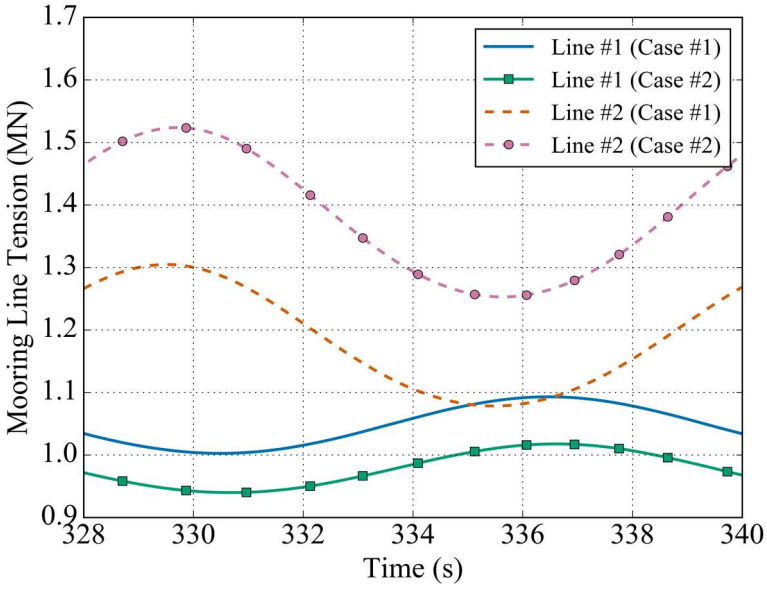

Figure 4.14 Mooring line tension for lines #1 and #2 of the floating platform under combined regular waves and steady wind

In order to illustrate the influence of the wind turbine on the mooring system of the floating platform, the mooring line tension for lines #1 and #2 in both Cases #1 and #2 is plotted in Figure 4.14. The RAO, mean and maximum of the line tensions for mooring line #2 are summarised in Table 4.8 for all working conditions, as well as the percentage differences over the corresponding data under the wave only condition. Mooring line #2 in the head wave direction is selected for analysis as it consistently experiences larger tension than mooring line #1 in the back wave direction. Due to an increased surge response caused by the additional aerodynamic thrust, the line tension increases when the wind turbine operates in steady wind. For Case #2, the maximum line tension increases by 17.9% and the mean line tension by 16.75% as compared to the case under the wave only condition. It is noted that, in the work of Tran and Kim (2016b), such increments are even more profound. The line tension RAO also becomes

larger when the aerodynamic thrust is added to the system, which is different from the platform motion RAO. The increase in the line tension RAO was also observed in the results provided by Tran and Kim (2016b), where this value was about 28.342 kN/m under the wave only condition but rises significantly to 74.142 kN/m under the specified combined wind-wave condition. As pointed out by Hall and Goupee (2015), the increase in the mooring line tension RAO was related to the nonlinear force-displacement relationship of the mooring lines as shown in Figure 3.15.

Table 4.8 Comparison for tension of line #2 under different working conditions (percentage in parentheses shows difference over data under wave only condition)

	Wave only	Case #1	Case #2	Tran (2016)
RAO (kN/m)	27.546	30.324 (+10.08%)	37.509 (+23.69%)	74.142
Mean value (MN)	1.146	1.194 (+4.19%)	1.394 (+16.75%)	2.134
Maximum value (MN)	1.251	1.313 (+4.96%)	1.548 (+17.90%)	2.415

4.3 Concluding Remarks

In this chapter, the OC4 DeepCWind semi-submersible FOWT is investigated with the developed tool under combined environmental conditions of regular waves and uniform wind. Wind turbine blades are assumed to be rigid and a quasi-static mooring line analysis method is adopted to solve its mooring system. Two operating conditions with same wave parameters but different wind speed and turbine rotation speed are simulated. Interactions between the floating platform and the wind turbine are studied by comparing and analysing numerical results between coupled simulations and wind/wave only cases.

Impacts of the floating platform on wind turbine aerodynamics are firstly examined by comparing wind turbine aerodynamic thrust and torque between floating and fixed-bottom turbine simulations. Compared to nearly constant turbine aerodynamics under the fixed-bottom condition, motion responses of the supporting platform result in variation of turbine thrust in the range of [-9.56%, +8.36%] and oscillation of turbine

torque from -15.11% to +14.23% for Case #1. For Case #2 with higher wind speed and turbine rotation speed than Case #1, oscillation amplitudes of wind turbine aerodynamic thrust and torque increase accordingly. In particular, the platform responses in surge and pitch impel the wind turbine to interact with incoming wind, and the vortices in the downstream of turbine, which leads to the variation of its aerodynamic thrust and torque. In order to further understand the relationship between turbine aerodynamics and platform motion responses, a resultant wind speed is defined by subtracting velocities induced by platform surge and pitch motion from incoming wind speed to represent the wind speed experienced by a turbine blade. As the wind turbine constantly rotates around its rotation axis which is different from the pitching axis of the floating system, the resultant wind speed varies both temporally and spatially at different spanwise locations of a blade. By examining time history data of the resultant wind speed at spanwise sections of 30%, 60% and 90% of blade length, aerodynamic thrust and torque are found to positively relate to the resultant wind speed, which is further corroborated by comparing the distribution of pressure coefficients along the three blade sections between different time instants. Sudden drops of wind turbine aerodynamic thrust and torque due to blades passing in front of the turbine tower, known as tower shadow effects, are also noted in our simulation results. Visualisation of flow field around the FOWT clearly reveals strong vortices generated near blade root and tip regions as well as the influence of the tower on wind turbine wake. The CFD tool developed in this work provides a great opportunity to examine in detail interactions between wind/wave and an FOWT, aerodynamic loading distribution around the wind turbine blades as well as the vortex wake structure in the downstream of turbine, which cannot be obtained from engineering models.

Effects of the wind turbine on the floating semi-submersible platform and its mooring system are also investigated. By comparing motion responses of the floating platform, i.e. surge, heave and pitch, under the combined wind/wave conditions to data of the wave only case studied in Section 3.3.3 as well as results from another coupled CFD simulation by Tran and Kim (2016b), it is found that under environmental conditions studied in this work motion RAOs for all three DoFs are hardly affected by the rotation of the wind turbine in wind. Comparison between time history data of hydrodynamic

and aerodynamic loadings exerted upon the platform reveals that the oscillation in the latter is so small compared to the variation of the former that the aerodynamic loading can be treated as a constant force in the present study, which explains the negligible changes in motion RAOs. However, the mean motion responses, particularly surge and pitch, are greatly affected by the wind turbine. The mean value for surge increases as the aerodynamic thrust produced by the turbine pushes the platform in the downwind direction. Meanwhile, due to the large distance (exceeding 100 m) between the turbine rotation centre and the system mass centre, the substantial pitching moment from the turbine thrust results in a positive equilibrium angle for the platform pitch motion. The mean heave position also moves downward possibly as a result of the change in the attitude of the platform associated with the positive mean pitch angle. As responses of the mooring system is largely determined by the platform surge motion, the mooring line tension force increases when the mean surge motion becomes larger. Nevertheless, in contrast to motion RAOs, it is found that mooring line tension RAOs increase with the aerodynamic thrust of the wind turbine, which can be explained by the nonlinear relationship between the restoring force provided by mooring lines and the platform surge motion.

Chapter 5 Aeroelastic Analysis of an Offshore Wind Turbine in Platform-Induced Surge Motion

In this chapter, an aeroelastic analysis is carried out for the NREL 5-MW offshore wind turbine with flexible blades using the coupled CFD-MBD method. This study serves as the second stage to achieve the goal described in Section 1.3. The floating platform supporting the wind turbine is not explicitly modelled as in Chapter 4 for simplification. Instead, its impacts are taken into consideration in a prescribed manner by imposing motion responses determined from other simulations to the wind turbine base. Specifically, two simulation conditions are studied: fixed-bottom and prescribed platform surge motion. Descriptions about the CFD and structural models are firstly provided in Section 5.1. Effects of blade flexibility and platform surge motion on wind turbine aerodynamics and structural responses are then investigated in Section 5.2.

5.1 Model Description

The NREL 5-MW baseline offshore wind turbine previously studied in Section 4.2.1 is analysed in this work, which is a conventional three-bladed upwind wind turbine with a rotor diameter of 126 meters. Figure 5.1 shows the geometry of the wind turbine subject to deformation. This model is selected because it is specifically designed for offshore applications and has been widely used as benchmark by the researchers in the offshore wind energy field. Detailed information about the wind turbine geometry and structural properties can be found in the report (Jonkman et al., 2009) published by NREL. It should be pointed out that although most properties adopted in this study are the same as those provided in the NREL report, some modifications are made to simplify our CFD modelling. Firstly, only the turbine blades are modelled while the tower, nacelle and hub are ignored, as can be seen in Figure 5.1. In addition, the shaft tilt angle is set to zero while the pre-cone angle is kept as 2.5°. These settings are also applied to simulations performed with the engineering tool FAST v8 so that results from the present tool and those predicted by FAST v8 can be compared and analysed.

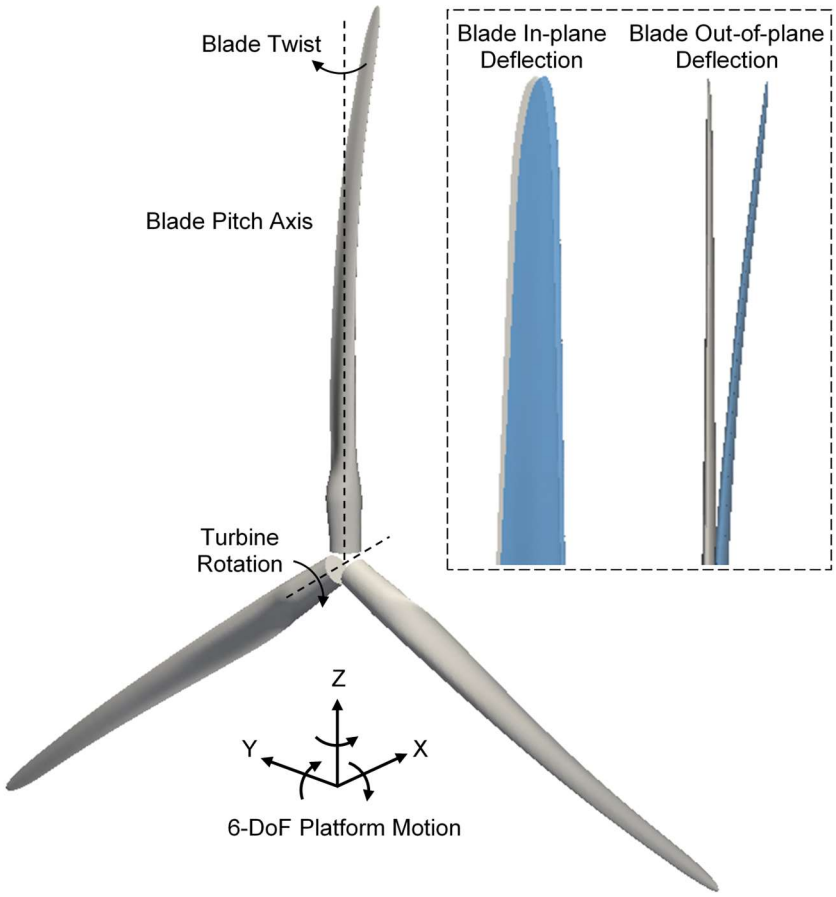

Figure 5.1 Illustration of complex structural responses involved in present simulations with flexible blades (light grey region shows un-deflected blade while light blue region shows deflected blade)

5.1.1 CFD Model

Figure 5.2 illustrates the dimensions of the computational domain and the boundary conditions applied in our CFD simulation for the above wind turbine model. The whole domain extends in three dimensions, i.e. $-5D \le x \le 10D$, $-5D \le y \le 5D$ and $-5D \le z \le 5D$, where D is the diameter of turbine rotor. The turbine is located at the origin of the coordinate system to minimise the influence of the boundaries. Constant wind speed in x direction is imposed for flow velocity at the Inlet boundary while zero pressure is applied at the Outlet boundary. The Neumann boundary condition is assumed for both velocity and pressure at all the four Farfield boundaries, and a moving wall boundary condition is applied to the turbine blades to impose the non-slip wall boundary condition on the rotating blades.

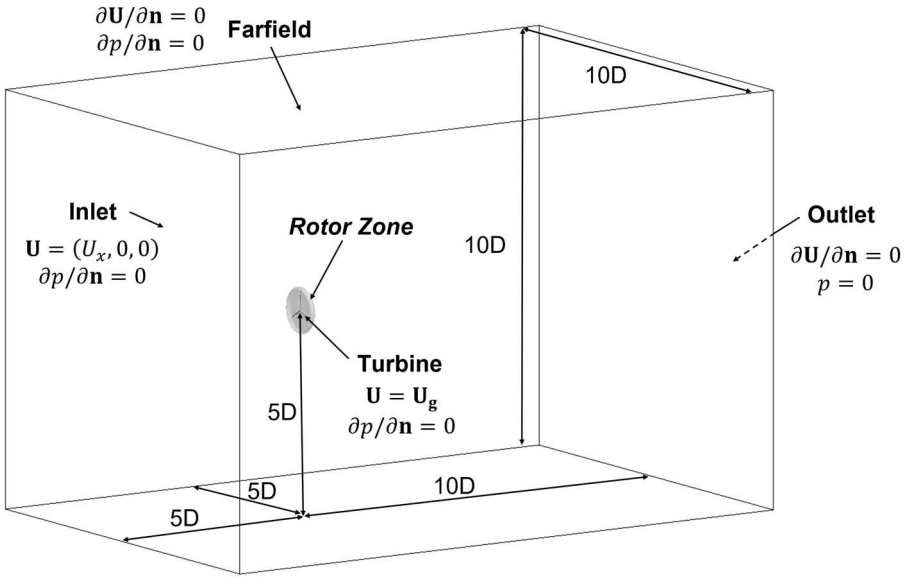

Figure 5.2 Dimensions and boundary conditions for NREL 5-MW offshore wind turbine simulations

A grey region is highlighted in Figure 5.2 as the rotor cell zone. The cell zone encompasses the wind turbine blades and rotates along with the turbine in accordance with the specified rotation speed while the outer grid remains static during turbine simulations. The rotation region connects with the outer region through a pair of AMI patches. For flexible turbine blade simulations, dynamic mesh motion due to blade deformation should be applied within the rotor cell zone as discussed in Section 2.3.2. Settings of mesh density used in Section 4.2.1 are adopted for consistency.

Table 5.1 Specifications for various working conditions used in benchmark tests for NREL 5-MW wind turbine

Wind Speed U (m/s)	Rotor Speed (RPM)	Blade Pitch Angle (degrees)
8	9	0
11.4	12.1	0
15	12.1	10.45
20	12.1	17.47
25	12.1	23.47

Simulations for a fixed-bottom NREL 5-MW wind turbine with rigid blades under a series of working conditions listed in Table 5.1 are conducted as benchmark tests. For

every case, the unsteady flow solver pimpleDyMFoam is adopted together with the sliding mesh or AMI technique. To speed up the computation, the built-in steady-state solver simpleFoam with the Multiple Reference Frame (MRF) functionality in OpenFOAM is firstly utilised until converged results are obtained. Subsequently, steady-state results are employed to serve as the initial conditions for unsteady simulations to skip the start-up stage and thus save computational time.

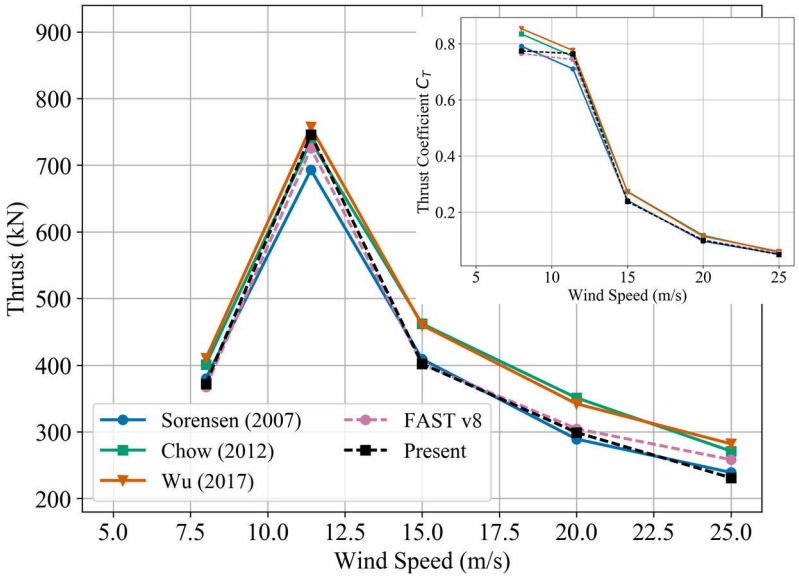

(a) Thrust

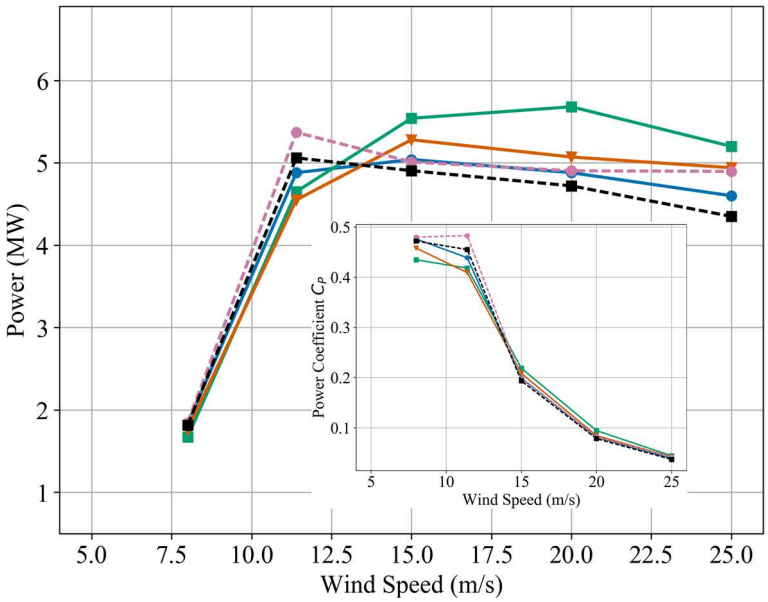

(b) Power

Figure 5.3 Aerodynamics of benchmark tests for NREL 5-MW wind turbine

Figure 5.3 shows the wind turbine thrust and power under various working conditions and the present results are generally in good agreement with other published data from previous CFD simulations (Sørensen and Johansen, 2007; Chow and van Dam, 2012; Wu and Nguyen, 2017) as well as the well-known offshore wind turbine analysis package FAST v8 (NREL, 2016), indicating that the flow solver in the present analysis tool is capable of predicting wind turbine aerodynamics under various working conditions.

5.1.2 Structural Model

The structural model used in MBDyn for one blade of the NREL 5-MW offshore wind turbine model is illustrated in Figure 5.4. All structural properties used in this study, e.g. inertia and sectional stiffness, are extracted from the NREL report (Jonkman et al., 2009). Twenty-five 3-node beam elements, i.e. 49 geometrical nodes in total, are used to represent one blade in MBDyn. These nodes are unevenly distributed along the blade. Specifically, more nodes are clustered towards the blade root and tip as the geometrical shape and structural properties in the vicinity of these regions varies more rapidly than other parts. Although not considered in the CFD model, the turbine hub is treated as a rigid body and is thus represented by only one node. A separate static node or ground node is also used as a fixed reference point for other nodes. For the three-bladed turbine, the total number of geometrical nodes reaches 149.

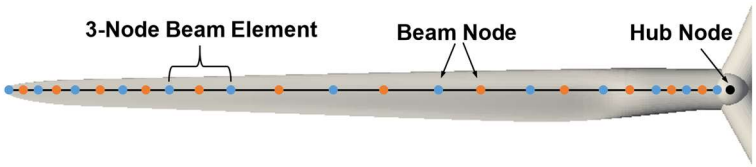

Figure 5.4 Structural model of NREL 5-MW wind turbine

The hub node is forced to rotate relative to the static ground node along the rotation axis at a specified turbine rotation speed using an axial rotation joint. The node at the blade root and the hub node are then clamped together with both a spherical hinge constraint and a prismatic constraint, i.e. no relative translational and rotational motion between the two nodes are allowed, so that the blade root node moves along with the

hub node when the latter rotates. Subsequently, all other blade nodes also rotate due to the restraint imposed by the beam elements these nodes are associated with.

The structural model is validated against the nonlinear structural solver BeamDyn newly introduced in FAST v8. In both models, aerodynamic loading is not considered and only a concentrated loading of 100 kN is applied at the blade tip node in the flapwise direction. Figure 5.5 compares the blade deflection in both flapwise and edgewise directions predicted by both MBDyn and BeamDyn. Good agreement between the results indicates that the current structural model set up in MBDyn can be used to calculate the structural response of the NREL 5-MW wind turbine.

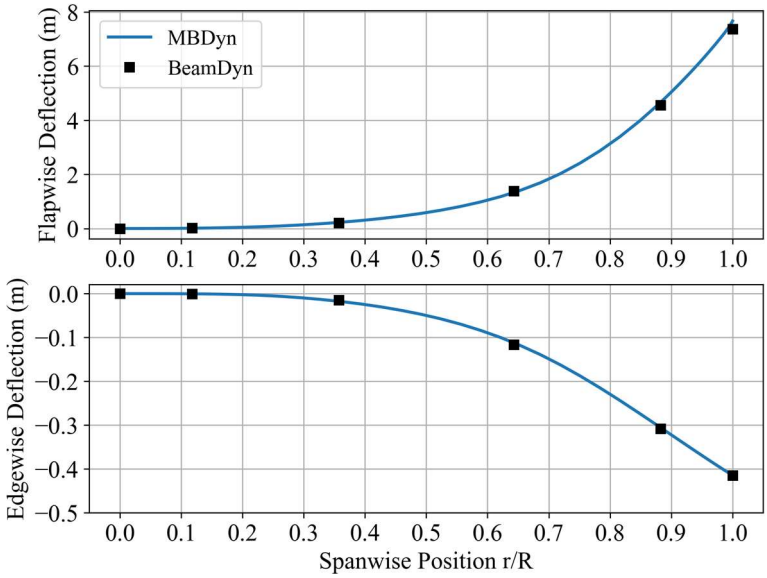

Figure 5.5 Blade deflection under single concentrated loading of 100 kN at tip in flapwise direction

5.1.3 Simulation Cases

Two simulation cases with different conditions are set up as summarised in Table 5.2. The turbine base in Case #1 is fixed to represent a fixed-bottom wind turbine installed nearshore in shallow water. A sinusoidal translational motion parallel to the wind direction is imposed upon the turbine base for Case #2. This is designed to analyse the influence of platform surge motion associated with a floating offshore wind turbine scenario. In reality, the supporting floating platform has six degrees-of-freedom motions. However, focusing on pure surge motion in the study makes it easy to

examine all flow and force field details, thus provide more insights as compared to a more complicated six DoF case. The amplitude of the oscillating surge motion is 2 m with a time period of 12 s. Figure 5.6 shows the surge displacement and velocity over one cycle. The motion parameters are extracted from the work of Wu et al. (2015). Therefore, a subsequent qualitative comparison between the present study and that from Wu et al. (2015), using different numerical tools, will be possible. The specific platform motion data represents the general surge response of a semisubmersible floating offshore wind turbine in typical sea states according to experimental data from Coulling et al. (2013).

Table 5.2 Specifications for simulation cases

Case	Platform Motion	Wind Speed	Rotor Speed
1	Fixed	11.4 m/s	12.1 RPM
2	Surge: Amplitude = 2 m, Period = 12 s		

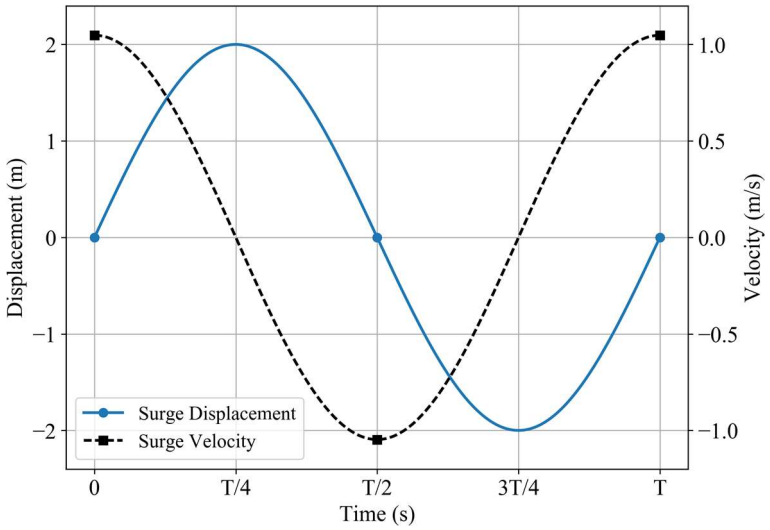

Figure 5.6 Prescribed platform surge displacement and velocity over one period

As to the wind conditions under consideration, the rated working condition for the NREL 5-MW wind turbine is selected, where the wind speed and rotor speed are 11.4 m/s and 12.1 RPM, respectively. Under such flow condition, the aerodynamic thrust applied on the turbine reaches its maximum as indicated in Figure 5.3, and the difference among various test cases can be best illustrated.

For all cases, simulations with both rigid and flexible turbine blades are carried out to investigate the effects of blade flexibility. To speed up simulations for flexible turbine and minimise CFD mesh distortion due to the local blade deformation, the aeroelastic turbine blades are pre-bent to an approximate deformed shape, as displayed in Figure 5.1. This is achieved by firstly running a steady-state CFD simulation for a rigid turbine case. The fluid force exerted upon each section of the blade surface is then extracted and subsequently applied to the corresponding geometrical nodes in MBDyn. The blade starts to deform until the external fluid force and the internal structural force are balanced. The deformed blade geometry is then used to generate a new CFD grid for flexible turbine simulations.

5.2 Results and Discussion

In this section, numerical results obtained from aeroelastic analysis of the NREL 5-MW wind turbine using the developed tool are presented and discussed, focusing on effects of blade flexibility on wind turbine aerodynamic performance and impacts of prescribed platform surge motion on aerodynamics and structural responses of the wind turbine.

5.2.1 Effects of Blade Flexibility

In this section, the influence of blade flexibility is investigated by setting up one rigid turbine case and another with flexible turbine blades under the Case #1 condition where the turbine base is fixed. Both simulations are run for a few turbine rotations using a transient solver pimpleDyMFoam until the aerodynamic loading acting upon the turbine varies within 0.1% over one complete rotation period. A quasi-steady state is then assumed to have been achieved and the time-averaged data over the last full cycle is extracted for analysis.

Table 5.3 summarises the predicted aerodynamic thrust and power of wind turbine using the present coupled CFD-MBD tool. It is shown in Table 5.3 that the thrust associated with the flexible turbine blades decreases by 1.7% compared to the data from the rigid case, and the power is smaller by 3.1%. The results calculated using the engineering tool FAST v8 are also listed in Table 5.3 for comparison. It should be

noted that the control module in FAST v8 is not activated throughout this study. The aerodynamic module AeroDyn v15 based on the BEM theory is employed for turbine aerodynamics, and the nonlinear structural solver BeamDyn introduced in FAST v8 is adopted for structural dynamics. As can be seen from Table 5.3, FAST v8 predicts a smaller thrust with a decrease of 3.3% for flexible blades compared to the rigid case, which is in good agreement with results from the present coupled tool. The power in the flexible turbine case predicted by FAST v8 is 3.9% smaller than in the rigid case, which is also consistent with the present results. In the case of fixed turbine base, the deformation of turbine blades results in reduced aerodynamic thrust and power, which was also pointed out by Yu and Kwon (2014).

Table 5.3 Aerodynamic thrust and power for NREL 5MW wind turbine under fixed condition (percentage in parentheses shows the difference of flexible case over rigid case for OpenFOAM and FAST v8 simulations, respectively)

	Thrust (kN)	Power (MW)
Present Rigid	746	5.06
Present Flexible	733 (-1.7%)	4.9 (-3.1%)
FAST v8 Rigid	725	5.37
FAST v8 Flexible	701 (-3.3%)	5.16 (-3.9%)

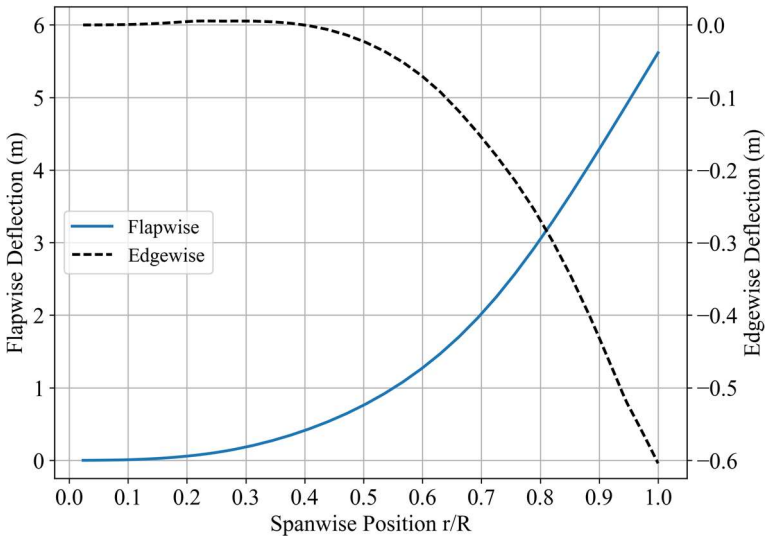

Figure 5.7 Spanwise distribution of blade deflection in flapwise and edgewise directions under fixed condition

Figure 5.7 illustrates the spanwise distribution of blade deflection in both flapwise and edgewise directions. The quantitative blade tip deflection is listed in Table 5.4. It is noted that, the present coupled CFD-MBD approach predicts a deflection of 5.6m or 8.89% of rotor radius (63m) in the flapwise direction, which is much larger than the deflection in the edgewise direction of about 0.6m or 0.95% of rotor radius. This can be attributed to a larger structural bending stiffness in edgewise than in flapwise direction according to the data provided by Jonkman et al. (2009). The edgewise deflection is defined along airfoil chord line, positive from the leading edge to its trailing edge. The negative sign in front of the edgewise deflection in Table 5.4 indicates that the aeroelastic blade deforms from the trailing edge towards the leading edge, induced by the aerodynamic torque which is in the same direction as the rotational motion. It is also noted that FAST v8 predicts fairly similar results to the present tool with the flapwise and edgewise deflections of 5.52m and 0.61m, respectively.

Table 5.4 Blade tip deflection for NREL 5MW wind turbine under fixed condition (percentage in parentheses shows the difference of prediction by FAST v8 over present results)

Solver	Present	FAST v8
Flapwise (m)	5.6	5.52 (-1.4%)
Flapwise/Radius (-)	8.89%	8.76%
Edgewise (m)	-0.6	-0.61 (+1.7%)
Edgewise/Radius (-)	-0.95%	-0.97%

The bending moment distribution in spanwise direction for the above case is displayed in Figure 5.8. It represents the internal structural moment at each section along the blade obtained from the structural stress-strain constitutive law. It is apparent that the bending moment is much larger in flapwise than in edgewise direction throughout the blade. At blade root, the flapwise bending moment increases to 10 MN*m, nearly 10 times of the edgewise bending moment, which further explains the significantly larger deflection in the flapwise direction than that in the edgewise direction.

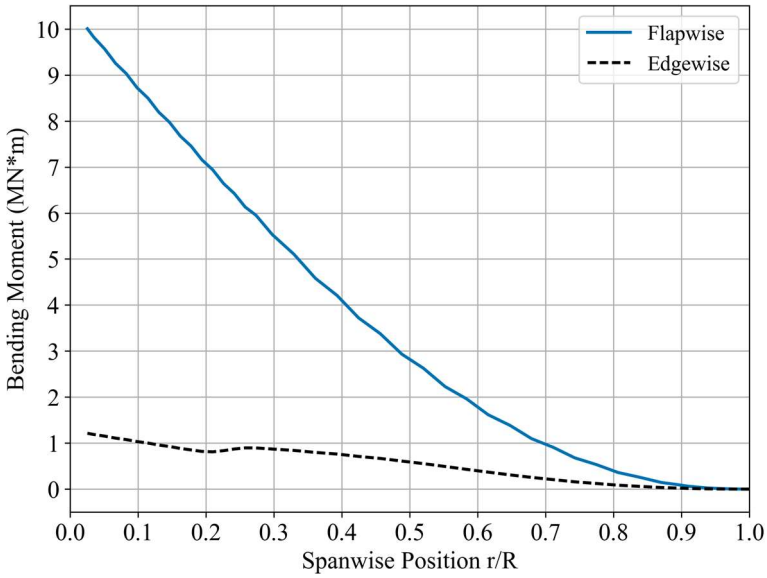

Figure 5.8 Spanwise distribution of blade bending moment in flapwise and edgewise directions under fixed condition

To better assess the influence of blade flexibility on turbine aerodynamics, the spanwise distribution of blade thrust and power for both rigid and flexible cases is displayed in Figure 5.9. It is shown that the general trend is the same for the two cases. However, there is a noticeable discrepancy around peak thrust region between 0.75R and 0.95R, near the blade tip. Particularly, a flexible blade has a smaller thrust than a rigid blade, which explains the decrease of overall turbine thrust. A similar trend can be observed for the spanwise distribution of power associated with a flexible blade.

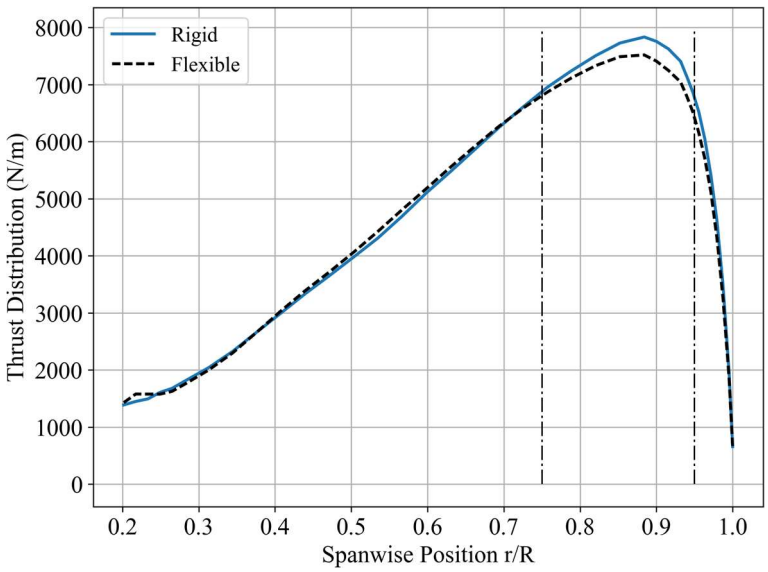

(a) Thrust

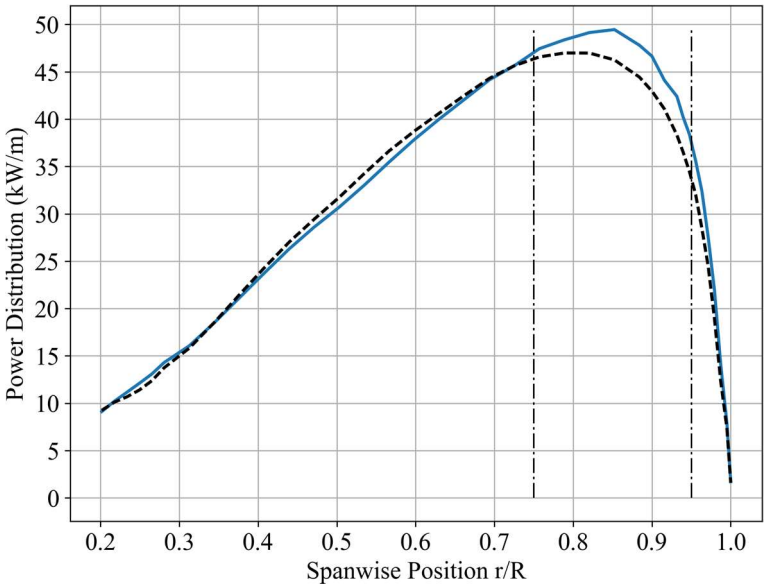

(b) Power

Figure 5.9 Spanwise distribution of blade aerodynamics under fixed condition

To further examine the underlying reasons behind the difference of blade aerodynamics between the two cases, the pressure distribution along the blade at a spanwise section of 0.9R, represented by the pressure coefficient Cp defined in Eq. (3.6), is plotted in Figure 5.10. Although the two curves closely resemble each other, a pressure drop near the leading edge on the suction side of airfoil is present, marked by a circle in the upper left corner of Figure 5.10.

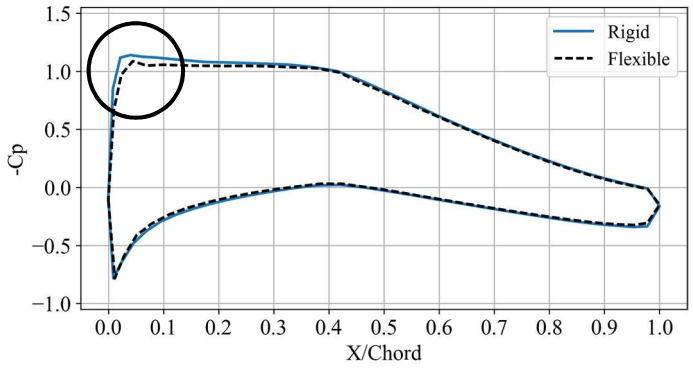

Figure 5.10 Pressure coefficient at spanwise section of r/R = 0.9

This could be associated with blade deformation in the flexible case, mainly the twist deflection shown in Figure 5.11. It should be pointed out that blade twist deflection, which results from the torsional loading acting on the blade, should not be mixed up with the aerodynamic twist, which is the design specification of a blade (Jonkman et

al., 2009). However, similar to aerodynamic twist, blade twist deflection affects the apparent or effective angle of attack (AOA) of an airfoil by altering its chord-line orientation as illustrated in Figure 5.12.

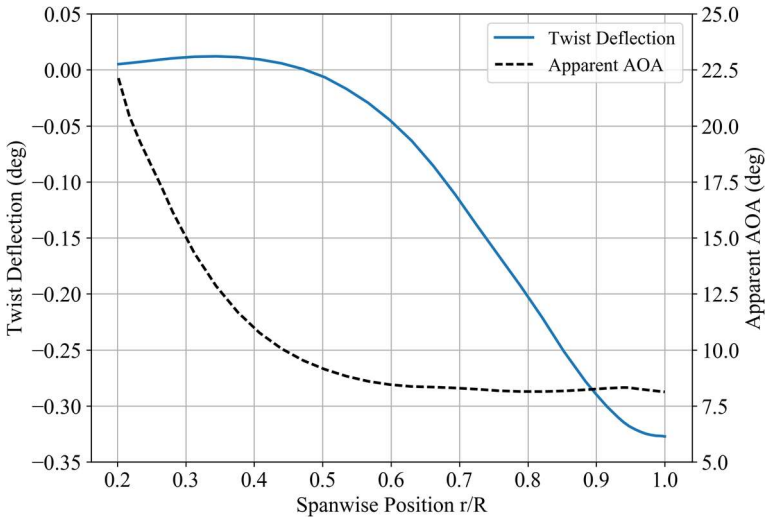

Figure 5.11 Spanwise distribution of blade twist deflection and apparent AOA

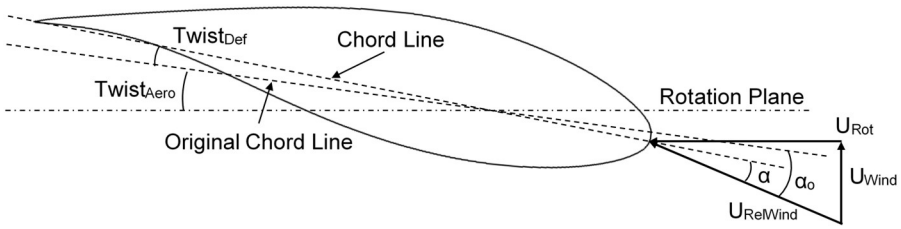

Figure 5.12 Definition of apparent AOA under fixed condition: $Twist_{Def}$ - twist deflection; $Twist_{Aero}$ - aerodynamic twist; $U_{RelWind}$ - relative wind speed; α - apparent AOA; α_o - AOA before twist deflection

It is worth noting that, the estimation of apparent AOA does not include the induced wind speed in axial and tangential directions in the incoming wind speed U_{Wind} due to the inherent challenges to quantitatively define induction factors as discussed previously in the work of Li et al. (2015c). Nonetheless, using this approach can still help understand the effects of blade flexibility in a qualitative manner. It is seen that, for a deformed blade, a negative twist deflection indicates a decrease in the apparent AOA (Yu and Kwon, 2014). Within the spanwise region from 0.75R to 0.95R, the geometrical shape of the blade section is NACA64 airfoil and the apparent AOA is around 8 degrees. As the stall angle for this shape is about 13.5 degrees according to

its aerodynamics data (Jonkman et al., 2009), a decrease in apparent AOA induced by the twist deflection leads to the reduction of the lift force and thus thrust and power.

5.2.2 Effects of Platform Surge Motion

In this section, the sinusoidal translational motion described in Section 5.1.3 as Case #2 is applied to the tested wind turbine for the investigation of platform surge motion impacts on the turbine. Both rigid and flexible blades are simulated, and each case runs for 60s, i.e. five platform motion cycles, using the transient solver pimpleDyMFoam until the variation of turbine aerodynamic loading reaches a periodic state. Data from the last platform motion cycle is then extracted for further analysis.

Time history data for the aerodynamic thrust and power of the wind turbine experiencing prescribed platform surge motion is plotted in Figure 5.13 along with FAST v8 results for comparison. Another CFD study performed for a rigid turbine by Wu et al. (2015) is also included in the plot. It is shown from Figure 5.13 that both thrust and power vary significantly with respect to time once platform surge motion is superimposed. For example, the power predicted by the present tool for the flexible case ranges from 3.85 MW to 6.21 MW, i.e. a variation of more than 20% compared to a fixed turbine base. All other curves exhibit a similar trend.

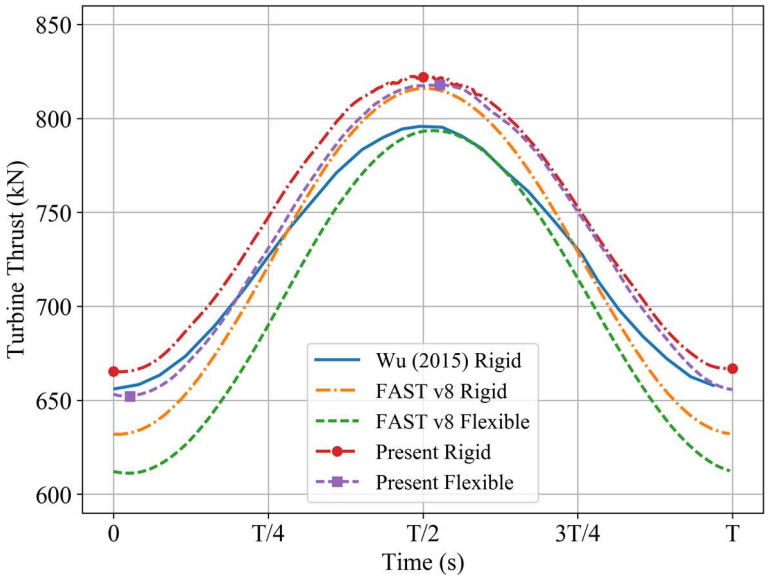

(a) Thrust

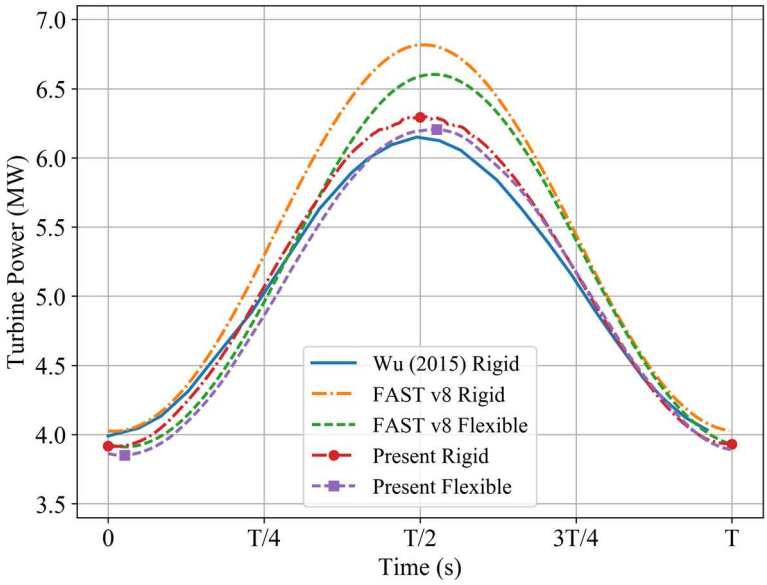

(b) Power

Figure 5.13 Time history of wind turbine aerodynamic thrust and power under prescribed platform surge motion

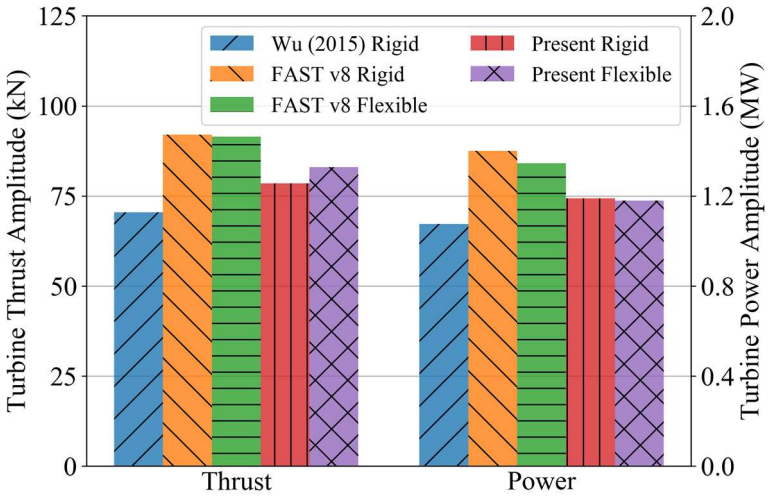

Figure 5.14 Variation amplitude of wind turbine thrust and power under prescribed platform surge motion

To further compare the results from different analysis tools, the variation of the amplitudes of both thrust and power are computed and shown in Figure 5.14, which is defined as A = (Max - Min)/2, where Max and Min are the maximum and minimum of either thrust or power over one platform oscillating cycle, respectively. Comparing the variation amplitude of thrust for the three rigid cases reveals that FAST v8 predicts 10-20% larger thrust variation than the other two CFD tools. The discrepancy among the results from different tools is also present for power variation. A likely reason for

such difference is that CFD tools inherently take into account the platform motion effects on the turbine wake via solving full Navier-Stokes equations, whereas the BEM theory adopted by engineering tools like FAST v8 utilises an empirical dynamic wake model to take into consideration the influence of rapid AOA variation due to the platform motion.

The variation of wind turbine aerodynamic loading under platform surge motion can again be associated with the change in the apparent AOA in a similar way as described in Section 5.2.1. Figure 5.12 shows that the apparent AOA is directly related to the wind speed U_{Wind} experienced by a blade airfoil section. Increasing U_{Wind} while maintaining turbine rotation speed U_{Rot}, leads to an increased AOA. When a platform surge motion is imposed to a wind turbine, the platform surge velocity U_{Surge}, shown in Figure 5.6, must be subtracted from U_{Wind}, resulting in an apparent wind speed represented by $U_{WindApp} = U_{Wind} - U_{Surge}$. At the start of a platform motion cycle, the turbine is at an equilibrium position with a maximum surge velocity U_{Surge}, pointing to the downwind direction. This results in the minimum apparent wind speed $U_{WindApp}$. As a consequence of that, the wind turbine thrust and power also reach their minima. It is thus logical that the maximum turbine aerodynamic loadings would occur at the time instant of T/2, where T is the time period of the platform surge motion.

On the other hand, the difference in thrust and power variation amplitude between rigid and flexible turbine simulations is relatively small. For example, the variation of thrust predicted by the present tool for the flexible case is about 5% larger than that for the rigid one, while the difference in power variation is less than 1%. For comparison, FAST v8 predicts a decrease of 0.5% and 4% for thrust and power variation respectively in the flexible turbine simulation.

However, there is a noticeable phase difference in the time history curve of the flexible case in comparison with the rigid turbine simulation. This is exemplified by highlighting the maxima and minima of CFD results for rigid and flexible cases with circular (●) and square (■) markers, respectively, as shown in Figure 5.13. It can be observed that the time at which either the maximum or the minimum thrust occurs for a flexible blade is always later than a rigid blade. A similar trend can be found from

FAST v8 results. Since all other parameters are the same for the rigid and flexible cases, this noticeable time-lag between wind turbine aerodynamic loading is directly related to the deflection of turbine blades.

To better analyse the influence of blade deflection on turbine aerodynamics, a blade element at the section of 0.9R in the spanwise direction is investigated where the maximum thrust and power per unit length are generated in the fixed condition as shown in Figure 5.9. Figure 5.15 demonstrates the time history of thrust variation per unit length at 0.9R for both rigid and flexible cases. The apparent wind speed $U_{WindApp}$ is also plotted, which is defined as $U_{WindApp} = U_{Wind} - U_{Surge} - U_{FlapDef}$. Compared to the rigid case, an additional blade flapwise deflection velocity $U_{FlapDef}$, which results from mass inertia forces and periodically varying aerodynamic loading, has to be considered for the flexible case. As shown in Figure 5.15, the flexible $U_{WindApp}$ has similar magnitude to its rigid counterpart, indicating that $U_{FlapDef}$ is much smaller than U_{Surge}. Nevertheless, the thrust per unit length for the flexible blade is in phase with the corresponding apparent wind speed $U_{WindApp}$, which confirms that the time lag in the flexible case is caused by the blade deflection velocity in the flapwise direction.

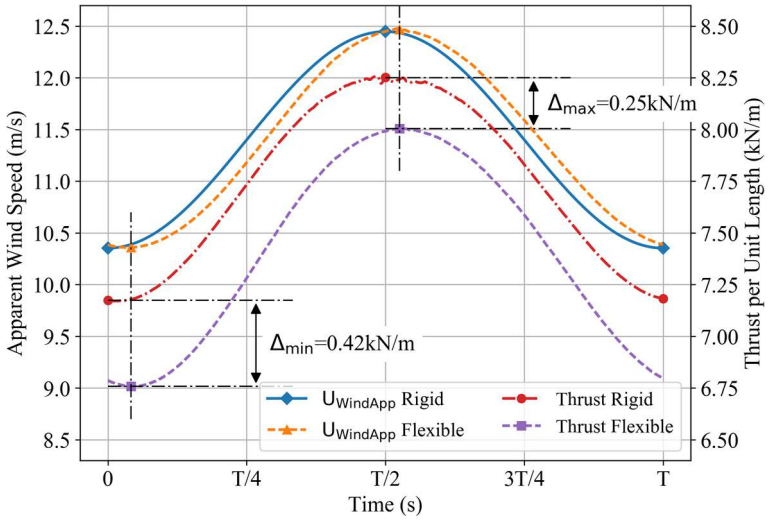

Figure 5.15 Time history of apparent wind speed and thrust per unit length at spanwise section of r/R = 0.9 under prescribed platform surge motion

In addition to the phase difference between the rigid and flexible cases, the gap between the minimum thrust per unit length in the rigid case and that in the flexible one is 0.42 kN/m while the difference for the maximum values decreases to 0.25 kN/m,

as annotated in Figure 5.15. The variation in the difference between the extrema can be associated with the twist deflection of the flexible blade. Figure 5.16 shows the time history curve of twist deflection at spanwise section of 0.9R as well as the apparent AOA defined in Figure 5.12. The twist deflection is also in phase with the flexible thrust per unit length. Near the start of the platform surge motion cycle, the twist deflection reaches its maximum in the negative direction at -0.46 degrees and gradually decreases to -0.1 degrees after half a period. It has been stated previously in Section 5.2.1 that a negative twist deflection reduces the apparent AOA. Therefore, the variation of twist deflection effectively changes the difference between the apparent AOA in the flexible case and that in the rigid simulation, and accordingly the thrust per unit length.

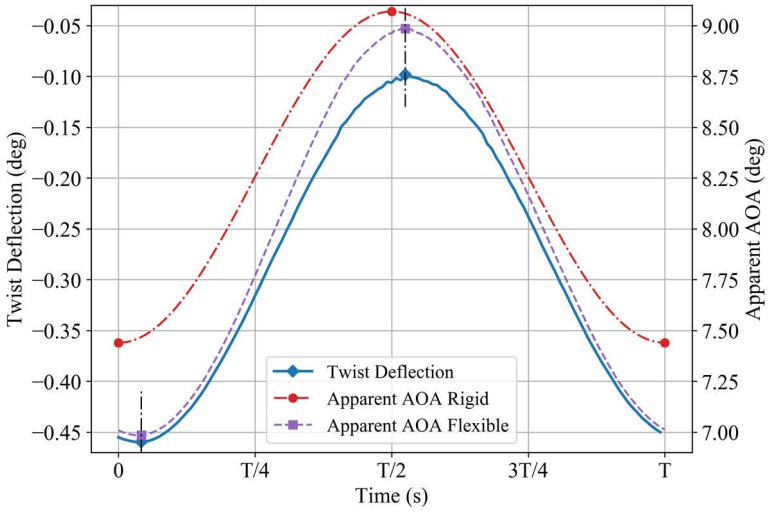

Figure 5.16 Time history of twist deflection and apparent AOA at spanwise section of r/R = 0.9 under prescribed platform surge motion

Figure 5.17(a) shows the pressure coefficient Cp distribution on the airfoil at the spanwise section of 0.9R for the flexible case. Data from two individual time instants is compared, i.e. when the thrust per unit length reaches its minimum and maximum. Significant variation of Cp is observed near the leading edge of the airfoil on both pressure and suction surfaces. Compared to the instant when maximum thrust is achieved, the decrease in Cp at its minimum spans from the leftmost leading edge to 60% of the chord length. Figure 5.17(b) compares the fluid field coloured by Cp at the spanwise section of 0.9R at these two instants. The difference in Cp is clearly visible

in the vicinity of leading edge and above the suction surface, demonstrating the significant impacts of platform surge motion on the fluid flow around wind turbine.

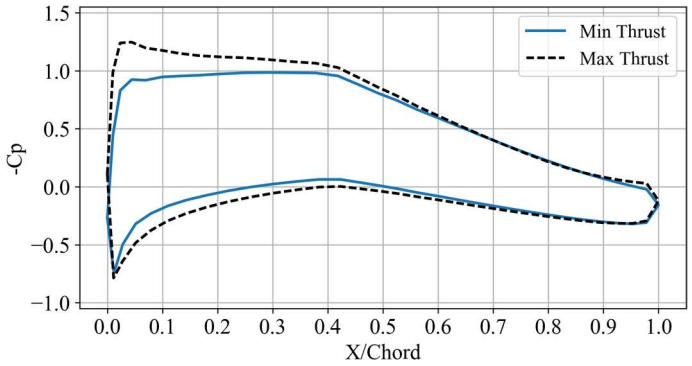

(a) Pressure coefficient distribution along blade section

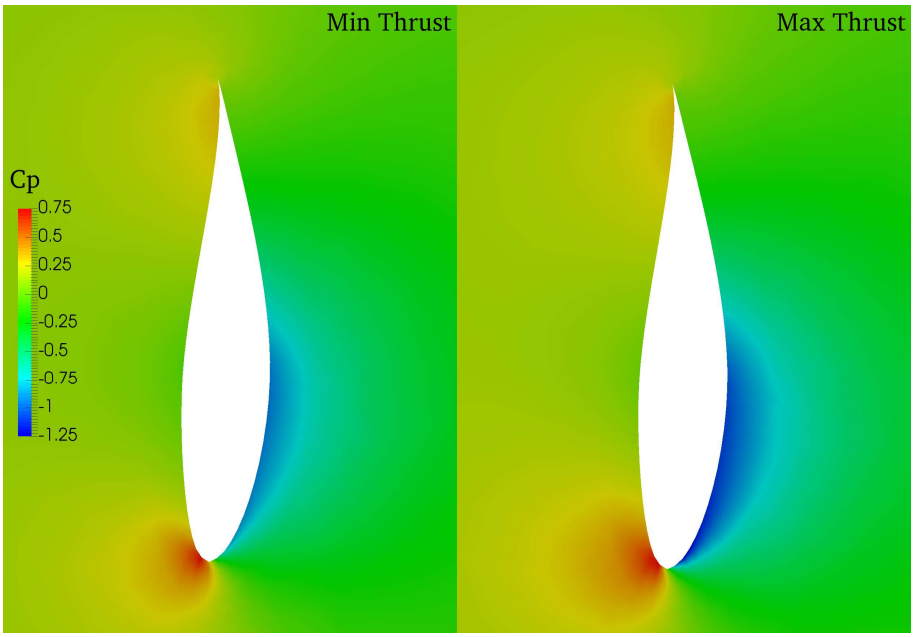

(b) Pressure coefficient contour

Figure 5.17 Fluid field information for flexible case at spanwise section of r/R = 0.9 under prescribed platform surge motion: Min Thrust – At time of minimum thrust per unit length; Max Thrust – At time of maximum thrust per unit length

Figure 5.18 illustrates the evolution of fluid flow over one platform surge motion cycle. The vortical structures of the flow field are represented by the contour of second invariant of the rate of strain tensor Q, which is coloured by the axial component of fluid flow velocity Ux. As can be clearly seen from these figures, strong vortices appear near the blade tip and root regions. The number and size of these vortex tubes vary considerably at different instants, indicating that the turbine violently interacts

with its wake due to the prescribed platform motion, which is similar to the observation from the work of (Tran and Kim, 2016a) for a wind turbine with rigid blades.

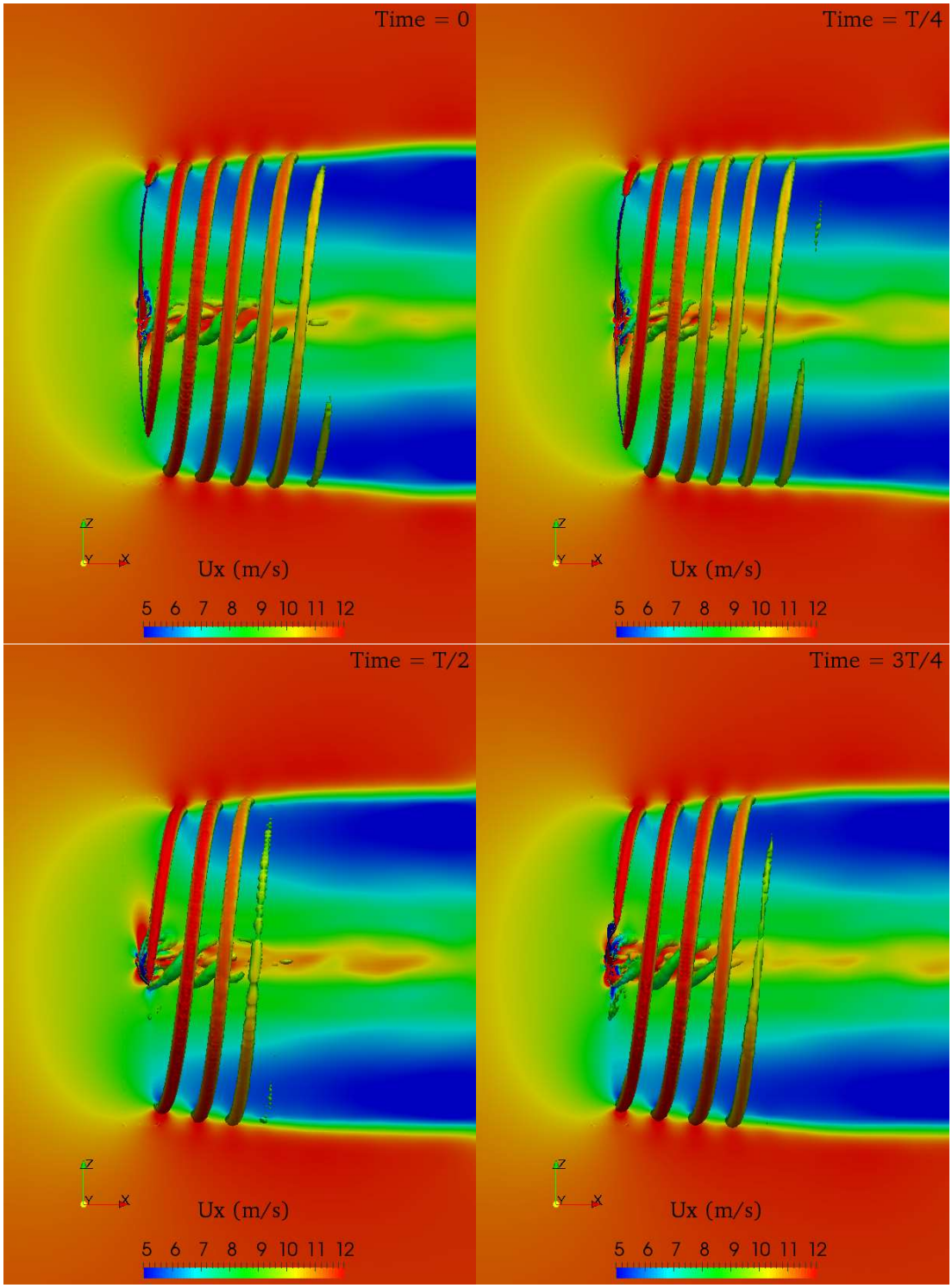

Figure 5.18 Vortex contour (Q = 0.1) and flow field at mid-plane coloured by axial velocity Ux under prescribed platform surge motion

The shape of deflected blade at its minimum and maximum flapwise deformation is illustrated in Figure 5.19(a) and compared to the rigid blade, indicating the significant variation in blade flapwise deflection. Figure 5.19(b) shows the time history of blade tip deflection in the flapwise and edgewise directions over one imposed platform surge motion cycle. The flapwsie blade tip deflection oscillates considerably due to the unsteady aerodynamic forces as well as inertia loads induced by the prescribed platform surge motion, reaching a minimum value of 5.1 m near the start of the platform motion cycle and then gradually rising to its maximum at 6.1 m after half a motion cycle. The edgewise deflection at the blade tip varies in a similar way within the range of [-0.53, -0.69] meters.

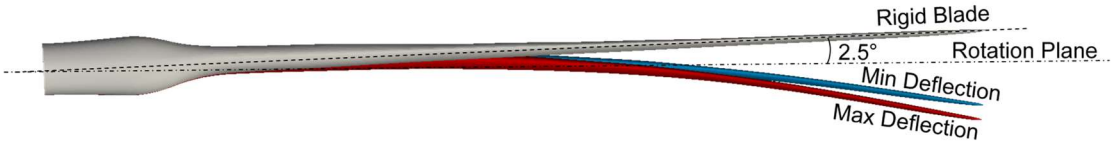

(a) Illustration of blade deflection

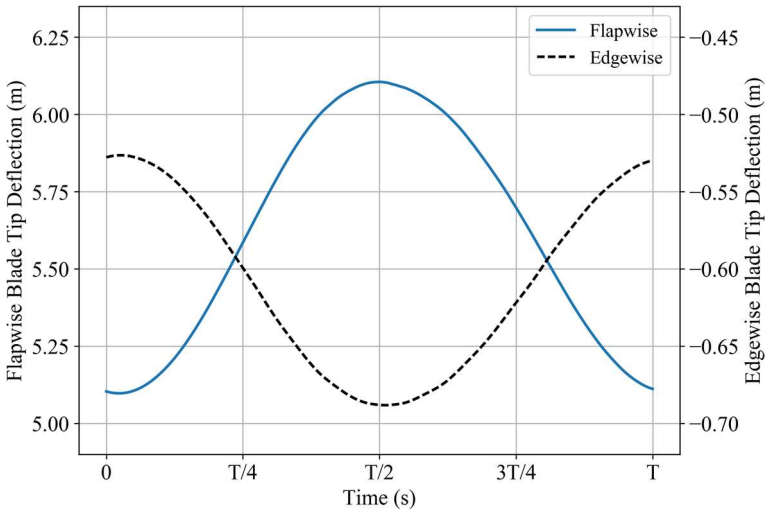

(b) Time history of flapwise and edgewise blade tip deflection

Figure 5.19 Blade tip deflection under prescribed platform surge motion

The prescribed platform surge motion also influences the bending moment at the blade root. Figure 5.20 plots the time history of the blade root bending moment in the flapwise and edgewise directions during one motion cycle. The flapwise bending moment changes from 9.02 to 10.97 MN*m, and the edgewise result, although much smaller compared to the former, also varies from 0.93 to 1.54 MN*m. The cyclic

characteristic of the internal loading can be associated with the unsteady aerodynamic forces and the periodic platform motion. In real world applications, complex working conditions, such as turbulent wind and irregular waves, and multiple DoF platform motion responses, could lead to significant changes in the internal loading of wind turbines and subsequently severe structural problems like fatigue. It is thus necessary to take wind turbine FSI into consideration during the design process.

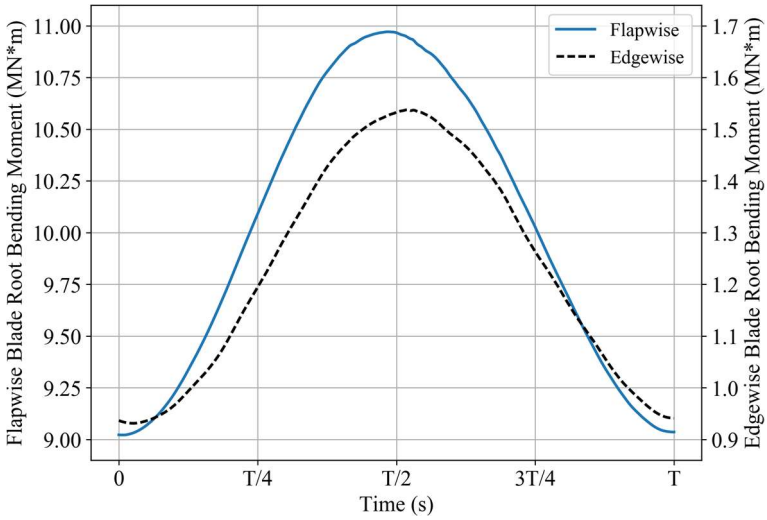

Figure 5.20 Time history of blade root bending moment under prescribed platform surge motion

5.3 Concluding Remarks

In this chapter, the NREL 5-MW offshore wind turbine with flexible blades is studied without modelling the supporting platform using the developed CFD-MBD tool. Uncoupled simulations are firstly carried out separately for both CFD and MBD models to ensure that they are correctly developed before fully coupled aeroelastic analysis is performed. Subsequently, two important problems in wind turbine aerodynamics are investigated, i.e. impacts of blade flexibility and platform surge motion on wind turbine aerodynamics and structural responses.

Blade flexibility is firstly analysed by comparing two cases with either rigid or flexible turbine blades while the turbine base is fixed. It is found that deformation of flexible blades slightly reduces the wind turbine aerodynamic thrust and power by less than 5%. Significant flapwise blade tip deflection as large as 8.89% of rotor radius is

predicted while the deflection in the edgewise direction is merely 0.95% of rotor radius, possibly due to the larger bending stiffness as well as smaller aerodynamic loading in the edgewise direction compared to those in the flapwise direction. Similar results are also obtained from the engineering tool FAST v8, which justifies its wide application in fixed-bottom wind turbine aeroelastic simulations. Afterwards, the decrease in turbine aerodynamic performance for the flexible case is analysed by inspecting the thrust and power distribution in the spanwise direction along a turbine blade. Comparison between the rigid and flexible cases shows that results from the flexible case are consistently smaller than those obtained with rigid blades for spanwise sections from 75% to 95% of the turbine radius, which is further reinforced by the difference of pressure distribution at a spanwise section of 90% of the turbine radius between the two cases. By defining an apparent AOA of a blade section while taking into account the twist deflection experienced by the section, subsequent analysis reveals that the decrease in thrust and power distribution of the flexible turbine blade is associated with the rotation due to blade twist deformation, which effectively reduces the apparent AOA.

A sinusoidal translational motion is then prescribed to the turbine base to investigate the effects of the platform surge motion on a floating offshore wind turbine with flexible blades. The aerodynamic thrust and power of the wind turbine vary considerably when the platform surge motion is imposed. However, FAST v8 overpredicts the variation of turbine aerodynamic thrust and power by 10-20% compared to CFD simulations, which is possibly due to the shortcomings of the empirical induction factors it uses to account for the changes in fluid flow induced by platform motion. The variations in turbine thrust and power are attributed to the additional superimposed platform surge velocity which influences the apparent wind speed and consequently the apparent AOA. The induced blade deflection velocity in the flapwise direction further changes the apparent wind speed experienced by the blade, leading to the time lag between turbine aerodynamic thrust and power of the flexible case and the prescribed motion. Meanwhile, analysis of the thrust per unit length at the blade spanwise section of 0.9R demonstrates the effects of the varying blade twist deflection due to platform motion on flexible turbine thrust. Visualisation

of fluid pressure and velocity obtained from CFD analysis clearly shows the influence of platform motion on the fluid field around the wind turbine, which cannot be predicted using engineering tools like FAST v8. Large variations are also observed for blade tip deflections and root bending moments in flapwise and edgewise directions, demonstrating the influence of platform surge motion on blade structural responses of FOWTs.

Chapter 6 Fully Coupled Analysis of a Semi-Submersible Floating Offshore Wind Turbine

In this chapter, with the high-fidelity aero-hydro-mooring-elastic analysis tool developed in the present project using a CFD-MBD method, a fully coupled analysis is conducted for the OC4 semi-submersible FOWT with flexible blades under a combined wind and wave condition to demonstrate the capabilities of the tool. As the last of the three objectives stated in Section 1.3, this study can be considered as a combination of those investigated in Chapter 4 and Chapter 5. Specifically, the deformation of the wind turbine blades is taken into consideration while the mooring system of the FOWT is modelled via the dynamic analysis method described in Section 2.4.2. Meanwhile, motion responses of the OC4 semi-submersible platform supporting the wind turbine are solved during the simulation rather than prescribed. Section 6.1 firstly describes the numerical model adopted in this study. Simulation results and discussion are then presented in Section 6.2. Further discussion on computational efficiency of the present tool is also made in Section 6.3.

6.1 Model Description

The FOWT model investigated in the present work consists of the aeroelastic wind turbine model with flexible blades studied in Chapter 5 and the supporting OC4 semi-submersible platform in Chapter 4, as demonstrated in Figure 6.1. A noticeable difference between the current model and the one analysed in Chapter 4 is that the wind turbine blades are able to deflect and are pre-bent to an approximate deformed shape to minimise the deterioration of the CFD mesh as a result of local mesh deformation, as previously discussed in Section 5.1.3. In addition, a shaft tilt angle of 5° is applied along with a pre-cone angle of 2.5° to maintain the clearance between the turbine blades and the tower. The overhang of the wind turbine is set to 5 m as defined in the NREL report (Jonkman et al., 2009), and a nacelle is added to the top of the turbine tower. In the meantime, the principal properties of the OC4 semi-submersible platform, tower and nacelle, i.e. mass and moment of inertia, are kept the same as those listed in Table 4.1 from MARIN's model tests (Coulling et al., 2013) so that the motion responses of the system between different cases can be compared. Structural properties

of the wind turbine blades defined in Chapter 5 are applied and the aeroelastic performance of the wind turbine can be analysed in a fully coupled scenario and compared to the prescribed platform-induced surge condition previously studied in Section 5.2.2.

Figure 6.1 Geometry of the OC4 semi-submersible FOWT with flexible blades

6.1.1 CFD Model

The CFD model set up for the present study is similar to the one described in Figure 4.5 of Section 4.2.2. However, compared to the cases with rigid blades investigated in Chapter 4, a fully coupled FSI simulation which takes wind turbine blade deformation into account is even more computationally expensive and requires a larger amount of computational time and resource. Several likely causes for the increase in computational time and possible ways to improve computational efficiency in future studies are discussed in Section 6.3. In order for the current simulation to complete within a reasonable time frame, i.e. weeks rather than months, the mesh density of the CFD model used in the present study is greatly decreased compared to that in Chapter 4 and the grid cell count is reduced from nearly 10 million to roughly 3 million. Figure 6.2 demonstrates the computational mesh used in this study. As a result, the primary objectives of this study are to demonstrate the capabilities of the numerical tool

developed for this project and to analyse the interaction between different components of the floating system in a qualitative manner.

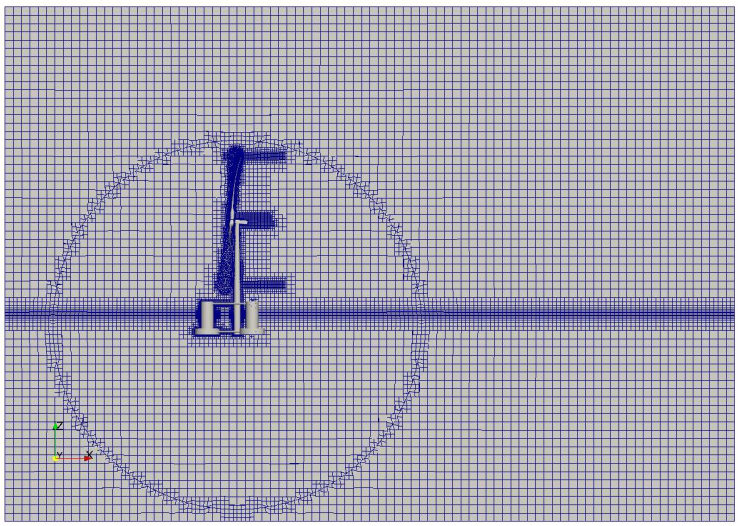

Figure 6.2 Computational mesh of the OC4 semi-submersible FOWT with flexible blades

Similar to the aeroelastic study of the wind turbine in Chapter 5, the geometry of the turbine blade in this case is also pre-deformed by applying the fluid force distribution from a steady-state simulation and then used for mesh generation. In such a way, the deterioration of grid quality due to local blade deformation can be minimised.

6.1.2 Structural Model

The structural model previously adopted for the prescribed platform surge motion case in Chapter 5, as described in Section 5.1.2, is further extended for the present study. Apart from the 149 geometrical nodes defined for the previous cases (49 nodes for each of the three blades, one hub node and one static ground node), an additional node is introduced to represent the floating platform in the fully couple case, resulting in a total number of 150 nodes. The hub node is forced to rotate relative to the platform node along its rotation axis at a specified turbine rotation speed using an axial rotation joint while the platform node is allowed to move with respect to the static ground node. As a result, the wind turbine moves with the floating platform when it responds to the excitation forces from environmental waves and wind.

It is worth mentioning that although it is preferable to define the nacelle, tower and platform as three separate bodies linked by constraints in a multi-body framework, some structural properties such as the moment of inertia for the nacelle and tower are not provided from MARIN's model tests (Coulling et al., 2013) and they are thus considered as one rigid body and represented by a single platform node. In the meanwhile, the mass and inertia properties of the platform-tower-nacelle assembly are determined in advance by utilising the parallel axis theorem as previously discussed in Section 4.1 while ignoring the unknown properties. Table 6.1 lists the gross properties of the platform-tower-nacelle assembly. Compared to Table 4.2 which presents the gross properties for the FOWT system, Table 6.1 excludes the contributions from the wind turbine which is discretised and represented by a large number of blade nodes with corresponding structural properties.

Table 6.1 Gross properties of the platform-tower-nacelle assembly

Properties	Unit	Value
Total mass of the assembly	kg	14,094,050
Assembly CM location below SWL	m	10.56
Roll inertia about assembly CM	$kg \cdot m^2$	1.267×10^{10}
Pitch inertia about assembly CM	$kg \cdot m^2$	1.265×10^{10}
Yaw inertia about platform centreline	$kg \cdot m^2$	1.393×10^{10}

Table 6.2 Inertia and drag coefficients for dynamic mooring line analysis

Properties	Value
Tangential Drag Coefficient C_{DT}	0.213
Normal Drag Coefficient C_{DN}	1.08
Tangential Added Mass Coefficient C_{AT}	0.269
Normal Added Mass Coefficient C_{AN}	0.865

Mooring system properties listed in Table 3.3 are still adopted for the present study. However, as dynamic mooring line analysis is carried out in the simulation, additional information such as the inertia and drag coefficients of the mooring lines in tangential and normal directions is required. The data estimated by Hall and Goupee (2015) to

validate their developed lumped-mass mooring line model against MARIN's model tests (Coulling et al., 2013) is utilised in this study and summarised in Table 6.2.

6.1.3 Simulation Case

In this study, the OC4 semi-submersible FOWT is subject to regular waves and uniform wind. Table 6.3 lists the environmental conditions adopted for the present simulation. The Stokes 2nd order wave theory is employed with the same amplitude of 3.79 m and period of 12.1 s as in Chapter 4 so that the influence of the wind turbine with aeroelastic blades on the hydrodynamic response of the floating platform can be assessed. The uniform wind speed, rotor speed and blade pitch angle specified in Chapter 5 is also applied to this case to analyse the aerodynamic performance and blade structural response of the wind turbine under predicted motion responses of the floating platform.

Table 6.3 Environmental conditions for the OC4 semi-submersible FOWT with flexible blades

Properties	Unit	Value
Wave Amplitude	m	3.79
Wave Period	s	12.1
Wind Speed	m/s	11.4
Rotor Speed	RPM	12.1
Rotor Rotation Period	s	4.96
Blade Pitch Angle	degrees	0

6.2 Results and Discussion

Numerical results obtained from the fully coupled aero-hydro-mooring-elastic simulation of the OC4 semi-submersible FOWT are presented and analysed from the following aspects: platform hydrodynamics, mooring dynamics, wind turbine aerodynamics and blade elasticity. The popular engineering tool FAST v8 is also adopted for comparison with the present tool. The calibrated model provided by FAST v8 for the OC4 semi-submersible FOWT is adapted by incorporating relevant changes

to the operating condition. It should be pointed out that the control system used in FAST v8 to regulate wind turbine operation is disabled in the present study.

6.2.1 Platform Hydrodynamics

Figure 6.3 shows time history curves of surge, heave and pitch motion responses under the combined wind/wave condition predicted by both the present fully coupled CFD-MBD tool and the engineering tool FAST v8. Periodic results for one complete wave period are depicted and extracted for further analysis.

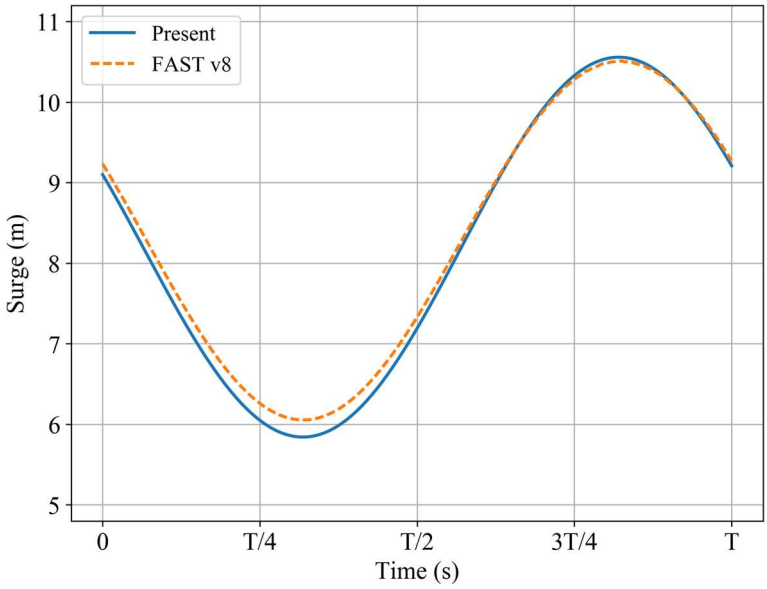

(a) Surge motion

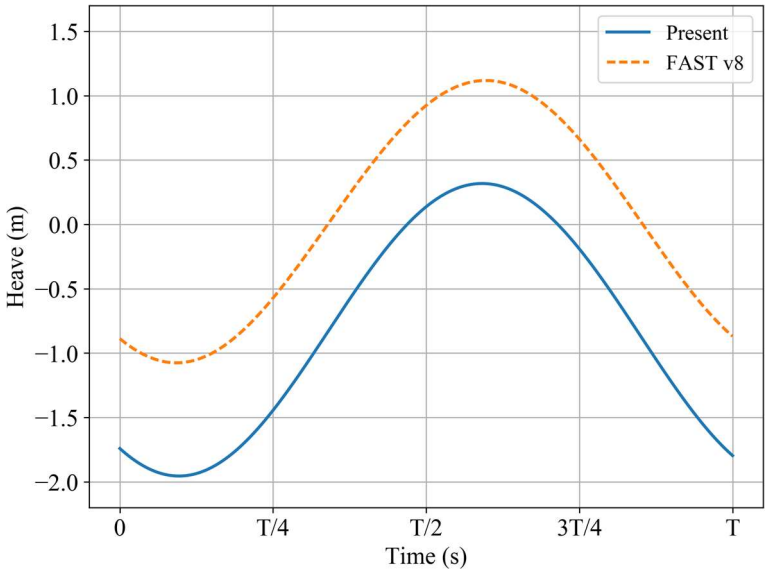

(b) Heave motion

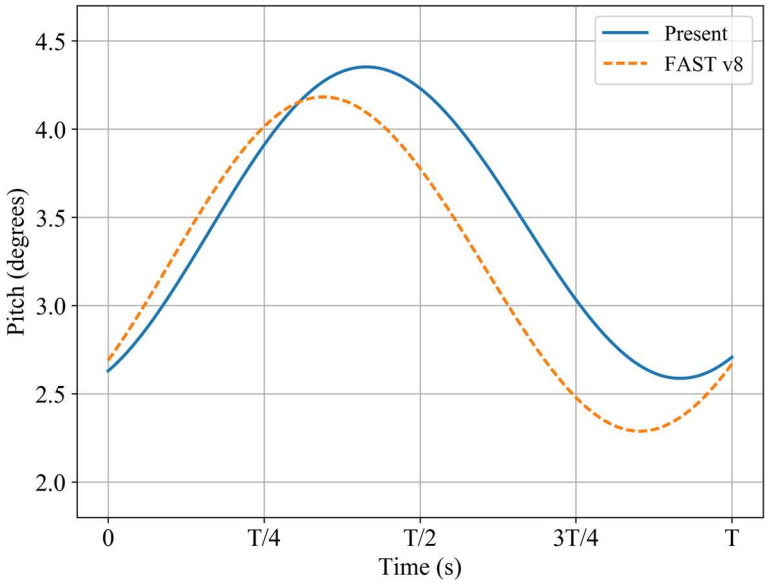

(c) Pitch motion

Figure 6.3 Time history of motion responses of the FOWT with flexible blades

Compared to the two cases studied in Chapter 4 where wind speed and turbine rotation speed are smaller than the operating condition in the present case, it can be easily seen that the maximum surge and pitch responses of the platform are much larger in this study. Specifically, the surge motion obtained using the present tool has a maximum value of 10.56 m with a mean position of 8.2 m, and the maximum angle for pitch motion reaches 4.35 degrees with an equilibrium value of 3.47 degrees. Results from FAST v8 also show similar trends for surge (max: 10.51 m, mean: 8.28 m) and pitch (max: 4.18 degrees, mean: 3.24 degrees). This can be explained by the significant increase in the aerodynamic thrust generated by the wind turbine under the present environmental condition as shown in Figure 5.3. The downward movement of the heave motion away from its initial position is possibly related to the orientation change due to the large mean pitch angle, as previously discussed in Section 4.2.3.

Table 6.4 compares RAO results of the three platform motion responses predicted by the two tools. In order to further analyse the effects of wind turbine aerodynamic loadings on the platform, data from a previously studied case (referred to as “Wave only”) in Section 3.3 is also listed, where the wind turbine is not modelled. Compared to the wave only condition, variations are present for results from the present tool under the combined wind/wave condition. For example, surge RAO increases from

0.5965 m for the wave only condition by 4.27% to 0.622 m for the combined wind/wave condition. Nevertheless, considering that the computational mesh for the present study is relatively coarse as mentioned in Section 6.1.1, difference between results under the two conditions is still small, which indicates that impacts of wind turbine with flexible blades on platform motion RAO are negligible for the investigated case.

Table 6.4 Motion RAO comparison between present tool and FAST v8 (percentage in parentheses shows the difference over data under wave only condition)

RAO	Wave only	Present	FAST v8
Surge (m/m)	0.5965	0.6220 (+4.27%)	0.5879 (-1.44%)
Heave (m/m)	0.2820	0.2998 (+6.31%)	0.2893 (+2.59%)
Pitch (°/m)	0.2470	0.2329 (-5.71%)	0.2499 (+1.17%)

Meanwhile, similar results from FAST v8 also suggests that the calibrated FAST model for the OC4 semi-submersible FOWT is able to accurately predict its hydrodynamic responses under the current operating condition of combined regular waves and uniform wind. However, it should be noted that the potential flow theory adopted by engineering tools like FAST v8 to deal with platform hydrodynamics is based on linear assumptions. Furthermore, drag coefficients required to take into account viscous damping have to be extracted from experimental tests and are assumed to be constant for all flow conditions. It is thus expected that these engineering tools might be inadequate for highly nonlinear problems, such as extreme and focusing wave conditions, which the present CFD-based tool is capable of.

6.2.2 Mooring Dynamics

Time history data of the tension force measured at the fairlead of mooring line #2 (Figure 3.11) in head wave direction over one wave cycle from the present tool and FAST v8 is plotted in Figure 6.4. Dynamic analysis is carried out for the mooring system in both simulations (labelled with Dynamic). The dynamic mooring line analysis module MoorDyn incorporated in FAST v8 adopts the same lumped mass model as the present tool (Hall and Goupee, 2015). The two curves are very similar in

terms of trend and magnitude. Particularly, the temporary plateau between T/4 and T/2, possibly due to the inclusion of nonlinear force terms in the dynamic model, is predicted by both simulations. Quantitative analysis listed in Table 6.5 also reveals that the difference between RAO predicted by the two tools is 4.6% and that discrepancies in mean and maximum tension are -2.97% and -1.66% respectively, which further validates the dynamic mooring line modelling feature implemented in the present tool. It is also noted that the fairlead tension force is largely out of phase with the platform surge motion, which can be attributed to the additional dynamic DoFs, i.e. acceleration and velocity, introduced in the lumped mass model.

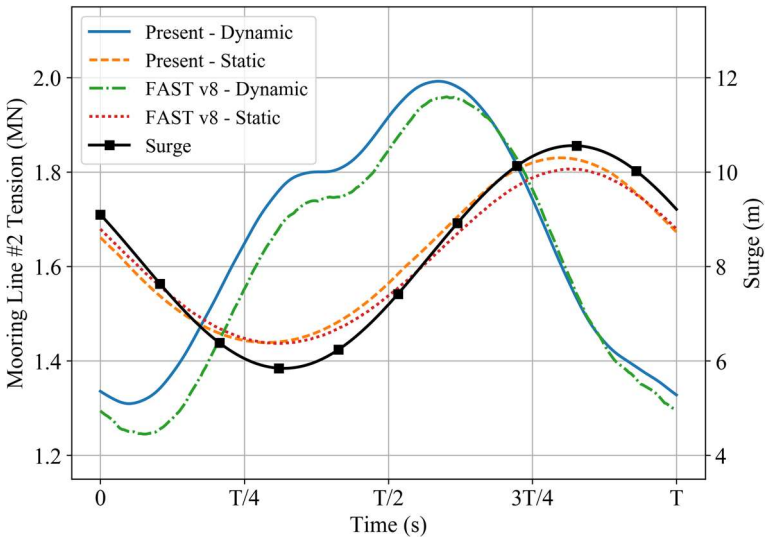

Figure 6.4 Time history of mooring line #2 tension of the FOWT with flexible blades

Table 6.5 Comparison for mooring line #2 tension with various methods (percentage in parentheses shows difference of FAST v8 results over corresponding present predictions)

	Wave only Static	Present Static	FAST v8 Static	Present Dynamic	FAST v8 Dynamic
RAO (kN/m)	27.546	51.586	48.680 (-5.63%)	90.036	94.200 (+4.62%)
Mean (MN)	1.146	1.634	1.622 (-0.73%)	1.651	1.602 (-2.97%)
Maximum (MN)	1.251	1.830	1.806 (-1.31%)	1.992	1.959 (-1.66%)

In order to assess the difference between the two different approaches in modelling mooring lines, i.e. quasi-static and dynamic methods, tension force results from simulations with quasi-static mooring line analysis (labelled with Static) are also included in Figure 6.4 and Table 6.5. Quasi-static results from the two tools agree reasonably well with a maximum difference of -5.63% in tension RAO. Comparison between data obtained with quasi-static and dynamic approaches in present simulations shows that tension RAO significantly increases from 51.586 kN/m by about 75% to 90.036 kN/m, which demonstrates the importance of a dynamic model in predicting mooring line tension and structural strength design. Meanwhile, the difference between mean tension predictions is small, i.e. 1.04%. However, Figure 6.4 shows that unlike the dynamic model, the tension force obtained with the quasi-static model is mostly in phase with the platform surge motion, which is likely due to lack of dynamic effects.

Results from the wave only case previously studied in Section 3.3, where the quasi-static method was adopted, are also listed in Table 6.5. By comparing the present case with quasi-static mooring line analysis to the wave only case, it is found that mean tension increases from 1.146 MN to 1.634 MN as a result of the wind turbine thrust force pushing the platform away from its equilibrium position. Besides, tension RAO from this study is 87.27% larger than that in the wave only case, which results from the nonlinear relationship between mooring restoring force and surge motion as previously discussed in Section 4.2.3.

6.2.3 Wind Turbine Aerodynamics

Figure 6.5 shows time history curves of aerodynamic thrust and power of the wind turbine within one wave cycle. Results from the present tool and FAST v8 are presented for comparison. There is a series of sudden drops in the curves of both aerodynamic thrust and power, which is caused by the presence of the turbine tower when turbine blades pass in front of it, also known as tower interference or tower shadow effects as previously discussed in Section 4.2.2. Both tools predict similar magnitude for these sudden decreases, i.e. approximately 25 kN for thrust and 300 kW for power.

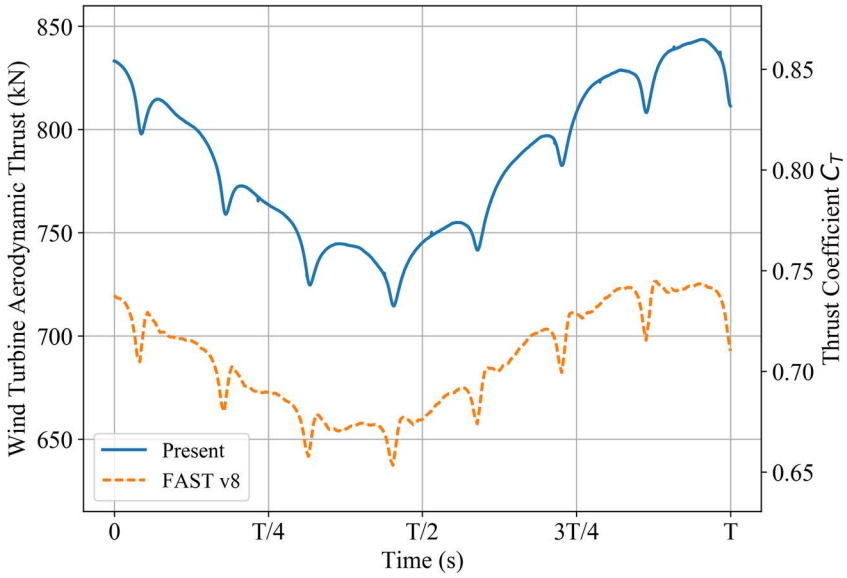

(a) Aerodynamic thrust

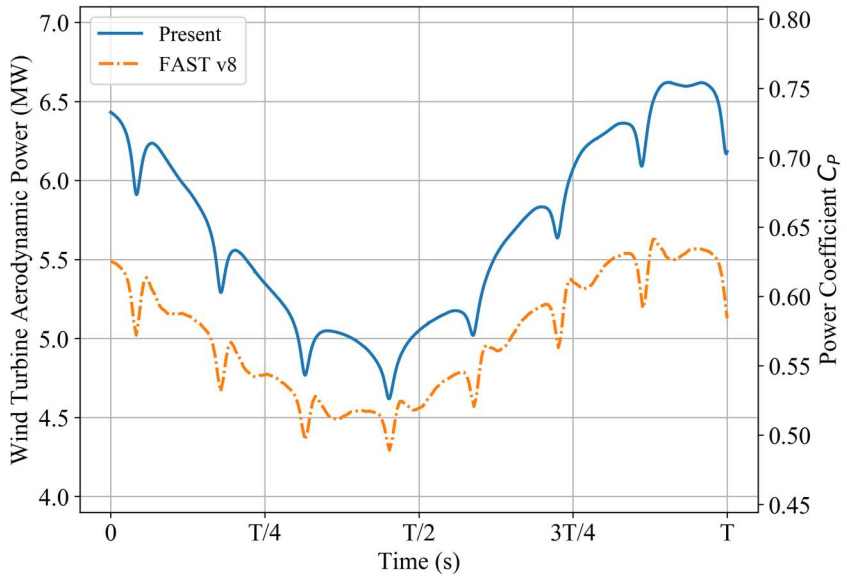

(b) Aerodynamic power

Figure 6.5 Time history of wind turbine aerodynamics of FOWT with flexible blades

Due to the platform motion responses, particularly surge and pitch, it can be found that wind turbine aerodynamic thrust and power oscillate over the time range of one wave cycle. The influence of platform motion on wind turbine is also illustrated in Figure 6.6, which shows the time history of the acceleration in X (surge) direction at the hub of the wind turbine with a variation of about [-0.25, 0.25] m/s^2. It is worth pointing out that tower shadow effects are also present in Figure 6.6.

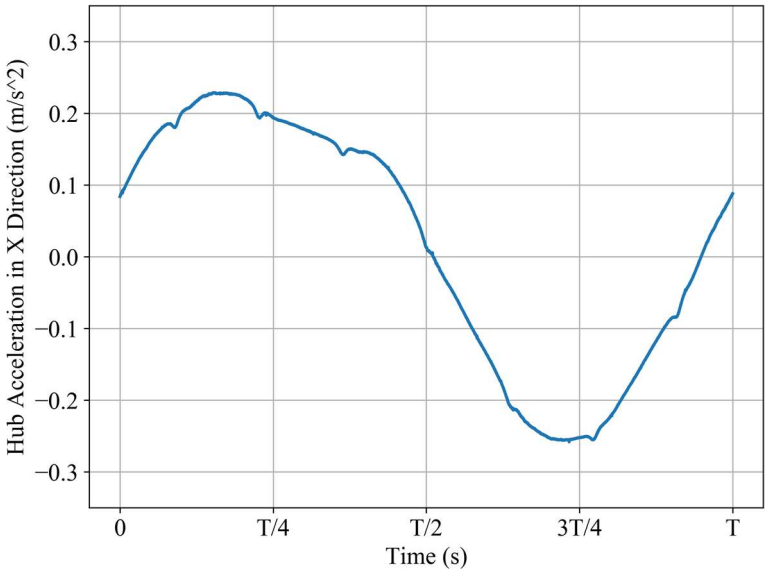

Figure 6.6 Time history of acceleration in X direction at turbine hub

Although oscillation is present for results from both tools, the amplitude of oscillation predicted by the present tool is different from that obtained with FAST v8. The current CFD-MBD tool predicts a variation of about 130 kN for thrust from maximum to minimum while results from FAST v8 show an oscillation of about 90 kN, which is 30% smaller. Difference in the oscillation amplitude is also present for power. The amplitude predicted by the present tool is about 2 MW, which is 50% larger than an oscillation of 1.3 MW from FAST v8.

Similar findings about smaller oscillation amplitudes from engineering tools like FAST v8 compared to CFD-based solvers were also pointed out by Quallen et al. (2014) and Tran and Kim (2016b) in their respective FOWT simulations. This is likely due to the adoption of many empirical models in these engineering tools, such as the dynamic wake model and skewed wake model. These models were originally formulated for applications of onshore and offshore fixed-bottom wind turbine, which might not be suitable for complex conditions experienced by wind turbines installed on floating platforms. Specifically, the wind turbine in this study undergoes both platform surge and pitch motion. In addition to the rotor tilt and blade precone angles, a positive equilibrium angle is present for the pitch motion, which forces the wind turbine to operate in skewed wake under constantly changing flow conditions caused by periodic platform surge and pitch motion responses.

Figure 6.7 illustrates four snapshots for fluid flow over one incident wave cycle. The vortical structures generated at blade tip and root areas are clearly visible, which are represented by the contour of second invariant of the rate of strain tensor Q and coloured by the axial component of fluid flow velocity Ux. Unlike the flow field results shown in Figure 5.18 for the prescribed platform surge motion case, the additional platform pitch motion induced in this study leads to further interactions between the wind turbine and its wake, which can be demonstrated by the variation in the distance between two adjacent vortex tubes in the lower part of the skewed wake (highlighted in black rectangles). It is very difficult for the empirical wake models adopted by FAST v8 to accurately take these interactions into account, which partly explains the difference between wind turbine aerodynamic performance from the two tools. Sectional view of fluid flow at the mid-plane of the computational domain is also exhibited in Figure 6.7 to analyse the spatial and temporal variation of velocity field influenced by platform motion. The black circles annotated in Figure 6.7 clearly show impacts of platform motion on incoming wind. Furthermore, it is worth mentioning that velocity of air flow is also affected by wave propagation, as indicated by decrease of wind speed above wave crests near free surface, which emphasises the coupling between wind and wave in FOWT simulations. Application of the present CFD method enables detailed investigation into the complex fluid flow around the FOWT via visualisation, which cannot be achieved by engineering tools like FAST v8.

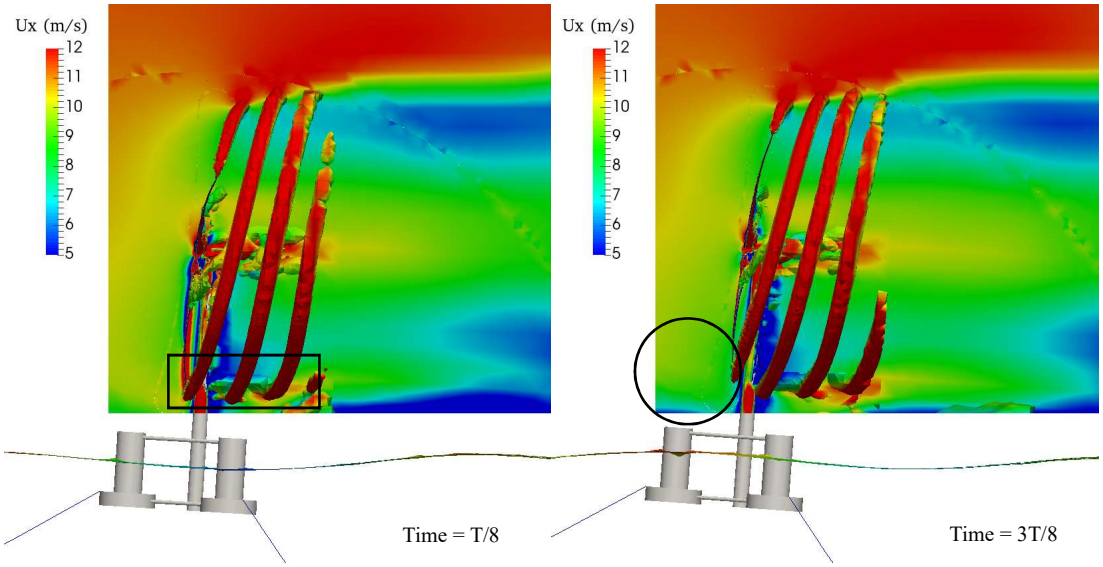

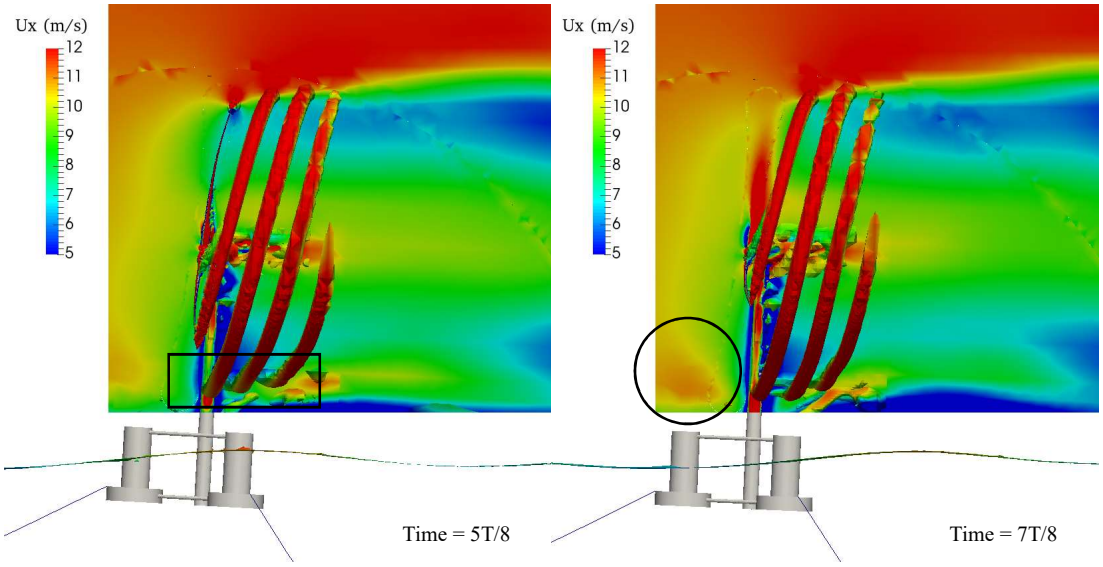

Figure 6.7 Vortex contour (Q = 0.05) and flow field at mid-plane coloured by axial velocity Ux for FOWT with flexible blades

6.2.4 Blade Elasticity

Figure 6.8 compares time history data of blade tip deflection in the flapwise direction within one wave cycle predicted by the present tool and FAST v8. The BeamDyn module implemented in FAST v8, which is based on the nonlinear beam theory, is selected to deal with deformation of flexible structures. Unlike results presented in Section 5.2.2 for the case with prescribed platform surge motion, both curves show rapid changes in blade deformation due to the influence of additional platform pitch motion induced by waves and non-zero tilt angle applied. Tower interference effects are also clearly visible in blade deflection results, indicated by the two sudden drops in the curves as annotated in Figure 6.8. When the blade passes in front of the turbine tower, the aerodynamic force exerted upon the blade decreases rapidly, leading to reduced blade deformation. Results obtained with FAST v8 are generally smaller than predictions from the present CFD-MBD tool, which is in accordance with the turbine aerodynamic loadings in Figure 6.5.

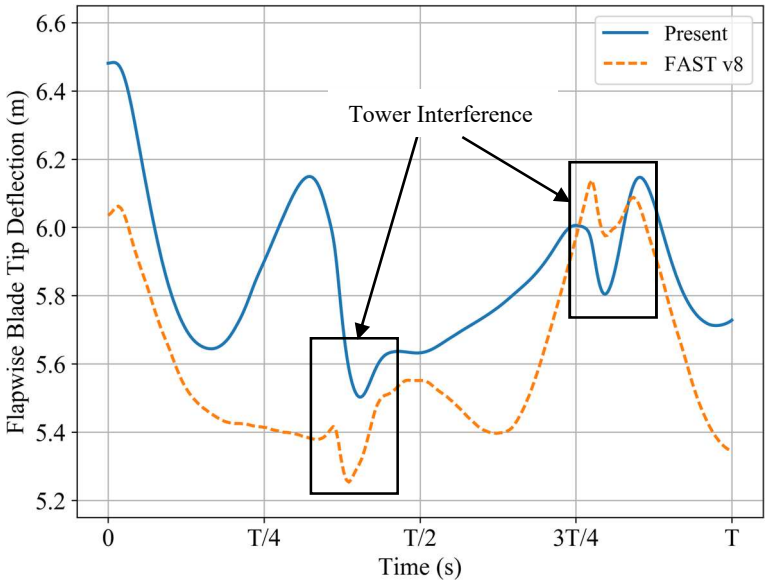

Figure 6.8 Time history of flapwise blade tip deflection

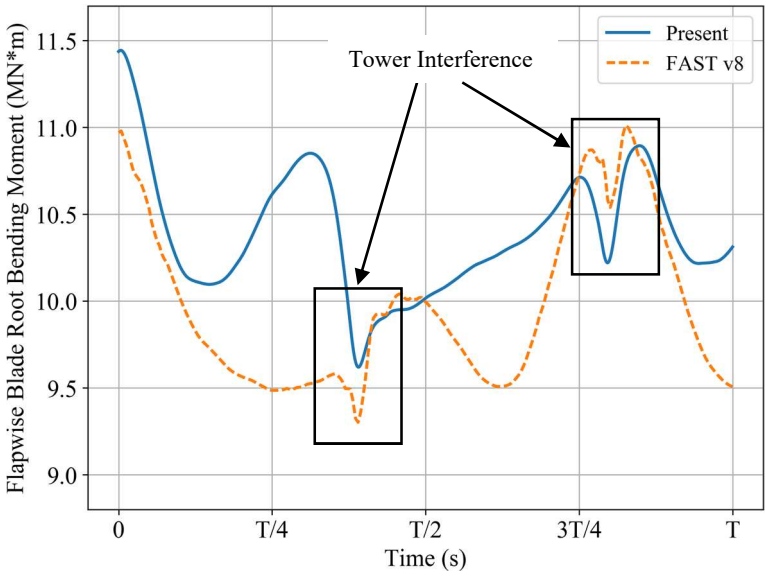

Figure 6.9 Time history of flapwise blade root bending moment

Figure 6.9 demonstrates time history curves of the bending moment at blade root in the flapwise direction within one wave cycle. The variation of blade root bending moment closely resembles that of blade tip deflection shown in Figure 6.8, including the sudden drops due to tower interference as annotated in Figure 6.9. It should be noted that in addition to frequency associated with wind turbine rotation and tower interference, the platform motion responses experienced by an FOWT also introduce a frequency related to the incident waves in temporal change of blade root bending

moment. For the current case with moderate wave height, a considerable amount of variation is present in blade root bending moment as shown in Figure 6.9. It is thus reasonable to expect even more significant changes in structural loading when the FOWT operates under conditions with higher wave height than the present study, which may lead to severe structural problems and therefore stresses the importance of taking into account platform motion responses in blade structural design of FOWTs.

6.3 Discussion on Computational Efficiency

As stated in Section 6.1.1, the computational mesh used in this study is significantly coarser than that in Chapter 4 due to the limited time and resource available as well as the large amount of computation required to complete a fully coupled simulation. Reasons for the intensive computation are discussed as follows.

On the one hand, simulations of an FOWT with rigid turbine blades are already rather time-consuming. For instance, for Case #1 in Section 4.2.2, the rotation period of the wind turbine T_{rot} is about 12 s and the wave period T_{wave} is 12.1 s. The time step size for this case was set to $T_{rot}/2500$, i.e. 0.005 s (as larger values led to instability and simulation crashes). The case ran for a total simulated time of 350 s, i.e. nearly $30T_{wave}$ or equivalent to 70,000 time steps, until the motion responses of the floating system reached a nearly periodic state. The simulation was performed on a cluster with 10 compute nodes, each of which contains two 2.7 GHz, 12-core E5-2697 v2 processors, i.e. 240 cores in total. As each time step took about 25 s, the overall computational time required for one case to finish amounted to almost 21 days. For the present case, the rotation period (about 5 s) is even smaller than Case #1, and the time step size also decreases to 0.002 s, leading to even longer computational time.

On the other hand, modelling structural deformation of turbine blades also results in substantial increase in computational time.

Firstly, although the computational demand of MBDyn is negligible compared to OpenFOAM, additional computation is introduced by solving the Laplace mesh motion equation, i.e. Eq. (2.35), to determine the updated point displacement of the CFD grid. The displacement variable is a vector and has three components, which have

to be solved separately. For an aeroelastic wind turbine case in Chapter 5, solving for CFD mesh motion accounts for roughly 10% of the computational time required within one time step.

Secondly, as already mentioned is Section 2.3.2, a flexible body is represented by a series of grid patches in the CFD model corresponding to the beam nodes in the MBD model. It was found during debugging that around 20% of the time in the aforementioned aeroelastic study was spent on force integration over the surface patches possibly because a large number of patches (about 150) were present and the operation could only be done sequentially across multiple processors.

Furthermore, a strong/tight coupling procedure between the fluid and structural solvers is currently implemented in the fully coupled CFD-MBD tool to achieve better stability. However, this requires the CFD grid to be updated at every sub-iteration within one time step. Meanwhile, the added complexity of a case with flexible bodies leads to more sub-iterations compared to one with only rigid structures, which further increases the computational time by about 30%.

In total, the estimated increase in the computational time due to the inclusion of structural deformation amount to 60%.

In an attempt to improve the computational efficiency and reduce the computational demand, several approaches are proposed and listed in the following:

1. Apply additional artificial damping to help surge motion quickly achieve a periodic state. The required simulated time is largely determined by the surge motion. At the start of a simulation, the thrust force generated from the wind turbine pushes the platform away in the surge direction and results in an initial low-frequency disturbance for the surge motion which is associated with the natural frequency of the system. As the natural period for the surge DoF of the semi-submersible platform (107.2 s as listed in Table 3.5 from free decay tests) is quite large compared to T_{wave}, the simulated time needs to be sufficiently long for the initial low-frequency disturbance to become fully dampened. Figure 6.10 illustrates the time history curve of the surge motion for Case #1

in Section 4.2.2. It can be seen that it takes more than 300 s of simulated time, i.e. three times the surge natural period, for the initial low-frequency motion disturbance to decrease significantly and become negligible compared to the dominant wave-frequency motion. By introducing an artificial damping close to the critical damping of the system, the low-frequency surge motion response can decay more quickly. As a result, the simulated time could be reduced, effectively decreasing the overall computational time.

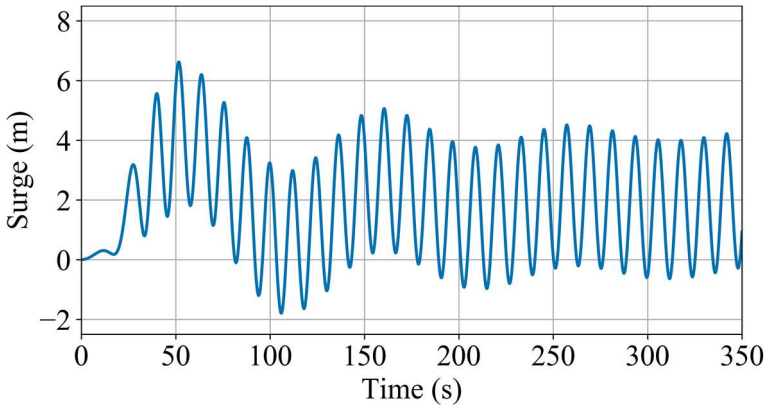

Figure 6.10 Time history curve of surge motion for an FOWT under a combined wind/wave condition

2. Start a simulation without considering blade flexibility until system responses become periodic then resume with deformable blades. As previously stated, a fully coupled simulation with aeroelastic turbine blades is more demanding in computational resource than that with rigid blades. It is thus viable to decrease the computational time by firstly performing the simulation while assuming that the turbine blades are rigid. Once a periodic state is achieved for the motion responses as well as loadings, the blades are allowed to deform and then the simulation continues.

3. Increase efficiency for force calculation over CFD surface patches. The present tool takes advantage of the built-in library in OpenFOAM to calculate the fluid force and moment exerted upon the surface patches in the CFD model of an aeroelastic simulation. In the current implementation, this operation is firstly executed by all the processes (equivalent to cores in the Messaging Passing Interface model) on the same patch separately but at the same time.

Subsequently, the force value from every process is sent to the master process for summation to obtain the integrated force result for that patch. This procedure is then repeated for other surface patches. The current workflow involves frequent communication between processes, which incurs a data transfer overhead and possibly leads to the surprisingly high computational cost for force integration in simulations with flexible turbine blades. One of the ways to improve the computational efficiency is to update the workflow by minimising inter-process communication. This can be realised by instructing each process to firstly perform force calculation on all patches and then send force data to the master process in a single communication step.

4. Adopt a weak/staggered coupling procedure between OpenFOAM and MBDyn. For the tight coupling procedure implemented in the present tool, force and motion data is exchanged between the two solvers during every sub-iteration along with an update of the CFD mesh. If a weak coupling procedure is to be utilised, both data exchange and mesh update need to be performed once within one time step, which could result in a significant decrease in the computational cost. However, it is worth noting that this approach might bring about additional stability problems.

5. Take advantage of GPU (Graphics Processing Unit) to speed up the process of solving equations. Thanks to its massively parallel architecture consisting of thousands of cores, a GPU is able to efficiently process multiple tasks simultaneously and is thus suitable for accelerating CFD simulations. There have been a few open source GPU-accelerated libraries for solving systems of sparse linear equations in OpenFOAM, such as ofgpu from Symscape (https://www.symscape.com/gpu-1-1-openfoam) and RapidCFD from SIMFLOW Technologies (https://sim-flow.com/rapid-cfd-gpu/). Figure 6.11 demonstrates an almost 50% decrease in execution time by running RapidCFD solvers on a Tesla K20X GPU compared to 8 Intel E5-2670 CPUs. If these GPU-accelerated solvers are utilised in the fully coupled simulations, computational time can be substantially decreased.

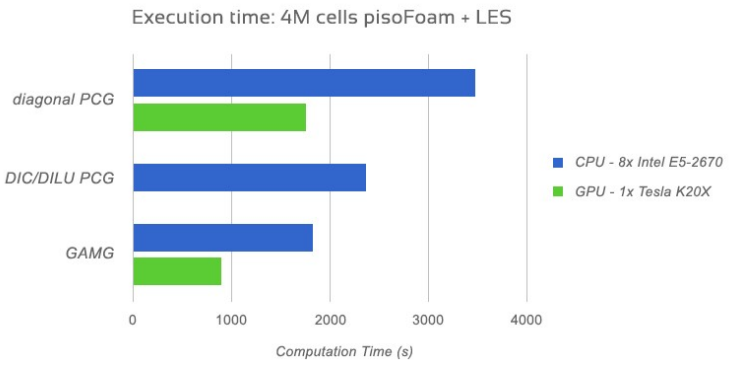

Figure 6.11 Comparison of performance between CPU and GPU (source: SIMFLOW Technologies)

6.4 Concluding Remarks

In this chapter, a fully coupled aero-hydro-mooring-elastic analysis is carried out for the OC4 semi-submersible FOWT with flexible blades under a combined wind/wave condition using the high-fidelity CFD-MBD tool developed in this project. Results from the present study are analysed and compared to data obtained with the engineering too FAST v8 from various perspectives, including floating platform hydrodynamic responses, mooring system dynamics, wind turbine aerodynamic performance and blade structural dynamics. Interactions among different components of the floating system are investigated.

Firstly, motion responses of the floating platform, namely surge, heave and pitch, under the present combined wind/wave case are compared with the wave only case previously studied. Apart from the significant increase in the equilibrium position of these three DoFs due to the substantial aerodynamic thrust of the wind turbine, motion RAOs of the platform in regular waves are generally unaffected by the operation of the turbine with aeroelastic blades. Similar results from FAST v8 demonstrate that it is capable of accurately predicting the hydrodynamic responses of the floating platform under normal operating conditions.

Mooring system dynamics is then investigated. The dynamic mooring system analysis module developed in this project is adopted to solve the mooring lines of the platform. Good agreement between line tension results from the present simulation and FAST v8 further validates the present implementation. Compared to quasi-static results, the

tension force RAO measured at the fairlead of the mooring line in head wave direction predicted via the dynamic approach increases considerably by 75%, underlying the importance of model fidelity in FOWT mooring system design. Nonlinear responses of the mooring line are also captured thanks to the inclusion of dynamic effects and nonlinear drag terms in the model.

Subsequently, comparing wind turbine aerodynamic thrust and power from the present high-fidelity CFD-MBD tool and the engineering tool FAST v8 reveals that FAST v8 under-predicts the oscillation amplitudes by 30% and 50%, respectively. This can possibly be explained by the adoption of many empirical models in FAST v8, which might be unable to take into consideration complex FSI caused by platform surge and pitch motion responses of an FOWT, such as constantly changing flow conditions and skewed wake. Visualisation of the flow field obtained via the CFD approach clearly shows the interaction between the wind turbine and its wake, the influence of platform motion on the wind field as well as the impacts of wave propagation on air flow.

Blade structural responses of the FOWT under the present combined wind/wave condition are lastly studied. By analysing the time history data of blade tip deflection and root bending moment, it is found that both deflection and bending moment change rapidly with respect to time. Tower interference effects result in a sudden drop of deflection as well as bending moment during every turbine rotation cycle. Additionally, the platform surge and pitch motion responses introduce an oscillation frequency associated with the incident waves, which should be taken into account during the structural design of FOWT blades.

Fully coupled simulations for FOWTs using the present high-fidelity CFD-MBD tool are exceptionally time-consuming. In Section 6.3, several potential reasons responsible for the high demand in computational time and resource are examined in detail. Afterwards, a number of suggestions aiming to boost the efficiency of the tool and decrease computational time are proposed for future improvements.

Chapter 7 Conclusions and Future Work

In order to numerically investigate fluid-structure interaction problems for floating offshore wind turbines, a high-fidelity aero-hydro-mooring-elastic analysis tool is developed in this thesis using a coupled CFD-MBD approach. The numerical tool is implemented progressively in three consecutive stages and utilised to analyse FSI problems of FOWTs under three different scenarios. Conclusions drawn from these studies are firstly reviewed in Section 7.1. Subsequently, some recommendations for future improvements and potential applications are provided in Section 7.2.

7.1 Conclusions

The main outcomes of this thesis are summarised as follows.

7.1.1 Aero-Hydro-Mooring Analysis of a Semi-Submersible Floating Offshore Wind Turbine

In order to achieve the first objective in Section 1.3, the OC4 DeepCWind semi-submersible FOWT is investigated under regular waves and uniform wind in Chapter 4 and the interactions between different components of the FOWT, including the wind turbine, the floating platform and its mooring system, are analysed. Wind turbine blades are considered rigid and mooring lines are modelled via a quasi-static method. The following conclusions are drawn from this study:

1. Compared to a fixed-bottom wind turbine, aerodynamic thrust and torque of an FOWT vary considerably due to the motion responses of its supporting platform. The oscillation amplitudes of thrust and torque increase with wind speed and turbine rotation speed when wave conditions are unchanged.

2. Platform surge and pitch responses result in additional induced speed for the wind turbine and thus influence the resultant wind speed experienced by turbine blades, which positively relates to the aerodynamic loadings. The correlation is further reinforced via further examination into pressure distribution along different blade sections.

3. Wind turbine aerodynamic thrust and torque suddenly decrease when a turbine blade passes in front of the turbine tower due to tower shadow or interference effects.

4. The influence of wind turbine aerodynamic loadings (including damping) on motion RAOs of platform surge, heave and pitch responses is negligible under the investigated conditions with relatively low wind speed and large wave height while it exerts great impacts upon the equilibrium position of the three DoFs.

5. Compared to platform hydrodynamic loadings, variation of wind turbine aerodynamic loadings is insignificant and their effects on the platform can thus be considered as constant force.

6. Unlike platform motion RAOs, the mooring line tension RAO is considerably affected by the wind turbine. Due to the nonlinear relationship between mooring line restoring force and platform surge motion, the increase in the mean position of the platform surge motion due to the significant wind turbine thrust results in larger tension RAO for mooring lines.

7.1.2 Aeroelastic Analysis of an Offshore Wind Turbine in Platform-Induced Surge Motion

The NREL 5-MW offshore wind turbine with flexible blades is studied in Chapter 5 and an aeroelastic analysis is carried out focusing on the impacts of blade elasticity on wind turbine aerodynamics and structural responses, which addresses the second objective listed in Section 1.3. The floating platform supporting the turbine is not directly modelled for simplicity and the effects of platform motion responses on the turbine are investigated via imposing a prescribed surge motion to the turbine base. The following conclusions are drawn from this study:

1. Under the fixed-bottom condition, flexible turbine blades produce slightly smaller aerodynamic thrust and power than rigid ones by less than 5%. The decrease in the aerodynamic performance of a flexible blade mostly occurs

within spanwise sections from 75% to 95% of the turbine radius, which is likely caused by the nose-down rotation of these blade sections due to the twist deformation predicted in flexible simulations.

2. Blade tip deflection and root bending moment in the flapwise direction are almost 10 times larger than those in the edgewise direction due to the larger structural bending stiffness and smaller aerodynamic loading in the edgewise direction.

3. Under the prescribed platform surge motion condition, significant variations in wind turbine aerodynamic thrust and power are present for both rigid and flexible cases with similar oscillation amplitudes.

4. While the aerodynamic loading of the rigid turbine is always in phase with the apparent wind speed, the induced blade flapwise deflection velocity by the prescribed platform surge motion leads to phase difference or time lag between the turbine aerodynamic performance and the prescribed surge motion in the flexible case.

5. In addition to flapwise deflection velocity, the oscillation of twist deformation at a blade section contributes to the variation of apparent AOA, which results in the difference in thrust per unit length between rigid and flexible simulations.

6. Blade tip deflection and root bending moment in both flapwise and edgewise directions oscillate significantly when the sinusoidal platform surge motion is imposed.

7.1.3 Fully Coupled Analysis of a Semi-Submersible Floating Offshore Wind Turbine

The third objective stated in Section1.3 is met in Chapter 6 by performing a fully coupled aero-hydro-mooring-elastic analysis for the OC4 semi-submersible FOWT with flexible blades under a combined wind/wave condition. Responses of the floating system are analysed in terms of floating platform hydrodynamics, mooring system

dynamics, wind turbine aerodynamics and blade elasticity. The following conclusions are drawn from this study:

1. Impacts of wind turbine aerodynamics with elastic blades on platform hydrodynamic responses the are still limited to their equilibrium positions while motion RAOs are generally unaffected.

2. Mooring line tension RAO predicted via a dynamic approach is 75% larger than data obtained with a quasi-static method, which is also unable to model the nonlinear responses of the mooring line.

3. Interactions between the FOWT and its skewed wake are demonstrated via visualising fluid flow results obtained in the CFD simulation.

4. Effects of tower interference and platform motion responses lead to rapid oscillations in blade tip deflection and root bending moment.

7.2 Recommendations for Future Work

This research focuses on the development of a fully coupled high-fidelity CFD-MBD tool for FOWTs and its applications to various FSI problems in the offshore wind field. However, due to the limited time and computational resource available, the present tool still has some shortcomings and numerical analysis for FOWTs was carried out under only a small number of environmental conditions. Recommendations for further improvements to the tool and potential applications are briefly outlined below.

1. The numerical tool developed in the present work is quite computationally demanding as discussed in Section 6.3. One of the priorities for future development is to improve its computational efficiency and significantly decrease the execution time required to complete simulations before the present CFD-MBD tool can be widely applied. A few suggestions have been provided in Section 6.3 to help alleviate this problem.

2. Modern wind turbines are regulated with an integrated control system to optimise power generation under complex operating conditions. Engineering

tools like FAST are already equipped with powerful control mechanisms. However, a control module for wind turbine operation is still lacking in the present tool and should be implemented in order to better simulate and analyse system responses of FOWTs in real world scenarios.

3. CFD mesh motion due to the complex global rigid body motion of FOWTs is handled in the present tool via a combination of the AMI sliding mesh technique and individual cell zone motion. Nevertheless, the overset grid technique is a more versatile approach to deal with compound mesh interactions in CFD simulations. In June 2017, a major feature of overset mesh functionality was introduced to OpenFOAM v1706 by OpenCFD Ltd and freely released to the public (https://www.openfoam.com/releases/openfoam-v1706/numerics.php#numerics-overset). Capabilities of the present tool can be further extended by integrating it with the new overset grid feature.

4. Present studies have mainly focused on the analysis of FOWTs under regular wave and uniform wind conditions. Future research can be extended to more complex environmental conditions, such as irregular and extreme waves, nonuniform wind with shear velocity profiles and initial explicit turbulence, as well as current.

5. The NREL 5-MW offshore wind turbine studied in this thesis is capable of generating 5 MW of power at its rated operating speed while new generations of wind turbines with even higher power capacity are being designed, such as the DTU 10-MW reference wind turbine with a blade length of nearly 90 m (Bak et al., 2013). Aeroelastic analysis can be carried out for these large-sized wind turbines to assess their aerodynamic performance as well as structural deformation and loading.

6. Wind turbines are mostly commonly installed in groups as wind farms to facilitate maintenance and power transmission. It is thus of significance to investigate wake interference effects on the downstream wind turbine in a two-

turbine configuration, which is beyond the capability of the normal BEM theory used by most engineering design tools like FAST v8.

7. Although it was primarily designed for FSI problems of FOWTs, the fully coupled analysis tool developed in this project can be applied to other similar fields, such as vertical axis wind turbines and floating tidal turbines. Furthermore, implementation of coupling between OpenFOAM and MBDyn enables its application to various multibody dynamics problems, for example, bio-inspired robotics.

References

Antonutti R, Peyrard C, Incecik A, Ingram D, Johanning L (2018). Dynamic mooring simulation with Code_Aster with application to a floating wind turbine. *Ocean Engineering*, **151**, 366-377.

Bachynski EE, Kvittem MI, Luan C, Moan T (2014). Wind-Wave Misalignment Effects on Floating Wind Turbines: Motions and Tower Load Effects. *Journal of Offshore Mechanics and Arctic Engineering*, **136**(4), 041902-041902-12.

Bak C, Zahle F, Bitsche R, Kim T, Yde A, Henriksen LC, Hansen MH, Blasques JPAA, Gaunaa M, Natarajan A (2013). The DTU 10-MW Reference Wind Turbine. *Danish Wind Power Research 2013*, Fredericia, Denmark.

Baudic SF, Williams AN, Kareem A (2001). A Two-Dimensional Numerical Wave Flume—Part 1: Nonlinear Wave Generation, Propagation, and Absorption. *Journal of Offshore Mechanics and Arctic Engineering*, **123**(2), 70-75.

Bayati I, Jonkman J, Robertson A, Platt A (2014). The effects of second-order hydrodynamics on a semisubmersible floating offshore wind turbine. *Journal of Physics: Conference Series*, **524**(1), 012094.

Bazilevs Y, Hsu MC, Kiendl J, Wüchner R, Bletzinger KU (2011). 3D simulation of wind turbine rotors at full scale. Part II: Fluid–structure interaction modeling with composite blades. *International Journal for Numerical Methods in Fluids*, **65**(1-3), 236-253.

Bazilevs Y, Hsu MC, Scott MA (2012). Isogeometric fluid–structure interaction analysis with emphasis on non-matching discretizations, and with application to wind turbines. *Computer Methods in Applied Mechanics and Engineering*, **249–252**, 28-41.

BBC. World's first floating wind farm starts generating electricity. 2017. Available from: http://www.bbc.co.uk/news/uk-scotland-41652707.

Benedict M, Mattaboni M, Chopra I, Masarati P (2011). Aeroelastic Analysis of a Micro-Air-Vehicle-Scale Cycloidal Rotor in Hover. *AIAA Journal*, **49**(11), 2430-2443.

Boger D, Paterson E, Noack RW (2010). FoamedOver: A Dynamic Overset Grid Implementation in OpenFOAM. *Proceedings of the 10th Symposium on Overset Composite Grids and Solution Technology*, NASA Ames Research Center, Moffet Field, CA, USA.

Cao H, Wan D (2014). Development of Multidirectional Nonlinear Numerical Wave Tank by naoe-FOAM-SJTU Solver. *International Journal of Ocean System Engineering*, **4**(1), 52-59.

Carrión M, Steijl R, Woodgate M, Barakos GN, Munduate X, Gomez-Iradi S (2014). Aeroelastic analysis of wind turbines using a tightly coupled CFD–CSD method. *Journal of Fluids and Structures*, **50**, 392-415.

Cermelli C, Roddier D, Aubault A (2009). WindFloat: A floating foundation for offshore wind turbines—Part II: hydrodynamics analysis. *ASME 2009 28th International Conference on Ocean, Offshore and Arctic Engineering*, p. 135-143.

Cha J, Wan D (2011). Numerical wave generation and absorption based on OpenFOAM. *The Ocean Engineering*, **29**(3), 1-12.

Chow R, van Dam CP (2012). Verification of computational simulations of the NREL 5 MW rotor with a focus on inboard flow separation. *Wind Energy*, **15**(8), 967-981.

Coulling AJ, Goupee AJ, Robertson AN, Jonkman JM, Dagher HJ (2013). Validation of a FAST semi-submersible floating wind turbine numerical model with DeepCwind test data. *Journal of Renewable and Sustainable Energy*, **5**(2), 29.

de Vaal JB, Hansen MOL, Moan T (2014). Effect of wind turbine surge motion on rotor thrust and induced velocity. *Wind Energy*, **17**(1), 105-121.

EWEA. Deep water: The next step for offshore wind energy. 2013: 51.

Fan T, Qiao D, Ou J (2012). Optimized Design of Equivalent Truncated Mooring System Based On Similarity of Static And Damping Characteristics. *The Twenty-second International Offshore and Polar Engineering Conference*, Rhodes, Greece, p. 959-966.

Farrugia R, Sant T, Micallef D (2014). Investigating the aerodynamic performance of a model offshore floating wind turbine. *Renewable Energy*, **70**, 24-30.

Ferede E, Abdalla MM, van Bussel GJW (2017). Isogeometric based framework for aeroelastic wind turbine blade analysis. *Wind Energy*, **20**(2), 193-210.

Ghiringhelli GL, Masarati P, Mantegazza P (2000). Multibody Implementation of Finite Volume C Beams. *AIAA Journal*, **38**(1), 131-138.

Ghiringhelli GL, Masarati P, Mantegazza P, Nixon MW (1999). Multi-Body Analysis of a Tiltrotor Configuration. *Nonlinear Dynamics*, **19**(4), 333-357.

Glauert H, Airplane Propellers, in Aerodynamic Theory: A General Review of Progress Under a Grant of the Guggenheim Fund for the Promotion of Aeronautics. 1935, Springer Berlin Heidelberg: Berlin, Heidelberg. p. 169-360.

Gould BJ, Burris DL (2016). Effects of wind shear on wind turbine rotor loads and planetary bearing reliability. *Wind Energy*, **19**(6), 1011-1021.

Gundling C, Sitaraman J, Roget B, Masarati P (2015). Application and validation of incrementally complex models for wind turbine aerodynamics, isolated wind turbine in uniform inflow conditions. *Wind Energy*, **18**(11), 1893-1916.

Guntur S, Jonkman JM, Jonkman B, Wang Q, Sprague MA, Hind M, Sievers R, Schreck SJ (2016). FAST v8 Verification and Validation for a MW-scale Wind Turbine with Aeroelastically Tailored Blades. *34th Wind Energy Symposium*, San Diego, California, USA.

Habchi C, Russeil S, Bougeard D, Harion J-L, Lemenand T, Ghanem A, Valle DD, Peerhossaini H (2013). Partitioned solver for strongly coupled fluid–structure interaction. *Computers & Fluids*, **71**, 306-319.

Hall M, Buckham B, Crawford C (2014). Evaluating the importance of mooring line model fidelity in floating offshore wind turbine simulations. *Wind Energy*, **17**(12), 1835-1853.

Hall M, Goupee A (2015). Validation of a lumped-mass mooring line model with DeepCwind semisubmersible model test data. *Ocean Engineering*, **104**, 590-603.

Han Y, Le C, Ding H, Cheng Z, Zhang P (2017). Stability and dynamic response analysis of a submerged tension leg platform for offshore wind turbines. *Ocean Engineering*, **129**, 68-82.

Hand MM, Simms D, Fingersh L, Jager D, Cotrell J, Schreck S, Larwood S. Unsteady aerodynamics experiment phase VI: wind tunnel test configurations and available data campaigns. 2001.

Hansen MH (2007). Aeroelastic instability problems for wind turbines. *Wind Energy*, **10**(6), 551-577.

Hansen MOL, Sørensen JN, Voutsinas S, Sørensen N, Madsen HA (2006). State of the art in wind turbine aerodynamics and aeroelasticity. *Progress in Aerospace Sciences*, **42**(4), 285-330.

Haselbach PU, Eder MA, Belloni F (2016). A comprehensive investigation of trailing edge damage in a wind turbine rotor blade. *Wind Energy*, **19**(10), 1871-1888.

Heinz JC, Sørensen NN, Zahle F (2016a). Fluid–structure interaction computations for geometrically resolved rotor simulations using CFD. *Wind Energy*, **19**(12), 2205-2221.

Heinz JC, Sørensen NN, Zahle F, Skrzypiński W (2016b). Vortex-induced vibrations on a modern wind turbine blade. *Wind Energy*, **19**(11), 2041-2051.

Hirt CW, Nichols BD (1981). Volume of fluid (VOF) method for the dynamics of free boundaries. *Journal of Computational Physics*, **39**(1), 201-225.

Horcas SG, Debrabandere F, Tartinville B, Hirsch C, Coussement G (2017). Extension of the Non-Linear Harmonic method for the study of the dynamic aeroelasticity of horizontal axis wind turbines. *Journal of Fluids and Structures*, **73**, 100-124.

Hsu M-C, Akkerman I, Bazilevs Y (2014). Finite element simulation of wind turbine aerodynamics: validation study using NREL Phase VI experiment. *Wind Energy*, **17**(3), 461-481.

Hsu M-C, Bazilevs Y (2012). Fluid–structure interaction modeling of wind turbines: simulating the full machine. *Computational Mechanics*, **50**(6), 821-833.

Hsu M. Wind Energy Research webpage. 2015. Available from: http://www.public.iastate.edu/~jmchsu/Research_Wind_Energy.html.

Jasak H, Tukovic Z (2006). Automatic mesh motion for the unstructured finite volume method. *Transactions of FAMENA*, **30**(2), 1-20.

Jeon M, Lee S, Lee S (2014). Unsteady aerodynamics of offshore floating wind turbines in platform pitching motion using vortex lattice method. *Renewable Energy*, **65**, 207-212.

Jeong M-S, Cha M-C, Kim S-W, Lee I, Kim T (2014). Effects of torsional degree of freedom, geometric nonlinearity, and gravity on aeroelastic behavior of large-scale horizontal axis wind turbine blades under varying wind speed conditions. *Journal of Renewable and Sustainable Energy*, **6**(2), 19.

Jonkman JM (2007). *Dynamics modeling and loads analysis of an offshore floating wind turbine*. Doctoral Dissertation, University of Colorado at Boulder, Boulder, Colorado.

Jonkman JM (2009). Dynamics of offshore floating wind turbines—model development and verification. *Wind Energy*, **12**(5), 459-492.

Jonkman JM, Butterfield S, Musial W, Scott G. Definition of a 5-MW reference wind turbine for offshore system development. 2009: 63.

Jonkman JM, Matha D (2011). Dynamics of offshore floating wind turbines—analysis of three concepts. *Wind Energy*, **14**(4), 557-569.

Karimirad M, Michailides C (2015). Dynamic Analysis of a Braceless Semisubmersible Offshore Wind Turbine in Operational Conditions. *Energy Procedia*, **80**, 21-29.

Kim T, Oh S, Yee K (2015). Improved actuator surface method for wind turbine application. *Renewable Energy*, **76**, 16-26.

Kumari Ramachandran GKV (2013). *A Numerical Model for a Floating TLP Wind Turbine*. Doctoral Dissertation, Technical University of Denmark, Lyngby, Denmark.

Lanzafame R, Mauro S, Messina M (2013). Wind turbine CFD modeling using a correlation-based transitional model. *Renewable Energy*, **52**, 31-39.

Larsen J, Dancy H (1983). Open boundaries in short wave simulations—a new approach. *Coastal Engineering*, **7**(3), 285-297.

Leble V, Barakos G (2016). Demonstration of a coupled floating offshore wind turbine analysis with high-fidelity methods. *Journal of Fluids and Structures*, **62**, 272-293.

Lee K, Huque Z, Kommalapati R, Han S-E (2017). Fluid-structure interaction analysis of NREL phase VI wind turbine: Aerodynamic force evaluation and structural analysis using FSI analysis. *Renewable Energy*, **113**, 512-531.

Li L, Gao L, Liu Y, Cui Y (2015a). Numerical simulation of wake interference effects on the downstream wind turbine. *International Conference on Renewable Power Generation (RPG 2015)*, p. 1-6.

Li P, Cheng P, Wan D, Xiao Q (2015b). Numerical Simulations of Wake Flows of Floating Offshore Wind Turbines by Unsteady Actuator Line Model. *The 9th International Workshop on Ship and Marine Hydrodynamics*, Glasgow, UK.

Li Y, Castro AM, Sinokrot T, Prescott W, Carrica PM (2015c). Coupled multi-body dynamics and CFD for wind turbine simulation including explicit wind turbulence. *Renewable Energy*, **76**, 338-361.

Li Y, Paik K-J, Xing T, Carrica PM (2012). Dynamic overset CFD simulations of wind turbine aerodynamics. *Renewable Energy*, **37**(1), 285-298.

Liu Y, Xiao Q, Incecik A (2017a). A coupled CFD/Multibody Dynamics analysis tool for offshore wind turbines with aeroelastic blades. *36th International Conference on Ocean, Offshore and Arctic Engineering*, Trondheim, Norway.

Liu Y, Xiao Q, Incecik A, Peyrard C, Wan D (2017b). Establishing a fully coupled CFD analysis tool for floating offshore wind turbines. *Renewable Energy*, **112**, 280-301.

Low YM, Langley RS (2006). Dynamic Analysis of a Flexible Hanging Riser in the Time and Frequency Domain. *25th International Conference on Offshore Mechanics and Arctic Engineering*, Hamburg, Germany, p. 161-170.

Ma Y, Hu Z (2013). Dynamic Analysis for a Spar-Type Wind Turbine Under Different Sea States. *ASME 2013 32nd International Conference on Ocean, Offshore and Arctic Engineering*, Nantes, France, p. V008T09A012.

Make M, Vaz G (2015). Analyzing scaling effects on offshore wind turbines using CFD. *Renewable Energy*, **83**, 1326-1340.

Manolas DI, Riziotis VA, Voutsinas SG (2015). Assessing the Importance of Geometric Nonlinear Effects in the Prediction of Wind Turbine Blade Loads. *Journal of Computational and Nonlinear Dynamics*, **10**(4), 041008-041008-15.

Manwell JF, McGowan JG, Rogers AL. Wind Energy Explained: Theory, Design and Application. 2 ed[M] Wiley. 2010.

Masarati P (2000). *Comprehensive Multibody AeroServoElastic Analysis of Integrated Rotorcraft Active Controls*. Doctoral Dissertation, Politecnico di Milano

Masarati P, Morandini M, Mantegazza P (2014). An Efficient Formulation for General-Purpose Multibody/Multiphysics Analysis. *Journal of Computational and Nonlinear Dynamics*, **9**(4), 041001-041001.

Masciola M, Jonkman J, Robertson A (2014). Extending the Capabilities of the Mooring Analysis Program: A Survey of Dynamic Mooring Line Theories for Integration into FAST. *Proceedings of the ASME 2014 33rd International Conference on Ocean, Offshore and Arctic Engineering*, San Francisco, California, USA, p. 13.

Masciola M, Robertson A, Jonkman J, Coulling A, Goupee A (2013). Assessment of the Importance of Mooring Dynamics on the Global Response of the DeepCwind Floating Semisubmersible Offshore Wind Turbine. *Proceedings of the Twenty-third (2013) International Offshore and Polar Engineering*, Anchorage, Alaska, USA, p. 359-368.

Mathieu O, Jean-Francois M, Guy D, A Fluid-Structure Interaction Solver for Nano-Air-Vehicle Flapping Wings, in 19th AIAA Computational Fluid Dynamics. 2009, American Institute of Aeronautics and Astronautics.

Matthies HG, Steindorf J (2003). Partitioned strong coupling algorithms for fluid–structure interaction. *Computers & Structures*, **81**(8–11), 805-812.

Meng F (2011). *Aero-elastic stability analysis for large-scale wind turbines*. Doctoral Dissertation, TU Delft, Delft University of Technology

Meng F, Masarati P, Van Tooren M (2009). Free/Open source multibody and aerodynamic software for aeroelastic analysis of wind turbines. *47th Aerospace Sciences Meeting and Exhibit*, Orlando, Florida, USA.

Menter FR (2009). Review of the shear-stress transport turbulence model experience from an industrial perspective. *International Journal of Computational Fluid Dynamics*, **23**(4), 305-316.

Miao W, Li C, Yang J, Xie X (2016). Numerical investigation of the yawed wake and its effects on the downstream wind turbine. *Journal of Renewable and Sustainable Energy*, **8**(3), 033303.

Moriarty PJ, Hansen AC. AeroDyn Theory Manual. 2005.

Morison JR, Johnson J, Schaaf S (1950). The force exerted by surface waves on piles. *Journal of Petroleum Technology*, **2**(5), 149-154.

Nakajima T, Motora S, Fujino M (1982). On the dynamic analysis of multi-component mooring lines. *Offshore Technology Conference*, p. 105-120.

Nematbakhsh A, Bachynski EE, Gao Z, Moan T (2015). Comparison of wave load effects on a TLP wind turbine by using computational fluid dynamics and potential flow theory approaches. *Applied Ocean Research*, **53**, 142-154.

Nematbakhsh A, Olinger DJ, Tryggvason G (2013). A Nonlinear Computational Model of Floating Wind Turbines. *Journal of Fluids Engineering*, **135**(12), 121103-121103.

Nematbakhsh A, Olinger DJ, Tryggvason G (2014). Nonlinear simulation of a spar buoy floating wind turbine under extreme ocean conditions. *Journal of Renewable and Sustainable Energy*, **6**(3), 20.

Newmark NM (1959). A method of computation for structural dynamics. *Journal of the engineering mechanics division*, **85**(3), 67-94.

Nilay S-U, Lyle L (2006). 3-D Time-Accurate CFD Simulations of Wind Turbine Rotor Flow Fields. *44th AIAA Aerospace Sciences Meeting and Exhibit*.

NREL. NWTC Information Portal (FAST v8). 2016. Available from: https://nwtc.nrel.gov/FAST8.

Oguz E, Clelland D, Day AH, Incecik A, López JA, Sánchez G, Almeria GG (2018). Experimental and numerical analysis of a TLP floating offshore wind turbine. *Ocean Engineering*, **147**, 591-605.

OpenFOAM. Arbitrary Mesh Interface (AMI). 2011. Available from: http://www.openfoam.org/version2.1.0/ami.php.

OpenFOAM. Mesh generation with the snappyHexMesh utility. 2013. Available from: http://www.openfoam.org/docs/user/snappyHexMesh.php#x26-1510005.4.

Pierangelo M, Jayanarayanan S (2011). Coupled CFD/Multibody Analysis of NREL Unsteady Aerodynamic Experiment Phase VI Rotor. *49th AIAA Aerospace Sciences Meeting including the New Horizons Forum and Aerospace Exposition*, Orlando, Florida, USA.

Principle Power. The WindFloat project. 2011. Available from: http://www.principlepowerinc.com/en/windfloat.

Proskovics R, Huang S, Feuchtwang J (2013). The importance of fully-attached unsteady aerodynamics in floating wind turbine design. *Renewable Power Generation Conference (RPG 2013), 2nd IET*, Beijing, China, p. 1-4.

Qiu Y-X, Wang X-D, Kang S, Zhao M, Liang J-Y (2014). Predictions of unsteady HAWT aerodynamics in yawing and pitching using the free vortex method. *Renewable Energy*, **70**, 93-106.

Quallen S, Xing T (2016). CFD simulation of a floating offshore wind turbine system using a variable-speed generator-torque controller. *Renewable Energy*, **97**, 230-242.

Quallen S, Xing T, Carrica P, Li Y, Xu J (2014). CFD Simulation of a Floating Offshore Wind Turbine System Using a Quasi-static Crowfoot Mooring-Line Model. *Journal of Ocean and Wind Energy*, **1**(3), 143-152.

Rafiee R, Moradi M, Khanpour M (2016). The influence of material properties on the aeroelastic behavior of a composite wind turbine blade. *Journal of Renewable and Sustainable Energy*, **8**(6), 063305.

Ren N, Li Y, Ou J (2014). Coupled wind-wave time domain analysis of floating offshore wind turbine based on Computational Fluid Dynamics method. *Journal of Renewable and Sustainable Energy*, **6**(2), 023106-1-13.

Roald L, Jonkman J, Robertson A, Chokani N (2013). The Effect of Second-order Hydrodynamics on Floating Offshore Wind Turbines. *Energy Procedia*, **35**, 253-264.

Robertson A, Jonkman J, Masciola M, Song H, Goupee A, Coulling A, Luan C. Definition of the semisubmersible floating system for phase II of OC4. 2014a.

Robertson A, Jonkman J, Vorpahl F, Popko W, Qvist J, Frøyd L, Chen X, Azcona J, Uzunoglu E, Soares CG (2014b). Offshore code comparison collaboration continuation within IEA Wind Task 30: Phase II results regarding a floating semisubmersible wind system. *ASME 2014 33rd International Conference on Ocean, Offshore and Arctic Engineering*, San Francisco, California, p. V09BT09A012-V09BT09A012.

Robertson AN, Jonkman JM (2011). Loads Analysis of Several Offshore Floating Wind Turbine Concepts. *Twenty-first (2011) International Offshore and Polar Engineering Conference*, Maui, Hawaii, USA, p. 443-450.

Robertson AN, Wendt F, Jonkman JM, Popko W, Borg M, Bredmose H, Schlutter F, Qvist J, Bergua R, Harries R, Yde A, Nygaard TA, Vaal JBd, Oggiano L, Bozonnet P, Bouy L, Sanchez CB, García RG, Bachynski EE, Tu Y, Bayati I, Borisade F, Shin H, van der Zee T, Guerinel M (2016). OC5 Project Phase Ib: Validation of Hydrodynamic Loading on a Fixed, Flexible Cylinder for Offshore Wind Applications. *Energy Procedia*, **94**, 82-101.

Robertson AN, Wendt F, Jonkman JM, Popko W, Dagher H, Gueydon S, Qvist J, Vittori F, Azcona J, Uzunoglu E, Soares CG, Harries R, Yde A, Galinos C, Hermans K, de Vaal JB, Bozonnet P, Bouy L, Bayati I, Bergua R, Galvan J, Mendikoa I, Sanchez CB, Shin H, Oh S, Molins C, Debruyne Y (2017). OC5 Project Phase II:

Validation of Global Loads of the DeepCwind Floating Semisubmersible Wind Turbine. *Energy Procedia*, **137**, 38-57.

Robertson AN, Wendt FF, Jonkman JM, Popko W, Vorpahl F, Stansberg CT, Bachynski EE, Bayati I, Beyer F, de Vaal JB, Harries R, Yamaguchi A, Shin H, Kim B, van der Zee T, Bozonnet P, Aguilo B, Bergua R, Qvist J, Qijun W, Chen X, Guerinel M, Tu Y, Yutong H, Li R, Bouy L (2015). OC5 Project Phase I: Validation of Hydrodynamic Loading on a Fixed Cylinder. *The Twenty-fifth International Ocean and Polar Engineering Conference*, Kona, Hawaii, USA.

Roddier D, Cermelli C, Aubault A, Weinstein A (2010). WindFloat: A floating foundation for offshore wind turbines. *Journal of Renewable and Sustainable Energy*, **2**(3), 1-34.

Rusche H (2002). *Computational Fluid Dynamics of Dispersed Two-phase Flows at High Phase Fractions*. Doctoral Dissertation, University of London, London.

Sackniess PT (2010). *Fluttereffect analysis of horizontal windturbines in example of a generic 61.5 m rotorblade via MBS-simulation with MBDyn*. Diploma Thesis, Rheinisch-Westfälische Hochschule Aachen

Sanderse B, van der Pijl SP, Koren B (2011). Review of computational fluid dynamics for wind turbine wake aerodynamics. *Wind Energy*, **14**(7), 799-819.

Santoni C, Carrasquillo K, Arenas-Navarro I, Leonardi S (2017). Effect of tower and nacelle on the flow past a wind turbine. *Wind Energy*, **20**(12), 1927-1939.

Sasan S, Hamid Sarlak C, Stefan I, Robert FM (2014). Numerical investigation of the wake interaction between two model wind turbines with span-wise offset. *Journal of Physics: Conference Series*, **524**(1), 012137.

Sebastian T, Lackner MA (2012). Development of a free vortex wake method code for offshore floating wind turbines. *Renewable Energy*, **46**, 269-275.

Sethuraman L, Venugopal V (2013). Hydrodynamic response of a stepped-spar floating wind turbine: Numerical modelling and tank testing. *Renewable Energy*, **52**, 160-174.

Shen M, Hu Z, Liu G (2016). Dynamic response and viscous effect analysis of a TLP-type floating wind turbine using a coupled aero-hydro-mooring dynamic code. *Renewable Energy*, **99**, 800-812.

Shen WZ, Zhang JH, Sørensen JN (2009). The Actuator Surface Model: A New Navier–Stokes Based Model for Rotor Computations. *Journal of Solar Energy Engineering*, **131**(1), 011002-011002-9.

Shen Z-r, Wan D-c (2016). An irregular wave generating approach based on naoe-FOAM-SJTU solver. *China Ocean Engineering*, **30**(2), 177-192.

Shen Z-r, Ye H-x, Wan D-c (2014). URANS simulations of ship motion responses in long-crest irregular waves. *Journal of Hydrodynamics, Ser. B*, **26**(3), 436-446.

Shen Z, Cao H, Ye H, Liu Y, Wan D (2013). Development of CFD Solver for Ship and Ocean Engineering Flows. *8th International OpenFOAM Workshop*, Jeju, Korea.

Shen Z, Wan D, Carrica PM (2015). Dynamic overset grids in OpenFOAM with application to KCS self-propulsion and maneuvering. *Ocean Engineering*, **108**, 287-306.

Sivalingam K, Bahuguni A, Gullman-Strand J, Davies P, Tan Nguyen V (2015). Effects Of Platform Pitching Motion On Floating Offshore Wind Turbine (FOWT) Rotor. *Offshore Technology Conference*, Houston, Texas, USA, p. 17.

Smith RJ, Colin J (2001). Statics of a three component mooring line. *Ocean Engineering*, **28**(7), 899-914.

Snel H (2003). Review of aerodynamics for wind turbines. *Wind Energy*, **6**(3), 203-211.

Sørensen JNr, Shen WZ (2002). Numerical Modeling of Wind Turbine Wakes. *Journal of Fluids Engineering*, **124**(2), 393-399.

Sørensen NN, Johansen J (2007). UPWIND, aerodynamics and aero-elasticity rotor aerodynamics in atmospheric shear flow. *European Wind Energy Conference*, Milan, Italy.

Statoil. Hywind-the world's leading floating offshore wind solution. 2009. Available from: https://www.statoil.com/en/what-we-do/hywind-where-the-wind-takes-us.html.

Subbulakshmi A, Sundaravadivelu R (2016). Heave damping of spar platform for offshore wind turbine with heave plate. *Ocean Engineering*, **121**, 24-36.

Tao L, Thiagarajan KP, Cheng L (2000). On the parametric dependence of springing damping of TLP and Spar columns. *Applied Ocean Research*, **22**(5), 281-294.

Thiagarajan KP, Troesch AW (1994). Hydrodynamic Heave Damping Estimation and Scaling for Tension Leg Platforms. *Journal of Offshore Mechanics and Arctic Engineering*, **116**(2), 70-76.

Tran T, Kim D, Song J (2014). Computational Fluid Dynamic Analysis of a Floating Offshore Wind Turbine Experiencing Platform Pitching Motion. *Energies*, **7**(8), 5011-5026.

Tran TT, Kim D-H (2015). The coupled dynamic response computation for a semi-submersible platform of floating offshore wind turbine. *Journal of Wind Engineering and Industrial Aerodynamics*, **147**, 104-119.

Tran TT, Kim D-H (2016a). A CFD study into the influence of unsteady aerodynamic interference on wind turbine surge motion. *Renewable Energy*, **90**, 204-228.

Tran TT, Kim D-H (2016b). Fully coupled aero-hydrodynamic analysis of a semi-submersible FOWT using a dynamic fluid body interaction approach. *Renewable Energy*, **92**, 244-261.

Tran TT, Kim D-H (2018). A CFD study of coupled aerodynamic-hydrodynamic loads on a semisubmersible floating offshore wind turbine. *Wind Energy*, **21**(1), 70-85.

University of Maine. Floating Offshore Wind in Maine. 2017. Available from: https://composites.umaine.edu/offshorewind/.

Van den Boom H (1985). Dynamic behaviour of mooring lines. *BOSS Conference, Delft*, p. 359-368.

van der Laan MP, Sørensen NN, Réthoré P-E, Mann J, Kelly MC, Troldborg N (2015). The k-ε-fP model applied to double wind turbine wakes using different actuator disk force methods. *Wind Energy*, **18**(12), 2223-2240.

Walton TS, Polachek H. Calculation of nonlinear transient motion of cables. 1959.

Walton TS, Polachek H (1960). Calculation of transient motion of submerged cables. *Mathematics of computation*, **14**(69), 27-46.

WAMIT. WAMIT User Manual. 2017. Available from: http://www.wamit.com/manual.htm.

Wang L-z, Guo Z, Yuan F (2010). Quasi-static three-dimensional analysis of suction anchor mooring system. *Ocean Engineering*, **37**(13), 1127-1138.

Wang L, Liu X, Kolios A (2016). State of the art in the aeroelasticity of wind turbine blades: Aeroelastic modelling. *Renewable and Sustainable Energy Reviews*, **64**, 195-210.

Wang L, Liu X, Renevier N, Stables M, Hall GM (2014). Nonlinear aeroelastic modelling for wind turbine blades based on blade element momentum theory and geometrically exact beam theory. *Energy*, **76**, 487-501.

Wang Q, Sprague MA, Jonkman J, Johnson N, Jonkman B (2017). BeamDyn: a high-fidelity wind turbine blade solver in the FAST modular framework. *Wind Energy*, **20**(8), 1439-1462.

Waris MB, Ishihara T (2010). Influence of mooring force estimation on dynamic response of floating offshore wind turbine system. *Renewable Energy 2010 International Conference*, Yokohama, Japan.

Waris MB, Ishihara T (2012). Dynamic response analysis of floating offshore wind turbine with different types of heave plates and mooring systems by using a fully nonlinear model. *Coupled Systems Mechanics*, **1**(3), 247-268.

WindEurope. The European offshore wind industry: Key trends and statistics 2016. 2017a.

WindEurope. Unleashing Europe's offshore wind potential - A new resource assessment. 2017b.

WindEurope. Wind energy in Europe: Outlook to 2020. 2017c.

WindEurope. Wind in power: 2016 European statistics. 2017d.

Wood C, Gil AJ, Hassan O, Bonet J (2010). Partitioned block-Gauss–Seidel coupling for dynamic fluid–structure interaction. *Computers & Structures*, **88**(23–24), 1367-1382.

Wu C-HK, Nguyen V-T (2017). Aerodynamic simulations of offshore floating wind turbine in platform-induced pitching motion. *Wind Energy*, **20**(5), 835-858.

Wu J, Ding J-h, He Y-p, Zhao Y-s (2015). Study on Unsteady Aerodynamic Performance of Floating Offshore Wind Turbine by CFD Method. *The Twenty-fifth International Offshore and Polar Engineering Conference*, Kona, Hawaii, USA, p. 554-560.

Yu DO, Kwon OJ (2014). Predicting wind turbine blade loads and aeroelastic response using a coupled CFD–CSD method. *Renewable Energy*, **70**, 184-196.

Zahle F, Sørensen NN, Johansen J (2009). Wind turbine rotor-tower interaction using an incompressible overset grid method. *Wind Energy*, **12**(6), 594-619.

Zhang P, Huang S (2011). Review of aeroelasticity for wind turbine: Current status, research focus and future perspectives. *Frontiers in Energy*, **5**(4), 419-434.

Zhang R, Tang Y, Hu J, Ruan S, Chen C (2013). Dynamic response in frequency and time domains of a floating foundation for offshore wind turbines. *Ocean Engineering*, **60**, 115-123.

Zhang Y, Gillebaart T, van Zuijlen A, van Bussel G, Bijl H (2017). Experimental and numerical investigations of aerodynamic loads and 3D flow over non-rotating MEXICO blades. *Wind Energy*, **20**(4), 585-600.

Zhao W, Cheng P, Wan D (2014). Numerical Computation of Aerodynamic Performances of NREL Offshore 5-MW Baseline Wind Turbine. *The Eleventh ISOPE Pacific/Asia Offshore Mechanics Symposium*, Shanghai, China p. 13-18.

Publications

Journal Articles

Liu Y, Xiao Q, Incecik A, Peyrard C, Wan D (2017). Establishing a fully coupled CFD analysis tool for floating offshore wind turbines. *Renewable Energy*, **112**, 280-301.

Liu Y, Xiao Q, Incecik A, Wan D (2016). Investigation of the effects of platform motion on the aerodynamics of a floating offshore wind turbine. *Journal of Hydrodynamics, Ser. B*, **28**(1), 95-101.

Liu Y, Xiao Q, Incecik A, Peyrard C. Aeroelastic analysis of a floating offshore wind turbine in platform-induced surge motion using a fully coupled CFD-MBD method. *Wind Energy* (under review).

Conference Papers

Liu Y, Xiao Q, Incecik A (2017). A coupled CFD/Multibody Dynamics analysis tool for offshore wind turbines with aeroelastic blades. In Proceedings of the *ASME 2017 36th International Conference on Ocean, Offshore and Arctic Engineering*. Trondheim, Norway. Paper No. OMAE2017-61062. (Received 2017 OMAE Subrata Chakrabarti Young Professional Award)

Liu Y, Peng Y, Wan D (2015). Numerical investigation on interaction between a semi-submersible platform and its mooring system. In Proceedings of the *ASME 2015 34th International Conference on Ocean, Offshore and Arctic Engineering*. St. John's, Newfoundland, Canada. Paper No. OMAE2015-41294.

Liu Y, Xiao Q, Incecik A, Wan D (2015). Investigation of the effects of the platform motion on the aerodynamics of a floating offshore wind turbine. In Proceedings of the *9th International Workshop on Ship Hydrodynamics*. Glasgow, UK.

Liu Y, Wan D, Xiao Q, Incecik A (2014). Investigation on motion responses of a semi-submersible platform and its mooring system. In Proceedings of the *2nd International Conference on Maritime Technology*. Glasgow, UK.